

A STUDY OF THE GLOBAL PROPERTIES OF HADRONIC MATTER AT LARGE DENSITIES

François Lamarche

Physics Department
McGill University, Montreal

A thesis submitted to the Faculty
of Graduate Studies and Research
in partial fulfillment of the
requirements for the PhD degree

May 14, 1989

(c) François Lamarche, 1989

Abstract

We present a study of the properties of the nuclear matter under extreme conditions of density and temperature, using collisions of heavy-nuclei measured in the experiment NA34. The emphasis is given to the study of the variation of the properties of average central collisions with the sizes of the colliding nuclei. The projectiles used are 200 GeV protons, 60 and 200 GeV/nucleon ^{16}O nuclei, and 200 GeV/nucleon ^{32}S nuclei. The targets are thin disks of aluminum, copper, silver, tungsten, platinum, lead and uranium nuclei. The energy density achieved in these collisions, of the order of $10 \text{ GeV}/\text{fm}^3$, is a necessary (but not sufficient) condition to create a plasma of quarks and gluons. We investigate whether an hydrodynamic description is appropriate for our data, in which case, from the observation of the work done by the hydrodynamic forces, constraints are obtained on the properties of the hypothetical plasma.

Résumé

Nous présentons une étude des propriétés de la matière nucléaire dans des conditions extrêmes de densité et de température, en utilisant des collisions d'ions lourds mesurées avec précision dans le cadre de l'expérience NA34. L'emphase est mise sur l'étude des variations des propriétés des collisions centrales moyennes avec la taille des noyaux. Les projectiles employés sont des protons de 200 GeV, des noyaux d'oxygène accélérés à 60 et à 200 GeV par nucléon, et des noyaux de soufre accélérés à 200 GeV par nucléon. Les cibles sont des disques minces d'aluminium, de cuivre, d'argent, de tungstène, de platine, de plomb et d'uranium. La densité d'énergie atteinte dans ces collisions est de l'ordre de $10 \text{ GeV}/\text{fm}^3$, ce qui est la condition nécessaire (mais non suffisante) de la création d'un plasma de quarks et de gluons. Nous recherchons dans quelle mesure une description hydrodynamique est appropriée pour nos données, et à partir du travail accompli par les forces hydrodynamiques, nous obtenons des contraintes sur les propriétés du plasma si celui-ci est formé.

Statement of originality

The following are original contributions by the author:

- development of the concept of hydrodynamic work done by longitudinal expansion.
- development of the computer code for simulating the longitudinal expansion.
- recognition that the freeze-out does not occur at a finite proper time but at a finite coordinate time.
- with A. Angelis and M. Sernan, maintenance of energy flow logic and design/construction of a new test set-up for testing $\Sigma 1$ units. Calibration of the energy flow system.
- participation in the maintenance of the energy flow triggers
- with Y. Sirois, 'offline' calibration of scintillator calorimeters
- with G. Poulard, event filtering from raw data tapes during the ion runs.
- suggested simple method for measuring transverse energy in the forward calorimeters.
- developed method for measuring transverse energy resolutions from measurements of transverse momentum imbalances.
- development with H.H. Thodberg of computer methods for evaluating number of collisions in NCM models.
- later development of analytical methods.
- with H.H. Thodberg, recognition of the effect of nuclear deformation.
- later development of analytic formula for effect of deformation.

- analytic formula for the volume of intersection of a sphere and a cylinder in the general case, implementation in a computer code, and use to compute the rapidity of the center of mass of participants.
- idea to use forward/backward symmetry of nature to intercalibrate the measurement of transverse energy in the scintillator calorimeters with the measurement of transverse energy in the liquid argon calorimeter.

Preface

In this work, we will present the results of researches made in the framework of the HELIOS Collaboration, to investigate the creation of hadronic matter with large energy densities in collisions of ions accelerated at relativistic energies with nuclei at rest at the CERN SPS. In 1984, the HELIOS multi-purpose experiment started the installation of its set-up in the north fixed target area of the Super Proton Synchrotron at the CERN European Laboratory in Geneva. The experiment (NA34) took data with oxygen ions accelerated to 60 and 200 GeV nucleon in november, december 1986, and with sulfur ions of 200 GeV nucleon energy in september october 1987. In the latter period, there was in addition a short run with 200 GeV nucleon ^{16}O ions. The data with 200 GeV protons, taken for comparison purposes, come from runs in november 1986, september 1987, and april 1988¹.

It is important to recognize the inherent complexity of the phenomenology of heavy-ion collisions before we attempt to make numerical estimates of the properties of hadronic matter at large energy densities. In the first chapter of this thesis, I will first introduce the relevant theoretical background, showing in which cases a thermodynamical, a classical, or a quantum mechanical approaches are relevant. Several models for describing high-energy hadron-hadron collisions (the simplest case of nuclear collisions) will be shown, together with their generalizations to large nuclei. The hydrodynamic picture will be presented, in which the fundamental concept is neither the amplitudes of quantum-mechanical waves, nor the individual particles, but classical waves together with thermodynamical properties.

In the second chapter, we will show how the HELIOS experimental set-up measures the properties of the large density hadronic matter. It provides, with the help of an efficient trigger system, a large statistics sample of events with distinctive characteristics instead of a reconstruction of

¹ Throughout this thesis, following the universal practice of the high energy physics community, energies are given in GeV ($1\text{GeV} = 10^9\text{eV} = 1.602 \times 10^{-13}\text{J}$), distances in fermi ($1\text{fm} = 10^{-15}\text{m}$), and cross-sections in barn ($1\text{b} = 10^{-28}\text{m}^2$). A complete list of equivalents in the SI (international system of metric units) can be found in the "Review of Particle Properties" by M. Aguilar-Benitez et al, Phys. Lett. B170(1986)1. Certain theoretical computations are eased by considering $\hbar = c = 1$. However, when a numerical evaluation is necessary, the factors of \hbar ($\approx 0.2 \text{ GeV}\cdot\text{fm}$) and c ($\approx 3 \times 10^8 \text{ m/s}$) needed by dimensional arguments are explicitied.

the 4-vectors of all the particles produced in each collision. Global measurements of energy flow and multiplicity are thus available with high statistics, using calorimeters and silicon hodoscopes. A spectrometer able to measure four-vector and charge of individual particles, on a limited solid angle, will also be presented.

The details of the analysis procedure, which provides an accurate counting of events together with a precise scale of energy and multiplicity for the computation of differential cross-sections, will be the subject of the third chapter. We use Monte Carlo simulations together with corrections by analytical functions to establish most exact distributions of the physical observables from imperfect measurements.

In the fourth chapter, we will present the corrected distributions and discuss their comparisons with a broad range of models. We show in details the repartition of the transverse energy $E_T = \sum p_T \sin \theta$ (where θ is the polar angle with respect to the beam direction) in pseudorapidity $^2 \eta = - \ln \tan \theta/2$. We attempt to synthesize and summarize the wealth of experimental informations gathered by the studies

In the fifth chapter, we draw strict conclusions from the experimental study, and present reaction models hinted by them

I would like to thank all members of the collaboration, and particularly all those who took an active part in the careful operation of the detector in the running periods ³. The measurements were made possible by the dedication of the CERN technical staff who contributed to the superb performance of the PS-SPS accelerator complex, and by the support of the CERN DD division staff.

I want to thank my supervisor, Professor Claude Leroy, for his continuous support, his productive criticism, and many hours of interesting discussions of subjects ranging from technical details to fundamental concepts

I am indebted to Dr C W Fabjan, Dr W. Willis and our spokesman Dr G. London for their encouragements and trust, and for many knowledgeable discussions. I would like also to express my gratitude to Dr G. London and Dr J P. Pansart for providing Monte Carlo data tapes produced by the Dual Parton Model physics generator IRIS 2.01.

² This variable is particularly useful since it approximates the Lorentz-invariant rapidity variable

³ The complete list of members of the HELIOS Collaboration can be found in ref. [85].

I gratefully acknowledge the help I have received from many people at CERN, too numerous to be individually thanked here, that have made my work most enjoyable.

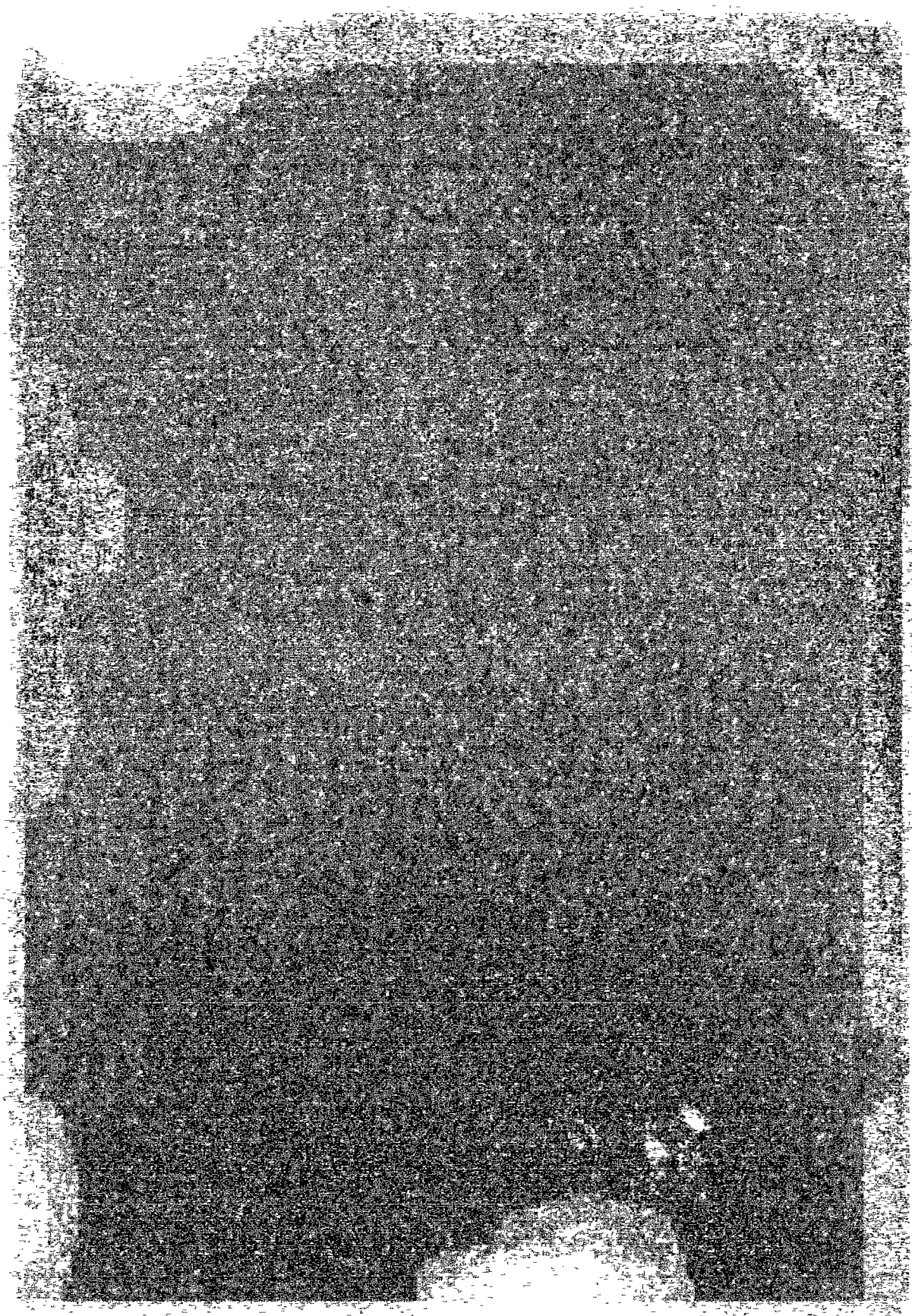
Finally, let me thank the National Science and Engineering Research Council of Canada for its financial support

Contents

Abstract	ii
Résumé	iii
Statement of originality	iv
Preface	vi
Chapter 1: Introduction: How one must describe relativistic nuclear collisions	1
1.1 The force between and inside hadrons.	1
1.2 Nuclear collisions at ultrarelativistic energies.	2
1.3 The different phases of nuclear matter	3
1.4 Phenomenology of the Quark Gluon Plasma	4
1.5 Quantum mechanical vs classical description of nuclear collisions.	10
1.5.1 Quantum effects	10
1.5.2 Classical effects	12
1.6 The evaluation of the 'maximum' energy density of a fireball	12
1.6.1 The contribution of cascading to the transverse energy production	13
1.7 Relativistic nuclear collisions as many hadron-hadron collisions	16
1.8 Model of nucleon-nucleon interactions and generalizations to nucleus-nucleus	17
1.9 The dual parton model	17
1.9.1 Extension to nucleus-nucleus collisions.	21
1.9.2 Monte Carlo realizations of the Dual Parton Model	22
1.10 The Lund model for hadron collisions and FRITIOF	23
1.11 Wounded nucleon models and overlap integral models.	23
1.12 The hydrodynamic approach	25
1.12.1 Some hydrodynamic phenomenology – the dominant longitudinal expansion	26
1.12.2 Shock waves.	28
1.13 A realistic hydrodynamic simulation.	30

1.13.1 Effect on angular energy correlations	35
Chapter 2: The HELIOS detectors and experimental conditions	37
2.1 The beam conditions	37
2.2 Survey of the experimental set-up	38
2.3 The HELIOS trigger system	39
2.3.1 Proper design of the beam telescope with respect to upstream interactions	43
2.4 Description of the silicon multiplicity detectors.	45
2.4.1 Analysis of the data from the Silicon detector PADC's	47
2.5 Description of the calorimeters	48
2.5.1 The uranium liquid argon calorimeter (ULAC)	55
2.5.2 The calibration of the uranium/liquid argon calorimeter	57
2.6 The energy flow trigger system.	58
2.7 The external spectrometer	66
Chapter 3: Data reduction and analysis	68
3.1 Selection of ^{16}O and ^{32}S interactions in the target	68
3.1.1 Non target interactions in the vicinity of the target.	71
3.2 The distributions of raw transverse energy.	75
3.2.1 The E_T trigger efficiency	75
3.2.2 The subtraction of empty target contamination	78
3.3 The absolute normalization of the cross-sections.	80
3.4 The pseudorapidity distributions of transverse energy.	81
3.5 The hadronic part of the ULAC	83
3.6 Event-by-event correction for the energy at zero degree	86
3.7 Monte Carlo correction of pseudorapidity distributions.	88
3.7.1 Principle of operation of the correction	89
3.7.2 Specific assumptions and results.	91
3.8 Monte Carlo corrections for the transverse energy distributions	93
3.8.1 The corrections	94
3.8.2 Deconvolution of the distributions.	94
3.8.3 A method of measurement of the transverse energy resolution	95

Chapter 4: Experimental results and discussion	100
4.1 Introduction	100
4.2 The differential cross-sections.	101
4.2.1 200 GeV/c proton	101
4.2.2 60 GeV/nucleon oxygen	103
4.2.3 200 GeV/nucleon oxygen	107
4.2.4 200 GeV/nucleon sulfur	111
4.2.5 Sulfur cross-sections for E_T in a large domain of η	116
4.2.6 ^{16}O -W E_T distributions at several energies	123
4.2.7 Multiplicity	126
4.2.8 Comparison with IRIS and FRITIOF Monte Carlo	128
4.2.9 The main features of the ion distributions	129
4.2.10 Reduction of the data from the curves: NCM parametrization	130
4.2.11 The effect of nuclear deformation on transverse energy fluctuations	132
4.2.12 Extraction of the mean transverse energy of central collisions	133
4.3 The A-dependence of the transverse energy production	136
4.4 Interpretation of the transverse energy in central collisions	138
4.4.1 Comparison with the Wounded Nucleon Model (WNM)	138
4.4.2 Comparison with the Nucleon collision model (NCM)	139
4.5 Correlations between the forward and the backward transverse energy	141
4.5.1 Double differential cross-section $d^2\sigma/dE_{TB}dE_{TF}$	142
4.6 Fractional E_T density in pseudorapidity	148
4.7 Hydrodynamic phenomenology and estimates of the energy density	157
4.7.1 Comparison with first moment	158
4.7.2 Comparison with width	159
4.7.3 Attempt to identify an exclusive signature of hydrodynamics	159
4.7.4 Stopping, energy density and Equation Of State (EOS).	161
4.8 Results from the external spectrometer	163
Chapter 5: Conclusions	165
Appendix A: Exact formulae for hard-sphere nuclei.	168
A.1 The number of nucleons in the central tunnel	168
A.2 The number of collisions and the overlap integral in the central case	169
A.3 Participant volume at non-zero impact parameter	170



Figures

1.	Phase diagram of hadronic matter.	4
2.	Energy density as a function of temperature.	7
3.	Pressure as a function of temperature.	8
4.	The contribution of non-directly hit nucleons (cascading)	14
5.	The two-chain structure of the basic diagram of the DPM.	19
6.	Rapidity distribution of transverse energy in the DPM.	21
7.	Collision of two slabs of non-viscous hadronic matter.	30
8.	Energy density from a simple hydrodynamic simulation.	32
9.	Contour plot of the invariant energy density.	33
10.	The rapidity distribution of invariant energy density.	34
11.	Fireball parameters as a function of the freeze-out time.	35
12.	Layout of HELIOS (NA34) experimental set-up.	38
13.	Block diagram of the trigger logic main components.	40
14.	E_T distribution of non-target interactions.	44
15.	Layout of the charged multiplicity counters.	46
16.	Pulseheight distribution of a silicon detector element.	47
17.	Overview of the calorimeters in the 1986 set-up.	49
18.	Overview of the calorimeters in the 1987 set-up.	50
19.	Artist's view of the calorimetrized dipole magnet.	52

20.	Linearity as a function of calibration constants.	54
21.	Towers in the electromagnetic part of ULAC.	57
22.	Linearity of the energy flow chain.	63
23.	Set-up for testing $\Sigma 1$ units.	64
24.	Digital summing tree for transverse energy.	65
25.	Plan view of the external spectrometer.	67
26.	Mass spectrum built from the measured energy with ^{16}O beam.	69
27.	Mass spectrum built from the measured energy with ^{32}S beam.	70
28.	Cuts for the 1986 data in measured multiplicity and E_T	72
29.	Lego plot of the correlation function and E_{TB} (target in).	73
30.	Lego plot of the correlation function and E_{TB} (no target).	74
31.	Overlap of the dN/dE_{TB} for the various E_{TB} thresholds.	76
32.	Overlap of the dN/dE_T for the various E_{TB} thresholds.	77
33.	Remaining background fraction in dN/dE_{TB}	79
34.	Remaining background fraction in dN/dE_T	80
35.	The face of all towers of the HELIOS calorimeter in η, ϕ space.	83
36.	Energy deposition lateral profile for protons.	87
37.	Energy deposition lateral profile for ^{32}S	88
38.	Matrix of response in pseudorapidity calculated by Monte Carlo.	90
39.	Correction factor as a function of pseudorapidity.	93
40.	Measurement of transverse energy resolution.	99

41.	E_{TB} differential cross-sections for incident 200 GeV p	102
42.	E_{TB} distributions for incident 60 GeV/nucleon ^{16}O .	106
43.	E_{TB} distributions for incident 200 GeV/nucleon ^{16}O .	110
44.	E_{TB} distributions for incident 200 GeV/nucleon ^{32}S .	115
45.	E_T distributions for incident 200 GeV/nucleon ^{32}S .	122
46.	E_T differential cross-sections in $^{16}\text{O} - \text{W}$ collisions.	125
47.	Charged multiplicity distribution in $^{32}\text{S} - \text{W}$ collisions.	127
48.	Comparison of transverse energy distributions with IRIS and FRTIOF	128
49.	A-dependence of transverse energy in central collisions.	137
50.	Transverse energy per wounded nucleon in central collisions.	139
51.	E_{TB} per nucleon-nucleon collision versus number of collisions.	140
52.	E_T per nucleon-nucleon collision versus number of collisions.	141
53.	Double differential cross-section to produce E_{TB} and E_{TF}	143
54.	Regression of the E_{TF} as a function of E_{TB} in $^{32}\text{S} - \text{W}$ collisions.	144
55.	Regression of the E_{TB} as a function of E_{TF} in $^{32}\text{S} - \text{W}$ collisions.	145
56.	Differential cross-section versus E_{TB} and E_{TF} in $^{32}\text{S} - \text{Al}$ collisions.	146
57.	Gaussian fit of the pseudorapidity distribution of transverse energy.	149
58.	Event-to-event fluctuations of the average pseudorapidity.	153
59.	First moment of the pseudorapidity distribution of transverse energy.	154
60.	Width of the pseudorapidity distribution of transverse energy.	155
61.	Width versus first moment for $^{32}\text{S} - \text{W}$ central collisions.	156

62.	Hydrodynamic prediction of the pseudorapidity distribution of transverse energy.	158
63.	Hydrodynamically induced energy flow correlation versus multiplicity.	160
64.	Inverse slope of transverse momentum distributions versus E_{TB}	164

Tables

1.	Calibration factors for the uranium modules.	55
2.	Summary of the factors implemented electronically in the summing	62
3.	^{16}O -Al backward transverse energy differential cross-section at 60 GeV nucleon.	103
4.	^{16}O -Ag backward transverse energy differential cross-section at 60 GeV nucleon.	104
5.	^{16}O -W backward transverse energy differential cross-section at 60 GeV nucleon.	105
6.	^{16}O -Al backward transverse energy differential cross-section at 200 GeV nucleon.	108
7.	^{16}O -Ag backward transverse energy differential cross-section at 200 GeV nucleon.	108
8.	^{16}O -W backward transverse energy differential cross-section at 200 GeV nucleon.	109
9.	^{32}S -Al backward transverse energy differential cross-section at 200 GeV nucleon.	111
10.	^{32}S -Ag backward transverse energy differential cross-section at 200 GeV/nucleon.	112
11.	^{32}S -W backward transverse energy differential cross-section at 200 GeV nucleon.	112
12.	^{32}S -Pt backward transverse energy differential cross-section at 200 GeV nucleon.	113
13.	^{32}S -Pb backward transverse energy differential cross-section at 200 GeV nucleon.	113
14.	^{32}S -U backward transverse energy differential cross-section at 200 GeV/nucleon.	114
15.	^{32}S -Al transverse energy differential cross-section at 200 GeV/nucleon.	116
16.	^{32}S -Ag transverse energy differential cross-section at 200 GeV/nucleon.	117
17.	^{32}S -W transverse energy differential cross-section at 200 GeV/nucleon.	118
18.	^{32}S -Pt transverse energy differential cross-section at 200 GeV/nucleon.	119
19.	^{32}S -Pb transverse energy differential cross-section at 200 GeV/nucleon.	120

20.	$^{32}\text{S-U}$ transverse energy differential cross-section at 200 GeV/nucleon.	121
21.	$^{16}\text{O-W}$ transverse energy differential cross-section at 60 GeV/nucleon	123
22.	$^{16}\text{O-W}$ transverse energy differential cross-section at 200 GeV/nucleon	124
23.	Summary of all geometrical parametrizations.	131
24.	Summary of the stopping fractions for average central collisions	162

Chapter 1

Introduction: How one must describe relativistic nuclear collisions

1.1 The force between and inside hadrons.

The discovery of the mechanism of the strong force has proceeded in two steps: It was first discovered that the nucleons (the proton, the neutron) that make up the nuclei were interacting via the exchange of mesons. In a second step, regularities in the spectrum of mesons, and scattering experiments at large momentum transfers, showed that mesons and nucleons, hadrons in general, are composite. The nuclear binding force would then be a residual manifestation of the strong force acting between the constituents (partons) that build the hadrons, this would be similar to chemical bonding, which is a residual manifestation of the electric force binding electrons in atoms. The relevant theory of the strong interactions between constituents is widely believed to be Quantum ChromoDynamics (QCD). The constituents are then coloured quarks, and massless vector gauge fields called gluons. Like quantum electrodynamics (QED), QCD is a gauge interaction, which means that massless vector gauge quanta ensure the invariance of the theory under local transformations of the quantum-mechanical phase. However, these two theories have a difference which lies in the fact that the $U(1)$ operators of QED commute, whereas the $SU(3)$ operators of QCD do not commute. The gluons are thus themselves colour charged. Non-abelian gauge theories such as QCD were shown to be renormalizable [1]. This gives QCD strong theoretical grounds as a candidate for explaining the strong force. Such theories have also the property of asymptotic freedom or antiscreening: the interaction becomes weaker at large momentum transfers, and stronger at small momentum transfers, resulting in confinement of quarks and gluons inside hadrons, consistent with the fact that a single quark or gluon has never been observed [2]. In very dense or hot hadronic matter, it is expected that a phase consisting of unbound quarks and gluons should appear as a consequence of asymptotic freedom; this would be the QCD (Quark - Gluon) Plasma [3] (QGP), the word 'plasma' coming from an analogy with similar phenomena in atomic physics. In the plasma phase, the interaction between constituents can be computed by a perturbative expansion in α_s , which is (to a factor 4π) the square of the momentum-dependent colour unit charge:

$$\alpha_s(Q^2) = \frac{4\pi}{(11 - \frac{2}{3}N_f)\ln(Q^2/\Lambda_{QCD}^2)} \quad (1)$$

Here, N_F is the number of flavours and Λ_{QCD} is the QCD mass scale ($\Lambda_{\text{QCD}} \approx 200 \text{ MeV}$ is a canonical value that appears to be confirmed experimentally [4]).

Continuing the analogy with atomic physics, it could be viewed as the equivalent of an insulator-conductor transition in atomic physics: at low density, quarks and gluons form colour-neutral bound states, and hence hadronic matter is a colour insulator. At sufficiently high density or temperature, the hadrons interpenetrate each other and the matter becomes a colour conducting plasma.

1.2 Nuclear collisions at ultrarelativistic energies.

The field of nuclear collisions at relativistic energies is one of considerable complexity. Elements from various fields of modern physics are needed to describe these collision processes and the subsequent particle production. The expression 'relativistic quantum statistical mechanics' summarizes the main aspects we will have to consider. Special relativity intervenes everywhere, not only because the incident beam has a velocity very close to the speed of light, but also since the produced particles have transverse energies frequently larger than their rest mass energy. Because very large numbers of particles are produced, we use statistical mechanics to compute inclusive cross-sections. If the number of particles and collisions becomes very large, the statistical mechanics yield a thermodynamical description of the production of secondaries, with an equation of state for nuclear matter, and possible phase transitions. Considering that the thermodynamical conditions are a function of space and time, we then have to consider the question of relativistic hydrodynamics [5][6]. The computation of the production rate of the various species of secondaries, requests the use of either equilibrium or out-of-equilibrium chemistry, especially for the production of strange quarks. It is important to note that the subjects of hydrodynamics and chemistry of the nuclear matter are only relevant if a thermodynamic description is possible, in other words, if the nuclear matter has undergone thermalization.

The aim of these studies of the complex details of nuclear collisions is to investigate the non-perturbative regime of QCD. QCD is the simplest theory devised yet for the nuclear forces, based on the principle of gauge forces, the postulated gauge group being $SU(3)$ colour. There is now quantitative evidence supporting QCD in its perturbative regime (see for instance [7]). To establish the QCD theory with the same level of confidence as the electroweak theory of Glashow, Weinberg and Salam [8], the other very successful non-abelian gauge theory, we need specific tests in the non-perturbative regime. In the non-perturbative regime, with the advent of lattice gauge theories [9], QCD can make numerical predictions for the masses of the hadrons, for the meson-nucleon couplings, and in particular it can very easily predict the equation of state of thermalized hadronic matter. There is the prediction of the existence of a state of deconfined constituents reached at large densities and pressures, and (at least in the case of zero net baryon density) of a first order phase

transition to reach this state starting from the normal confined state.

The study of heavy-ion collisions is thus a very complicated field of physics, where many different formalisms are needed to describe various aspects of the behaviour of matter, motivated by the hope of revealing the deconfinement phase transition predicted by the non-perturbative QCD theory.

1.3 The different phases of nuclear matter

The observation of a phase transition in a fluid composed of only a few particles in an extremely small volume (typically the size of a nucleus) may seem impossible considering the large difference of the scales with those at which solid-state physicists usually study phase transitions. Yet there is a recent precedent in the observation of a phase transition between the 'nuclear liquid' and the 'hadron gas' [10]. Thus there are known methods for observing phase transitions in nuclear matter. There are however many difficulties present in the case of the hadron gas plasma phase transition that were not present in the case of the nuclear liquid/hadronic gas phase transition. In contrast to the case of low energy nuclear reactions, in ultrarelativistic nuclear collisions the relativistic effects cannot be neglected, and the majority of the observed particles are created during the reaction. It has to be noted that independently of the existence or not of a first or second order phase transition, it is a fundamental prediction of QCD [11] that at sufficient density the quarks and gluons will be deconfined, yielding a state of matter known as the Quark Gluon Plasma (QGP). One possibility is that the hadronic gas will transform gradually into a QGP at high temperature just like an ordinary gas transforms into a ionized plasma when heated, without a phase transition [12].

The existence of a quark gluon plasma is compulsory in QCD since all the hadrons are colour neutral systems occupying a small volume, separated by regions of vacuum with a non-zero value of the gluon condensate. If the density is sufficient, the vacuum is expelled and the constituents of many hadrons share the same 'bag'. The existence of yet another phase has been suggested: the pion condensation phase. Since the pions are bosons, it is possible that they will undergo Bose-Einstein condensation at sufficient density and low enough temperature. At higher densities, the constituents of many pions will 'see' each other and the deconfined QGP phase will be reached.

The various phases of nuclear matter are summarized in Figure 1 where the temperature/density boundaries for the pion condensate and the QGP are pure guesses, but are of the right order of magnitude. The curve with an arrow is the expected evolution of the matter in a ultrarelativistic nuclear collision (heating and compression followed by cooling and expansion).

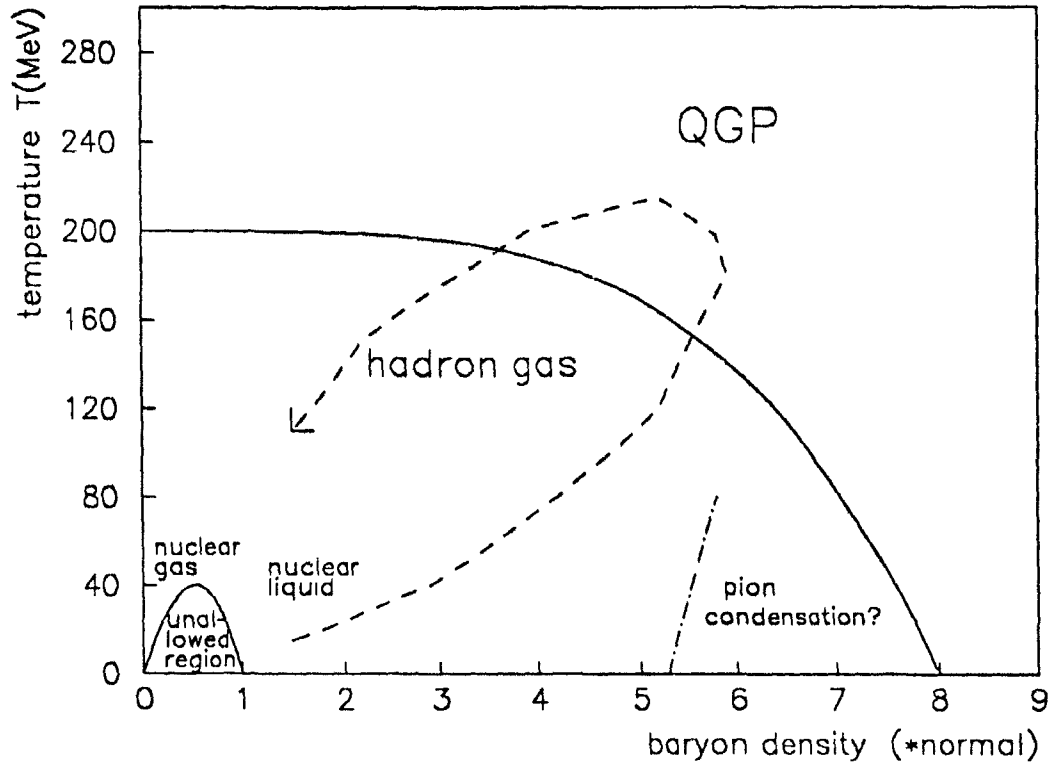


Figure 1: The various phases of nuclear matter, as a function of the temperature T and of the net baryon density, measured in units of the normal baryon density of nuclear matter. For the quark gluon plasma phase, the boundary is only an estimate of the order of magnitude.

1.4 Phenomenology of the Quark Gluon Plasma

Due to the larger number of degrees of freedom (8 types of gluons with 2 spin states ⁴, 18 types of (anti-)quarks with 2 spin states), the equation of state of the quark gluon plasma is different of that of the hadron gas. The quark-gluon plasma is an ideal gas in the sense that since the quarks and gluons are point-like, there is no Van der Waals correction for occupied volume. However, the

⁴ Like photons, the gluons are vector particles and should have 3 spin states, but they are massless, so that longitudinal degrees of freedom are unphysical and the number of spin states gets reduced to 2

plasma as a whole costs some energy per unit volume to expel the non-perturbative (physical) vacuum and replace it with the perturbative vacuum. The hadron gas does not have this term, but because the hadrons occupy a finite volume, there is a Van der Waals term to account for the volume occupied by the hadrons; In both cases, the particle density n and the energy density ε are function of the temperature only (the baryon density is considered as a negligible 'impurity'), and the pressure is obtained from the work done at constant number of particles:

$$P = \left(\frac{n}{\varepsilon} \frac{d\varepsilon}{dT} - \frac{dn}{dT} \right) \varepsilon \quad (2)$$

For a hadron gas with n_h massless bosonic degrees of freedom,

$$\varepsilon \approx n_h \frac{\pi^2}{30} T^4$$

while in the QGP, with $N = 3$ the number of colours:

$$\varepsilon = B + \frac{\pi^2}{30} T^4 \left[2(N^2 - 1) + \frac{7}{8}(4NN_F) \right]$$

where the constant B is called the bag pressure, and the number of flavours N_F can conservatively be taken as 2. The assumption of quasi-massless quarks was implicitly made. The factor $\frac{7}{8}$ accounts for the Fermi-Dirac statistics instead of Bose-Einstein, the factor 2 represents the counting of gluon spin states and the factor 4 accounts for the number of quark spin states and polarities (quark, antiquark). With these values:

$$\varepsilon_{QGP} = B + \frac{37\pi^2}{30} T^4$$

This value is about 10 times larger than the one that would be obtained in the gas of massless hadrons, taking $n_h = 3$ to count the three states of isotopic spin of the pion. This would also be the case if we consider $n_h = 4$ by including the contribution of the η meson, although it does not behave like a massless particle in the range of temperatures that we consider. However, it is not clear whether higher resonance (ρ , ω , etc . .) should be included. If we consider ρ as a distinct meson, it must be considered on the same footing as the pion. If the rho is just a bound state of two pions, the contribution of the rho is part of the contribution of the pion. The question is not purely academic, it has important consequences on the equation of state assumed by the hadron gas. If each resonance is taken to be a fundamental particle, due to the very large number of resonances, the energy density would reach very large values for relatively small temperatures. In the Hagedorn statistical bootstrap hypothesis [13] of an exponentially rising mass spectrum, the energy density

would even be infinite at a finite 'limit' temperature. A proper description of the hadron gas must certainly take into account the resonances, but it must also take into account the volume occupied by the various resonances. There is a logical way to take into account the volume occupied by the particles in the hadron gas, using the Van der Waals formalism [14]; however, in this work, we shall stay with a description of the hadron gas as a pion gas. The reader should simply remember that the real hadron gas can have less energy density than the idealized pion gas, and more pressure, due to the volume taken up by the pions. Also, the inclusion of massive resonances in the hadron gas would increase the energy density and decrease slightly the ratio pressure/energy density near the threshold for the massive particles.

In order to have mechanical stability when the two phases coexist (mixed phase), the phase transition occurs when the pressure in the two phases are equal. The pressure in the ideal pion gas is simply one third of the energy density:

$$P = \frac{1}{3}\varepsilon = \frac{\pi^2}{30} T^4$$

while in the QGP, application of (2) gives:

$$P = \frac{37\pi^2}{90} T^4 - B$$

So, at the critical temperature T_c :

$$\frac{37\pi^2}{90} T_c^4 - B = \frac{3\pi^2}{90} T_c^4 \quad \rightarrow \quad B = \frac{34\pi^2}{90} T_c^4 \quad \text{and} \quad T_c = \left(\frac{90B}{34\pi^2} \right)^{1/4}$$

The phase transition occurs at the temperature where the pressures of the two phases are equal. The 'latent heat' is then equal to the difference between the energy densities of the two phases:

$$\Delta\varepsilon = B + \frac{37\pi^2}{30} T_c^4 - \frac{3\pi^2}{30} T_c^4 = B + 3B = 4B$$

Using the standard value of the bag constant $B=0.6\text{GeV}/\text{fm}^3$, we get the critical temperature $T_c = \left(\frac{90B\hbar^3}{34\pi^2} \right)^{1/4} \approx 200\text{MeV}$ and the critical energy density $4B = 2.4 \text{ GeV}/\text{fm}^3$. Our approximate expressions for the energy density and for the pressure in each phase are plotted in Figure 2 and Figure 3 respectively, along with results from lattice gauge theory simulations.

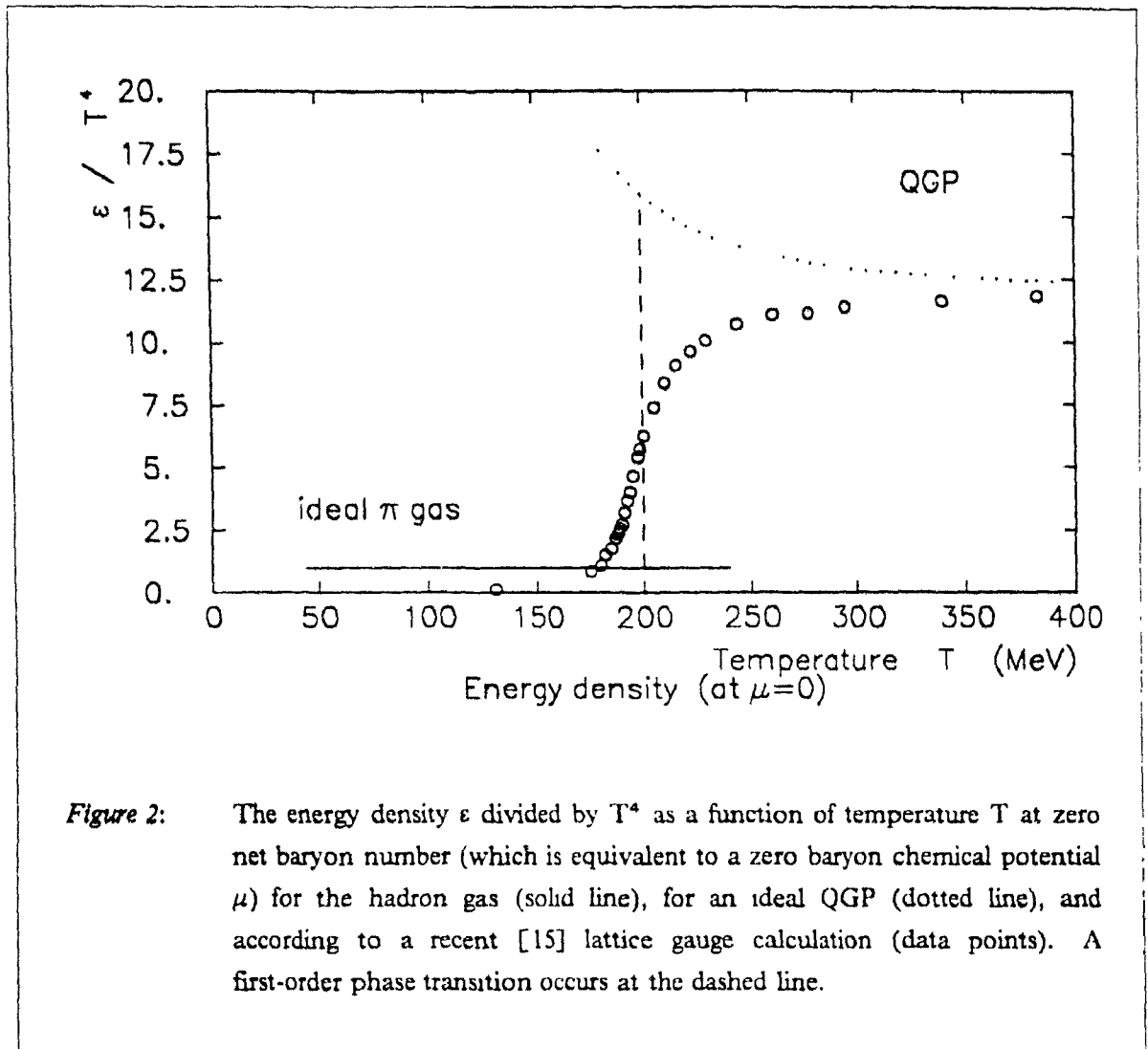


Figure 2: The energy density ϵ divided by T^4 as a function of temperature T at zero net baryon number (which is equivalent to a zero baryon chemical potential μ) for the hadron gas (solid line), for an ideal QGP (dotted line), and according to a recent [15] lattice gauge calculation (data points). A first-order phase transition occurs at the dashed line.

The results from [15] are actually for a SU(2) model. These results have been scaled to match the critical temperature of 200 MeV and the number of degrees of freedom of SU(3) with light quarks. The comparison shows that while the exact nature of the transition can be fairly model dependent, a large increase in the energy density at a finite temperature is common to all these models.

In our simplified picture, and zero net baryon number, QCD predicts a first-order phase transition, during which the temperature stays constant while the energy density increases. For a range of energy density, the nuclear matter will be in a mixed phase with 'bubbles' of QGP imbedded in the hadron gas. For larger energy densities, all the matter is converted to QGP, and the temperature rises again as a function of energy density.

In a plot of temperature as a function of energy density, the prediction of QCD is thus a flattening followed by a sharp rise [16]. If the mixed phase is reached, the temperature would only show a plateau. The observation of increased temperatures would then reveal the emergence of a pure

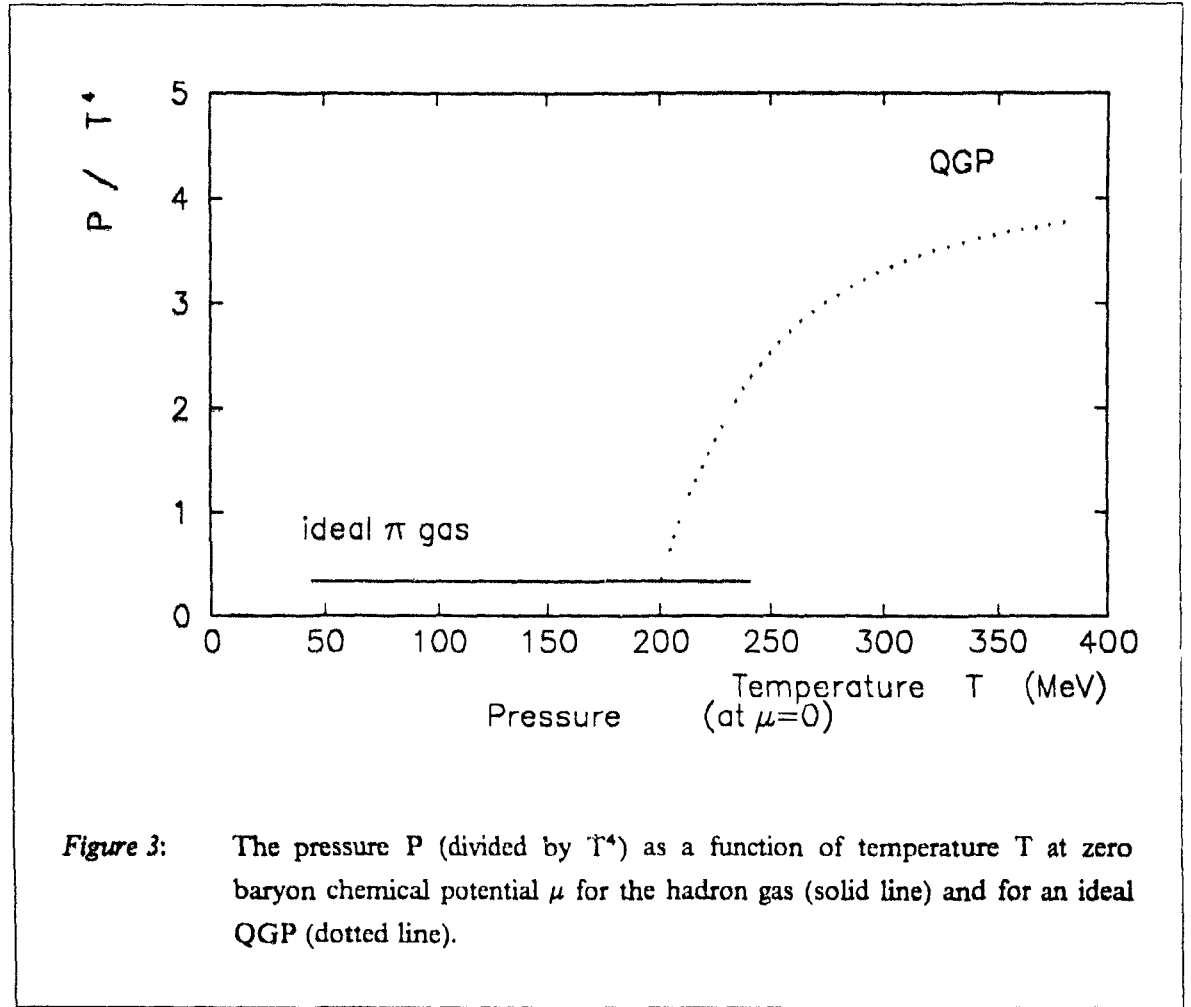


Figure 3: The pressure P (divided by T^4) as a function of temperature T at zero baryon chemical potential μ for the hadron gas (solid line) and for an ideal QGP (dotted line).

QGP phase.

One of the consequences of this phase transition is a low pressure of the mixed phase compared to the energy density that it reaches. Indeed, with the above simple model for the phase transition, the ratio of the pressure to the energy density in the QGP is $(1 - \frac{136}{111 + 34T^4/T_c^4})\frac{1}{3}$ instead of $\frac{1}{3}$ in the ideal hadron gas. This means the pressure is decreased by a factor of 10 (relative to $1/3 \epsilon$) immediately after the phase transition, and remains significantly smaller than this value up to $1.4T_c$. The non-observation of large collective effects due to large pressures has been suggested [17] [18] as a evidence for the deconfinement. However, in the advent of QGP supercooling, deflagration waves [19] might be the source of the intermittency [20] which is observed experimentally [21].

In order to determine the temperature, it is not sufficient to measure the momentum distribution of the pions (the dominant secondaries) in the final state. The matter undergoes a cooling during the expansion, and the pions, strongly interacting during all the stages of the collision, probe the

temperature at the moment of the very last collisions. Particles that decouple earlier, because of smaller cross-section, measure higher temperatures, a fact well established in experiments at the BEVALAC [22][23]. The total cross sections of mesons containing a strange or a charm quark are less than that of pions and therefore they can probe somewhat earlier times. The best measurement of the initial temperature is provided by photons and lepton pairs, that traverse nuclear matter virtually unaffected.

The photons and lepton pairs are interesting in another respect: the rate of production of soft photons and low mass lepton pairs (in the range 30 MeV to 200 MeV) is significantly larger in a quark gluon plasma than in a hadron gas.

The abundance of strange particles has been suggested to be an effective probe of the quark gluon plasma: despite the larger mass, the production of pairs of strange quarks is favoured compared to the production of up and down quarks since the Fermi sea of quarks and antiquarks is quite occupied, and by the Pauli exclusion principle, a gluon cannot materialize if the phase space cell of the quarks is already occupied. In contrast, if the hadronic gas is made of mesons (bosons), at large densities, the production of further non-strange mesons would not be suppressed but enhanced. An enhancement of the strange particle production, that would be linked clearly to this mechanism would be a direct proof of the presence of the quark-gluon plasma.

Unfortunately, the production of strange hadrons does not usually follow the prediction of equilibrium thermodynamics. The production of strange quarks increases instead as the momentum distributions of the other hadrons approaches thermal equilibrium [24]. A spectacular increase of the production of K^+ in heavy-ion collisions at 15 GeV/nucleon is an example of such a thermalization that must not be mistaken as evidence for the plasma [25]. The production of multi strange baryons or antibaryons [26] is much more sensitive to the deconfinement in the thermalization, and would constitute excellent probes for the QGP if it were not for the extraordinary experimental difficulties measuring the production of rare particles in a high multiplicity environment.

Another probe for the deconfinement of QGP is the screening [27] of the colour force between a heavy quark-antiquark pair. The intuitive picture is that the merging of all the bags together allows the flavour to flow at large distances. The probability would then be very small that a heavy quark and its antiquark, that are initially bound, will recombine at hadronization time. In presence of the deconfined quark gluon plasma, the heavy quark-antiquark resonances are suppressed, shifted, and broadened [28][29]. At present, there is already some experimental indications of a suppression of the J/ψ narrow resonance [30]. However, it has been suggested that a sufficiently dense hadron gas could produce the same suppression.

1.5 Quantum mechanical vs classical description of nuclear collisions.

If certain features of heavy-ion collisions are dominated by quantum mechanical effects, others effects are essentially classical. For nuclei of finite size, the wavelength of the produced particles is often comparable to the longitudinal size of the system. In the given range of fireball sizes (from proton-aluminium to sulfur-uranium collisions), we can thus expect a gradual change from a description in terms of diffraction to a description in terms of thermodynamics or hydrodynamics. The phenomenon of transparency also depends on the size being finite. For small nuclei, transparency means that the pions produced in the collisions do not re-interact, since they are formed *outside* the interaction region *after* the collision. For large enough nuclei, most of the created particles would be inside the nuclear matter when they are formed, and there would be no transparency. Thus transparency appears when the size of the system is small enough that quantum effects are important. However, we will see that transparency is not just an effect of the quantum-mechanical uncertainty on the time of production of the particle, but results from the production of the particle by the inside-outside cascade.

1.5.1 Quantum effects

When a particle is confined inside a certain volume, the vanishing of the wave function at the boundary imposes a minimum curvature of the wave function. This produces a minimum kinetic energy for the particle. One instance is the nucleons confined inside the nucleus, where in addition, states of higher and higher energy have to be occupied, since the fields of the nucleons obey anti-commutation rules. This produces the concepts of Fermi energy and Fermi motion in large nuclei. Similarly, the confinement of low-mass quarks in a 'bag' [31] produces kinetic energies in the ground state responsible for a large fraction of the mass of the nucleon. The inner making of the hadrons must therefore be considered quantum mechanically.

Although we will see that the description of the collision of two heavy-ions can be done to some extent using classical mechanics, the production of secondary particles has to be described quantum mechanically, in the favoured hypothesis of 'string fragmentation'. In this picture, the particle creation occurs via the pair creation of light quarks in the intense chromoelectric field of the string. The string can be thought of as a tubular region where the field extends, with a circular cross-section of area $\pi\Lambda^2$ where Λ (the 'string radius') ≈ 0.5 fm. The process is the QCD analog of the well known QED 'vacuum sparking' observed in the intense electric field of large Z nuclei. The rate of the process is determined by the probability of a tunneling, and is thus easily calculable by integrating the action, giving the following rate of pair creation per unit time per unit volume [32][33]:

$$\frac{dN}{dt dV} = \frac{\sigma^2}{4\pi^5} \sum_{n=1}^{\infty} \frac{1}{n^2} \exp\left[-\frac{m^2 m^2}{\sigma}\right]$$

where σ is the string tension ($\approx 1 \text{ GeV}^2$ or equivalently $\approx 5 \text{ GeV/fm}$), and m is the transverse mass ($\equiv \sqrt{m_0^2 + p_T^2} \approx 300 \text{ MeV}$, m_0 being the bare quark mass) of one of the quarks. This rate of pair creation has to be summed over all possible flavours, spin, and colours, and multiplied by the transverse area of the string $\pi\Lambda^2$. When this is done, we obtain the constant K such that $Kd\lambda dt$ is the probability of forming a meson in a length of string $d\lambda$ during the proper time dt . The value $K \approx 7.5/\text{fm}^2$ is consistent with the width of the ρ resonance.

After its creation, the proper length of the string rises with proper time like:

$$\lambda = \Delta y \tau$$

where Δy is the length of the string in rapidity. Note that the description is semi-classical, and not completely quantum mechanical. This can be shown to be a valid approximation in the path integral formulation of quantum mechanics (see for instance [34]). The probability of creating a quark-antiquark pair first rises with time. At later times, the length of string available for producing more particles is reducing because of the screening caused by the already created pairs. Statistically, about half of the pairs are created after a time $\frac{\pi}{2} \frac{1}{\sqrt{2K}}$, which corresponds to 0.40 fm. This means that at that proper time, only half of the 'future secondaries' exists and can make further collisions. This is the explanation of the transparency: the potential re-interactions of secondaries do not occur because the creation mechanism requires a certain amount of *proper* time. Particle creation after a certain proper time implies that the centrally produced, low energy particles will materialize before the outward going ones (in center-of-mass time), hence the name of inside-outside cascade. The uncertainty principle is not a sufficient explanation for transparency, as very energetic secondaries might be produced very fast while respecting the equation $\Delta E \Delta t = \hbar$.

The quantum mechanics of the inside-outside cascade also explains the constant shape of transverse momentum distributions of secondaries. In this model, the transverse momentum distribution is just the power Fourier transform of the field strength in the string; for a field with a Lorentzian intensity, of radius Λ , an approximately exponential distribution of p_T would result, with an asymptotic inverse slope of $1/2 \hbar/\Lambda$. For $\Lambda = 0.5 \text{ fm}$, this is equal to 200 MeV, not far from the measured value of $\approx 180 \text{ MeV}$.

At least at the qualitative level, we have seen that the string fragmentation can be understood as an essentially quantum mechanical process of tunnelling applied to light quarks. If quarks lighter than the typical mass scale of QDC, Λ_{QCD} , did not exist, the multiplicity characteristics of hadronic collisions would have been radically different.

1.5.2 Classical effects

The distance between two nucleons in a nucleus amounts to about 1 fm. Let us see what happens if we adopt the picture that a projectile proton is confined inside the bag of the target proton while it is interacting with it. By the uncertainty principle that $\Delta x \Delta p_x$ has a minimum value of \hbar , given the size of a proton (1 fm), we introduce extra momenta of the order of 200 MeV, which are small compared with the typical longitudinal momenta. The conclusion is that the classical picture, where a nucleon has *successive* interactions with several nucleons, is viable.

Similarly, in the transverse direction, we can resolve instantaneous 'classical' details larger than the de Broglie wavelength of the incident particles. To compute the resolving power of the heavy-ion microscope, let us consider the typical momentum of a point-like constituent in the center-of-mass system. A constituent (quark or gluon) carries about one sixth of the 19 GeV of a nucleon incident in the center of mass, ≈ 3 GeV. Thus, it can resolve details of the size $200 \text{ MeV}\cdot\text{fm} / 3 \text{ GeV} \approx 0.07$ fm. It makes sense then to say that an incident nucleon makes a collision with one nucleon in the target and not on a neighbour 1 fm away. It is even possible to define with some precision the impact parameter between two 'bags'.

Finally, it is sometimes incorrectly said [35] that the uncertainty principle limits the longitudinal size of the fireball to a minimum size of 1 fm. The uncertainty principle says that, when resolving longitudinal momenta with a precision better than $(\hbar/2)/1 \text{ fm} \equiv 100 \text{ MeV}$, the fireball has a minimum size of 1 fm. But the momenta of the particles do not have to be measured with such a precision until the end of the evolution of the system. The estimates of energy density must use the *classical* Lorentz contracted size as the longitudinal size of the fireball.

1.6 The evaluation of the 'maximum' energy density of a fireball

It was seen from the previous discussion that it is possible to calculate 'classically' the positions of the particles as a function of time. In general, the distribution of the available energy is likely not to be uniform. In particular, the 'edges' of the projectile are likely to produce a smaller energy density than the center. However, we are going to proceed to the evaluation of the *mean* initial energy density. We shall also assume, as usual, that nuclei are spheres of constant density, of radii:

$$r = r_0 A^{1/3} \equiv 1.12 \text{ fm } A^{1/3} \quad (3)$$

There exists a considerable literature on the energy density achieved in heavy-ion collisions in the central region [36] and in the fragmentation regions [37]. The assumption is that the net baryon density (baryon density minus antibaryon density) is zero in the central region, and that two distinct

regions with large baryon density are formed close to the original rapidities of the target and of the projectile. These articles were written before the first round of heavy-ion collision experiments showed a complete stopping at energies of 15 GeV/nucleon [38], and a very large stopping in central collisions of oxygen nuclei on heavy targets at energies of 60 and 200 GeV/nucleon [39][40]. In these experiments at energies of 15, 60, or 200 GeV/nucleon, it appears that the fragmentation regions are not easily distinguished from the central region. There remains the possibility that the central region is baryon free at higher energies that might be reached in heavy-ion colliders [41].

Therefore, we shall consider that the participants from the two nuclei stop each other completely. The energy density is the ratio of the stopped energy to the volume. The stopped energy is just the center of mass energy of the participants. For a central collision, the volume is approximately a cylinder of section given by the edge of the smaller nucleus. The longitudinal size of this cylinder is given by the longitudinal size of the largest nucleus, divided by a factor γ_{CMS} to take the Lorentz contraction into account. The size of the largest nucleus (usually the target) is taken rather than the size of smallest because the reaction continues to take place until the back edge of the largest nucleus is reached. With the aforementioned assumptions:

$$\epsilon_M \approx \frac{\sqrt{s} - m(N_T + N_P)}{\frac{4\pi}{3} r_0^3 N_T / \gamma_{CMS}} \quad (4)$$

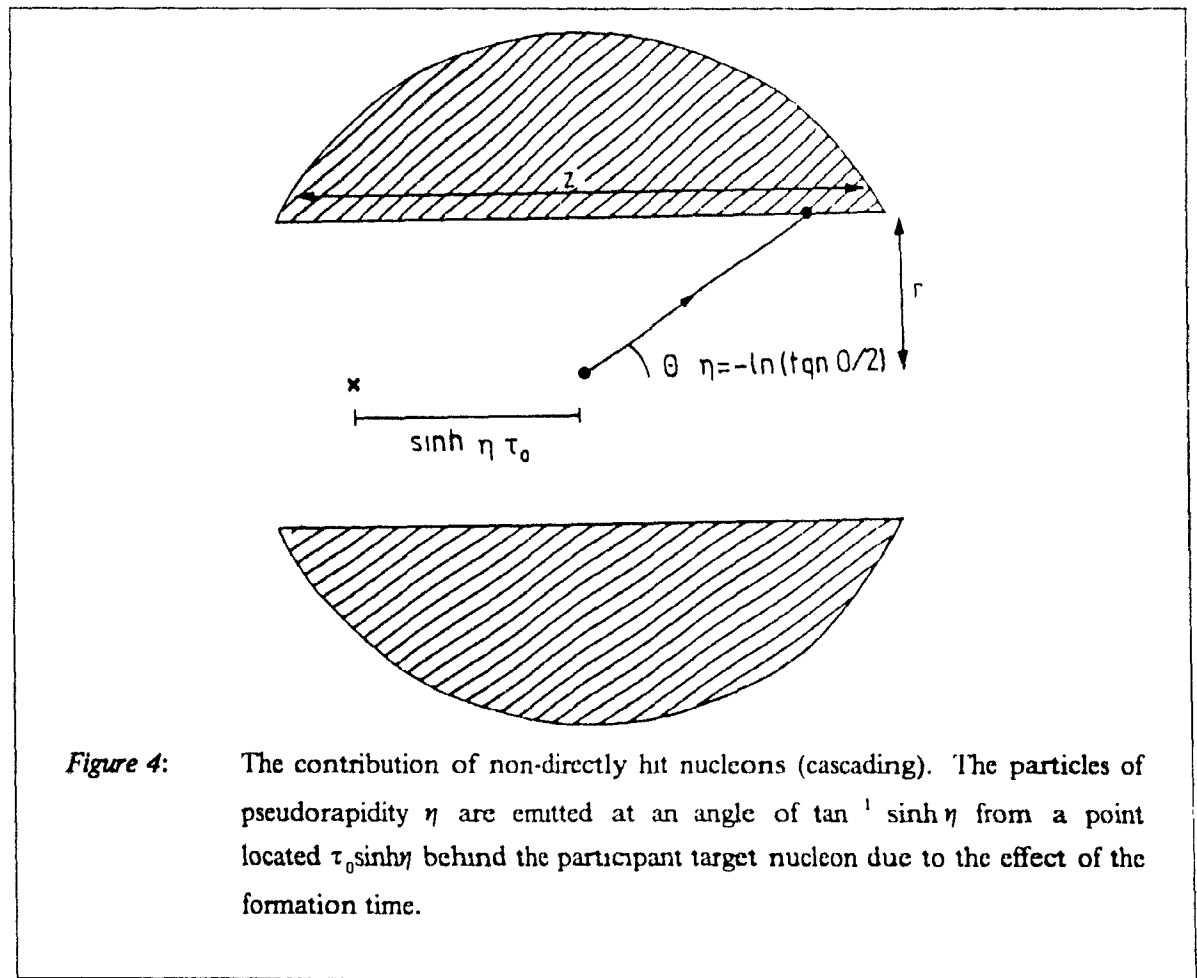
where the invariant s is the square of the c. m. energy, m is the nucleon mass and $(4\pi/3) 3r_0^3 N_T / \gamma_{CMS}$ is the contracted volume of the central tunnel, with $\gamma_{CMS} \equiv E_{beam} / \sqrt{s}$. The number of participating nucleons in the target and in the projectile N_T and N_P are obtained by straight line geometry. Note that equation (4) is sometimes multiplied by a factor $\pi/4$; it becomes then a lower bound for the energy density, since a fraction $\pi/4$ of an isotropic distribution of energy is transverse, and can be considered unambiguously coming from the fireball. To be used in experimental analysis, this equation is multiplied by a factor S that represents the fraction of the energy available in the center-of-mass that is actually stopped in the fireball. Since the resulting transverse energy is also proportional to the fraction of stopped energy, S can be measured by $E_T / E_{T,MAX}$. With equation (4), we have thus derived the mean energy density at full stopping ($S = 1$) with the ansatz that the energy stays inside the cylinder defined by straight line geometry. Whether this is true, or whether the energy spreads to the full volume of the largest nucleus, will be answered in the next section.

1.6.1 The contribution of cascading to the transverse energy production

The cascading is used in many contexts to designate secondary processes of interactions. A primary process forms most of the particles; cascading is said to take place when some of these formed particles interact with nucleons. The cascading can occur on baryons that have already participated

in several collisions, however we shall only consider here those who would have been *spectators* if all particles travelled exclusively longitudinally. The cascading on *participants* exists, but it can be considered to be part of the hydrodynamic evolution.

The contribution of cascading to hadron-nucleus reactions is reduced by the fact that in the laboratory frame the particles are not created immediately but only after a certain time, and therefore at a certain distance from the point of the first interaction, as shown in Figure 4. The more energetic a particle is, the more forward it is created. It is known since a long time [42] that if it were not for this phenomenon, a naive evolution of the cascade would predict the production of thousands of particles in complete thermalization and isotropy in every collision. In contrast, the average hadronic collision was found to be only mildly dependent on the atomic mass number of the target, indicating a form of transparency [43] recently understood in terms of the QCD form for the interaction and the inside/outside cascade (it is important to note that the word cascade in the term 'inside/outside cascade' is not, in any way, related to the phenomenon of 'cascading').



In order to fix our minds on the possible magnitude of cascading effects in heavy-ion collisions, let us consider the case of a central collision of a small projectile nucleus (^{16}O , or ^{32}S) on a larger target. Supposing that we know the rapidity distribution that would be produced by the collision of the projectile on the 'central tunnel' of the large nucleus, it is relatively easy to obtain a limit on the contribution of cascading in the rest of the nucleus to the transverse energy. For this, we are going to make the simplifying assumption that most of the generated transverse energy is from a region close to the center of the target. This is suggested by the fact that in models where we consider that the transverse energy is produced by a superposition of many nucleon-nucleon collisions, the overlap integral is maximum at the center. We obtain a limit on the transverse energy produced by the cascading if we assume that the secondary particles that hit the edges of the tunnel are interacting there with probability one and distribute their energy isotropically. Given the $dE_T/d\eta$ distribution, the secondary particles are generated with an angle given by $2 \tan^{-1} e^{-\eta}$ from positions $\beta\gamma\tau_0 = \sinh\eta\tau_0$ downstream of the positions of the contributing target nucleons. The fraction of the 'central tunnel' which will produce transverse energy that hits the walls of the tunnel is therefore given by:

$$\frac{z - (r + \tau_0) \sinh \eta}{z}$$

where z is the length of the central tunnel and r its radius. The isotropic re-emission of the transverse energy thus captured implies a multiplication of the transverse energy by:

$$\frac{\pi}{4} \cosh \eta - 1$$

An estimate of the amount of cascading is therefore:

$$E_{T,casc} = \int d\eta \frac{dE_T}{d\eta} \left(1 - \frac{r + \tau_0}{z} \sinh \eta\right) \left(\frac{\pi}{4} \cosh \eta - 1\right)$$

Using the measured distribution $dE_T/d\eta$ as an upper limit for the $dE_T/d\eta$ before cascading, we obtained a value for the additional E_T due to cascading of about 6 GeV (for ^{32}S -W collisions at an energy of 200 GeV/nucleon producing 300 GeV of transverse energy, with $r = 3.5$ fm and $z = 12.7$ fm obtained from equation (3), and considering a hadronization time τ_0 of 1 fm/c).

The conclusion is that the non-geometrically participating nucleons do not increase very much the transverse energy. The cascading, in this sense, is negligible⁵. In contrast, a rather large fraction of the secondaries produced by the first collision, will have formed before reaching the back edge of

⁵ This is considering a beam energy of 200 GeV/nucleon. At 60 or 15 GeV/nucleon, the relative importance of cascading is larger.

the opposite nucleus, and should contribute to the production of transverse energy by colliding with nucleons located there [44]. However, to arrive to this conclusion, we have to consider that it is still possible to consider the evolution of matter as a succession of collisions of individual particles, while a description in terms of chromoelectric fields or of a energy density function of space and time may be more appropriate.

1.7 Relativistic nuclear collisions as many hadron-hadron collisions

As far as the strong force is concerned, the nuclei can be considered as weakly bound assemblies of protons and neutrons, occupying the nuclear volume at a rather constant density of baryons per unit of volume. A remarkable numerical coincidence exists at the energies at which we are working:

$$\sigma^3 \rho_B^2 \approx 33 \text{fm}^6 (0.17)^2 \text{fm}^{-6} \approx 1$$

where ρ_B is the normal baryon density of nuclear matter⁶, and $\sigma = 3.2 \text{ fm}^2$ the total inelastic cross-section. This relation appears naturally in the bag model, because of the relation between the area of a bag and the number of bags that can be put per unit of volume. The primary consequence for us is that the number of collisions is at least of the order of the number of participants, and for central collisions, this is fairly large. It also means that a nucleon could in principle interact simultaneously with two nucleons of the opposite nucleus.

Some of the characteristics of the heavy ion collisions are directly derived from those of hadron collisions. In particular, the proton-proton collisions have been extensively studied [45], and considerable effort has been made to understand their properties in terms of constituents [46][47][48]. In collisions of small nuclei, it is expected that the production of secondaries, apart from spectators, is simply a sum of secondaries from a number of nucleon-nucleon collisions. This has been verified experimentally in high energy α - α collisions [45]. This should also be the case in peripheral collisions of large heavy ions, with the difference that some of the secondaries may create low energy cascade in the 'spectator nuclei'. This is to be contrasted to central collisions of heavy ions, where a nucleon undergoes several simultaneous or successive collisions.

A very general remark can be made about the relativistic heavy-ion collisions : if we admit that no signals propagate faster than the speed of light, then the collision volume is divided into several non-communicating regions along the transverse direction. This was the physical basis for the row-on-row models [49]; if we forget later interactions, the production of transverse energy, and the

⁶ $\rho_B = 1 / (\frac{4\pi}{3} r_0^3)$

production of secondaries in general, is the sum of the contributions of several pairs of rows, the production of each pair of rows being completely determined by the number of nucleons initially present in each of the two rows.

1.8 Model of nucleon-nucleon interactions and generalizations to nucleus-nucleus

In all the phenomenological models inspired by QCD, the secondaries are ultimately created by the strings. There is ample evidence in favour of the concept of a string where a large constant chromoelectric field, by 'vacuum sparking', results in the production of the mesons and resonances. In high-energy e^+e^- collisions, the final state consists of a pair of a quark and of an antiquark that move apart from each other at a speed close to that of light. By considering the two-jet events, we obtain a sample of single string fragmentations. The fragmentation of such isolated strings has been extensively studied by experiments at e^+e^- storage rings, and have been parametrized. We can then test if we understand nucleon-nucleon interactions and nuclei-nuclei collisions by trying to reproduce their characteristics with a sum of string fragmentation phenomena.

1.9 The dual parton model

For processes involving large momentum transfers, we can compute successfully the cross-section for the production of jets from a knowledge of the structure functions and of the strong coupling constant. But in the average collision, the momentum transfer is quite small, and the perturbative approach fails since the strong coupling constant blows up (as seen in equation (1)). Thus it is not clear how to apply QCD in that limit. A possible solution is given in the Dual Parton Model, where we keep the idea of structure functions, but consider the formation of strings between partons (via colour exchange) instead of elastic collisions between them. Although the exact fragmentation of the strings into the observed particles remains a fundamental problem to be solved in non-perturbative QCD, this fragmentation is known phenomenologically for e^+e^- collisions, allowing a straightforward comparison.

In the Dual Parton Model (DPM), the first step is an interaction between two partons (they exchange colour with little momentum transfer). These partons are exclusively the quarks, never the gluons. This simplified approach is partly supported by the prediction of the Altarelli-Parisi evolution equations that at low momentum transfer, the gluon content of the hadron is lower. However, the 'sea' quarks and antiquarks do participate in the DPM, although only in higher order graphs. These quarks, exchanging colour, getting themselves exchanged between hadrons, or 'held back', carry charge and flavour with them. It is in this sense that the DPM reflects QCD, and the observation of the predicted mean charge, or mean flavour, as a function of pseudorapidity, is one of

the most spectacular verification of the ideas of the DPM

By some other aspects, the DPM does not intuitively derive from QCD. The strong coupling constant α_s , for instance, which is fundamental in the formulation of QCD as a gauge force theory, does not appear anywhere in the DPM. Instead, QCD results in the formation of strings between quarks that completely enclose the region of intense chromoelectric and chromomagnetic fields. Also note that until the final use of fragmentation functions, the DPM is a purely one-dimensional model, in contrast with QCD and the concurrent QCD inspired approach, FRITIOF [50].

For these reasons, the DPM predicts no jets. Within our energy regime, this does not matter, since jet phenomena are either very rare or very hard to recognize as such [51].

The word 'Dual' in the name 'Dual Parton Model' comes from the concept of duality in 'Dual resonance model'. The duality is the equality of the complex amplitude in the s-channel (direct) and of the complex amplitude in the t-channel (crossed). This equality being a too strict requirement, the duality in a broader sense is the fact that the *average* amplitude in the two channels agree. In the s-channel, at low center-of-mass energy, two hadrons interact because they make a resonant intermediate state which decays back in the two hadrons. There exists a series of resonances of higher and higher mass with higher and higher spin, but these resonances are broader and broader until they overlap. In the t-channel, at large center-of-mass energies, but relatively small momentum transfers, the interaction can be described in a very different way. The two hadrons interact by exchanging a virtual particle. This off-shell particle can be of various spins and masses, but the asymptotic limit for infinite energies is a power law. The duality is the requirement that these two description — sum of bumps and power law — give the same results, at least on average, in the intermediate region.

Unitarity is also an important concept. It imposes a relationship between the S-matrix and products of S-matrices, in such a way that contributions to the scattering amplitude with more complex topology are automatically present. They are however suppressed by higher powers of $1/N_f$ in the topological expansion.

Let us examine the most probable topology for a high energy nucleon-nucleon collision. In the collision, one of the quarks from one nucleon exchanges colour with one of the quarks of the opposite nucleon. This creates two strings, one connecting the diquark of the first nucleon to the quark of the other nucleon, and one connecting the quark of the first nucleon to the diquark of the opposite nucleon (see Figure 5). Although this varies from event-to-event, typically the diquark carries a large fraction of the momentum of the nucleon, and the isolated quark, a small fraction of the momentum of the nucleon; hence the name 'held back quark' for the quark which has interacted in each nucleon.

Each string will then hadronize. The interesting assumption, here, is that the fragmentation of each string is independent of the presence of the other string, and of the flavour of the quarks located at its

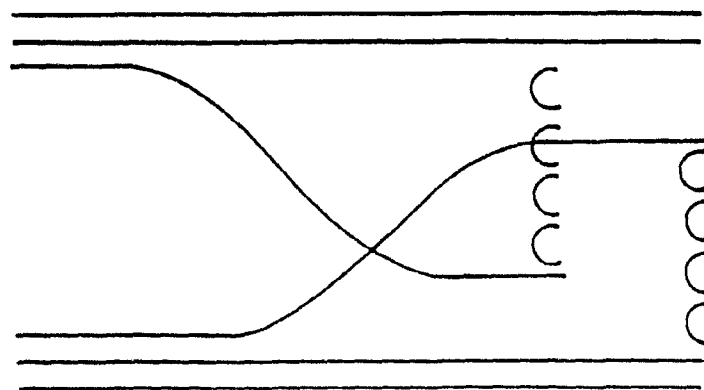


Figure 5: The two chains between the valence quarks and diquarks of two hadrons in collision in the framework of the DPM. This represents the simplest topology.

ends. We suppose that such a string produces exactly the same distribution of secondary particles as a string produced between quarks in e^+e^- collisions. The only difference is that whereas the strings in e^+e^- collisions have a broad distribution of angles, the 'jets' of minimum-bias nucleon-nucleon collisions are always forward and backward.

The structure functions of valence quarks in hadrons are presently well known from measurements of 'Deep Inelastic Scattering', being described by empirical formulas of the type $x^\alpha(1-x)^\beta$. The exponents α and β can be given the values -0.45 and 3.2 respectively, according to [52], but the exponents should be considered as approximate, since the structure functions might change slowly with energy and with the square of the momentum transfer (scaling violations). In the DPM, however, we make use of duality to obtain the relevant form near $x=0$ and near $x=1$. At large enough beam momenta, the exponent of the momentum fraction is the opposite of the intercept of the Regge trajectory of the exchanged particle in the crossed diagram, where s and t are exchanged. This result, coming from an analysis in partial waves of the amplitude, shows that the fraction of the quark must behave like $x^{-1/2}$, since the 'meson' trajectory (ρ, A_2, \dots) has intercept $1/2$, while the fraction of the diquark ($1-x$) must behave, near $1-x=0$, like $(1-x)^{3/2}$ because the $qq\bar{q}\bar{q}$ 'exotic' trajectory has intercept $-3/2$. It is natural to incorporate these limiting behaviour by considering that the distribution $\rho(x)$ of the momentum fraction of the quark is the product $x^{-1/2}(1-x)^{3/2}$ [48], and it is also a reasonable extrapolation of deep inelastic scattering measurements to low momentum transfers.

With this simple two-string topology, we can compute the multiplicity and transverse energy distributions of nucleon-nucleon collisions:

$$\frac{1}{\sigma} \frac{d\sigma}{dy} = \frac{dN}{dy} = \int_0^1 dx_1 \int_0^1 dx_2 \rho(x_1) \rho(x_2) \left[\frac{dN_{string}}{dy}(y - \Delta_1, \bar{P}_1) + \frac{dN_{string}}{dy}(-y - \Delta_2, \bar{P}_2) \right]$$

$$\text{where } \Delta_{1,2} = \frac{1}{2} \ln \left(\frac{1 + \beta_{1,2}}{1 - \beta_{1,2}} \right) \quad \beta_{1,2} \approx \frac{1 - x_{1,2} - x_{2,1}}{1 - x_{1,2} + x_{2,1}} \quad \bar{P}_{1,2} = \frac{\sqrt{s}}{2} \sqrt{(1 - x_{1,2})x_{2,1}}$$

$\frac{dN_{string}}{dy}(y, \bar{P})$ represents the multiplicity produced at rapidity y in its center of mass by a string whose both ends carry a momentum \bar{P} ; this can be measured in e^+e^- collisions. Similarly, for the transverse energy flow:

$$\frac{dE_T}{dy} = \int_0^1 dx_1 \int_0^1 dx_2 \rho(x_1) \rho(x_2) \left[\frac{dE_{T,string}}{dy}(y - \Delta_1, \bar{P}_1) + \frac{dE_{T,string}}{dy}(-y - \Delta_2, \bar{P}_2) \right]$$

The distributions of multiplicity for jet fragmentation is known from e^+e^- , and can be parametrized [53][48][54] as :

$$\frac{dN_{string}}{dy}(y, \bar{P}) = \frac{0.05 + 1.3(1 - \zeta)^2}{1 - 0.5\zeta} \quad \zeta = \left| \frac{\mu}{\bar{P}} \sinh y \right|$$

or sometimes as $1.35(1 - \zeta)^3$. μ is the 'pion transverse mass' $\sqrt{p_T^2 + m_\pi^2}$, the typical transverse energy per particle. This parametrization shows the existence of a plateau of quasi-constant dN/dy at very high energy, falling off at the edges in about one unit of rapidity. Incidentally, remarking that the typical momentum fractions of the held-back quarks x_1, x_2 are quite small (of the order of 0.10) the observed multiplicity distribution, for beam energies of the order of 200 GeV, is then due to the sum of two relatively narrow 'string plateaus' shifted by about 2 to 3 units of rapidity. This is shown in Figure 6. The explanation of the width and height of this distribution for nucleon-nucleon collisions is a major success of the DPM.

In summary, the DPM, which describes remarkably well the average 'minimum-bias' nucleon-nucleon collision, corresponds to a picture where two quarks, each carrying a small fraction of the momentum of their respective hadron, exchange colour but only a very small momentum, as can be expected since the gluon propagator has a pole at zero momentum transfer. Color neutralization causes two strings to form, and hadronize. More complicated topologies must exist, by unitarity, but they are suppressed by factors of the order of $1/N_F$ in the topological expansion. These low momentum fractions are imposed by Regge phenomenology, while e^+e^- data give the

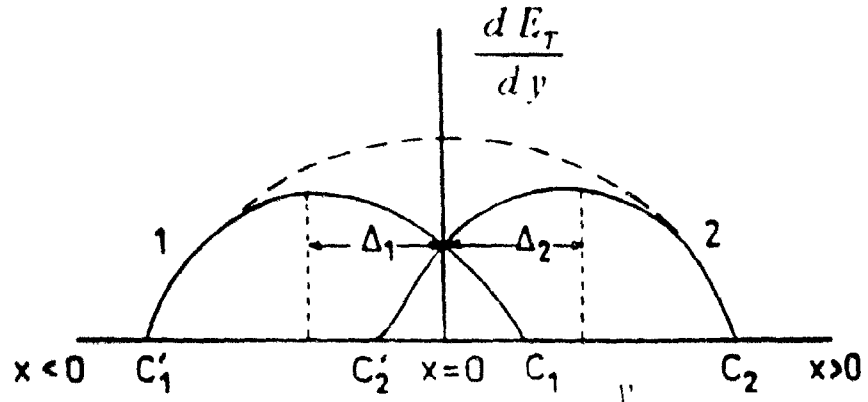


Figure 6: The rapidity distribution of transverse energy produced in a proton-proton collision having the simplest-topology diagram. The two individual curves represent the contributions of each held-back quark - diquark combination. The top curve represents their sum.

distribution of particles in the high-energy fragmentation. In this model, a baryon coming from the hadronization of a diquark contains quite naturally a large fraction of the initial momentum, which corresponds to the experimentally observed 'leading baryon effect' [55].

1.9.1 Extension to nucleus-nucleus collisions.

In a certain limit, the DPM can be extended to nuclear collisions. For collisions of small nuclei, first, we may consider that several nucleon-nucleon collisions can occur concurrently. For example, in α - α collisions, 4 nucleons from one nucleus could collide with 4 different nucleons of the opposite nucleus. Then, when we consider collisions of larger nuclei, by geometry a given nucleon is likely to make collision with several nucleons of the opposite nucleus. Because of the 'leading baryon effect', it seems possible to consider such multiple collisions in the framework of the DPM. Let us see how this will work, when n_A nucleons from the target collide with n_B nucleons from the projectile in a cylindrical tube of cross-section $\sigma = 32\text{mb}$. The leading baryon effect observed in nucleon-nucleon collisions, continues to apply here. This is because in the DPM the simplest topologies are enhanced with respect to more complicated ones, since they have lower order in the topological expansion. Therefore, although the 'sea' quarks have smaller momentum fraction probabilities, it is more 'economical' to create and split a pair of sea quark-antiquark near the diquark, than to split the

diquark, which would result in very complex topologies. Therefore, the diquarks remain intact through the many interactions—we can view them as sitting through the opposite nucleus. Then we are left with a mere problem of counting. There are $n_p \cdot n_t \cdot n_s$ interactions. Each of these, in order to have a quasi-constant cross-section at high energy, must correspond to the exchange of a pomeron and thus to the creation of 2 chains. Therefore, there is a total of $n = 2n_p \cdot n_t \cdot n_s$ chains. There are $n_q + n_s$ chains with diquarks, of which (taking $n_p \cdot n_t$) $2n_q$ are with valence quarks and $n_s \cdot n_t$ are with sea quarks. Then there will be $n_q \cdot n_t$ chains linking a quark with a sea antiquark. The rest of the n collisions will be between sea quarks and antiquarks. As an example, when 2 nucleons collide with 5, there are 20 chains, 7 of which have a diquark (4 with a valence quark and 3 with a sea quark). 3 chains are stretched between a valence quark and a sea antiquark, and 10 are between a sea quark and a sea antiquark. The momentum fractions are harder to compute, since they are not necessarily independent after several collisions (the leading baryon may be losing energy). A Monte Carlo calculation is needed to compute these. At this stage, we may simply observe that the chains between quarks and antiquarks are short, so that they possibly do not contribute to the production of multiplicity and transverse energy. If this were the case, the production of transverse energy and multiplicity would be proportional to the number of chains containing diquark, and that is also the number of wounded nucleons. Moreover, among these, the chains that are shifted towards forward rapidities come from fast forward going diquarks, therefore, from projectile wounded nucleons, and the backward moving chains come from target wounded nucleons. Therefore, the transverse energy and multiplicity in each 'hemisphere' can be dominated by the corresponding number of wounded nucleons.

Finally, it is important to note that we do not normally expect that the dual parton model will describe properly the collisions of very large nuclei. The assumption that each chain fragments independently must normally fail when there is a very large density of chains. For large enough nuclei, we also expect large amounts of additional transverse energy and multiplicity to result from cascading of the produced mesons after the formation time has elapsed. The goal of the nucleus-nucleus DPM is rather to give a representation as exact as possible of the small nuclei limit of nucleus-nucleus collisions, so that we know, when there is a deviation, that the nuclei are large enough to produce effects fundamentally different from nucleon-nucleon collisions.

1.9.2 Monte Carlo realizations of the Dual Parton Model

IRIS 2.01 is a Monte Carlo realization of the Dual Parton Model that uses a Woods-Saxon nuclear density distribution to compute the geometry of the collision, the simplest topology of the dual parton model to compute the strings and their lengths, and the Lund fragmentation Model to fragment these forward backward strings into hadrons and resonances [56]. The Lund fragmentation program has several parameters, but these parameters have been adjusted to fit the e^+e^- data from PETRA, so that in principle IRIS is a parameter-free simulation of the situation of independent

nucleon-nucleon collisions.

The Ranft realization of the dual parton model [57] uses different codes (BAMJET, DECAF, HADRIN) to realize essentially the same computation, with the exception that the produced particles are allowed to re-interact after a proper time τ_0 after the collision responsible for their creation. This 'cascading' makes it possible for the nucleons of the largest nucleus to participate more in the collision, resulting in a rapidity shift with respect to a naive DPM superposition that neglects the fate of the produced particles.

1.10 The Lund model for hadron collisions and FRITIOF

The Lund group [47] has developed a quite general code to simulate the scattering of partons and their fragmentations in Deep Inelastic Scattering experiments and high- p_T hadron-hadron collisions. The same group proposes, with the FRITIOF model [50], a distinct way to generalize the characteristics of hadron-hadron collisions to nucleus-nucleus collisions. It is assumed that there is no colour exchange or flavour exchange, but a considerable momentum transfer. In each collision, both of the colliding nucleons get 'excited' and a string is stretched between a quark and a diquark *of the same nucleon*. Comparing with the dual parton model, we see that the strings in FRITIOF are the same as the dominant kind of string of the Dual Parton Model: quark-diquark; the difference here is that the quark and diquark are from the same nucleon. The important *dynamical* difference is that while the length of all quark-diquark strings are fixed in advance in the DPM, the length of the internal string, or equivalently, the excitation of the 'leading baryon' increases with the number of collisions experienced. This excitation saturates asymptotically after many collisions.

Compared to the DPM, FRITIOF avoids the problem of giving somewhat arbitrary structure functions at low momenta to quarks. However, it misses colour exchange, cannot reproduce the amount of flavour transfer, and it does not have unitarity constraints to fix the amplitude of higher order graphs.

1.11 Wounded nucleon models and overlap integral models.

The basis for these models is that although we do not know the details of the reaction at the quark level, we can probably compute some of the global properties of the heavy-ion collisions, such as the total transverse energy, using the global properties of hadron-hadron collisions.

In the wounded nucleon models (WNM) [58], the assumption is the following: Each of the participating nucleons (their number is obtained by multiplying the nuclear density by the volume

representing the intersection of a sphere with a cylinder) gets wounded, going into an excited state that will result in transverse energy at the end of the collision. The drastic assumption is that the nucleon does not become more wounded when it makes several collisions than when it makes one (when sea-sea chains can be neglected, the Dual Parton Model becomes effectively a WNM, since the number of quark-diquark chains, being proportional to the number of diquarks, is proportional to the number of participating nucleons). Each wounded nucleon decaying into particles independently, the model has two parameters to be fitted: the average transverse energy produced by a wounded nucleon, and the magnitude of the event-to-event fluctuations of the transverse energy produced by a wounded nucleon.

In the original version of the WNM, applicable to hadron-nucleus collisions, the transverse energy distribution for collisions where N nucleons are wounded is the N -fold convolution with itself of a known transverse energy distribution (this distribution is obtained by identifying the proton-proton transverse energy distribution with the 2-fold convolution). However, in the case of heavy-ion collisions, the number of wounded nucleons is sufficiently large that the central limit theorem applies.

It can be generally expected that the pseudorapidity density of transverse energy of the wounded target nucleons will be different from that of the wounded projectile nucleons. The transverse energy production in a backward region of pseudorapidity, such as $-0.1 < \eta < 2.9$, would then preferentially measure the number of wounded nucleons in the target.

A similar model, perhaps more naturally consistent with the assumption of high-energy leading baryons, is the Nucleon Collision Model (NCM) [59]. We assume that each participating nucleon can interact several times. A particularly simple description is obtained if we assume that the transverse energy and the secondary particles are not emitted until the end of the collision, and that each of the collisions, irrespective of whether the interacting nucleons have already interacted, produces a similar amount of transverse energy. From a probability distribution for N nucleon-nucleon collisions, and a N -convolution of the proton-proton transverse energy distribution, we obtain a prediction for the differential cross-section. When N is sufficiently large, the N -convolution approaches a Gaussian, whose parameters are determined by the first and second moments of the proton-proton distribution. These characteristics are very well known, both at 60 and 200 GeV per nucleon, from ISR studies [60]. It turns out that while for small nuclei, the agreement with the NCM is excellent [45], for large nuclei the NCM grossly overestimates the transverse energy, and underestimates the fluctuations, the general shape being approximately right. In the context of the NCM model, the less transverse energy per nucleon-nucleon collision would be explained by the energy loss of the nucleons in the successive collisions. Some attempts have been made to compute what would be the effect of the energy loss of the nucleons [61] but carried away to such an extent, the NCM has self-contradictions. In the framework of QCD, the energy loss process should only take place at the end of the collision, since we assume that the secondaries are created only then.

The observation that the shape of the transverse energy distribution is reproduced by the NCM suggests a generalization of the NCM whereby the first and second moments of the nucleon-nucleon differential cross-section are left as free parameters: ε_0 and $\sqrt{\omega}\varepsilon_0$. The only physics input is the geometry of the collision for the calculation of the overlap integral and the probability for N nucleon-nucleon collisions. This geometrical parametrization (so-called geometrical model) is interesting because the parameters measure the increasing deviation from a superposition of nucleon-nucleon collisions as the size of the colliding nuclei increases.

1.12 The hydrodynamic approach

Whereas superpositions of individual nuclear collisions are justified for collisions of small nuclei, the statistical mechanics of several collisions becomes more and more important for larger nuclei. Clearly, for collisions of neutron stars, classical hydrodynamics will apply. At what size of nuclei, and how the transition between the two descriptions will occur has to be found experimentally. In the hydrodynamic models, we consider the mean behaviour of a macroscopic number of quanta as a function of space and time. Such a description is only useful if the quanta have several interactions, transferring momentum and energy from one region of space to the next without themselves moving to it. If this condition of several momentum-transferring collisions is not satisfied, it is simpler and even more adequate to consider the motion of the individual quanta. In heavy-ion collisions, as we have already seen, an hydrodynamic description is needed for at least a fraction of the space-time traversed by the produced particles, since if all the produced particles (typically 1000, charged + neutral, in central S-W collisions) are in the initial volume (of transverse area S , $S \approx 41 \text{ fm}^2$ for ^{32}S , and longitudinal size L_i), the mean free path $\frac{1}{\sigma} \frac{S}{N} L_i$ is several times (about 16 times, if we take $\sigma = 20 \text{ mb}$ for pions) smaller than L_i . It results that the 'fireball' is opaque to a particle starting from center, and that a hydrodynamic evolution is needed from this initial state to the final state where the density is sufficiently low that the produced particles do not interact between themselves and fly to the detectors. The only possible loophole in this argument is that the fireball might be produced in a freeze-out state non-hydrodynamically. In such a freeze-out initial state, the particles would be produced with a longitudinal momentum proportional to the longitudinal position right from the beginning. This possibility must always be considered, although by causality arguments, it is unlikely in the case of collisions of large nuclei.

Paradoxically, the hydrodynamic model has had a considerable phenomenological success [62][63] in describing collisions of hadrons with protons and small nuclei, where the hypothesis that the quanta have numerous interactions before they leave the small interaction region (size $\approx 1 \text{ fm}$) seems hard to justify.

Conversely, in the limit of very large nuclei, we are largely justified to treat hadronic matter hydrodynamically, like a fluid characterized by an equation of state specifying the pressure as a function of the density and of the temperature. The pressure gradients generate hydrodynamic forces which act to modify the motion of the fluid, and thus the final energy flow. The conservation of energy and momentum yield the following equations for the Einstein energy-momentum tensor $T^{\mu\nu}$

$$\frac{dT^{\mu\nu}}{dx^\mu} = 0$$

Following the analysis of Landau [6], only two kinds of terms satisfy Lorentz invariance and can enter the expression for the energy-momentum tensor of a non-viscous fluid, a term in $g^{\mu\nu}$ and a term in $u^\mu u^\nu$. u^μ is the local velocity 4-vector verifying $u^\mu u_\mu = 1$. The coefficients of the two terms might be defined as we wish, however, in order to obtain the Euler equations in the non-relativistic limit, we write:

$$T^{\mu\nu} = (\varepsilon + P)u^\mu u^\nu - P g^{\mu\nu}$$

The quantity ε is the energy density, including the rest mass, and P is the pressure. The units of pressure are (GeV/fm)/fm² (\equiv force/area) which is equivalent to the units of energy density GeV fm⁻³. The full equations of motion in space-time coordinates are

$$\frac{d}{dt}((\varepsilon + P)\gamma^2 - P) = -\vec{\nabla} \cdot [(\varepsilon + P)\gamma^2 \vec{u}] \quad (5)$$

$$\frac{d}{dt}((\varepsilon + P)\gamma^2 u^i) = -\vec{\nabla} \cdot [(\varepsilon + P)\gamma^2 \vec{u} u^i] - \frac{dP}{dx^i}, \quad i = 1, 2, 3 \quad (6)$$

In the non-relativistic limit $\gamma \rightarrow 1$, this reduces to the Euler equations:

$$\frac{d}{dt}((\varepsilon + P) u^i) = -\vec{\nabla} \cdot [(\varepsilon + P) \vec{u} u^i] - \frac{dP}{dx^i}, \quad i = 1, 2, 3$$

1.12.1 Some hydrodynamic phenomenology – the dominant longitudinal expansion

The hydrodynamics equations can be solved (analytically or by relatively simple numerical algorithms) for a few simple cases. Using simple geometries, and considering the ideal-relativistic equation of state $P = \varepsilon/3$, we obtain exact results which outline certain characteristics of the data

Taking the case of 'Gaussian ellipsoid' energy density ($\epsilon = \epsilon_0 e^{-\frac{x^2}{2x_0^2} - \frac{y^2}{2y_0^2} - \frac{z^2}{2z_0^2}}$ at $t=0$), we consider a non-relativistic expansion. The parameters x_0, y_0, z_0 characterize the initial size of the system. Since the Gaussian has the property that its derivative is proportional to the coordinate times the Gaussian, the three components of the velocity of each part of the fireball are proportional to its coordinates, making the energy density distribution remain Gaussian while expanding. At time t , the energy density is $\epsilon = \frac{x_0 y_0 z_0}{x_0 y_0 z_0} e^{-\frac{x^2}{2x_0^2} - \frac{y^2}{2y_0^2} - \frac{z^2}{2z_0^2}}$. The Euler equations are then satisfied everywhere if x_0, y_0, z_0 , the sizes of the 'Gaussian fireball' at time t , obey the equations:

$$\frac{d^2 x_0}{dt^2} = K/x_0 ; \quad \frac{d^2 y_0}{dt^2} = K/y_0 ; \quad \frac{d^2 z_0}{dt^2} = K/z_0$$

we can integrate these equations for the coordinate x , and obtain⁷:

$$\frac{dx_0}{dt} = \sqrt{2K \ln(x_0/x_i)}$$

$$t = \frac{x_i}{\sqrt{K}} \operatorname{erfi}(\sqrt{2 \ln(x_0/x_i)}) \quad , \quad \text{where } \operatorname{erfi}(y) \text{ is the primitive of } e^{\frac{y^2}{2}}$$

$$\text{therefore } \frac{dx_0}{dt} \text{ is also } \sqrt{K} \operatorname{erfi}^{-1}\left(\frac{\sqrt{K}t}{x_i}\right)$$

The implication is that, for small times, the r.m.s. velocity of matter in a given direction is inversely proportional to the initial spatial extent of the fireball in that direction. For larger times, the velocity does not increase as much, but the larger velocity is still associated with the smallest spatial dimension. The Lorentz contraction of the nuclei in the center of mass causes the fireball to be spatially very anisotropic, smaller by a factor γ_{CMS} (typically ≈ 10) in the longitudinal direction than in the transverse direction. This is the reason why we expect that the hydrodynamic expansion will be mostly longitudinal (see also [64][65]).

⁷ the derivation is similar for y and z

1.12.2 Shock waves.

Another way in which hydrodynamics can influence the energy flow is the possibility of shock waves. These shock waves would transport the initial longitudinal momentum through the fireball, and therefore they also contribute to increase the longitudinal energy flow with respect to the transverse energy flow. Shock waves play an important role in hadronic matter with densities of $\approx 0.5 \text{ GeV fm}^{-3}$ [66]. As an instructive approximation to collisions of nuclear pancakes, we will consider the collision of two infinite walls of a finite thickness, for which there exists a fully relativistic, exact solution.

Working in the nucleon-nucleon center of mass, we designate by \mathbf{E} the local 'energy density' $(\varepsilon + P)\gamma^2$, and by $\beta\mathbf{E}$ the local momentum density. The two slabs are providing energy to the central region at a rate of $2K = 2\gamma_{CM}^2 \rho_0$ per unit area per unit time, and no net momentum (γ_{CM} is the Lorentz factor of each slab in the center of mass system, and ρ_0 is the energy density of normal nuclear matter). Landau's equations in this special one-dimensional case read

$$\frac{d}{dt}(\mathbf{E} - P) = -\frac{d}{dx}(\beta\mathbf{E}) \quad (7)$$

$$\frac{d}{dt}(\beta\mathbf{E}) = -\frac{d}{dx}(\beta^2\mathbf{E} + P) \quad (8)$$

where $\mathbf{E} = (\varepsilon + P)\gamma^2$, ε being the energy density in a co-moving frame of reference, and P is called the pressure.

There exists a solution in terms of two shock waves moving forwards and backwards at a velocity v_s . In between the two shock wave planes, the matter is not moving, having an 'energy density' $\mathbf{E} = jK$ and a pressure $P = f\mathbf{E}$. For a perfect gas, we expect $f = 1.4$ but this particular value is not essential, and we can continue the discussion with f left variable.

At the passing of the shock waves, both function \mathbf{E} and P have discontinuities both as a function of space and time. Therefore, the derivatives in the Landau equations are δ functions. The coefficients multiplying the delta functions in these derivatives are related, applying equations (7) and (8), by the velocity of the shock waves:

$$v_s \Delta(\mathbf{E} - P) = \Delta(\beta\mathbf{E})$$

$$v_s \Delta(\beta\mathbf{E}) = \Delta(\beta^2\mathbf{E} + P)$$

In the incoming ultrarelativistic nuclei, $E = K$, $\beta E \approx K$ (or $-K$), $\beta^2 E \approx K$, and $P = 0$, while in the central region, $E = jK$, $\beta E = \beta^2 E = 0$, and $P = fjK$. Therefore, we are left with the equations:

$$v_s(j - 1 - fj) = 1$$

$$v_s = fj - 1$$

with the solution:

$$j = \frac{1}{f(1-f)}$$

$$v_s = fj - 1 = \frac{f}{1-f}$$

This description of a shock is idealized in that we neglect viscosity altogether. As shown in Figure 7, when the shock wave reaches the back side of the slab, it turns around into a rarefaction wave. Ultimately, all the momentum of each slab is returned to them as the region of high density shrinks, with the surprising consequence that the slabs finally appear as not having interacted. Because of the many assumptions⁸, this result cannot directly be applied to the heavy-ion collisions, but we must remain aware that a shock wave might carry a large amount of the energy available initially into longitudinal momentum. Another very interesting property of this model consists in showing that the initial energy density can indeed be fairly constant over space and time, and depends on the relative velocity of the two slabs but not on their size. This is normal, considering that the information of the size of the slab ('How far is the back edge?') would have to travel faster than the speed of light in order to influence the very initial energy density. The extremely large values of energy density ($\approx \gamma_{beam}^2 / f \rho_0$, where ρ_0 is normal nuclear density) appearing behind the shock wave are probably never realized. However, they would certainly occur if indefinitely large nuclei could be made to collide.

⁸ 1) that the nuclei are flat 2) that they are infinite in the transverse direction 3) that their edges are perfectly sharp 4) that there is no viscosity 5) and no turbulence.

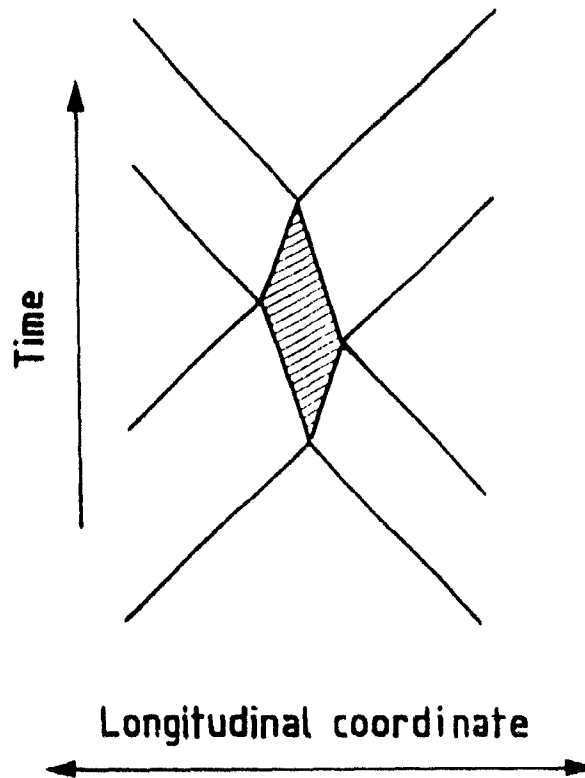


Figure 7: Light cone diagram of the collision of two slabs of non-viscous hadronic matter at high energy.

1.13 A realistic hydrodynamic simulation.

Since the final characteristics of an event are most determined by the longitudinal expansion, it is interesting to simulate this one-dimensional expansion for simple cases. The analytical formula obtained for an expanding Gaussian profile is only valid non-relativistically. In order to study the expansion of a fireball with a given initial profile of energy density up to relativistic velocities, a numerical simulation has been built. We only consider the simple case where the pressure is one third of the energy density. The simulation is a straightforward incremental procedure, using the equations (7) and (8). Such a direct integration/differentiation is possible in spite of the intrinsic computational noise induced by numerical derivatives by using the REAL*16 high precision floating point numbers of the IBM370 (36 decimal digits precision). If this precision was not available, we would have to make use of the much more complicated particle-in-cells methods [66][67].

The solution to these equations possesses the property of scale invariance which is typical of solutions to hydrodynamics of perfect fluids. The expansion of a perfect fluid continues in principle for ever. In practice, we consider that the expansion stops when the density is sufficiently low that the collisions are rare and do not contribute to an hydrodynamic evolution. Afterwards, the particles travel to the detectors with constant velocities. A possible criterion for choosing the instant at which the freeze-out would occur is when the gradient of the velocity is larger than the average velocity divided by the mean free path. This has been studied in [40]; it was shown that if the freeze-out occurs for most of the material at a finite *coordinate* time after the collision, and not at a given *proper* time. The case of freeze-out at a finite proper time is only relevant when we consider extremely relativistic collisions (with a rapidity plateau) and very small initial volumes [5]. Because the solution to hydrodynamic equations are scale-invariant, the freeze-out time is proportional to the initial width x_1 of the Gaussian profile of energy density. The freeze-out time, for ^{32}S on W at 200 GeV per nucleon⁹, is $8 \pm 2 x_1$, where the error represents our lack of knowledge of the mean free paths of mesons in a gas of mesons.

The profile of the energy density in the frame-of-reference of the fireball is shown, at various values of the coordinate time, in Figure 8. At the beginning the profile widens while remaining Gaussian, like in the non-relativistic limit. At later times, two bumps are developing. They appear because of the γ^2 of the receding matter. However, the invariant energy density does not have two bumps, it simply decreases with time while the spatial size increases. This is shown in the contour plot of the invariant energy density of Figure 9. The longitudinal space coordinate is shown in abscissa, and the time in ordinate in a light-cone diagram.

In this model, where an ideal gas equation of state (EOS) has been assumed, all the measurable properties of the energy flow are simply given by the ratio τ of the freeze-out time to the initial width of the Gaussian profile. The rapidity distribution of energy density is shown for a few values of τ in Figure 10.

The longitudinal expansion is followed by an isotropic free expansion ('decay'), and thus $dE_T/d\eta$ is obtained by convoluting de/dy with the function $1/\cosh^3 y$, the later being the shape of an isotropic distribution in dE_T/dy . The width of de/dy and of the resulting $dE_T/d\eta$ distribution are plotted as a function of τ in Figure 11 (b) and (a) respectively.

The interesting point here is that this isotropic decay will involve less energy than that initially available in the fireball. Some of the available energy has been converted into the kinetic energy of a collective longitudinal expansion. By conservation of energy, it is easy to see that this energy corresponds precisely to the work done by the fluid while it was expanding, which we call α_L . The ratio of this longitudinal work α_L to the total energy is shown as a function of τ in Figure 11 (c).

⁹ Similar values are obtained if we assume that the longitudinal expansion stops when the longitudinal size has reached the transverse size.

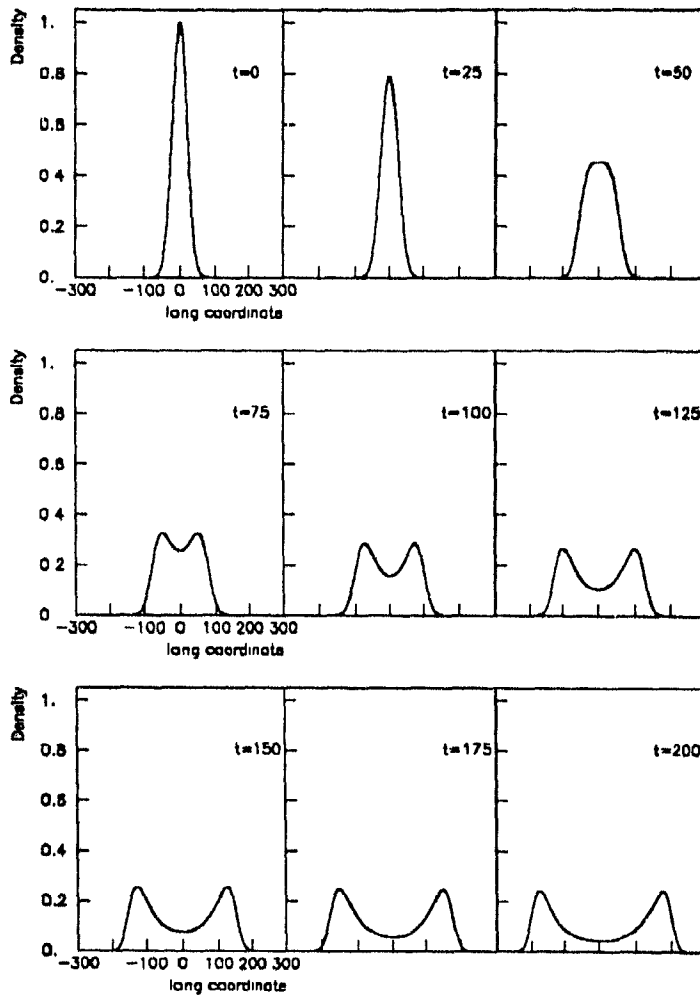


Figure 8: The relative energy density as a function of space and time. The initial width is 20 units in space. Since the solutions to the equations of hydrodynamics are scale invariant, time and distance are not specified in fm/c and fm. For $^{32}\text{S-W}$, one space unit is $1/30$ fm and one time unit is $1/30$ fm/c.

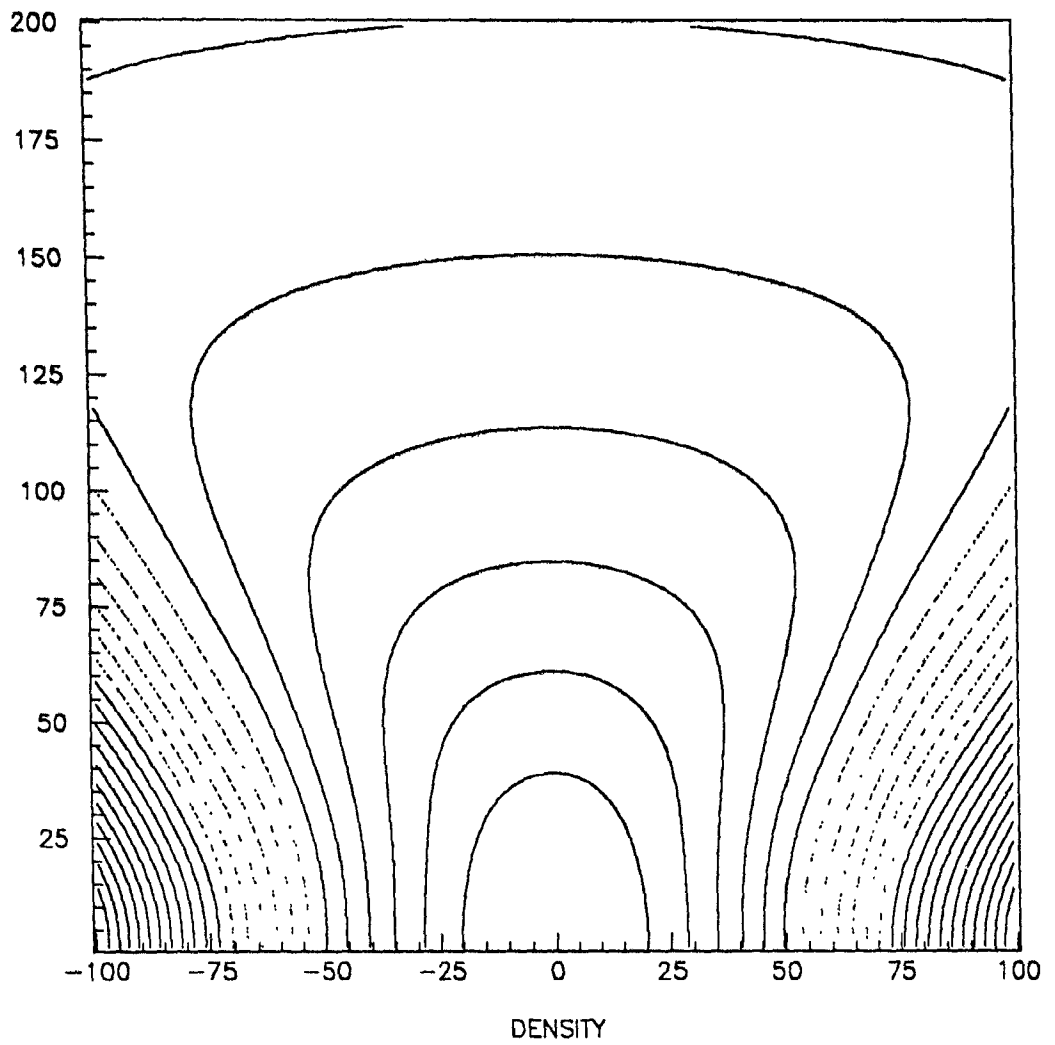


Figure 9: Contour plot of the invariant energy density. It is shown as a function of longitudinal coordinate and time in the frame of reference of the fireball. The distance between two contours is a factor of two.

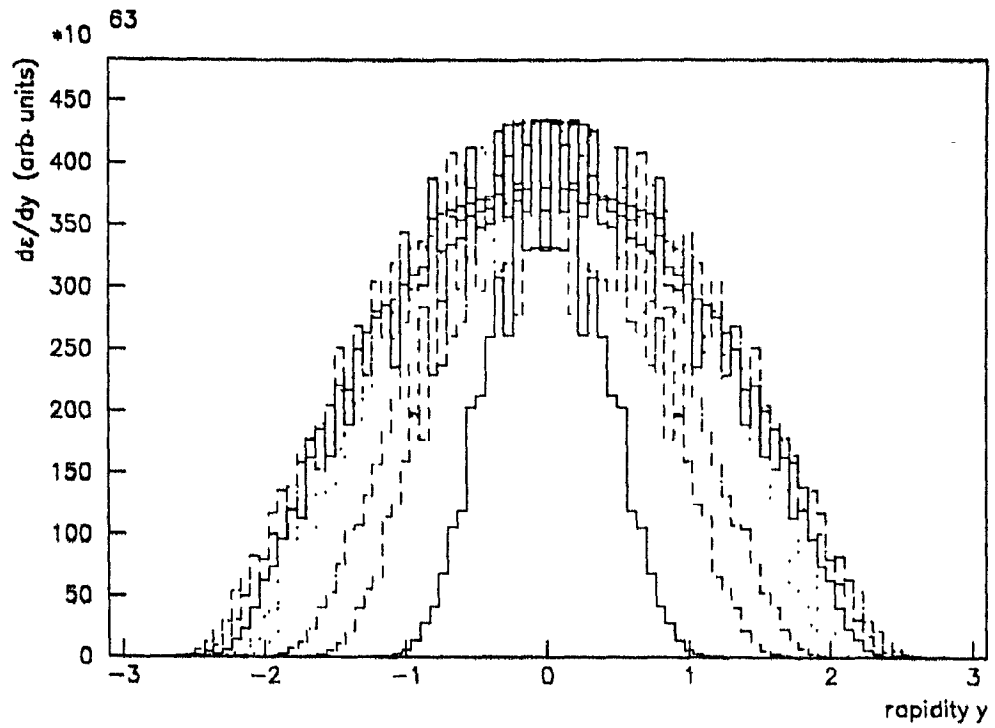


Figure 10: The rapidity distribution of invariant energy density at times corresponding to $\tau=1.25, 2.5, 3.75, 5.0, 6.25, 7.5, 8.75,$ and 10.0 . The shapes are Gaussian, and the widths are increasing (but in a more and more gradual way) with increasing freeze-out times.

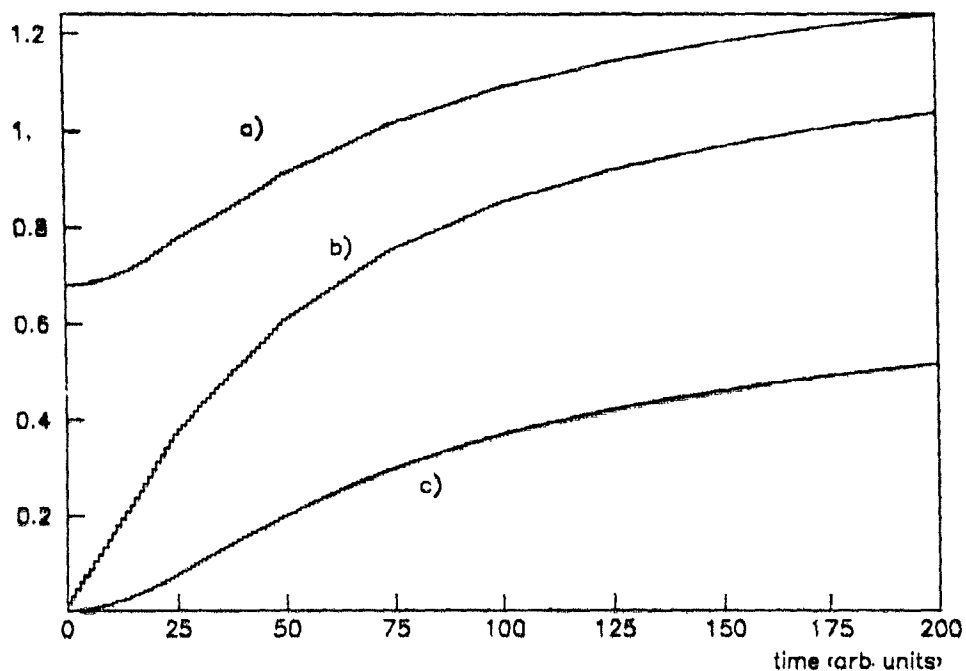


Figure 11: As a function of freeze-out time: a) the width of the rapidity density of transverse energy b) the width of the rapidity distribution of invariant energy density c) the fraction of the available energy taken by the longitudinal expansion. The time is measured in units of $\tau_1/20$ (1/30 fm/c for $^{32}\text{S-W}$ at 200 GeV per nucleon).

1.13.1 Effect on angular energy correlations

The hypothetical existence of a compressed fireball, whose subsequent expansion causes the observed distributions, is the source of, or should be the source of a measurable angular correlation. This is because collisions producing transverse energies corresponding to the plateau region of differential cross-sections have a small but non-zero impact parameter b ; the resulting fireballs have some angular momentum, and rotate while expanding. With z designating, like usual, the longitudinal coordinate, we define here the coordinate x in the plane of the vector impact parameter, and y perpendicular to this plane. The fireball has an initial energy density $\varepsilon = \varepsilon_0 e^{-\frac{x^2}{2r^2} - \frac{y^2}{2r^2} - \frac{z^2}{2r^2}}$. Due to the finite impact parameter, each part of the fireball has an initial velocity in the longitudinal direction depending on its initial x -coordinate $v_z = f \frac{x}{x_1}$ where $f \approx b / b_{\text{max}}$. Using the notations of 1.12.1,

during the expansion, this cell of fireball gets in addition a velocity $\frac{dz_1}{dt} = \frac{z_1}{w_T}$ in the longitudinal direction and $\frac{dx_1}{dt} = \frac{x_1}{w_T}$ in the transverse direction (we are not concerned here by the velocity it gets in the direction perpendicular to the reaction plane). By this mechanism, we generate a rapidity-dependent net transverse momentum, which is in principle observable [68].

As we have seen in 1.12.1, the velocity of longitudinal expansion is larger than the velocity of transverse expansion by a factor equal to the ratio x_1/z_1 of the initial transverse size of the fireball to the initial longitudinal size. As a result, considering the velocity distribution:

$$\exp \left[- \left((v_z - f \frac{v_x}{w_T})^2 / (2w_T^2) + (v_x)^2 / (2w_T^2) \right) \right]$$

the coefficient of the regression $v_x \rightarrow v_z = f_1 v_z$ of the transverse velocity on the longitudinal velocity is much smaller than the coefficient of regression $v_z \rightarrow v_x = f_2 v_z$ of the longitudinal velocity on the transverse velocity $f_2 \approx (w_T/w_L)^2 f_1 \approx (z_1/x_1)^2 f_1$. This is the reason why large collective transverse momenta cannot develop.

A approximate expression for f_{xz} taking into account a distribution of added 'thermal' velocities (of width w_T) after freeze-out is:

$$f_{xz} = \frac{f w_x}{w_L^2 + w_T^2}$$

To make an estimate of the regression of the net transverse velocity on the rapidity, we use $f = 0.4$ in $^{32}\text{S-W}$ ('plateau region'), with $w_x = 0.1 w_T$ (from $x_1/z_1 \approx 10$), $w_L^2 \approx 0.35(w_T^2 + w_T^2)$ (from the longitudinal work computed in 1.13), and $w_T \approx 1$ (from the rapidity width computed in 1.13). We obtain $f_{xz} = 0.014$. It must be stressed that this is an extrapolation of a non-relativistic calculation to the relativistic region, so this estimate must be taken *cum grano salis*. The knowledge of the exact produced net transverse momentum¹⁰ at non-zero impact parameter would certainly be useful, but a fully relativistic three dimensional hydrodynamic calculation is outside of the scope of this thesis.

¹⁰ By summing over several particles and over several events, the non-zero regression of transverse velocity on rapidity results in transverse energy correlations in azimuth.

Chapter 2

The HELIOS detectors and experimental conditions

2.1 The beam conditions

The data presented in this thesis were taken with the HELIOS experimental set-up installed in the H8 beam line of the CERN Super Proton Synchrotron (SPS). The SPS nominally operates at intensities up to 10^{12} protons per burst (2.4 sec) with a maximal momentum of 450 GeV/c. An attenuated primary beam of $\approx 10^6$ protons per burst can be deflected in H8. Beams of secondary high energy hadrons with momentum of 200 GeV/c at rates of $\approx 10^7$ per burst are also available, by means of a production target.

In 1986, the CERN accelerator complex proceeded to the extraction and acceleration of fully stripped oxygen ions. In 1987, fully stripped sulfur ions were similarly accelerated. The ions are 'picked' in a SO_2 plasma by a pinhole, and pre-accelerated in a Radio-frequency quadrupole (RFQ). At this stage, the oxygen ions are in the ionization state O^{6+} , and the sulfur ions in the ionization state S^{12+} . They get fully stripped by traversing a thin beryllium sheet, and are then accelerated to 12 MeV/nucleon in the linear accelerator (LINAC1), transferred in a synchrotron from where they were injected at 260 MeV/nucleon in the CERN Proton Synchrotron (PS). The precise tuning of the PS causes the selection of either the sulfur or the oxygen, because of a slight difference of the charge to mass ratio between ^{32}S and ^{16}O . The nuclei were boosted up to 10 GeV/nucleon in the PS before injection in the SPS where they were finally accelerated to energies of up to 200 GeV/nucleon. Intensities of $\geq 10^8$ ions per burst (4.2 sec) were transported in the SPS where high rate is a minimum requirement for adequate beam control. This intensity is reduced to a few times 10^5 ions per burst to achieve optimum acquisition rate of interesting events. The rate capability is essentially limited by the rate capability of the uranium/liquid argon calorimeter (ULAC), due to the time constant of shaping amplifiers and the time needed to fully integrate the hadronic response (slow neutrons). This reduction was achieved on the extracted ion beam by means of steel-septum magnets, and in the H8 secondary transport beam system by using cylindrical and slit collimators. In 1986, the beam used for heavy-ion physics had an intensity of $\geq 10^5$ ions per burst, and was focused at the target position, to an ellipsoidal gaussian profile $I \propto \exp(-x^2/(2\sigma_x^2) - y^2/(2\sigma_y^2))$ with $(\sigma_x, \sigma_y) \sim (0.5\text{mm}, 1.2\text{mm})$. In 1987, the sulfur had a similar intensity, and the parameters of the beam profile were (0.8 mm, 1.0 mm). In this chapter, after a brief general overview of the HELIOS experimental

set-up, I will describe the elements of the detector and of the trigger that are essential for the precise study of the characteristics of nuclear matter in the tails of transverse energy distributions

2.2 Survey of the experimental set-up

The HELIOS detector is designed for a multi-purpose experiment. More precisely, two research programs share the use of most of the detectors in distinct running periods. The lepton program is aimed at answering open questions in the production of electrons, muons and neutrinos in $p-p$ and $p-A$ interactions. The high-rate capabilities of the experiment allows precise studies of $e\mu$ universality, anomalies in the production of single leptons, contribution of charm decay to lepton pair (Drell-Yan) production, and "anomalous" low mass pairs. The ion program, to which the present thesis is connected, examines the questions concerning energy and particle flow, with particle identification [69], in fireball of dense hadronic matter extending over large volumes, that are produced in ultrarelativistic nucleus-nucleus collisions.

A schematic top view of the set-up is shown in Figure 12.

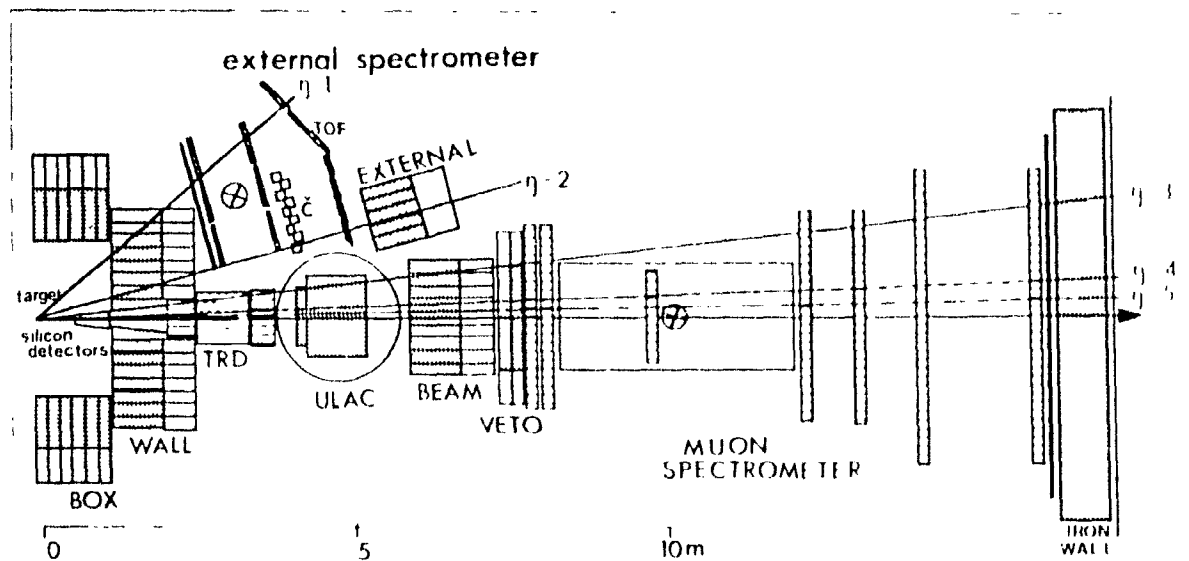


Figure 12: Layout of HELIOS (NA34) experimental set-up

Used exclusively for the 'lepton' program, the compact electron spectrometer utilizes drift chambers with high multitrack capability, a "weak field" calorimetrized magnet, transition radiation detectors, a

scintillator hodoscope and the high granularity liquid argon electromagnetic calorimeter; the muon spectrometer, comprising a magnetic spectrometer and an hadron filter, is used in both programs. In the 'ion' program, the study is aimed at the question of low-mass muon pair production [70]. The 4π -coverage of the calorimeter for the measurement of the energy flow, in the center-of-mass (c.m.) frame, is a powerful tool in the ion program, allowing a full reconstruction of the events topologies as well as providing a trigger on transverse energy in various pseudorapidity intervals. The last component of large size, used exclusively in the 'ion' program, is the external spectrometer that views the target through a slit in the calorimeter wall. It uses Time-Of-Flight and Threshold Cerenkov detectors giving good $\pi/K/p$ separation, two proportional chambers spaced by a thin converter for photon detection and drift chambers coupled with a magnet for momentum analysis.

Small detector components surrounding the target have changed during the duration of the experiment. In the 1986 set-up for the 'ion' program, the multiplicity of charged particles is measured by one silicon-ring counter and one silicon-pad counter. The silicon-pad detector, whose geometry is optimized for electron identification in the context of the lepton-program electron spectrometer, was also used to provide an interaction trigger. In the 1987 set-up for the 'ion' program, three silicon ring detectors were used for the measurement of multiplicity, the most downstream one being used to provide the interaction trigger. The trigger for the arrival of a beam particle is provided by a 'beam telescope', consisting of a series of fast plastic scintillators put in coincidence. As will be discussed in the next section, the proper design of the beam telescope is very important.

2.3 The HELIOS trigger system.

The HELIOS trigger system acts like an asynchronous signal processor using three main modules surrounded by logic 'glue'. The main three modules are the pretrigger, the first-level trigger, and a second-level trigger called the Very Fast Bus (VFB); each of which is a computer-programmable logic array. The working of the trigger system can best be understood by considering the sequence of events following the arrival of a particle in the beam. The general arrangement of these trigger elements is shown in Figure 13.

The arrival of a beam particle is detected by a scintillator located 1.5 m upstream from the target in 1987. The scintillator was located 28 cm upstream from the target in 1986. The light signal from this fast plastic scintillator is amplified by a fast photomultiplier, and discriminated. This signal is used for three purposes:

- produce a general start for the operation of the trigger logic
- produce a time reference for time-of-flight measurements.

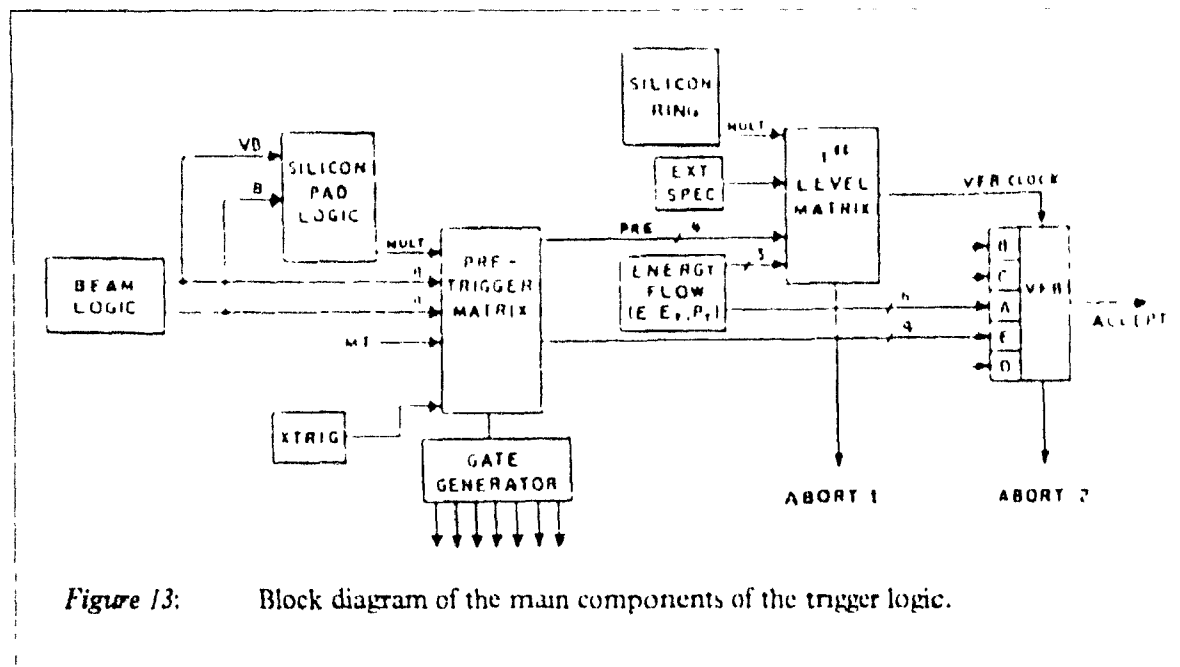


Figure 13: Block diagram of the main components of the trigger logic.

- measure the ionization dE/dx of the incoming ion, which is recorded by a charge-ADC (Analog-to-Digital Converter)

For studies of the calibration and of the beam profile, the discriminated signal of the beam scintillator can be used directly as a pretrigger. For the physics studies, an interaction is required, and therefore the system has a built-in interaction pretrigger. The fast interaction pretrigger is obtained by discriminating the signal from each of the elements of a segmented silicon detector. An analog sum is made of these signals, and if it exceeds a given threshold, an interaction pretrigger signal turns true. In order to avoid that the signals from different events overlap in certain detectors, there is a 'before and after protection system'. When the protection is active, no pretrigger is allowed. This protection is 250 ns after a beam pretrigger, and 50 ns before, and 700 ns after an interaction pretrigger, and 100 ns before. In 1986, the detector used for the interaction trigger is the silicon pad detector, in 1987, the detector used for the interaction trigger is the most downstream of three silicon ring detectors.

In the 1987 set-up, the ionization dE/dx as measured in a thin plastic scintillator was used in the trigger. The coincidence of two discriminators is used in the first-level trigger to select heavy-ions of the proper charge. This is needed due to the contamination of the beam by ions with same rigidity as the primary beam, but with smaller charge, produced by interactions far upstream. This contamination, reaching up to 15% in certain cases [71], was not removed online in the 1986 set-up. In the 1987 set-up, helped by the results of the analysis of the data taken in 1986, it was possible to remove these incident ions with bad charge at the trigger level; by doing so, we also removed some non-target interactions.

In the meanwhile, the physical processes at the basis of the detection take place in the various detectors. In the calorimeters, after the secondary particles have interacted to produce showers, the fast plastic scintillators produce their light with a typical rise time of 10 ns. The light bounces back and forth in the light guides for also about 10 ns. The light reaches the phototubes, where it takes about 20 ns to be amplified. Finally, the short pulses of charge travel for 500 ns in the 100 m long cables to the charge integrating ADC's in the counting room. The speed of signals in the cables is about 2/3 of the speed of light, due to the geometry of the coaxial cable and the dielectric constant of the insulator. This cable delay is useful since the gate for integrating charge from the detector is open 50 ns before the charge arrives to the charge-ADC.

The fraction of the signal which is dedicated to the online measurement of the energy flow similarly travels with small delays through the summation units, and with a longer delay (320 ns), through 'grey cables', in the final amplifiers and shapers to the input of the Flash Analog-to-Digital Converters (FADC). This happens for any signal that may come from the detector at any time, quite independently of the detected presence of a beam particle. However, the gate of the FADC, derived from the pretrigger, happens precisely at the peak of the shaped signal coming from an interaction, thanks to a suitable delay. While any time during the positive lobe of the shaped signal would in principle be sufficient, the calibration of the energy flow system is obviously more immune from possible variations of the timing of the trigger system, if the sampling happens precisely on the peak. This ideal timing cannot be determined with sufficient accuracy without measurements with actual interactions (in particular, the average time of flight to the calorimeters depends slightly on the physics). The timing of each FADC gate was therefore studied in special runs (prior to the 1986 data taking) using programmable delay generators. When the proper timing was established, it was set permanently using cables for delay.

The generated pretrigger is used to start the processes of converting the magnitude of electrical signals in ADC's (either charge-ADC's, or peak-ADC's, or single and multiple samplings voltage-measuring flash-ADC's), and for starting the fast clocks used for drift time measurements or time-of-flight measurements. It is also used as one input in a second block of combinatorial logic called the first-level trigger. In the first-level trigger, the pretrigger is logical-ANDed with a programmable combination of logical signals from the energy flow system, beam counter discriminators, the external spectrometer, or a silicon ring multiplicity. The output of the first-level trigger is several signals derived from the pretrigger, starting at known delay after the arrival of the beam particle, and remains active for a precise period of time.

In the final step of the trigger logic, all the elements of information available for deciding whether the event should be recorded on tape or not, obtained in a time of $\approx 1 \mu s$, are gathered in the VFB second-level trigger. The organization in two levels of trigger was chosen because some of the criteria for accepting or rejecting an event are available within 250 ns, while some others take more than one microsecond. In this way, the dead-time of the system is reduced, since in some cases it can be found that the event is not interesting, and the trigger system can be freed for another event,

in only 250 ns instead of 1 μ s.

The second-level trigger is a Random Access Memory (RAM) Programmable Logic Array (PLA) which permits up to 51 different combinations of signals to be considered as interesting. The exact set of combinations of all the selected logic conditions that will lead to the collection of an event is stored in special files of the online data acquisition computer, and is known as a 'VFB'. The VFB has an additional feature. It is possible to impose that only a fraction of the accepted triggers will generate a signal for transferring data to the online data acquisition and recording system. The fraction is specified as $1/(N + 1)$, where N is an integer known as the 'downscale factor'. Only one time out of $N + 1$ times, in a regular sequence, the VFB will cause the activation of the data acquisition system. The other N times, the system will be immediately free to potentially accept another event. This gives yet another way to improve the throughput, by avoiding a flood of less interesting events.

The energy flow summation is one criterion of many for accepting or rejecting an event. It participates in the first-level trigger, by giving a signal if the quantity reaches the first of five trigger thresholds. The second-level trigger then receives from the energy flow a 3-bit encoded value of the threshold reached. In the normal data taking, there is a second-level trigger ('VFB') for each threshold value of the transverse energy, and also a simple trigger for an interaction without requirement of transverse energy. The interaction trigger and the triggers with lowest thresholds are strongly downscaled, to save live-time, while the trigger corresponding to the highest threshold is not downscaled, to investigate the tail of the transverse energy with as many statistics as possible.

The complete set of informations relevant to a single event, represented by approximately 16 K-bytes of binary coded data, is recorded (transferred under CAMAC¹¹ control to a recording buffer in the VAX data acquisition computer) in approximately 5 ms. During this time, all the events (some of them being rare and interesting ones) produced by the incoming beam particles are not recorded. This is the reason why the criteria for selecting an event are as stringent as possible.

The trigger logic hardware has allowance for an 'ABORT' signal. This signal is generated when a beam particle hits the 'after' part of the 'before and after protection' time window. In this case, the ADC's are cleared as fast as possible to make the system ready for another event.

¹¹ Computer Automated Measurement And Control.

2.3.1 Proper design of the beam telescope with respect to upstream interactions

One of the important lessons of the online experimentation is that the contamination by upstream interactions can represent a serious problem for transverse energy triggers. The upstream interactions have recognizable properties offline (see section 3.1), and therefore it is not a problem to remove them from our samples early in the analysis. However, in the online system, these interactions represent a serious problem if they dominate the target interactions at large transverse energy. The data acquisition system, which has a finite rate for collecting events, is then swamped by non-target interactions. The interactions with the target nuclei with the largest transverse energies are then accepted with a severely impaired efficiency, and/or with a downscale factor. The problem becomes even more severe with the lightest target nuclei, since the tail of the distributions occurs at moderate transverse energies where the upstream interactions have all chances to be dominating unless they are well under control.

The motivation for spending considerable efforts in making sure that the target interactions dominate at large transverse energy lies in the physics that we are studying. We attempt to explore, with the highest possible statistics, nucleus-nucleus collisions where a large energy density has existed. If the upstream interactions dominate, we lose in statistics (number of events). If we increase the target thickness, we gain in target-in statistics, but the highest transverse energies are likely to be due to multiple interactions. Thus the optimal operating conditions are finally dictated by the physics requirements. With a given integrated flux, we are likely to probe transverse energies up to a certain value $E_{T,MAX}$, and therefore we must make sure that the resolution of the calorimeter, the smearing due to target position variations, or due to multiple interactions, do not degrade significantly the selection of the events with transverse energy $E_{T,MAX}$.

Events with large transverse energy in collisions of oxygen or sulfur ions with light target nuclei (aluminium) are potentially more interesting than in the case of collisions with heavy nuclei, due to the lesser importance of cascading or of geometry in the determination of the transverse energy. This is the reason why the target-in interactions must dominate the upstream interactions at the largest transverse energies of the collisions with Al as the target nuclei. This means in practice, for the case of ^{32}S projectile, that the contamination of non-target interactions producing 100 GeV or more transverse energy must be suppressed. With a preliminary design of the online system, this was not the case, as can be seen in Figure 14. Some non-target events have transverse energies larger than would have interactions with a *tungsten* target.

This is at first paradoxical, since there are no elements heavier than tungsten present in the experimental apparatus. The principal 'background targets' consist of light target nuclei: the beam pipe window (Be) and the scintillators (C, H). Two mechanisms are responsible for the production of large transverse energies. First, the target position is more upstream, causing all angles to change. It has been estimated that this effect amounts to a 1% change in the scale of transverse energy per cm of target position change. Secondly, and this fact was only fully realized by the actual

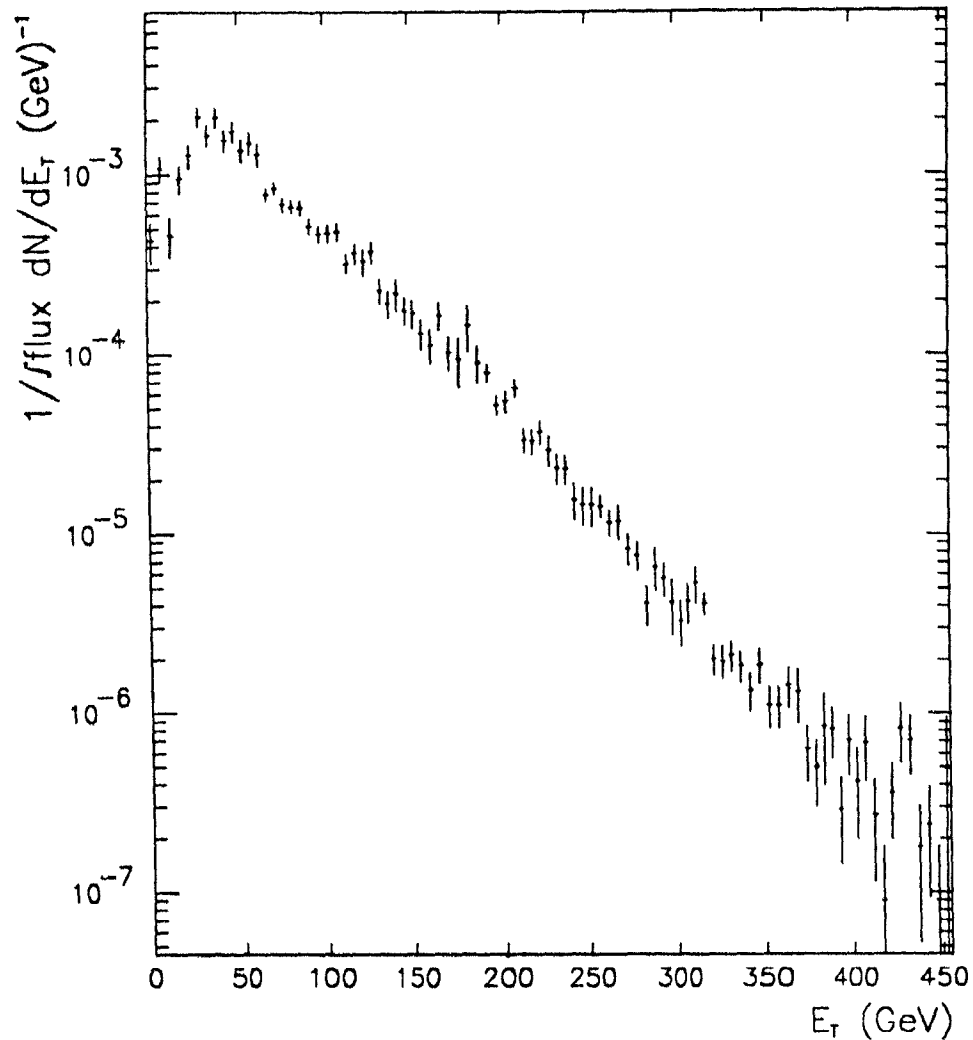


Figure 14: The E_T distribution of non-target interactions. The projectile was 200 GeV/nucleon and the beam counter cut is disabled in this plot.

experimentation, energetic secondary particles from an upstream interaction meet thick metal structures where large amounts of transverse energy is produced. The same does not occur with the interactions in the target, because the path to the calorimeters is as free as possible of materials, by design. Events with medium to large apparent transverse energy are produced with large cross-sections through this mechanism of transverse energy 'multiplication' by the thick metal support structures of the target region. As we have seen above, although these events can be removed offline, their presence online can severely impair the realization of the physics programme.

The solution is to make sure, at the online stage, that the full projectile reaches the position of the target. In the 1987 set-up, this function is provided by the 'B3' scintillator located only a few centimeters upstream from the target. The ionization dE/dx is measured with some precision, and a rather tight 'window' is imposed at the trigger level to check that the ionization is that of the sulfur ion. Upstreams are likely to produce either a too low or a too high ionization, and are thus efficiently rejected.

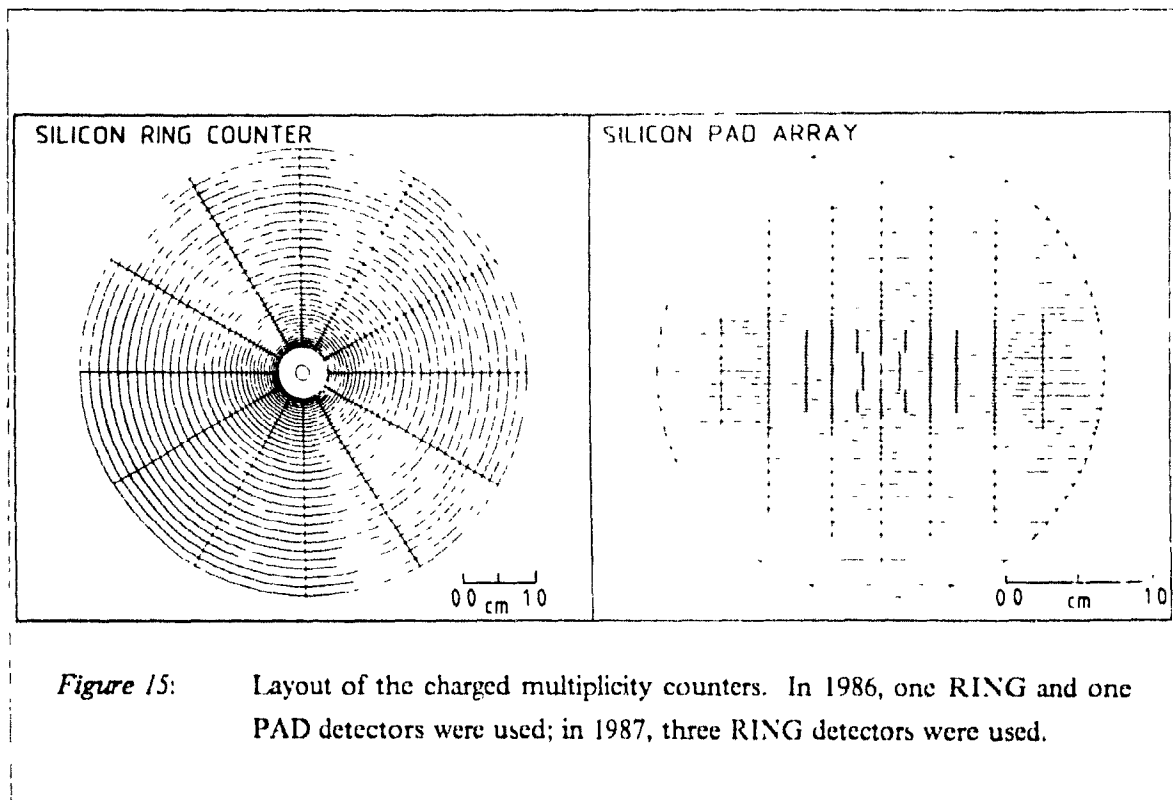
2.4 Description of the silicon multiplicity detectors.

In the 1986 data taking period, two detectors were used to measure the charged multiplicity, one RING counter, located at 3 cm downstream of the target, and one silicon-pad counter (PAD), at 9 cm from the target. In the 1987 data taking period, three identical RING counters were used, located at 1, 6 and 26 cm downstream from the target. In 1986, the PAD counter covers the pseudorapidity range $2.5 < \eta < 5.0$, and the silicon-ring counter covers the pseudorapidity range $0.9 < \eta < 2.8$. In 1987, the ring counters located at 1 cm (RING1), 6 cm (RING2), and 26 cm (RING3) downstream from the target, cover the pseudorapidity ranges $0.33 < \eta < 1.8$, $1.4 < \eta < 3.5$, and $2.8 < \eta < 5.0$ respectively.

These counters are basically silicon hodoscopes for the counting of tracks of charged particles [72]. The 400 sensitive sub-areas of the PAD [73] counter, and the 386 sensitive sub-areas of the RING counter are indicated in Figure 15. The radii of the rings in the RING counter go in geometrical progression, such that each ring covers an almost equal region of pseudorapidity, $\eta = -\ln \tan \theta/2$

The silicon elements are connected to fast charge pre-amplifiers located within a small distance from the detector itself. This is in order to reduce the capacitance at the input, which is the major source of noise. The noise, due to the capacitance of each element, is a serious problem: the Landau peak of the ionization distribution is located at only about 10 r.m.s. widths from the pedestal. The fast charge preamplifier is followed by a driver to bring the signal to the counting room through long cables.

A part of the signals goes to the fast interaction trigger logic which consists firstly of two-level discriminators (one level for single particle, another level for double particle). An analog sum of single-particle logic signals is realized, and this analog sum is measured in a FADC clocked by the Valid Beam (VB) signal. The VB valid beam signal is simply the discriminated signal of the upstream scintillator, subject to the conditions of the 'before and after' protection, and of adequate dE/dx in the B3 additional scintillator in 1987. The value measured by the FADC is compared digitally with a computer-loaded threshold, and if the multiplicity is sufficient, an interaction pretrigger is generated. In 1986, these discriminators were thus connected to the PAD detector. In the



1987 set-up, they were connected to the most downstream RING detector (RING3).

Another part of the signal is measured, after shaping, by Peak-ADC's (PADC). These measurements are recorded for the offline analysis.

Yet another part of the signal is discriminated in a distinct set of programmable discriminators. The signals from the discriminators are summed, analogically in the 1986 set-up, and digitally in the 1987 set-up. A digital comparator finally compares the value of the multiplicity with a threshold value loaded from the computer, and sets a flag, indicating that the multiplicity is larger than the threshold. This flag is available at the second-level trigger (VFB) for the making of a high-multiplicity 'VFB'.

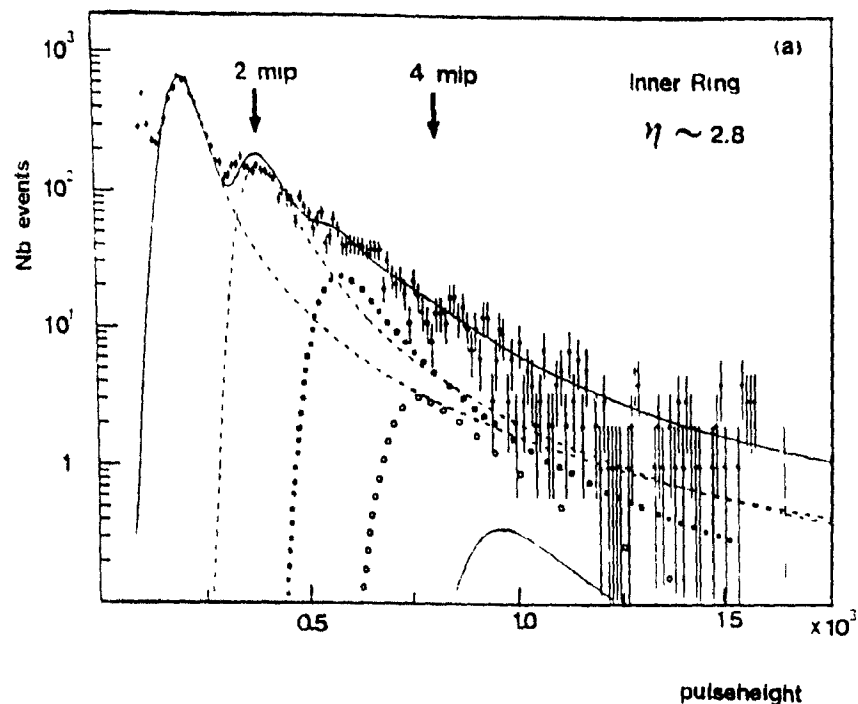


Figure 16: Pulseheight distribution of a PADC measuring the ionization of secondary particles in one element of the RING detector for ^{16}O -W collisions. The peaks corresponding to 2 and 4 minimum-ionizing particles are indicated.

2.4.1 Analysis of the data from the Silicon detector PADC's

In a typical sample of events recorded with a heavy-ion beam on a large target nucleus, one sees the pulseheight spectrum shown in Figure 16. Most of the particles are minimum ionizing, (e.g. pions with average $p_T \simeq 350$ MeV). In this pulseheight spectrum, we see peaks corresponding to a pulseheight of two times minimum ionizing, three times minimum ionizing, etc..., indicating the importance of pile-up. Once we identify the position of the pedestal and of a single minimum-ionizing particle for each channel, for the rest of the analysis we will just consider 'a hit' if the pulseheight exceeds the offline threshold. This threshold is chosen for each channel 140 ADC counts above the pedestal pulseheight, that corresponds to about 2/3 of the difference of counts between the pedestal and the peak of the Landau distribution for single minimum ionizing particles. Although all detectors are fully depleted, the charge corresponding to a minimum-ionizing particle is not the same for all channels, due to variations of the angle of incidence.

2.5 Description of the calorimeters

Seven types of calorimeter modules are being used in HELIOS: Cu/scintillator, U/Cu/scintillator, U/scintillator with optically coupled towers, U/scintillator with optically decoupled towers, Fe/scintillator, U/liquid argon with tower read-out and U/liquid argon with strip read-out. Their arrangement is schematically represented in Figure 17 for the data taken in 1986 and in Figure 18 for the data taken in 1987 (and 1988). The target is surrounded by the BOX calorimeter, covering the pseudorapidity $-0.1 < \eta < 0.9$, then the pseudorapidity $0.9 < \eta < 2.9$ is covered by the WALL calorimeter, at the center of which is the MAGCAL calorimeter. The energy going through the slit is measured in the EXTERNAL calorimeter. In 1986, the energy that goes through the hole in the MAGCAL is measured in the ERSATZ calorimeter and the BEAM calorimeter further downstream.

In 1987, the energy that goes through the hole in the MAGCAL is measured in the ULAC, that provides high granularity, and the BEAM calorimeter absorbs any leakage from the back of the ULAC. Both set-up provide 4π coverage in the center-of-mass, but the granularity in the forward region is insufficient in the 1986 set-up. The VETO calorimeter, located downstream of the BEAM calorimeter measures leakage of energy in rare events where a shower starts very late.

The first two types of module were used previously in the AFS experiment that ran at the ISR from 1978 to 1983. The scintillator modules consist of metal plates interleaved with 2.5 mm thick plastic scintillator plates (Altustipe, acrylic material manufactured by Altulor, Paris, France)

The U/Scintillator and U/Cu/scintillator modules are divided in two sections. The front or 'electromagnetic' section, is 6.4 radiation lengths deep and contains 2 mm thick depleted uranium plates. The back 'hadronic' section is 4 interaction lengths deep in the U/scintillator case and 3.8 interaction lengths deep in the U/Cu/scintillator case. In back section, the depleted uranium plates are 3 mm thick. In the U/Cu/scintillator back section, one out of every three metal plates is a 5mm copper plate instead of a uranium plate. The read-out is organized in stacks containing each 6 towers of $\approx 20 \times 20 \text{ cm}^2$. Each section of each tower is read-out on each of its two sides by separate wavelength shifters and phototubes. In some stacks (*decoupled* stacks), the scintillator is laser-cut at tower boundaries, reducing the light sharing between towers

The ultraviolet light from the scintillator is collected by BBQ wavelength shifters bars (80 mg/l Benzimidazo-benzisoquinoline-7-one imbedded in plexiglas). The resulting green light is measured in XP 2008/UB Phillips phototubes using a Bi-Alkali photocathode. The gain (current/incident light quanta) of these phototubes is a sensitive function of the applied voltage, approximately the fourth power of the applied voltage or about a doubling of the gain for each additional 200V (in the operating region $V \approx 1000V$). These calibration of these modules among themselves and as a function of time is maintained by a measurement of the beta and gamma radioactivity of the depleted uranium. This measurement is performed in between the data taking periods using a gate time for the charge-integrating ADC which is much longer than that used to record an event (10 μs instead of 80 ns). The calibration constants are presented in Table 1.

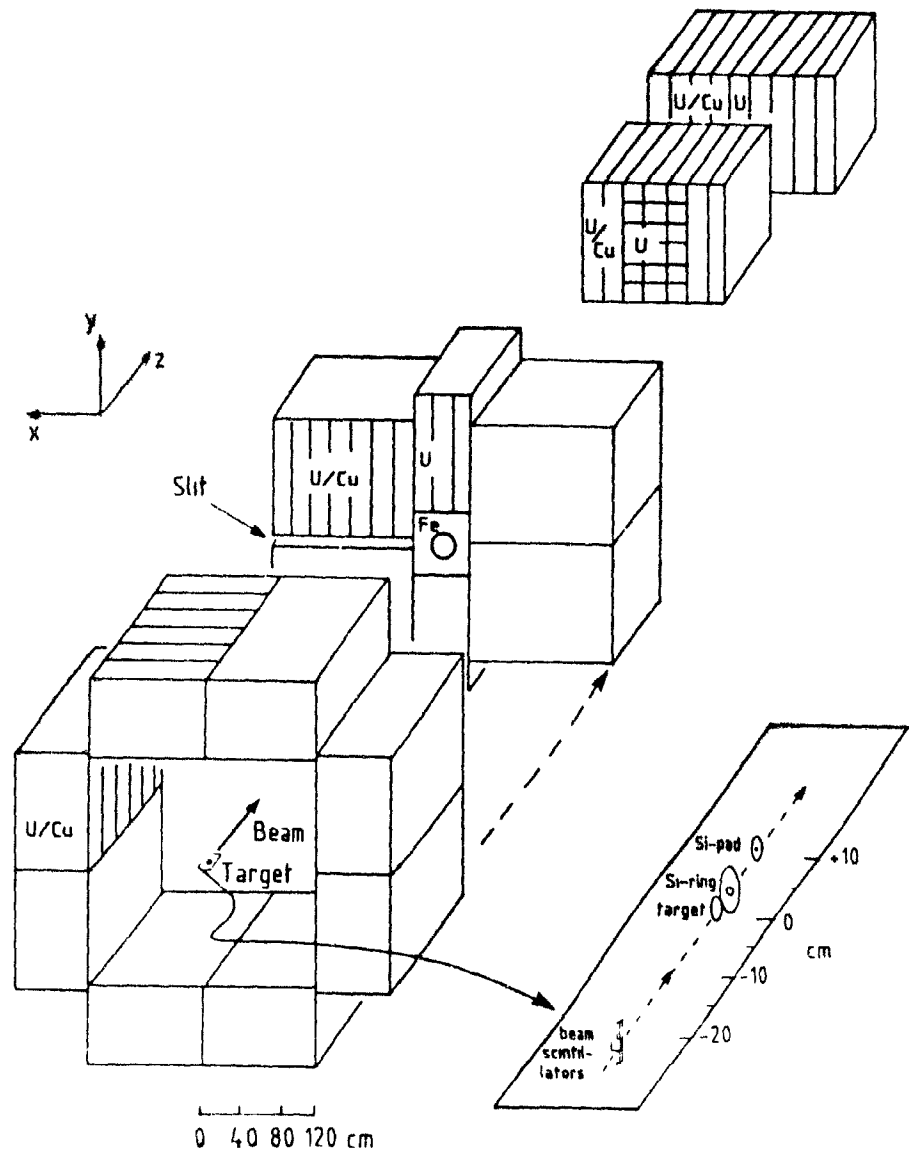


Figure 17: Overview of the calorimeters in the 1986 set-up.

The Fe/scintillator calorimeter is made of 15 mm iron plates alternating with layers of scintillator of 5 mm. Each scintillator layer is divided in 24 'petals' covering 15 degrees of azimuth each. The resulting 24 towers are each readout via wavelength shifter bars, and optical fibers carrying the light to the 24 photomultipliers. For the Fe/scintillator calorimeter, it is not possible to calibrate using the radioactivity since the iron is not radioactive. For this calorimeter, the maintaining of the calibration as a function of time is achieved by sending a fixed amount of light to the wavelength shifter and photomultiplier by means of a light emitting diode. The intercalibration is achieved by means of a 'source scan' whereby a radioactive source is put successively in front of each petal of the

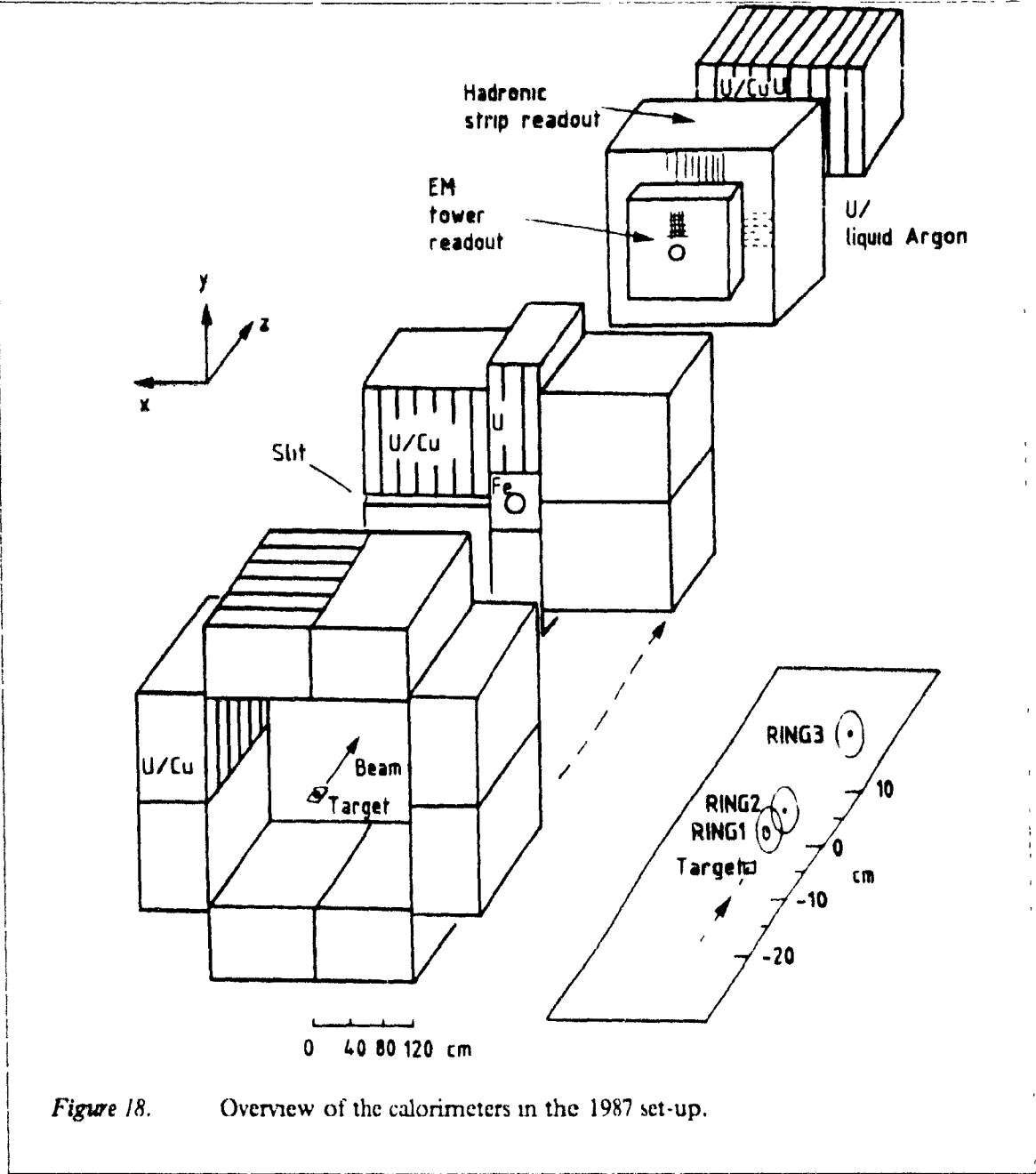


Figure 18. Overview of the calorimeters in the 1987 set-up.

iron/scintillator calorimeter, and the current is measured each time. Finally, the absolute calibration, for electrons, is obtained by sending an electron beam of known energy (deviated for the axis of the beam line by a powerful dipole magnet) in a few petals

Because the calibration of the Fe scintillator calorimeter relies on three different techniques for the intercalibration, the calibration as a function of time, and the absolute calibration, it is prone to minor calibration errors. Because, however, the most exact calibration is needed in this central pseudorapidity region, an offline recalibration has been performed after each running period. The

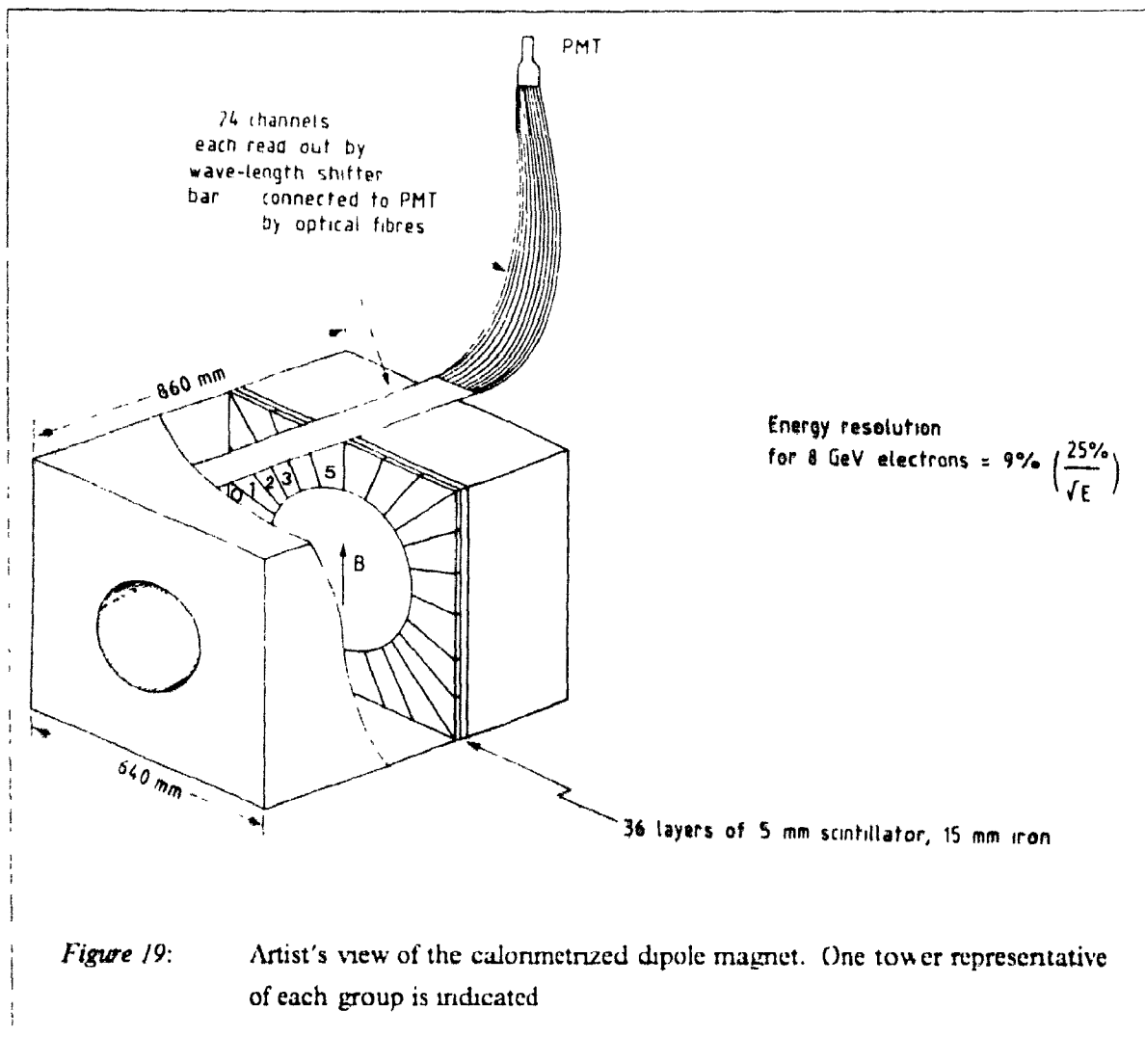
steps of the recalibration procedure will now be outlined.

A first step is to impose the azimuthal symmetry of five groups of towers. The arrangement of 24 towers in azimuth inside a square calorimeter produces three different kinds of towers by geometry: The 'axis' towers, the 'diagonal' towers, and the 'intermediate' towers (see Figure 19). A further division arises because four of the eight 'axis' towers are different, by construction, from the four others. They have iron replacing scintillator (this was needed for mechanical reasons) in a upstream layer of the sandwich structure (LAYER2), whereas the other four have this iron in LAYER5, this affects the response. Similarly, four of the eight 'diagonal' towers have a 'hole' and four have not. The towers are numbered from 0 to 23 in increasing azimuth starting from the HELIOS positive X-axis (the HELIOS X, Y and Z axis are presented in Figure 18). Towers (0,6,12,18) are thus 'axis LAYER5', towers (5,11,17,23) are 'axis LAYER2', towers (1,4,7,10,13,16,19,22) are 'intermediate', towers (2,8,14,20) are 'diagonal with holes', and finally towers (3,9,15,21) are 'diagonal no holes'.

Using unbiased data, we can then use the azimuthal symmetry of nature on average, to deduce an intercalibration of towers up to five constants. Furthermore, the energy deposition does not depend on the construction of the readout, so that the groups of towers which are identical by geometry should also have the same energy deposition. This reduces the number of unknowns in the calibration to three. Then, knowing the relative sizes of the three groups of towers in η, ϕ space, it is possible to deduce that the axis, intermediate, and diagonal groups of eight towers should receive energy in the proportion 1.115 : 1.000 : 0.840. With this process, it is possible to calibrate the towers comparatively to each other.

There remains one undetermined constant, the global energy scale of the MAGCAL calorimeter. For the 1986 data, this constant has been determined using an average of the energy calibrations obtained in a few towers using 8 GeV electrons. For the 1987 data taking, the results of the 1986 calibration have been approximately applied in order to obtain a more precise measurement of the transverse energy at the triggering level. For the 1987 data, with the goal of maintaining an optimum consistency of the heavy-ion data sets so as to reduce systematic errors in comparisons, the procedure of offline calibration was special: we chose, for each tower of the Fe-scintillator calorimeter, a calibration such that the ratio of the energy present in that tower to the energy in the wall calorimeter is the same in 1986 and in 1987 for central collisions of ^{16}O on W.

The calibrations of uranium-scintillator modules (coupled and decoupled) cannot be deduced from the calibration constants of U-Cu-scintillator modules; they have been obtained from measurements with beams of electrons of known energy. The electron calibration of modules having two sections is however complicated by the fact that part of the shower is in the 'electromagnetic' section, and part is in the 'hadronic' section. There are two unknowns (the two calibrations) and an infinity of solutions that will give back the energy of the beam on average. Firstly, the high voltages for each section have been set such that the calibration with uranium noises have the values shown in Table 1. These values were chosen such that, by construction, we could expect a similar response



of the uranium/scintillator modules and of the U,Cu.scintillator modules to a minimum ionizing particle. With the high voltages thus fixed by a precise required uranium noise, we proceed to determine the constants A and B of energy per unit charge from the photomultiplier.

One solution, that might be considered the best, is that for which the distribution of reconstructed energy has an average equal to the beam energy, and the smallest possible width in the r.m.s. sense. Such a solution has the further advantage that it can be simply deduced from the moments of the distributions of the signals S_{em} and S_{had} of the two sections.

Imposing that $\sum_{i=1}^n (E(\text{beam}) - AS_{em,i} - BS_{had,i})^2$ is minimum gives :

$$A = E(\text{beam}) \frac{\langle S_{em} \rangle \langle S_{had}^2 \rangle - \langle S_{had} \rangle \langle S_{em} S_{had} \rangle}{\langle S_{em}^2 \rangle \langle S_{had}^2 \rangle - \langle S_{em} S_{had} \rangle^2}$$

$$B = E(\text{beam}) \frac{\langle S_{had} \rangle \langle S_{em}^2 \rangle - \langle S_{em} \rangle \langle S_{had} S_{em} \rangle}{\langle S_{had}^2 \rangle \langle S_{em}^2 \rangle - \langle S_{had} S_{em} \rangle^2}$$

When this procedure is applied on the sample of calibration electrons, the values of A and B give a ratio B/A of the order of 3.3. The minimum is however very shallow, and depends from the sample considered [74][75]. Another criterion for choosing B/A would be to require that the linearity has to be retrieved for electrons. We define a measure of the linearity by computing the root-mean-square variation of the ratio of the average energy to the nominal energy, normalizing the average ratio to one. This is shown in Figure 20 as a function of B/A. The fact that the curve does not reach zero, while electromagnetic showers are known to be very accurately linear, indicates that some errors exist in the definition of the beam energy in these calibration studies.

The requirements of best resolution and electron linearity indicate that the value of B/A should be taken in the range 3 to 4, and the very best value seems to be of the order of 3.4. However, we must remember that the calibration that gives the best overall resolution for signal is not necessarily the most appropriate calibration in each section. It has been remarked [74] that the constant of proportionality between signal and energy deposition may change locally by as much as 30%. Furthermore, if the intrinsic resolutions in the different sections are different, this minimization will be biased in favor of the section with the best resolution.

The possibility of an equal response to pions and electrons is more constraining on the ratio B/A. In fact, the electrons deposit their energy mostly in the front section and pions mostly in the back section, so that there is a quasi proportionality (in any case, a strong dependence) of e/π on B/A. At both 17 and 45 GeV, $e/\pi = 1$ is achieved for B/A of the order of 4.

The value of exactly 4 was finally chosen. This precise value of B/A, by construction of the calorimeters, would give a response to a minimum ionizing particle (mip) proportional to the actual thickness of scintillator that it traverses [74]. Such a choice gives us an almost ideal e/π at the expense of only a slight degradation of the resolution for electrons with respect to the absolutely best resolution. Once B/A is fixed, the values of both B and A follow from the electron calibrations, and are shown in Table 1.

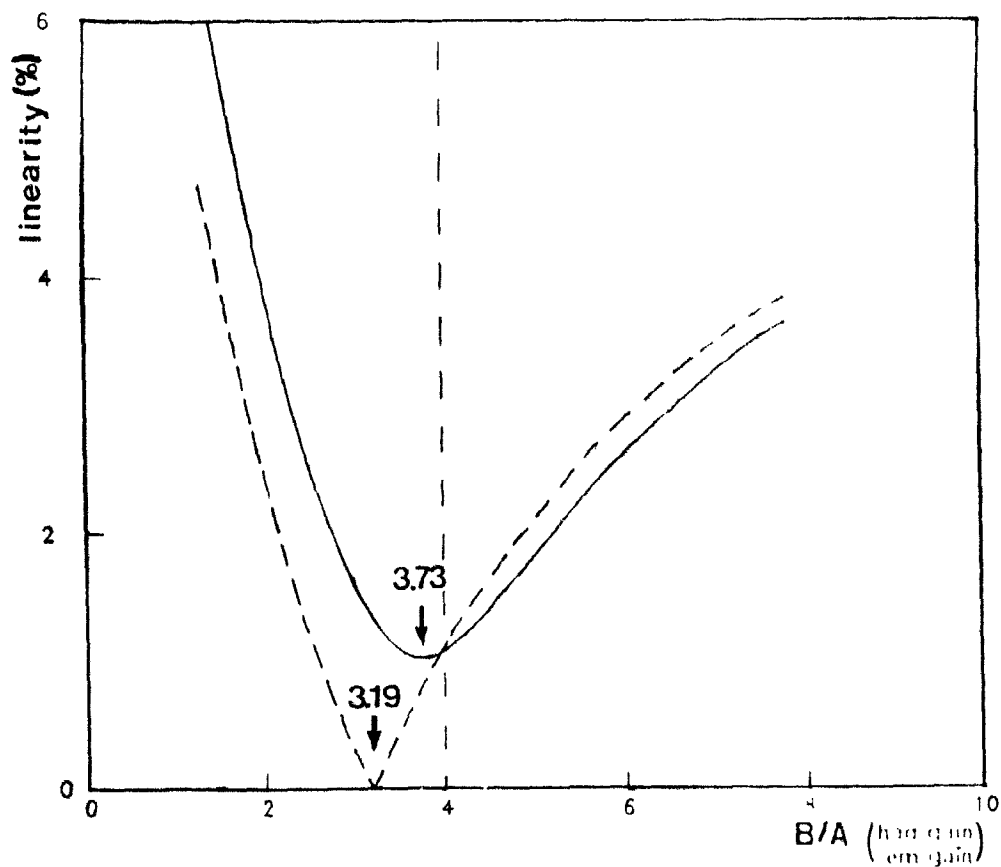


Figure 20. The linearity in coupled stacks when considering electrons of energy 8, 17, and 32 GeV as a function of the ratio of the calibrating constants B/A . The full line is for decoupled stacks. The dashed line represents the same analysis for electrons of energy 17 and 45 GeV in U-scintillator decoupled stacks.

Table 1: Calibration factors for the uranium modules.

Module type	Required signal for uranium noise equalization pC/10 μ s	Calibration factors MeV/pC
U/Cu/scintillator EM	24.11	15.884 ¹⁾
HD	70.40	63.377
U/scintillator EM	24.11	14.844 \pm 0.634
HD	116.16	59.376 \pm 2.535
U/scintillator EM	24.11	16.191 \pm 0.606
(decoupled towers) HD	116.16	67.765 \pm 2.408

1) Provided by the R807 Collaboration.

2.5.1 The uranium/liquid argon calorimeter (ULAC)

The major problem in the operation and calibration of a liquid argon calorimeter is the purity of the argon. The contamination of the liquid argon by oxygen or other electronegative elements results in a trapping of the charge carriers that directly affects the response.

For the HELIOS uranium liquid argon calorimeter (ULAC), the problem is solved by having the liquid argon enclosed in a vessel cooled by liquid nitrogen, hermetically sealed and maintained at a pressure slightly higher than the atmospheric pressure (so that the flow from any leak will be outwards). After a flushing, the same liquid argon is used for a full running period of the SPS accelerator (approximately 3 months)

The purity of the liquid argon is checked regularly by measuring the ionization produced by a radioactive source of a known strength in a test cell.

After the calibration of the ULAC is made, it is maintained over a full running period using a charge calibration with test pulses [76]. A system of micro-processor controlled analog switches distributes a precise test charge to one out of every twenty channels in the electromagnetic section, and to each channel in the hadronic section. The readings of all PADCs of the ULAC, when the electronic chain is excited by this test pulse, and when there are no signals at the input, are recorded

on tape for later analysis at the beginning of each run of physics data-taking.

Incidentally, there is a provision (a computer control of the gain in each unit) to equalize the peaks of the response to the test pulse of all the channels. However, the peaks for various channels do not occur precisely at the same time, and it was chosen instead to equalize the magnitude of the shaped signal at a fixed time after the injection of the test pulse. This choice results in an optimization of the performances of the Energy Flow Logic (EFL) system, since this system samples the shaped voltage at a fixed time. The gain adjustments of the individual channels is then made to equalize the response to a test pulse at the level of the 'TOT' FADC. The gain for each PADC is then different, but these various calibrations are recorded and used in the analysis, as we saw in the previous paragraph.

Both the electromagnetic and the hadronic sections of the ULAC have a repetitive structure of uranium, liquid argon gap, readout plane, liquid argon gap, (uranium and repeat...) The uranium is depleted and is 1.7mm thick in the electromagnetic section and 3.4mm thick in the hadronic section (this thickness is obtained by the assembly of two uranium plates). The liquid argon gaps are 2.0 mm in the electromagnetic part, and 2.5 mm in the hadronic part. The readout planes are 1.7 mm thick and are printed boards with three layers of copper. The middle layer is providing the high voltage, and the two outside copper layers define the read-out.

The electromagnetic section of the ULAC starts 4.2 m downstream of the target and has a 5 cm diameter hole to permit the projectile fragments and nucleons that have not interacted (so-called projectile spectators) to go through the region of the electromagnetic section without interacting. The hadronic section, immediately behind the electromagnetic section, has no holes. The electromagnetic section has 1920 towers (arranged inside a 35 by 35 square grid, as shown in Figure 21), most of them 2 by 2 cm² except for larger guard areas around the periphery of its acceptance, and has 2 floors; The most upstream floor has 8 radiation lengths and the most downstream floor has 12 radiation lengths. The hadronic section has strips 2.5 cm wide, in the x and in the y direction (standard HELIOS coordinate system), and is divided in depth into 3 floors each about 1.5 interaction lengths deep.

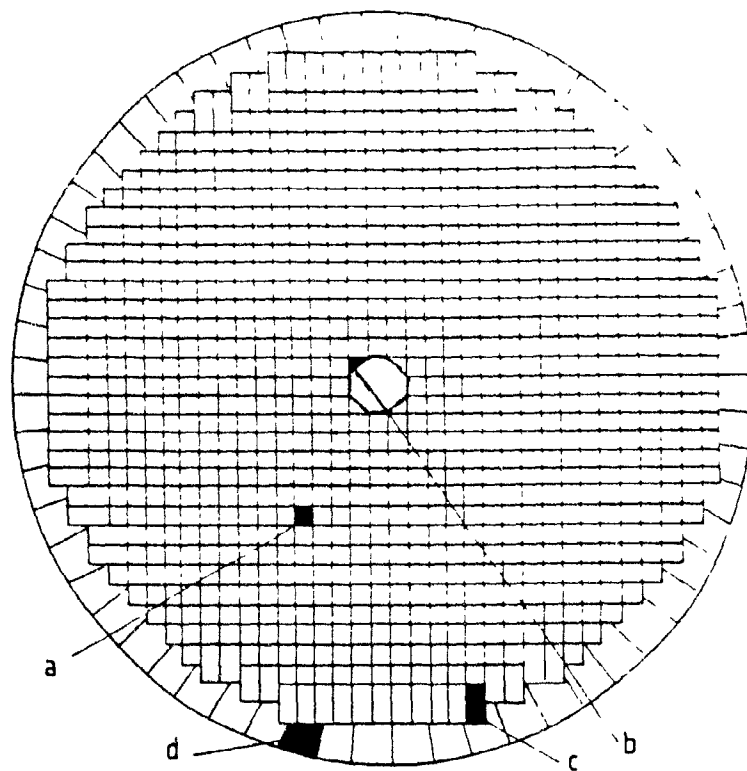


Figure 21: The geometrical arrangement of towers in the electromagnetic part of the ULAC. There are 4 sorts of towers: a) normal b) half size c) double size d) veto pads.

2.5.2 The calibration of the uranium/liquid argon calorimeter

The ULAC was calibrated with electron and pion beams of momenta 17, 45, 70, and 200 GeV/c in the H8 beam line. The electron-pion selection in the secondary beam is done at the trigger level using a 6-fold coincidence of two ring-imaging Cerenkov detectors (CEDARs) and was improved offline using the signals from the transition radiation detector as well as the longitudinal shower profile to obtain uncontaminated pion and electron samples. The calibration showed an e/π ratio of about 1.1. The energy being measured by considering an electron calibration, the distributions are corrected for the effect of the e/π by Monte Carlo procedures (see section 3.7). Since the ULAC is sitting on a movable platform, it is possible to make the beam impinge outside of the 5-cm-hole in the electromagnetic section. It was observed that the resolution and e/π characteristics of the combined electromagnetic and hadronic sections are very similar to the corresponding numbers for the hadronic section alone, a result that could be expected if we admit that these characteristics are mostly determined by the nature of the materials. The fact that the e/π is noticeably different from 1.0 was

to be expected for an uranium calorimeter without hydrogen atoms in the read-out [77][78].

Further measurements have shown that the e/π ratio varies as a function of the integration time. In particular, the fast online measurement of the energy contained in the ULAC using FADCs has a time constant different from that of the PADC's used offline. As a result, the online e/π is different from the offline e/π . This introduces complications in determining the optimal calibration for missing energy studies. In 1987, the missing energy studies were using a set of weights that minimized the r.m.s. width of the calorimeter response at the trigger (online) level. This variation of e/π has only minor effects on the forward transverse energy trigger: it causes some loss of correlation between the online and offline transverse energy, but the contribution of that effect is not dramatically larger than that of other effects (uranium noise in the UCAL, slight mismatches between the online and offline weights, the addition under the square root sign, etc. .)

2.6 The energy flow trigger system.

The exact energy flow characteristics of an event can only be obtained by reading out all the charge integrating ADC's which takes several milliseconds, not to mention several milliseconds of computing time on the online computer to retrieve the characteristics of the event. In contrast, the signals produced by the calorimeter have an actual duration of the order of a microsecond. In order to have the best possible statistics on the rare events, the beam must obviously have the highest possible intensity, and the limit is given by this duration of a microsecond. It results that only a fraction of the events can be read-out.

The energy flow system, by providing the readout and the calculations in less than one microsecond, increases substantially the number of rare events that can be collected per unit of time.

Three kinds of rare events can be collected efficiently using three energy flow trigger subsystems:

First, the ETOT trigger selects events with large 'missing' energy. The term 'missing' means 'carried by particles that do not interact in the calorimeter', such as neutrinos and muons. Rare proton-nucleus events with energetic muons and neutrinos (from leading charmed baryons) are efficiently collected with this ETOT trigger in the context of the lepton physics programme. If only one muon is present, a so-called muon-update of the total energy will make it possible to be sensitive only to the energy carried away by the neutrinos. In the context of heavy-ion collisions, the hardware for this trigger has been used for a very different goal. The energy from only the external calorimeter is used for the selection, and the requirement of a minimum ETOT energy in the external calorimeter yields a sample significantly enriched in antiprotons (an antiproton releases a least 2 GeV when annihilating).

Secondly, the PT trigger selects the events with large 'missing transverse momentum'. The sum of the transverse momentum vectors of all the particles in the event should be zero, but this needs not be the case if a neutrino carries a large transverse momentum. The trigger works by building a two-component transverse momentum vector, taking its magnitude, and comparing it to chosen thresholds. In the context of the lepton programme, this is again a neutrino trigger, but with a taste for large transverse energy neutrinos rather than for energetic neutrinos. In the context of heavy-ion collisions, this trigger could have been used to select events with a large collective motion that produces large local imbalances of transverse momentum in each half of the pseudorapidity domain.

Third, the events with large transverse energy. In hadron-nucleus collisions, the transverse energy is a fundamental probe of the dynamics. As we will see, in heavy ion collisions, transverse energy is sometimes a probe of the dynamics (in the extreme end of the distributions) and sometimes a tool to vary the impact parameter (for most of them having medium transverse energies).

The strategy to realize the system in hardware has been to do linear, and analog, processing, of the ETOT, PX+, PX-, PY+, PY-, and ET signals from each calorimeter separately, then to do the summing of the various calorimeters, subtraction of PX- from PX+ and of PY- from PY+ in a digital electronics realization. Then, the non-linear operation needed to extract PT from PX and PY ($PT = \sqrt{PX^2 + PY^2}$) is done with a digital electronics involving several look-up tables. Finally an adjustable digital comparator is used to take the decision to take or reject the event in conjunction with the rest of HELIOS trigger logic.

Let us first look at the analogic summation chain for the UCAL. The current from the photo-multiplier tubes is split using a resistor array with matched impedance. Two thirds of the current go to the charge-integrating ADC's, and one third enters the EFL. We rely on current, rather than voltage, to carry the signals through the many cables between the various summing units, and we maintain impedances of 50Ω at both ends each time a signal has to travel inside a cable.

The signals enter Σ1 units. The very first stage is a passive element, a resistor. Each resistor corresponds to a weight, either ETOT, ET, PX or PY, and the conductance of each is proportional to the weight. A fifth resistor 'R5' with a precise value is connected to the ground; it is needed to produce a parallel resistance of exactly 50 ohm at each input.

$$\frac{1}{R5} = \frac{1}{50\Omega} - \frac{1}{R(ETOT)} - \frac{1}{R(ET)} - \frac{1}{R(PX)} - \frac{1}{R(PY)}$$

Note that a zero weight is obtained by no resistor at all. The currents travelling in the resistances corresponding to the 4 signals are then amplified by a series of 'current mirror' electronic circuits. Since the ETOT weight is always one, the ETOT resistor always has the same conductance, one exception being the central tower of the ersatz, for which there is a conductance which is a factor 4 larger to compensate for the fact that the calibration of that tower is reduced by a factor of 4.

The analog summing chain consists of four kind of electronic modules. A $\Sigma 1$ summing unit collects the currents from a 48 photomultipliers (up to 4 stacks of a given section of a given quadrant of a given calorimeter), and, multiplying by the weights, builds ETOT, PT, PX and PY analog signals. We do not need to indicate the sign for the 'PX' and 'PY' symbols since the sign is unambiguous inside one quadrant. The individual weights are determined by resistors inside the $\Sigma 1$ boxes. In addition, there is a test input with a unit weight for each of the ETOT, ET, PX and PY quantities.

The signals from up to four $\Sigma 1$ units are summed in a $\Sigma 2$ unit. At the output of the $\Sigma 2$, are the four quantities (ETOT, ET, PX, PY) for one quadrant of one section (electromagnetic (EM) or hadronic (HD)) of one calorimeter. There is a special copy made of the ETOT signal for a system of monitoring of the time evolution of the signal called the History ADC's (HADC). A computer controlled gain selection is performed in each $\Sigma 2$. Each quantity of each $\Sigma 2$ has a normal gain, and a special gain suitable for heavy-ion running. However one must note that during heavy-ion running, not all $\Sigma 2$'s are attenuated.

A $\Sigma 3$ consists of 6 channels and performs the summation of all the quadrants of a given section (HD or EM) of a given calorimeter. The 6 resulting signals are called: (PX+, PX-, PY+, PY-, ETOT, ET).

A $\Sigma 4$ is actually identical to a $\Sigma 3$, but its function is different. It performs the summation, for the six quantities, of both sections of a calorimeter. There is one such final summation module for each calorimeter, except the ERSATZ. All these units use fast transistors (2N3904, 2N3906) as current amplifiers with unit gain. The design insures a linear response for currents up to 5 mA.

In order to transmit the summed signal to the counting room where they will be used for the trigger, the signals are transformed by accurately linear differential drivers. The received signals, at the end of the 65m cables, are then given a bipolar 'S' shape with shaping amplifiers. The signal then goes to a buffer amplifier to produce a voltage suitable for the FADC from the current-driven shaping amplifiers. A trimming pot (10 turns) makes a fine adjustment of the gain to be done at this stage. This adjustment is necessary to compensate the errors in gain of a few percent that accumulate through the chain of amplifiers. These trimming pots were adjusted in August 1986 during special EFL calibration runs after the tuning was established, and have not been touched since then. The signals are finally sampled by the FADC's.

The gains implemented in the chain were multiplied by special factors for the various running periods, as summarized in Table 2. The factors built into the hardware at various stages were chosen to fully exploit the dynamic range of all channels. At the $\Sigma 1$ level, the factors are implemented directly in the weights (i.e. in the beam, the ET weight in the hadronic section is $8 \sin\theta$ instead of $\sin\theta$). At the $\Sigma 2$ level, the factors are implemented by deviating a fraction of the current. The current reduction factors are computer-controlled by analog switches called ' $\Sigma 2$ attenuators'. The $\Sigma 3$, $\Sigma 4$, and

differential drivers have the same gains for all channels. Then the gain factors of the shaping amplifiers is shown as the third entry of Table 2. Next, the factors at the FADC level occur because some of the FADC's used are 9-bit ADC's producing 4 counts per 10 mV instead of 1 count per 10 mV for the majority of the FADC that are 7-bit.

The product of the electronic gain factors in the Energy Flow (EF) summing chain is also shown in Table 2 for all paths. The calibration of the calorimeters, in other words, the charge produced by unit energy, determined by the high-voltages applied to the photomultipliers, is also modified during the heavy-ion running periods. This is in order to match the dynamic range of the charge-ADC's. The product of the factors applied to the EF chain, and to calorimeter calibration, is such that 1 GeV of ETOT corresponds to 1 FADC count, 1 GeV of ET corresponds to 2 FADC counts, and 1 GeV of PX or PY corresponds to 4 FADC counts. During heavy-ion running, this is modified so that 2 GeV of PX or PY correspond to 1 FADC count, 4 GeV of ET correspond to 1 FADC count, and 8 GeV of ETOT correspond to 1 FADC count in 1986, while in 1987, 20 GeV of ETOT correspond to 1 FADC count.

The linearity of the whole chain is tested injecting 50 ns pulses in the test input, and after they travel through the summation circuitry, the response is measured in the FADC. The result of such a test is shown in Figure 22. Despite the very large complexity of the linear summation system, and about 150m of cables, the whole chain is linear within 1%. The long-term stability of the gain is also of the order of 1%.

In order to test the summation units, an electronic test set-up under CAMAC control was used, shown in Figure 23. Its principle is to use 'Wide-Band Routers' (electro-mechanical relays) to transfer test pulses either directly to a $\Sigma 3$ connected to a charge ADC, or through one of the 48 inputs of a $\Sigma 1$, to the same $\Sigma 3$. In this way, the current gain of any given $\Sigma 1$ channel is directly measured. The resistors with 5 percent tolerances that are used to establish the gains are not usually sufficiently precise, so that several modifications of the resistor values are normally done to achieve precisions of the order of 1%. A 'certificate' is granted to a summing unit only when the weights are all within 1 percent of specified values. Most of the $\Sigma 1$ units were adjusted and given certificates in 1985. In 1986, before the data-taking period, the weights in the $\Sigma 1$ of the MAGCAL were found to be erroneous, so a modified version of the above test set-up had to be rebuilt. The MAGCAL $\Sigma 1$ were then modified and given new certificates. The compatibility of the old and the modified test set-ups was checked with a $\Sigma 1$ of the WALL calorimeter. Further documentation of the performances of the EFL can be found in [74].

In the ULAC, the energy flow summing is first an analog passive summing at the board level. In the liquid argon calorimeter, unlike in the scintillator calorimeters, the same cable brings both the signals for the fast EFL and for the slower but more precise measurement by PADC's. The signals are received on amplifier boards located in the counting room; each board, which controls the amplification of 24 signals, contains resistors to make the ETOT, ET, PX, and PY signals in the case of a board connected to towers in the electromagnetic section of the ULAC; only ETOT and either PX or PY signals are produced in the case of a board connected to strips in the hadronic section of

Table 2: Summary of the factors implemented electronically in the summing

The numbers in parentheses represent the modified gains during ion running. When there are two numbers, the first is for 1986, the second is for 1987. When there is no parenthesis, it means that there is no change for heavy-ion running. The EXTERNAL and VETO entries are the same as the corresponding BOX entries.

Path	$\Sigma 1$	$\Sigma 2$	shaping amp.	FADC	EF chain gain	Calib- ration
BOX HD ETOT	1	1(1/8,1/20)	8	1	8(1,2/5)	1
BOX HD ET	1	1(1/8)	16	1	16(2)	1
BOX HD PX,PY	1	1(1/8)	32	1	32(4)	1
BOX EM ETOT	1	1/4(1/32,1/80)	8	1	2(1/4,1/10)	4
BOX EM ET	1	1/4(1/32)	16	1	4(1/2)	4
BOX EM PX,PY	1	1/4(1/32)	32	1	8(1)	4
WALL HD ETOT	1	1(1/2,1/10)	2	4	8(2,8/5)	1(1/2,1/4)
WALL HD ET	1	1(1/2,1/4)	4	4	16(4,8)	1(1/2,1/4)
WALL HD PX,PY	1	1(1/2,1/4)	32	1	32(8,16)	1(1/2,1/4)
WALL EM ETOT	1	1/4(1/8,1/40)	2	4	2(1/2,2/5)	4(2,1)
WALL EM et	1	1/4(1/8,1/16)	4	4	4(1,2)	4(2,1)
WALL EM pt	1	1/4(1/8,1/16)	32	1	8(2,4)	4(2,1)
BEAM HD ETOT	1	1(1,2/5)	2	4	8(8,16/5)	1(1/8)
BEAM HD ET	8	1	2	1	16	1(1/8)
BEAM HD PX,PY	8	1	4	1	32	1(1/8)
BEAM EM ETOT	1/4	1(1,2/5)	2	4	2(2,4/5)	4(1/2)
BEAM EM ET	2	1	2	1	4	4(1/2)
BEAM EM PX,PY	2	1	4	1	8	4(1/2)
ERSA HD ETOT	1	1	2	4	8	1(1/8)
ERSA HD ET	4	1	4	1	16	1(1/8)
ERSA HD PX,PY	4	1	8	1	32	1(1/8)
ERSA EM ETOT	1/4	1	2	4	2	4(1/2)
ERSA EM ET	1	1	4	1	4	4(1/2)
ERSA EM PX,PY	1	1	8	1	8	4(1/2)

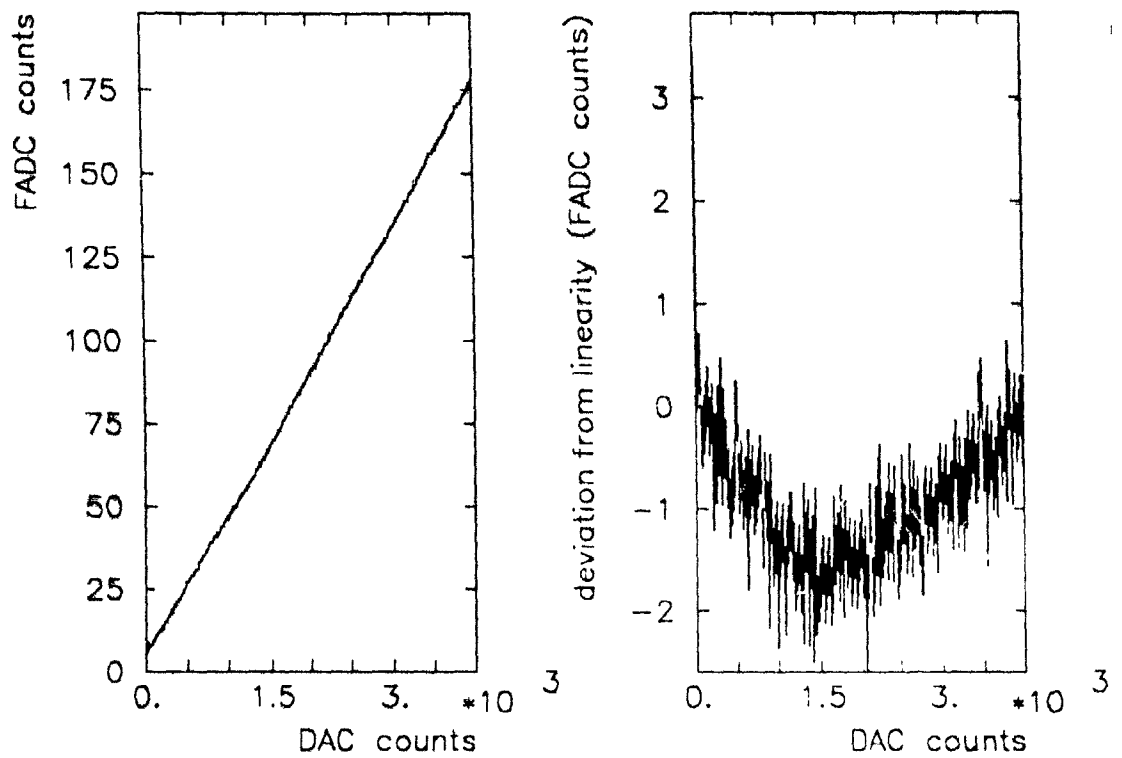


Figure 22: The number of counts of the FADC for the WALL transverse energy versus the number of counts of the Digital-to-Analog Converter (DAC) generating a test signal. The observed linearity of the combined DAC pulser and energy flow chain is better than 1%; the linearity of the energy flow chain alone is at least as good.

the ULAC. For every 20 boards, i.e. one per crate, the energy flow signals are merged on a common backplane connection and amplified by a specialized board.

The summation is finally completed by 'Linear summing units', that merge the signals from up to 4 boards (but are distinct from $\Sigma 3$ and $\Sigma 4$ units) followed by 'programmable attenuators', that provide up to 100 decibels of attenuation under computer control. The output of the 'programmable attenuators' is then connected to FADC's of exactly the same kind as the ones used for the scintillator calorimeters.

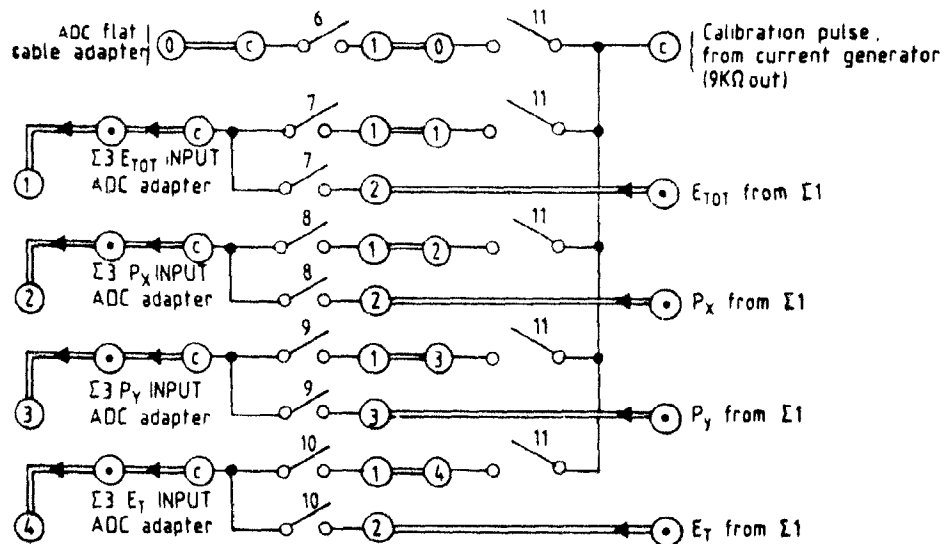


Figure 23. Set-up for testing $\Sigma 1$ units. The $\Sigma 1$ units passing the tests are given 'certificates' if all weights are accurate within one percent.

The energies of the various calorimeters (scintillator, liquid argon) are summed digitally using the outputs of the FADCs. This final stage of the energy flow system is the digital summing tree, a part of this tree is shown in Figure 24

For the hadronic part of the ULAC, it is necessary to combine the signals from the strips (P_{x+} , P_{x-} , P_{y+} , P_{y-}) to obtain the contribution to the transverse energy. The addition under the square root sign, which is needed to reconstruct properly the transverse energy when there is a single secondary particle reaching the hadronic part of the ULAC, is inappropriate for several particles.

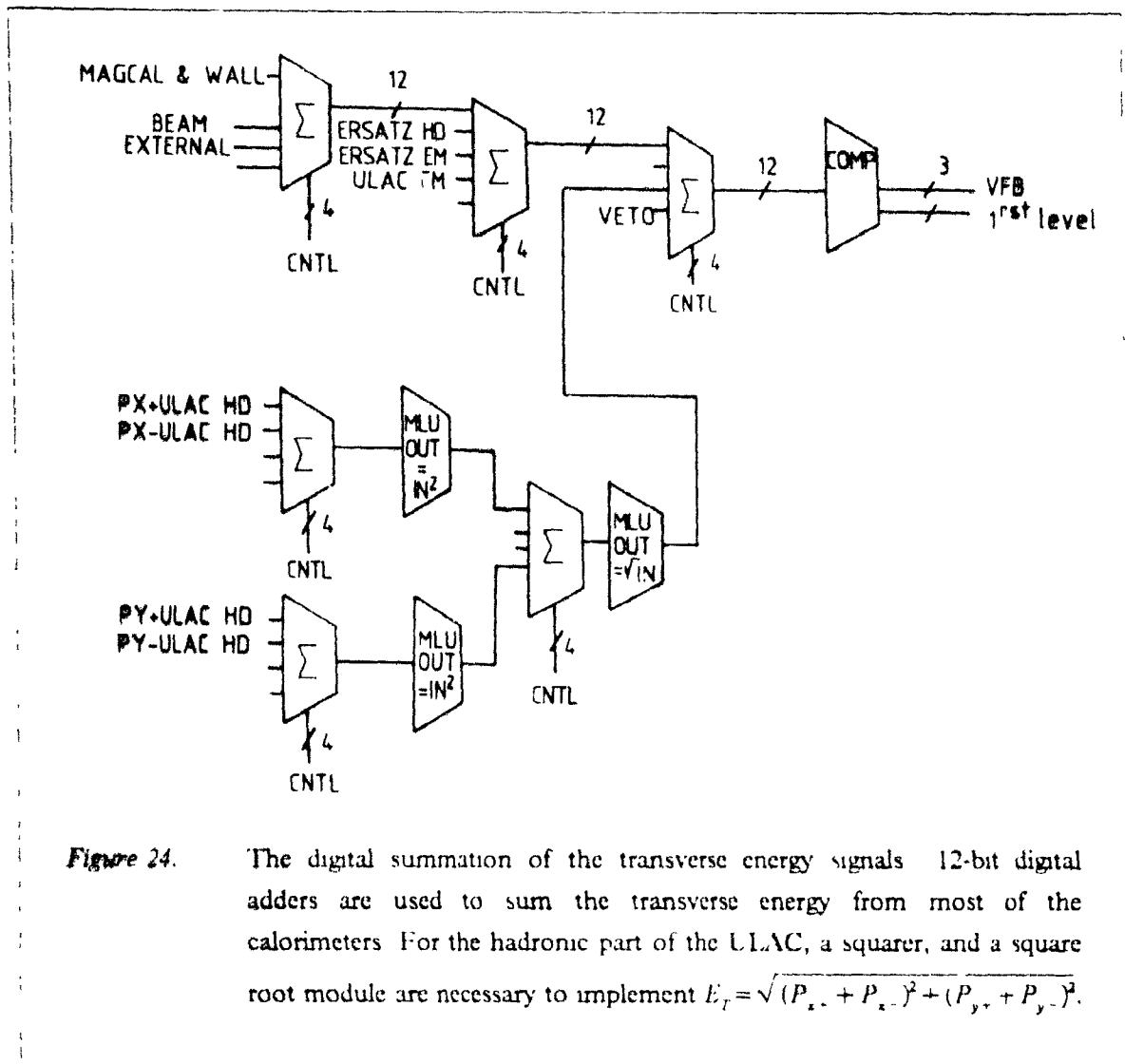


Figure 24. The digital summation of the transverse energy signals. 12-bit digital adders are used to sum the transverse energy from most of the calorimeters. For the hadronic part of the ULAC, a squarer, and a square root module are necessary to implement $E_T = \sqrt{(P_{x+} + P_{x-})^2 + (P_{y+} + P_{y-})^2}$.

Fortunately, for very large numbers of particles such as the ones met in heavy-ion collision, the error is relatively harmless. When the number of particles is large enough, $P_{x+} + P_{x-} \approx P_{y+} + P_{y-}$, so that the computation of the forward transverse energy is almost linear:

$$\sqrt{(P_{x+} + P_{x-})^2 + (P_{y+} + P_{y-})^2} \approx \frac{1}{\sqrt{2}}(P_{x+} + P_{x-} + P_{y+} + P_{y-})$$

2.7 The external spectrometer

An ideal detector for heavy-collisions would give us the identification and the exact momentum of each secondary particle. In the HELIOS experimental set-up, we attempt particle identification and precise momentum measurement in a small part of the phase space only, a window in η, ϕ . The edges of the window are dictated by the edges of the calorimeter slit, and by a copper wedge. In a fiducial area smaller than the physical size of the slit, the exact angle of the track, its momentum, its charge and mass, and its energy are recorded. The exact angle of the track is obtained from the position of the hits in the wire chamber DC4 (see Figure 25), using the known position of the target. The segment reconstructed in DC4 is used as a check that the track comes from the target. The position of a track is obtained by a measurement of charge sharing (precision 1 cm in the y-direction) and of drift time (precision about 180 microns in the x-direction). The momentum and charge of the particles are obtained by a measurement of the bending under a magnetic field of a strength of 0.7 T, acting on a distance of ≈ 36 cm to provide a transverse kick of 75 MeV/c. The bending is measured 50 cm downstream of DC4 by the DC5 wire chamber having the same resolution characteristics as DC4. From this, we see that momentum measurements will be possible up to an absolute maximum momentum of $\frac{500}{0.180 \times 2} 75 \text{ MeV/c} \approx 150 \text{ GeV}$. The resolution becomes insufficient for reliable particle

identification at a lower energy. The measurement of the mass takes place via a time-of-flight measurement. The clock, measuring in 0.25 ns units, is started by the small beam counter scintillator used for the definition of the beam, and is stopped by one of several IOF scintillators. The IOF resolution is 500 ps. A complementary measurement of the velocity, important at velocities close to the speed of light, is provided by aerogel threshold Cerenkov counters. The energy of the particle is finally measured in a calorimeter (EXTERNAL) similar in nature to the BOX calorimeter. The measurement of the deposited energy does not have sufficient precision to allow the deduction of the mass by comparison with the momentum, except in the case of antiprotons.

The acceptance of the external spectrometer is extended to photons by the use of a converter of a length which represents 5% of one radiation length. The converter is sandwiched between two planes of multiwire proportional chambers, so that it can be made certain that the conversion of the photon into an e^+e^- pair took place in the converter and not upstream. The momentum of both the electron and the positron are measured as any other charged particle in DC5. The energy of the photon is then the sum of the energy of the electron and of the positron.

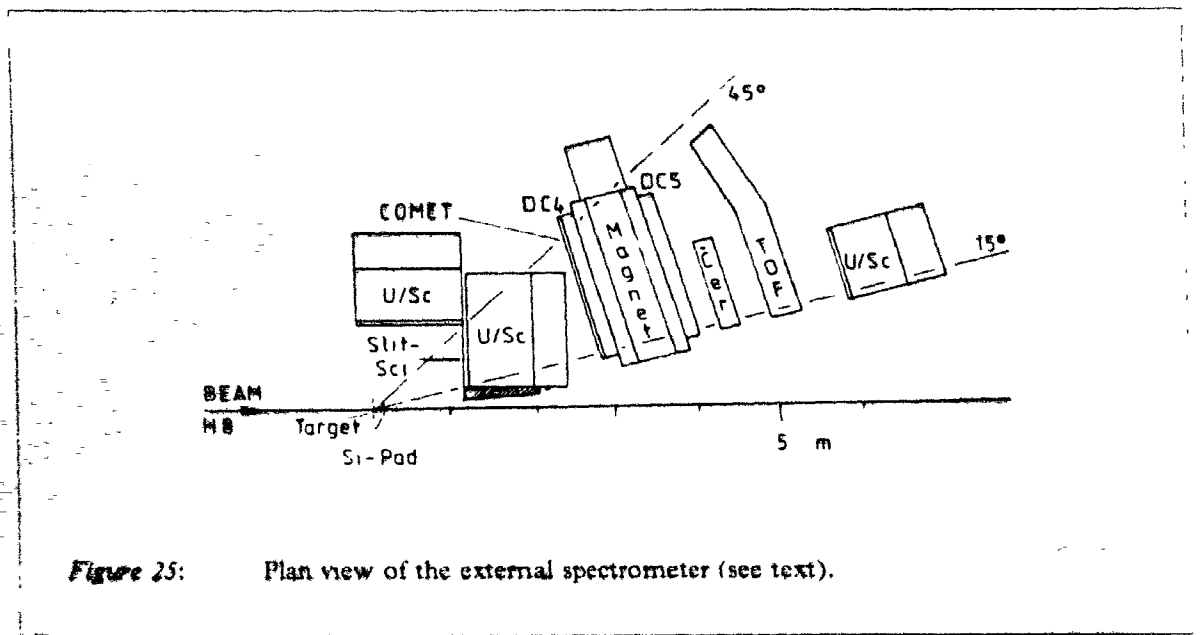


Figure 25: Plan view of the external spectrometer (see text).

Chapter 3

Data reduction and analysis

In this chapter, we will describe how we rejected a fraction of the events that do not originate in the target, while maintaining a good efficiency for the events coming from the target. We will then summarize the analysis methods used and developed to extract precise information on the energy flow, the cross-section, and the multiplicity, from the raw data provided to us by the detectors. This includes discussions of the methods of construction of the transverse energy and discussions of the corrections which must be applied, deduced by simulating the calorimeter response by running Monte Carlo simulation programs.

3.1 Selection of ^{16}O and ^{32}S interactions in the target

Because of the changes in the set-up and improvements in the performance of the detectors, the cuts on the data in 1986 and 1987 are different. In each case, we have designed two sets of cuts, each aimed at a particular goal, a large efficiency cut, designed to measure cross-sections accurately, and a stricter cut, which does not accept 100% of the events occurring in the target, but which almost totally eliminates the background. That second cut can be used in the making of pseudorapidity distributions of transverse energy, for which a subtraction of the background would be difficult and inaccurate.

Let us first consider the intensity and composition of the beam. The oxygen beam data taken with the Al, Ag, and W targets correspond to an integrated incident flux of 8.5×10^8 , 4.8×10^8 and 1.6×10^9 nuclei at 60 GeV/nucleon, and to 7.9×10^8 , 3.8×10^8 and 2.3×10^9 nuclei respectively at 200 GeV/nucleon incident beam energy. Similarly, in 1987, with ^{32}S beam, the integrated fluxes on Al, Ag, W, Pb, Pt, and U were 5.11×10^8 , 1.17×10^8 , 6.26×10^8 , 7.3×10^7 , 1.11×10^8 , 5.2×10^7 respectively, while the integrated flux of ^{16}O on a W target has been 4.8×10^7 . A fraction of the ions of the primary beam get broken into nuclear fragments during extraction from the main accelerator ring to the beam transport line of the experiment. In peripheral collisions with nuclei in the collimators, the spectator nucleons can remain with essentially the same momentum per nucleon as the incident nucleus. Various nuclei smaller than the primary heavy-ion are produced in the

forward fragmentation region. If, in addition, these have $Z/A = 0.5$, they will have the same rigidity as the accelerated ions ^{16}O and ^{32}S , and therefore will be bent and focussed in exactly the same way as the 'primary' ions. The secondary particles produced in the upstream interactions do not usually cause an interaction trigger. Instead, the interaction trigger, the transverse energy and multiplicity, result from the tertiary particles produced when the ion having first undergone spallation, interacts in the target region. Everything happens as if the beam contained a component of ions with different charge and energy. In the calorimeters, we then observe a 'mass spectrum' of incident ions. This is shown in Figure 26 for oxygen ions of 200 GeV/nucleon in 1986, and in Figure 27 for sulfur ions of 200 GeV/nucleon in 1987.

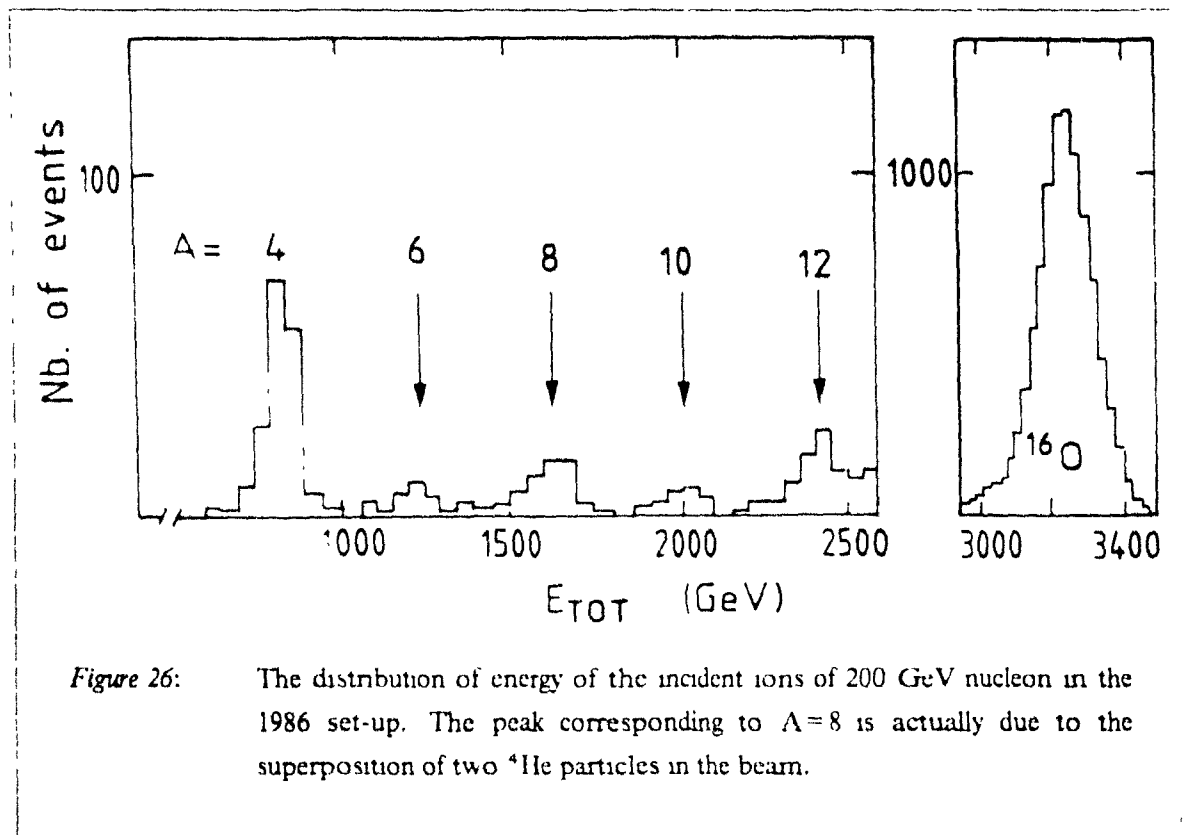


Figure 26: The distribution of energy of the incident ions of 200 GeV/nucleon in the 1986 set-up. The peak corresponding to $A=8$ is actually due to the superposition of two ^4He particles in the beam.

Fortunately, it was observed that at the target, the nominal ion charge represented $\geq 94\%$ of the incident flux in all cases (60 and 200 GeV/nucleon ^{16}O and 200 GeV/nucleon ^{32}S beams).

Some of the interactions occur in the scintillator that measures the ionization of the beam. It must be noted that with heavy-ion projectiles, an interaction does not always cause an increase of the ionization, since the original ionization of a relativistic heavy-ion is quite large. For instance a sulfur collision producing 100 minimum-ionizing secondaries would cause a diminution of the ionization ($16^2 = 256 \rightarrow 100$). In contrast, for a proton, an interaction necessarily results in increases of the multiplicity and of the ionization. For heavy-ions, an interaction can also result in an increase of the

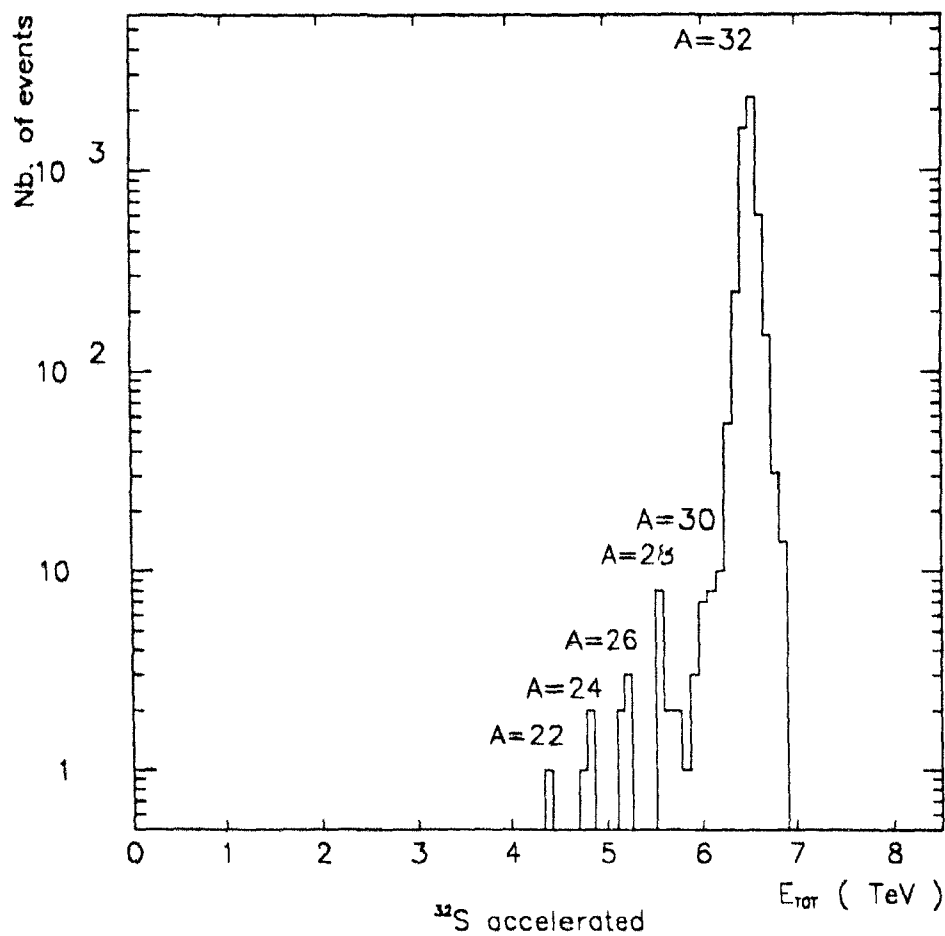


Figure 27: The distribution of measured energies of the incident ions during the 1987 ^{32}S running period. The beam also contains some ions with A less than 22, in particular ^4He , but they do not appear here since a minimum ionization in B3 is required at the trigger level.

ionization, if the multiplicity of secondaries is large, or if very ionizing slow fragments are released ('black tracks'). It is thus conceivable that some interactions will leave the measurement of the ionization unaffected, either if the total ionization of the secondaries is close to the ionization of the projectile, or if the incident nucleus interacts close to the downstream side of the plastic scintillator, or if the interaction occurs in the aluminium wrapping the scintillator on the downstream side.

Both in 1986 and in 1987, the first cut consists of isolating a 'window' in the plane of measured total energy and measured energy loss by ionization in the scintillator. In 1987, because of the

instabilities in the scintillator far upstream from the target, and since the ionization in the scintillator B3 immediately upstream with respect to the target is already tested at the trigger level, only a cut on the total energy is used in the first analysis cuts. An offline cut on the ADC connected to B3, that improves and tightens the online cut, is made in the next stage of the offline analysis, that we will describe now.

3.1.1 Non target interactions in the vicinity of the target.

Further cuts are introduced to remove interactions in the low- Z materials surrounding the target. These cuts differ for the 1986 and 1987 data-taking runs.

In 1986, the removal of the spurious interactions was based on the recognition of the pathological properties of these events. At low transverse energy, these events, resulting from interactions in the downstream part of the beam counter, in the air, and in the support of the multiplicity counter, are not distinguishable from interactions in the target. However, as E_T rises, they exhibit increasingly recognizable pathological properties, for example, an interaction in the RING (silicon ring detector) gives no detected multiplicity in the RING, but high multiplicity in the PAD, and large E_T in the pseudorapidity region overlapping the RING. We can profit from such behaviour to develop simple empirical cuts. By comparing the empty target data with the data taken with a target, we define allowed regions in the correlation plots of E_{\perp} , the multiplicity in the RING and the multiplicity in the PAD. In figure 28, we show these correlations for empty target and with a 0.1 mm target, and the cut regions that we have defined.

In the sulfur data, the three ring counters provide an efficient way of recognizing upstream interactions. Therefore cuts of the transverse energy compared to multiplicity are not needed. The upstream interactions are recognized because the secondaries that they give-off, travelling in straight line through the three counters, will produce hits at the equivalent positions in the three RING counters, since these detectors are all built similarly.

The pattern of hits in the three RING-counters is used offline to recognize and remove upstream interactions which show easily recognizable correlations of the hits in RING1 and RING2. A table is made of the RING2 element which corresponds the most in this respect to each RING1 element. When there is a hit in RING1 accompanied by the corresponding hit in RING2, it is called a 'matched hit'. By counting the number of hits in RING1 that have a matching hit in RING2 and comparing with statistical expectations, we build a likelihood function C_{12} that represents the probability that a random distribution can account for the number of matching hits seen. This function has very small values for most of the upstream interactions. For cross-sections, we have chosen to impose a cut on this probability function at 0.05, which leaves at least 95% efficiency for interactions in the target. For the making of pseudorapidity distribution, the threshold was instead 0.20, in order to obtain a large background reduction at low transverse energies. A scatter plot of C_{12} versus the transverse energy in the range $-0.1 < \eta < 2.9$ is shown in Figure 29 (for a 0.2mm

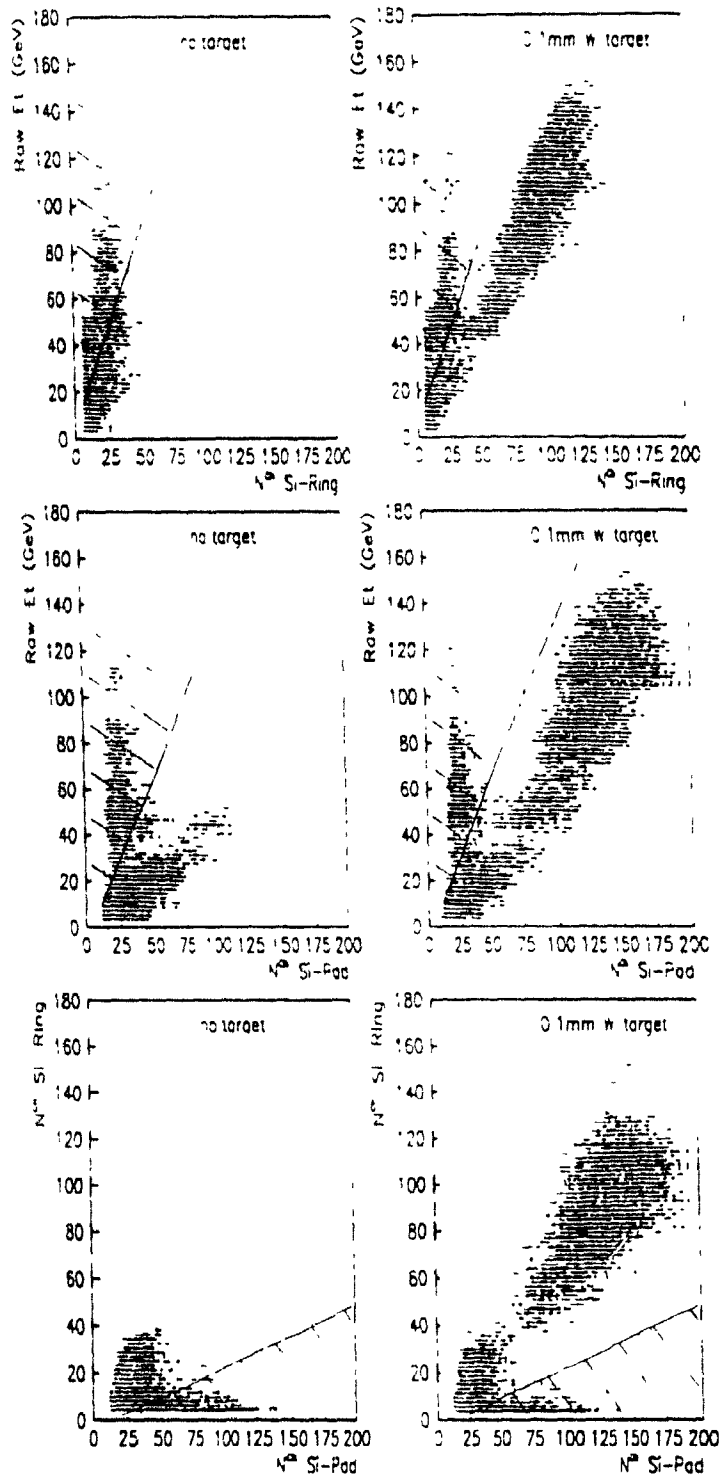


Figure 28: The correlation of transverse energy and multiplicity in 1986 with a 200 GeV/nucleon oxygen beam. The shaded regions indicate the regions of the cuts, where the events have pathological properties.

W target) and in Figure 30 (for no target). By removing events with C_{12} less than 0.05, we achieve an optimum separation of the events in target and non-target. We remove non-target and target events with a level of confidence of 90 %.

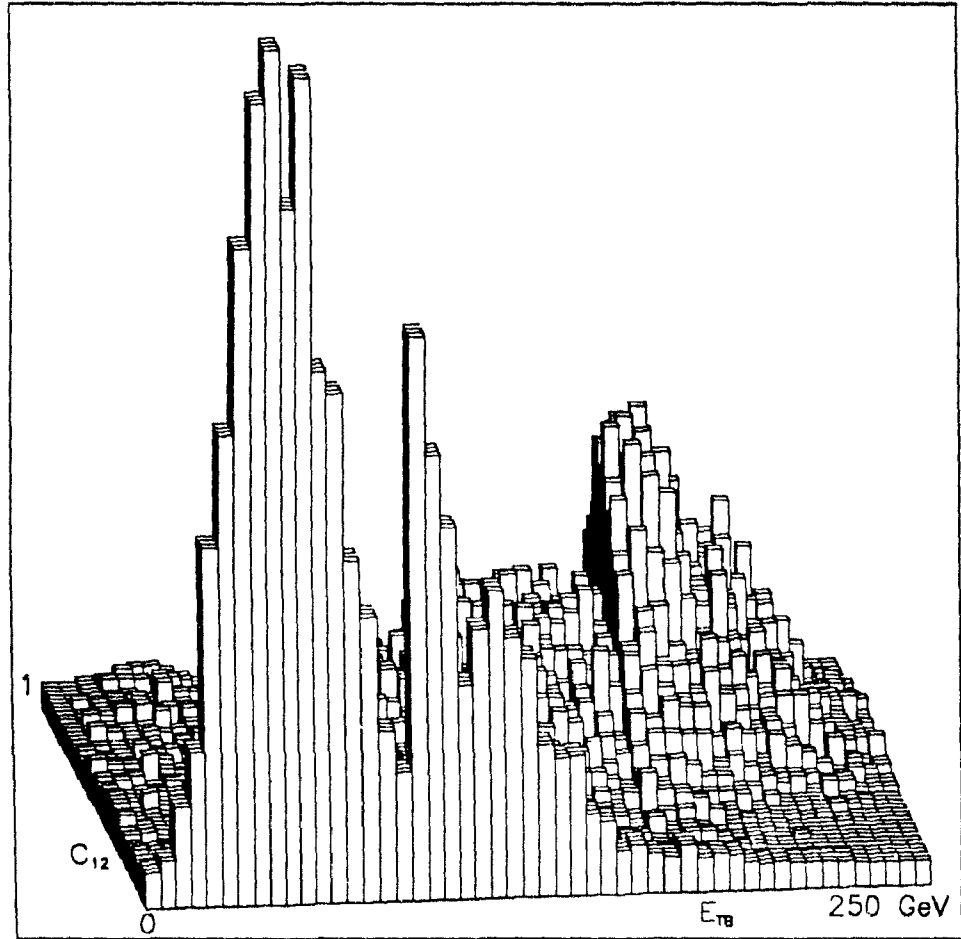


Figure 29: Lego plot of the transverse energy in the backward region (horizontal) and the likelihood function C_{12} . The beam is ^{32}S at 200 GeV/nucleon and the target is 0.2mm W. The background is seen at low values of C_{12} (≤ 0.05).

In addition, in order to remove the events where the principal collision is in RING1 or RING2, there is a cut on the comparison of the raw multiplicities in RING3 and RING1. The events are

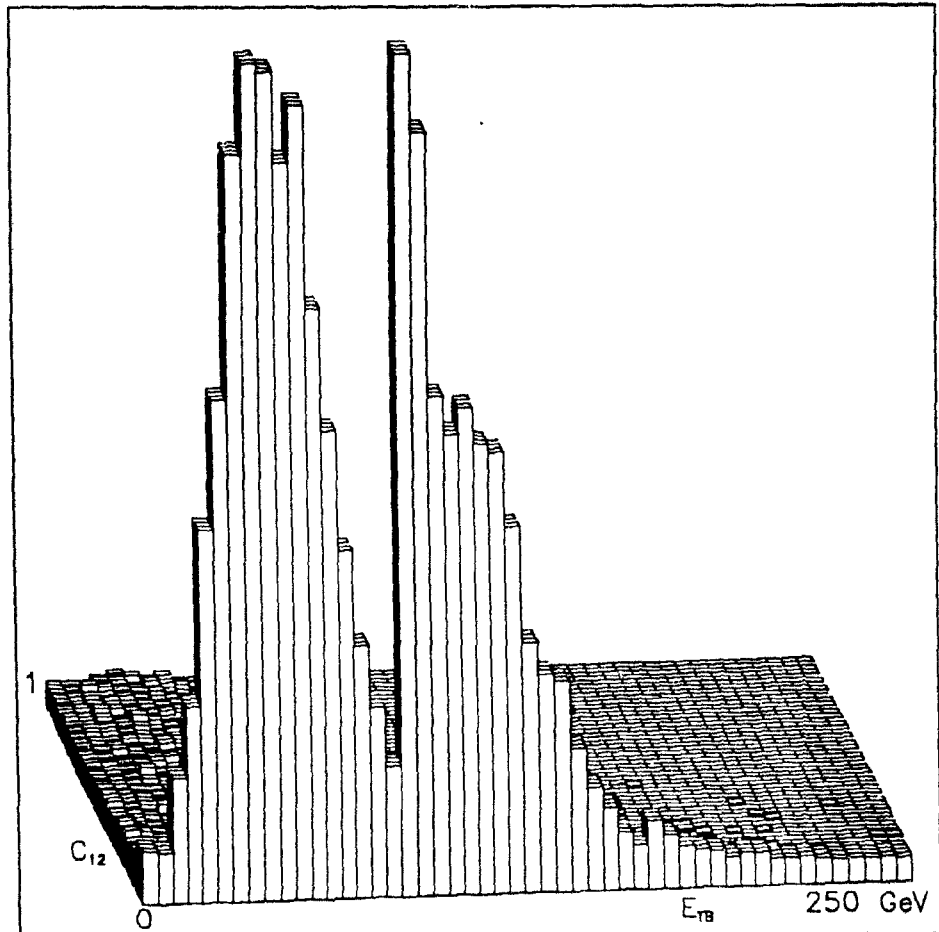


Figure 30: Lego plot of the transverse energy in the backward region (horizontal) and the likelihood function C_{12} . The beam is ^{32}S at 200 GeV/nucleon and there is no target. There are however spurious interactions, mainly many upstream interactions efficiently recognized by their low likelihood C_{12} .

rejected if:

$$\text{mult.}(RING3) \geq 1.1 \times \text{mult.}(RING1) + 10 \text{ and } \text{mult.}(RING1) \leq 40 \quad ; \quad \text{all but Al target}$$

$$\text{mult.}(RING3) \geq 5.0 \times \text{mult.}(RING1) + 40$$

; for Al target

3.2 The distributions of raw transverse energy.

3.2.1 The E_T trigger efficiency

We have seen that a fraction of the data was taken by requiring a large transverse energy E_{TB} in the region $-0.1 < \eta < 2.9$. The number of thresholds used depends on the target element, because the strategies for obtaining as much statistics as possible per unit time, in all regions of E_{TB} , are different in each case. The number of thresholds has been 2 in ^{32}S -W data taking and 5 in ^{16}O -W data taking, for instance. From each trigger then results a differential cross-section for the production of E_{TB} while satisfying the threshold condition. Three such distributions of backward transverse energy E_{TB} are shown in Figure 31, in the case of a W target with a 200 GeV/nucleon ^{32}S incident beam.

Similarly, four distributions of full- η transverse energy are shown in Figure 32, for a sample of ^{32}S -Pt collisions having an online requirement for a large transverse energy in the domain of pseudorapidity $-0.1 < \eta < 2.9$. In both cases, the shape of the distributions results from the convolution of online FADC distributions, which have a sharp starting edge due to the trigger requirement, with a Gaussian smearing.

In the case of the distributions of backward transverse energy, this Gaussian smearing is instrumental: the width of the distribution of the asymmetry between the FADC's and the charge ADC's is mostly due to the uranium noise of the calorimeters, and partly to errors in the online implementation of the weights.

In the case of the distributions of forward transverse energy, the source of the smearing is the uncertainty on the forward transverse energy for a given backward transverse energy. The width, in this case, is not entirely due to instrumental effects but is affected by the physics of the collision itself. However, the forward transverse energy is observed to be Gaussian fluctuating around a value determined by the backward transverse energy. Although the magnitude of the fluctuations are different, the physical fluctuations pose no particular problem, and were treated in exactly the same way as the instrumental fluctuations.

The result of convoluting the product of a slowly varying function and of a step function with a Gaussian is the slowly varying function multiplied with a normalized error function $P\left(\frac{E_T - E_T(\text{threshold})}{\text{width}}\right)$. The error function is precisely the integral of the Gaussian:

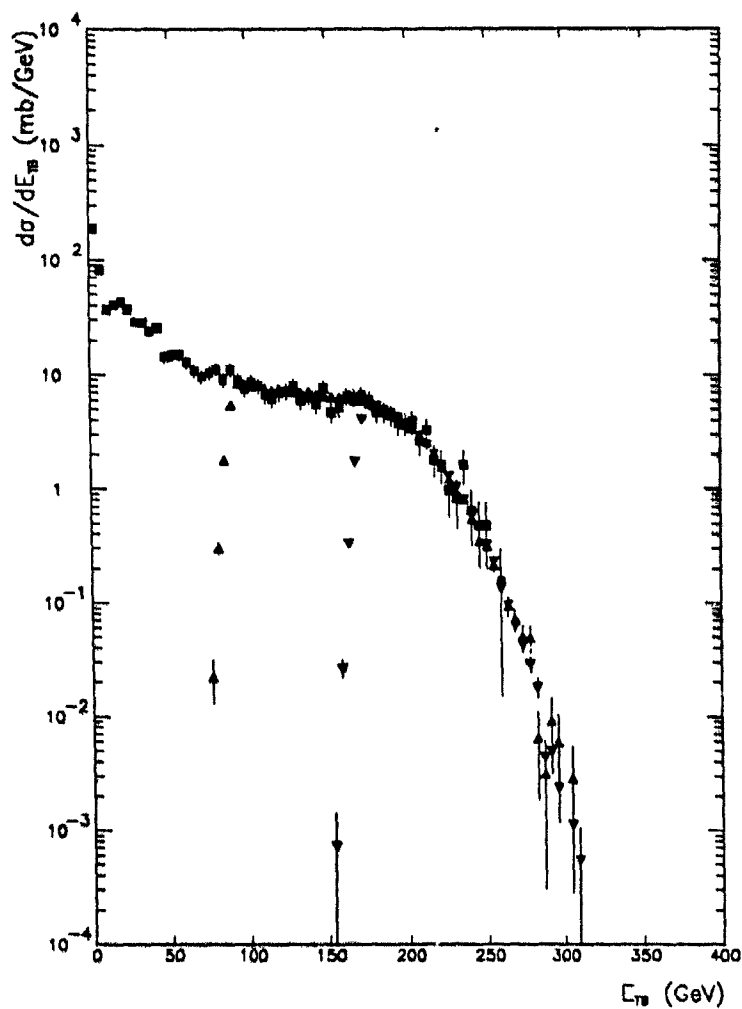


Figure 31: Overlap of the dN/dE_{TB} distributions for data taken with various E_{TB} thresholds online for 0.2 mm W target with a 200 GeV/nucleon ^{32}S beam. Both the E_{TB} online and offline are measured in $-0.1 < \eta < 2.9$.

$$P(x) = \frac{\int_{-\infty}^x e^{-(z^2)/2} dz}{\int_{-\infty}^{+\infty} e^{-(z^2)/2} dz}$$

and is related to the standard error function $\text{erf}(x)$ by:

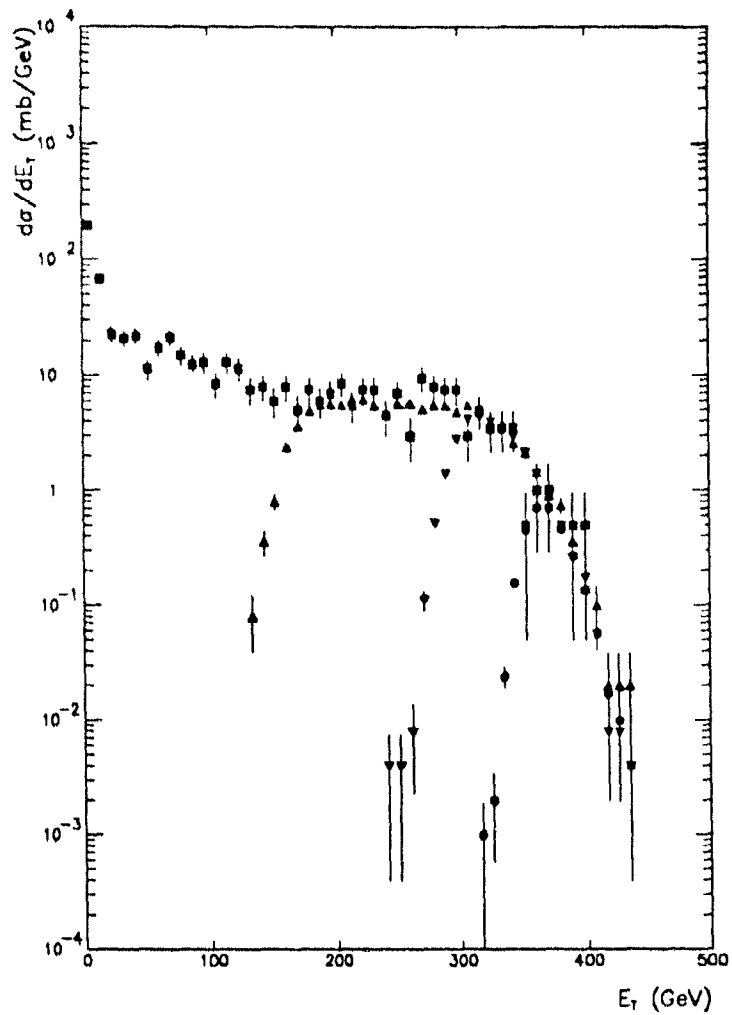


Figure 32: Overlap of the dN/dE_T distributions for data taken with various E_{TB} thresholds online for 0.25 mm Pt target with a 200 GeV/nucleon ^{32}S beam. The online transverse energy is measured in the pseudorapidity range $-0.1 < \eta < 2.9$, and the offline E_T is measured in the pseudorapidity range $-0.1 < \eta < 5.5$.

$$P(x) = \frac{1 + \operatorname{erf}\left(\frac{x}{\sqrt{2}}\right)}{2}$$

The systematic error, which is made by replacing the cross-section with the cross-section constrained by an online requirement, is measured by the difference of this function P from one.

The final distributions of transverse energy are made by combining the several curves, selecting always the curve corresponding to the highest threshold as soon as the online requirement of transverse energy does not cause a too large systematic error. Numerically, we are allowed to consider that the systematic error is negligible provided it is an order of magnitude less than the statistical error. Given that the largest counts in a bin are in practice of the order of 10 000, corresponding to a statistical error of the order of one percent, a systematic error of 0.1 % was considered negligible. Because $P(x) = 0.999$ corresponds to $x = 3.1$, this 'offline threshold' sits at 3.1 standard deviations above the value of transverse energy corresponding to the online threshold. This corresponds to about 8 GeV for backward transverse energy distributions and about 25 GeV for distribution of transverse energy in the pseudorapidity interval $-0.1 < \eta < 5.5$. These numbers are quoted for illustration purposes, since anyway the required offset of the offline threshold with respect to the online threshold is determined in each individual case by the *local* width of the difference between the two quantities.

3.2.2 The subtraction of empty target contamination

Most of the non-target interactions are identified by our carefully designed cuts. However, the low multiplicity interactions are very hard to identify. Some events with low transverse energy survive the cuts when no target is present. The distribution of transverse energy of these 'unremovable' non-target interactions is subtracted from the target-in distributions to correct for the presence of these non-target interactions. As an example, we consider the 'unremovable' non-target interactions produced when a ^{32}S beam hits on a W target in the 1987 set-up. The fraction of interactions due to this unavoidable background is shown in Figure 33 as a function of E_T in the pseudorapidity region $-0.1 < \eta < 2.9$, and in Figure 34 as a function of E_T in the pseudorapidity region $-0.1 < \eta < 5.5$. The cut on the correlation of the three RING counters ensures a total suppression of the background above 50 GeV in the pseudorapidity region $-0.1 < \eta < 2.9$, or 90 GeV in the pseudorapidity region $-0.1 < \eta < 5.5$. Prior to the cut, the background extends beyond 200 GeV.

It is seen that we have achieved the condition that the target events represent more than half of the events after the cuts. For the ^{16}O beam in 1986, at both incident energies, the remaining non-target contamination varied from about 75% at $E_T \approx 10$ GeV to $\leq 1\%$ at $E_T > 50$ GeV.

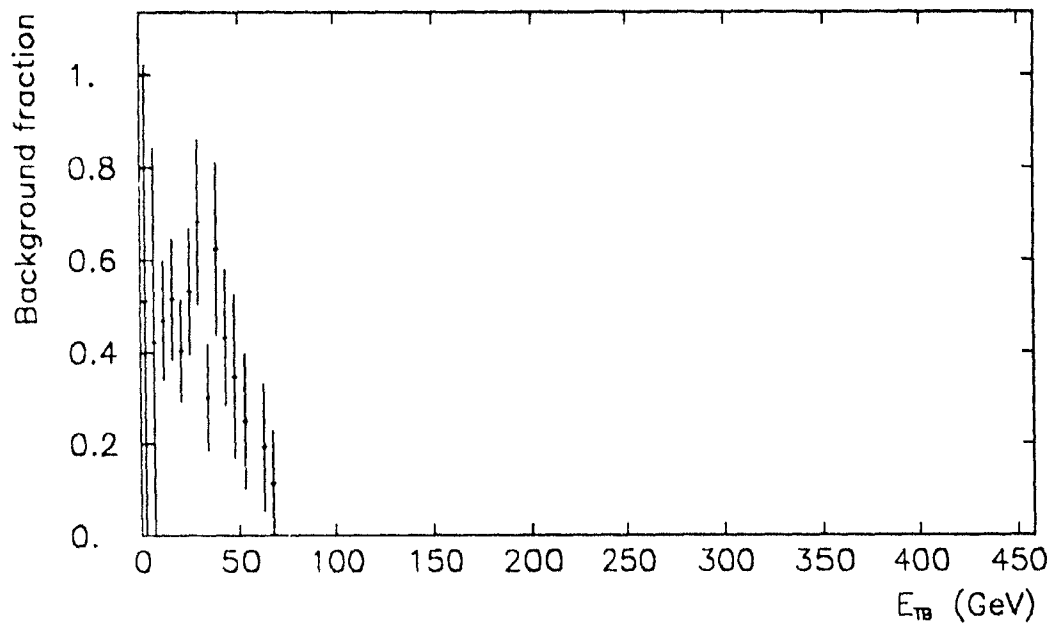


Figure 33: The ratio of the $1/\text{flux } dN/dE_{TB}$ distribution taken in absence of a target to the same quantities taken in presence of a target. This ratio is a measure, as a function of E_{TB} , the transverse energy in the pseudorapidity region $-0.1 < \eta < 2.9$, of the remaining non-target contamination for the data taken with W targets with a 200 GeV/nucleon ^{32}S projectile.

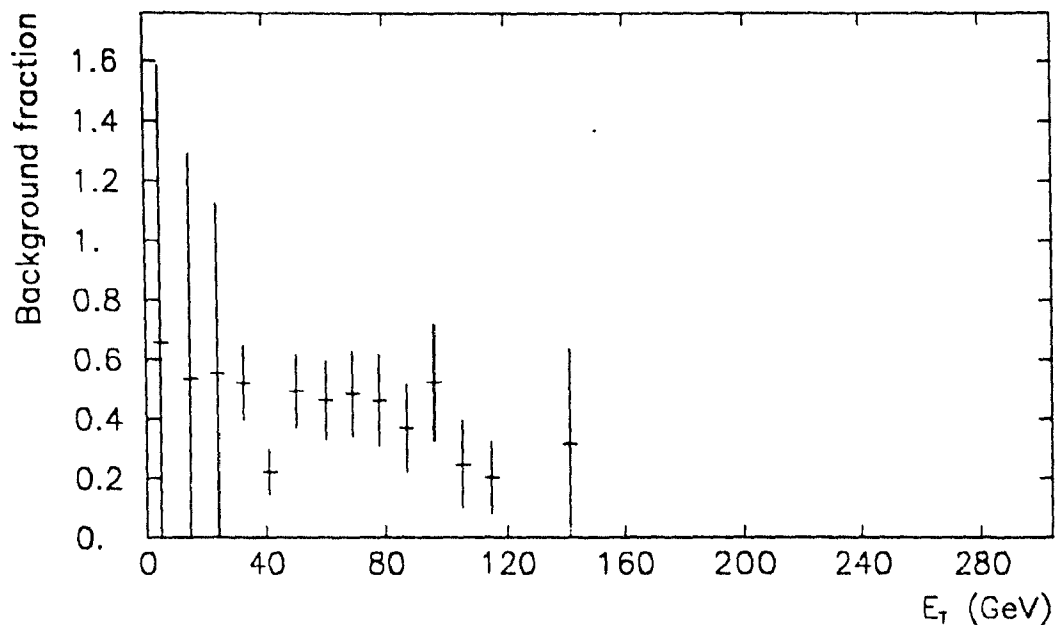


Figure 34: The ratio of the $1/\text{flux } dN/dE_T$ distribution taken in absence of a target to the same quantity taken in presence of a target. This ratio is a measure, as a function of E_T in the pseudorapidity region $-0.1 < \eta < 5.5$, of the remaining non-target contamination for the data taken with W targets with a 200 GeV/nucleon ^{32}S projectile.

3.3 The absolute normalization of the cross-sections.

The final differential cross-sections (in mb/GeV) make use of a value of flux, called the effective beam, which is the total number of beam particles detected while the acquisition system is active. This is less than the actual number of particles that arrived, because of the time that the online acquisition system is busy. The effective beam is further diminished in the analysis, to reflect the fact that the analysis rejects the ions that do not have the nominal charge or mass, that some events ($\leq 0.01\%$) are lost at random due to problem in the online acquisition software. We thus have

$$\frac{d\sigma}{dE_T} \text{ (mb/GeV)} = \frac{1}{\tau} \times \frac{1}{\text{flux}} \frac{dN}{dE_T}$$

The target thicknesses are calculated in the thin target approximation as $\tau = (\rho \cdot N_A \cdot L) / A \times 10^{-24}$ (in mb^{-1}) where ρ is the density in gr/cm^3 , N_A is the Avogadro number of atoms per mole, L is the thickness of the target in cm along the beam direction, and A is the atomic weight in gr/mole.

3.4 The pseudorapidity distributions of transverse energy.

In the UCAL and in the electromagnetic part of the UIAC, the read-out of the energy deposition is made by arrays of towers. The hermetic calorimetry means that for each polar and azimuthal angle, the particles will meet the front face of a tower. Equivalently, the plane of pseudorapidity and azimuthal angle is completely filled by the front faces of the towers, as can be seen in Figure 35.

For the scintillator calorimeters (UCAL), the weights implemented in the hardware of the EFL, and the weights used in the offline analysis are not exactly the same. The small differences, less than 5%, are due to improvements in the knowledge of the performances of the calorimeters that have occurred after the hardware was installed, and of course to imperfections in the electronic amplification chain. The weight to be attributed to a given tower is not simply the sine of the angle of the geometrical center of the tower, but rather a weighted average of the sine of the angle of the particles that have contributed to the energy measured in that tower in Monte Carlo simulations of the detector. The weight of each Monte Carlo particle is simply the energy contribution. That method gives a better precision on the measurements of transverse energy, provided the Monte Carlo simulation generates a pseudorapidity distribution of transverse energy close to reality. In particular, it is easy to see that the weight of one tower differs from the sine of the angle of the geometrical center of that tower by an amount that depends on the local slope of the pseudorapidity distribution. The more positive the slope of $dE_T/d\eta$, the more the effective center of the tower is at a smaller angle than the geometrical center, and the weight should be reduced.

The code HIJET was used to generate the input pseudorapidity distributions of transverse energy and particle composition. Its $dE_T/d\eta$ is only slightly different from the actual one in the region of pseudorapidity $-0.1 < \eta < 2.9$. The fact that the weights are thus not exactly the optimal ones results in a slight degradation of the resolution of the transverse energy resolution.

A Monte Carlo [79] was used to simulate the calorimeter response for the calculation of the weights implemented in the EFL, and the PROPHET Monte Carlo program [80] based on the GEANT simulation program together with a parametrization [81] of the longitudinal shower profile was used for the calculation of the optimal weights used in the offline analysis. The latter simulation program is also used to calculate the final corrections of the transverse energy.

The pseudorapidity distributions of transverse energy are made from the contributions of all towers to the transverse energy by attributing each of them to one bin. With a very large granularity, this attribution would be unambiguous. A simple method to choose the pseudorapidity of all towers would be $\eta = -\ln(\tan(\theta_w/2))$ where $\sin\theta_w$ is the weight for transverse energy. This method unfortunately produces accumulations of channels, and gaps; in particular, as an example of gap, there would be no description of $dE_T/d\eta$ at the pseudorapidity where the BOX and WALL calorimeters meet.

It was chosen instead to attribute the transverse energy of towers according to the η, ϕ map shown in Figure 35. When the front face of a tower is entirely contained in a η -bin, its transverse energy is entirely attributed to that bin of $dE_T/d\eta$. When the front face of a tower is shared between several bins, the transverse energy contained in that tower is split according to the fractions of the area of the front face of the tower in the η, ϕ space overlapping the various bins. In general, the contributions to the transverse energy of the towers are binned not only according to pseudorapidity, but also according to azimuthal angle. For the present analyses all azimuthal angles are simply added together.

This splitting of transverse energy between bins obviously degrades the η -resolution, but improves the local uniformity of the distribution. Note that the finite size of hadronic (and electromagnetic) showers, and the light sharing in light-coupled stacks also degrades the η -resolution. This smearing of the transverse energy deposition is partly corrected for in the Monte Carlo correction procedures.

What was said above regarding the towers of the scintillator calorimeter also applies to the towers of the electromagnetic section of the ULAC. The only difference is that the weighted sine of the angles used to produce the E_T weight of a tower is computed only with photons, in order to optimize the resolution for these. As a result, the weights differ only infinitesimally from the sines of the geometrical centers of the towers.

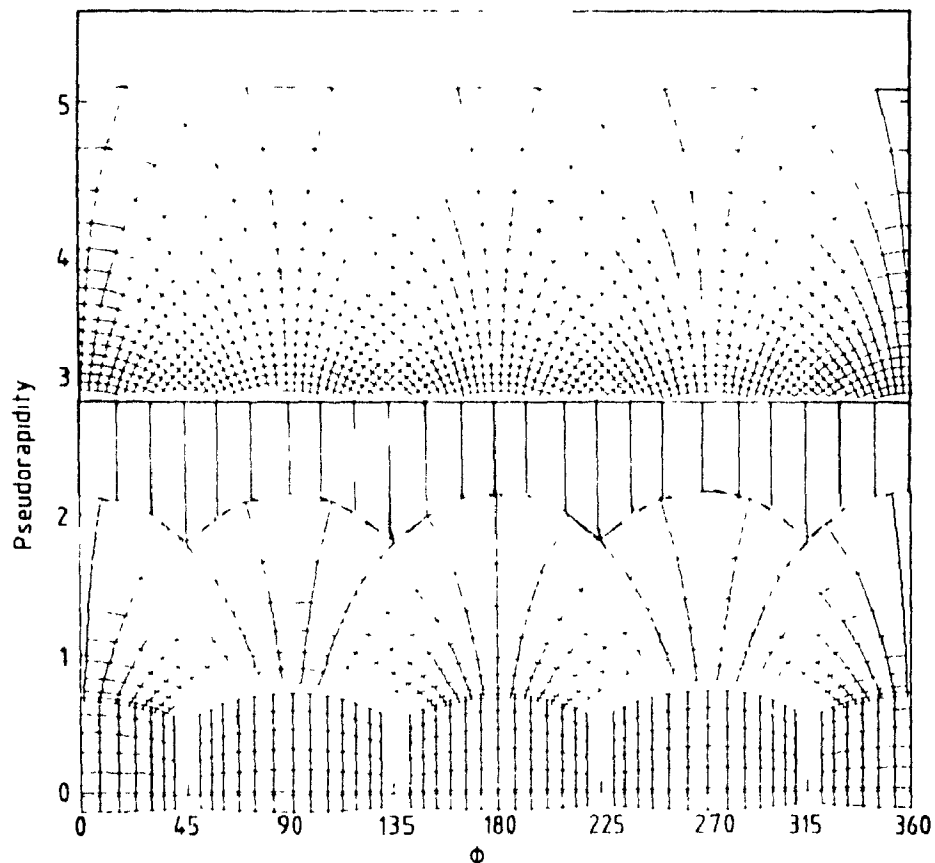


Figure 35: The face of all towers of the HELIOS calorimeter in η, ϕ . The pseudorapidities from -0.1 to 2.9 are covered by scintillator calorimeters, and the pseudorapidities from 2.9 to 5.5 are covered by the ULAC.

3.5 The hadronic part of the ULAC.

Because of its strip read-out, the hadronic part of the ULAC presents serious difficulties for the analysis; since it receives about half of the forward transverse energy, it *cannot* simply be neglected. It is not easy to find the E_T -weights that should be given to each tower. It is even more difficult to decide to which bin of pseudorapidity each strip should be attributed, and almost impossible to decide to which bin of azimuthal angle it might be attributed. Note that for a strip read-out, the weighted sum is not necessarily the best way to evaluate the transverse energy. We will show in the next paragraphs how the weights were computed, and how the transverse energy was binned in pseudorapidity. The separation of the transverse energy in bins of azimuth was not attempted.

The transverse energy in the hadronic part of the ULAC has been calculated online with a set of weights determined by the method of average sine of the particles contributing to each strip in a Monte Carlo simulation, as was done in the backward region. This set of weights appears to have large fluctuations, and that is probably due to insufficient statistics of Monte Carlo events. Due to a positive weight in the central strip, the online forward transverse energy has an 'offset', i.e. a positive transverse energy even for beam particles having no transverse energy. The transverse energy in the x and y directions are then summed quadratically under the square root sign, instead of linearly. The online transverse energy in the hadronic part of the ULAC is therefore a complicated function of the real transverse energy. This does not have catastrophic consequences, since for trigger purposes, it is sufficient that the online ET is a locally linear function of the actual transverse energy.

One method to evaluate the forward transverse energy is to use the online version of the hadronic weights, except that the weight of the central strip is negative, which is equivalent to a null weight on the central strip together with a subtraction of the leakage contribution to the outer strips. This is the method used in the computation of the transverse energy for differential cross-sections.

For pseudorapidity distributions of transverse energy used a different method¹², based on the regularity of the geometry of hadronic section of ULAC. Each strip is given a weight proportional to the sine of the angle of its geometrical center. We temporarily call K the proportionality constant. Since each strip covers regions of very different polar angles, an average weight must somehow be defined for it. The solution is model-independent and shows up by considering the effective weight of the area of intersection of a strip in the x direction with a strip in the y direction.

$$\sin \theta(\text{eff}) = K \left[\frac{1}{2} \frac{|x|}{L} + \frac{1}{2} \frac{|y|}{L} \right]$$

where the factor 1/2 comes from the obvious fact that half of the energy is dissipated in x strips and half in y strips. This can be re-expressed, as a function of azimuthal angle, as:

$$\sin \theta(\text{eff}) = K \sin \theta \left[\frac{1}{2} |\cos \phi| + \frac{1}{2} |\sin \phi| \right]$$

Since the average of both $|\cos \phi|$ and $|\sin \phi|$ over one period are $2/\pi$, we need $K = \pi/2$ to obtain $\sin \theta(\text{eff}) = \sin \theta$. This method to obtain transverse energies from a cartesian readout is standard [82].

Within this method, we can now attribute each strip to a pseudorapidity bin. We have chosen to give each strip a single pseudorapidity. Certainly, each strip receives contribution from several bins of pseudorapidity, but the 'smearing' of the transverse energy on the pseudorapidity axis would only be worsened if the transverse energy of a strip was split between several bins. If each strip is

¹² Including the same subtraction of leakage

attributed to the pseudorapidity of its geometrical center, minus a constant η_0 , it is easy to determine the value of η_0 that is needed to correctly measure the first moment of the pseudorapidity of transverse energy. For simplicity, let us consider a δ -function 'ring' of transverse energy arriving in the hadronic part of the ULAC. The average pseudorapidity differs from the maximum one (obtained with the strip tangential to the 'ring') by:

$$\frac{\int_0^{\pi/2} d\phi [\sin\phi (\ln \sin\phi) + \cos\phi (\ln \cos\phi)]}{\int_0^{\pi/2} d\phi [\sin\phi + \cos\phi]}$$

where we have used the small-angle approximation repeatedly. This mathematical constant amounts to 0.307. We have therefore attributed the transverse energy of each strip to the pseudorapidity bin 0.31 less than the pseudorapidity of the geometrical center of the strip, splitting between bins when necessary. This solution does not avoid the smearing, but it makes the correction of the smearing easier, because the average position of the transverse energy is already correct, as we will see in a forthcoming section devoted to the presentation of the Monte Carlo corrections.

In addition, let us mention a method that does not involve a linear combination of the energies measured in the different channels, but instead a linear combination of the products of energies of a X strip with a Y strip. It is supposed that the energy deposited in the small square area of intersection of two strips by the product of the energies in the two strips (divided by 1/4 of the total energy in the hadronic section of the ULAC in order to conserve the energy). This method is sometimes called the maximum entropy method [83] since the product of the energies of the strips represents the most probable energy from a probabilistic/statistical point of view. It can in principle provide a 20% better resolution¹³, and was observed to improve resolution, but the non-linearity is deemed to be too dangerous for a first analysis, so it is not used in the results shown here.

¹³ This can be shown by linearizing the response locally in a high multiplicity environment.

3.6 Event-by-event correction for the energy at zero degree

In the forward calorimeters, either the ERSATZ calorimeter for the 1986 data taking or the ULAC for the 1987 data taking, a fraction of the total energy is carried by particles having essentially a zero polar angle. The numerical threshold for the definition of energy as energy at zero degree is usually taken as the pseudorapidity corresponding to the rapidity of the beam. The problem caused by this energy at zero degree is the 'fake' transverse energy that appears in the calorimeter elements surrounding the central one, due to the lateral size of hadronic showers. This problem has to be solved by a subtraction in the neighbouring strips of the leakage of energy at zero degree. This is done by using the energy in the most central detector elements (the central strips in the 1987 set-up, the central tower of the ERSATZ calorimeter in the 1986 set-up) as a measure of the energy at zero degree. The procedure is of course not exact, because of the calorimetric fluctuations of the energy deposition by the particles at zero degree, and because of the contribution to the energy deposition in the central detector element of particles with larger polar angles. However, the Monte Carlo corrections are correcting for the inefficiencies and loss of resolution caused by this subtraction procedure as they are for the effect of $e\pi$, leakage from modules, decays in flight, and many other effects.

In order to estimate the correction to the energy in the forward region, a knowledge of the shape of the spatial distribution of energy is needed. For this purpose, we can use the data which was taken with a 'VB' trigger, which selects the events where the beam particle arrives within a small window onto the center of the ULAC. A proton of 200 GeV produces the profile shown in Figure 36. The fluctuations in the shower profile play an important role in the resolution of the transverse energy. A similar plot with a ^{32}S nucleus projectile is shown in Figure 37. The shape is not very different; the shower profile is somewhat narrower, probably because the secondaries from the first collision in the calorimeter are more forward when the projectile is a ^{32}S than when it is a proton. The reduction of the fluctuations is due to the larger number of secondary showers.

This pattern of energy deposition E_{dep} can be reasonably well reproduced by a sum of two exponential profiles, $\frac{dE_{\text{dep}}}{dxdy} = Ae^{-r/\lambda_1} + Be^{-r/\lambda_2}$; $r = \sqrt{x^2 + y^2}$. The projection of this profile¹⁴ is also shown in the figure. 58% of the energy is carried by the narrow component with $\lambda_1 \approx 2.55$ cm (approximately one Molière radius) and 42% by a broad component with $\lambda_2 \approx 10$ cm (approximately one interaction length). These experimental characteristics have been implemented in the Monte Carlo simulation program PROPHET for the calculation of corrections. The profile itself has been implemented in the reconstruction program; We subtract a fraction h_1/h_0 of the energy of the central strip from the i -th strip, where h_1 and h_0 are the fractions of the beam energy in the i -th and central strips respectively, as given by Figure 36. The hadron profile can be used, rather than the heavy-ion

¹⁴ The projection in one dimension of an exponential profile is the function $xK_1(x)$, K_1 being the modified Bessel function of the second kind of order 1.

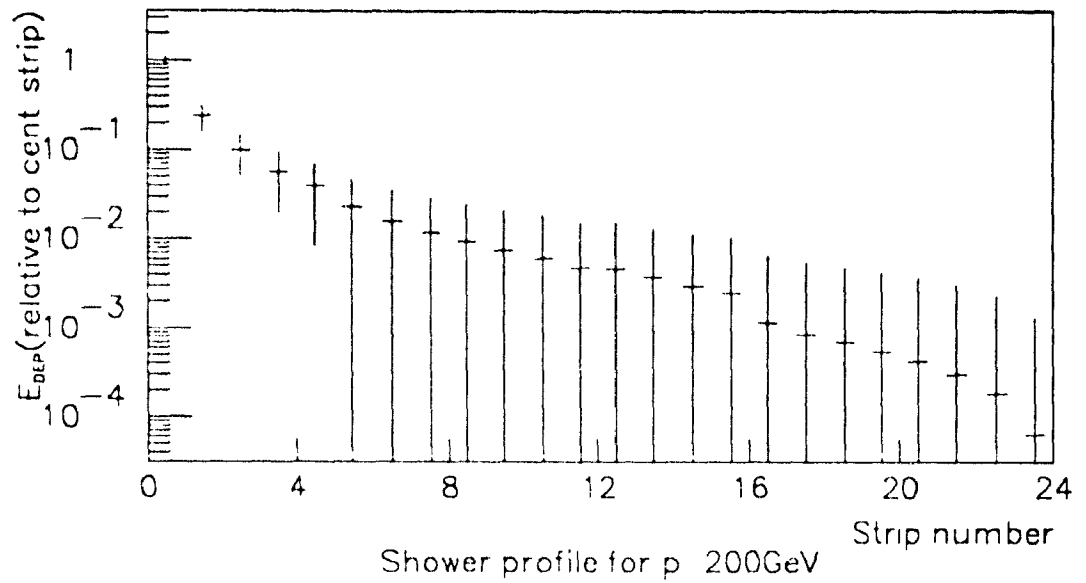


Figure 36: The energy deposition as a function of strip number for a 200 GeV proton beam hitting directly the center of the ULAC. The vertical error bars indicate the magnitude of the event-to-event fluctuations.

one, since the heavy-ion is likely to break-up into individual nucleons even for very peripheral collisions. The success of this procedure is verified by the fact that the regression of the forward transverse energy E_{TF} onto the backward transverse energy E_{TB} has an intercept very close to zero.

Similarly, the energy in the hadronic part of the central tower of the ERSATZ has been used to correct the energy deposition in the neighbouring towers with the aim of commissioning a measurement of the forward transverse energy with the 1986 calorimetric set-up.

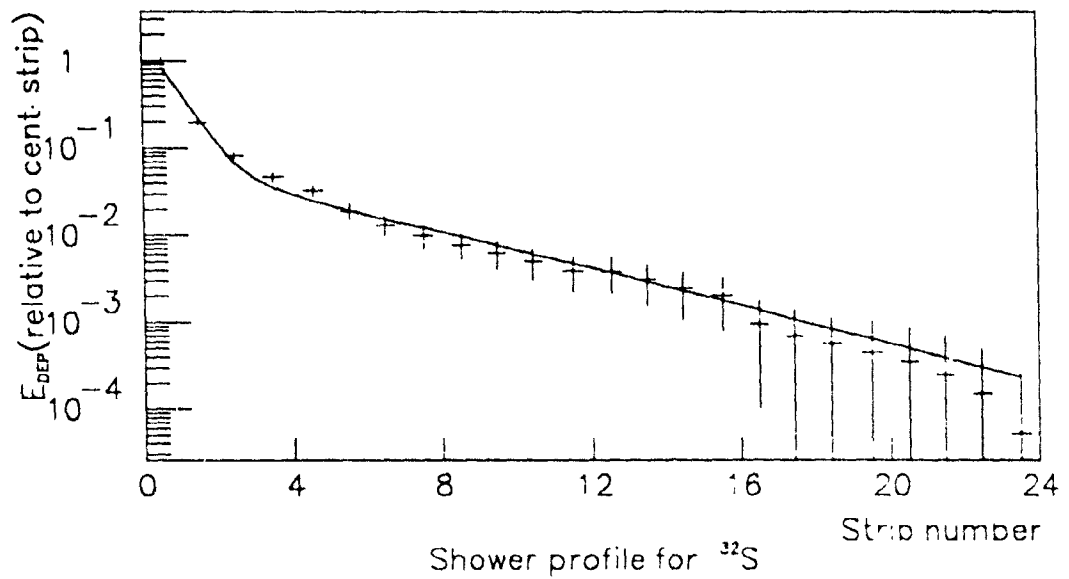


Figure 37: The energy deposition as a function of strip number for a 200 GeV/nucleon ^{32}S beam impinging directly in the center of the ULAC. The vertical error bars indicate the magnitude of the event-to-event fluctuations. The straight line is the shape resulting from the fit by a sum of two exponentials.

3.7 Monte Carlo correction of pseudorapidity distributions.

The pseudorapidity distribution is built from the energies measured in the various calorimeters by attributing each channel to a pseudorapidity/azimuth bin. This first attribution of the pseudorapidity and azimuth is done on the basis of the geometrical position of the sensitive volume which the channel is measuring (tower). When a given tower overlaps between two or more bins of η, ϕ , a fraction of the transverse energy of that channel, proportional to the overlap, is given to each bin. There was an exception to this rule in the case of the channels measuring the hadronic section of the ULAC. In that case, although each strip covers a large domain of pseudorapidity, a single pseudorapidity is given to each strip. As we have seen in section 3.5, the justification is that the strip read-out already causes a considerable smearing of the pseudorapidity distribution. The strips near to the center, for example, receive contribution from $\eta = 3$ to $\eta = 5.5$. Luckily, each strip is dominated by the contribution of a given pseudorapidity. If the energy sensed in a strip were split among several pseudorapidity bin, the problem of smearing, already quite serious, would be worsened. The chosen

solution was to attribute to each strip a pseudorapidity shifted by a constant $\eta_0 \approx -0.31$ from the pseudorapidity of its geometrical center, in such a way that the average pseudorapidity is correctly measured

The 'smearing' of the transverse energy on a domain of pseudorapidity is particularly obvious in the case of the hadronic part of the UIAC. It is however a general problem for the reconstruction of rapidity distributions of transverse energy.

Another region where the smearing has important consequences is in the light-coupled stacks of the 'WALL' calorimeter. The part of these stacks closer to the beam axis receives more energy than the rest, but the coupling by light redistributes the apparent energy deposition. Further smearing results from the lateral size of the showers, and the longitudinal size of the shower, when the towers are not collinear with the incident secondary particles

3.7.1 Principle of operation of the correction

It is quite clear what should be done in principle to reconstruct the pseudorapidity distribution of the transverse energy. In principle, the shapes of the showers are known, and the calorimeters are linear. Therefore, we could, in principle, establish the matrix \mathbf{M} which multiplies the vector of *real* transverse energy deposition per pseudorapidity bin to give the *measured* transverse energy deposition per pseudorapidity bin. For instance, when a transverse energy E_{T_i} is sent to bin i , a transverse energy $(\mathbf{M})_{ji} E_{T_i}$ is measured in bin j . So, *in principle*, we could invert the matrix \mathbf{M} to reconstruct the real transverse energy. A fraction of this matrix, as PROPHEET calculates it, is shown in Figure 38.

While this matrix \mathbf{M} is not singular mathematically speaking, it is in practice quasi-singular, and the approach described above would result in very large errors in the inverse matrix, and in catastrophic amplification of the various calorimeter noises. Instead, we have used a different method to obtain a numerically stable solution to the problem, which we will now describe. Suppose we have a 'test'

pseudorapidity distribution of transverse energy $(\frac{dE_T}{d\eta})_{test}$, not very different from the actual one. By using a Monte Carlo (PROPHEET) simulation of the calorimeter, we obtain the image by matrix \mathbf{M} of the test distribution, $\mathbf{M}((\frac{dE_T}{d\eta})_{test})$. On the other side, $(\frac{dE_T}{d\eta})_{meas}$ is $\mathbf{M}((\frac{dE_T}{d\eta})_{real})$. Now if 'test' is sufficiently close to 'real', we can simply obtain $(\frac{dE_T}{d\eta})_{real}$ by:

$$(\frac{dE_T}{d\eta})_{meas} = \frac{(\frac{dE_T}{d\eta})_{test}}{\mathbf{M}((\frac{dE_T}{d\eta})_{test})}$$

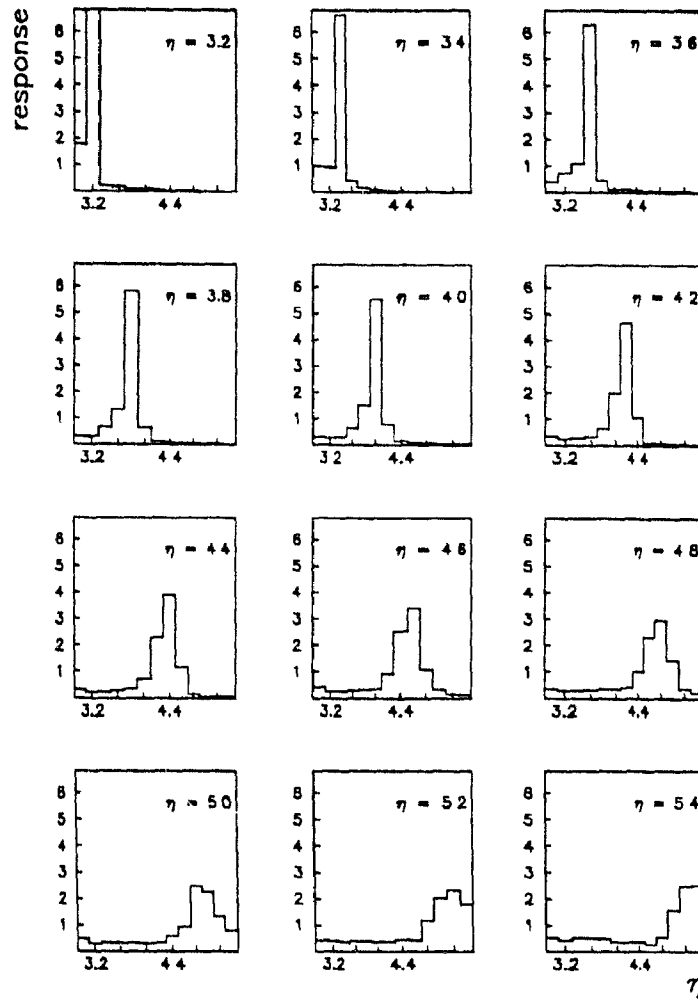


Figure 38: The response of the 12 last bins of $dE_T/d\eta$ when particles are sent into one bin at a time. The histograms are in consecutive order, and constitute a representation of the matrix M .

This approximation $(\frac{dE_T}{d\eta})_0$ to the real distribution can eventually be used as input instead of the test distribution in the Monte Carlo simulation, to verify our estimate:

$$\left(\frac{dE_T}{d\eta}\right)_1 = \left(\frac{dE_T}{d\eta}\right)_{\text{meas}} \frac{\left(\frac{dE_T}{d\eta}\right)_0}{M\left(\left(\frac{dE_T}{d\eta}\right)_0\right)}$$

If $(\frac{dE_T}{d\eta})_1$ is equal to $(\frac{dE_T}{d\eta})_0$ within the errors, we have, by definition, found a solution. If not, we can use $(\frac{dE_T}{d\eta})_1$ in place of the test distribution and find an improved $(\frac{dE_T}{d\eta})_2$. We can generally expect the procedure to converge very rapidly if the 'matrix' is well behaved.

3.7.2 Specific assumptions and results.

Having shown the principle of the Monte Carlo correction to the pseudorapidity distribution of transverse energy, let us examine the specific input of calorimeter physics in the Monte Carlo simulation.

The size of the showers, which affects the amount of smearing of the pseudorapidity distribution due to the sharing of a shower between two towers, is affected by the energy of the incident particle. It is therefore important to know the spectrum of energy of the particles reaching our calorimeter at each angle. The spectrum taken was an exponential distribution of transverse momenta with the same constant slope everywhere. This seems to be an approximately valid assumption in all the data taken until now (see section 4.8), but in any case the average transverse does not change very much, and the effect on smearing is a relatively weak one: even for a doubling of the average p_T , the purely hadronic fraction, and therefore the smearing constants, would change by $\approx 0.1 \ln 2 \equiv 7\%$ [84]. We are much more sensitive to the assumption of a certain fraction of the energy being carried by neutral hadrons that decay and produce electromagnetic showers. The 20% allowance that we leave on the fraction of the transverse energy carried by π^0 's is responsible for a large part of the systematic error on the transverse energy scale.

Following reference [81], the longitudinal shower profile for an electromagnetic shower was taken to be:

$$\frac{dE}{d\eta} \propto \left(\frac{l}{X_0}\right)^\alpha e^{-\beta \frac{l}{X_0}}$$

where X_0 is the radiation length in the material of the calorimeter, $\beta \approx 0.5$, and $\alpha \approx 2$ to 3 depends logarithmically on energy. The longitudinal shower profile for a hadronic shower was taken to be:

$$\frac{dE}{d\eta} \propto f_{em} \left(\frac{l}{X_0}\right)^\alpha e^{-\beta \frac{l}{X_0}} + (1-f_{em}) \left(\frac{l}{\lambda_I}\right)^\alpha e^{-\delta \frac{l}{\lambda_I}}$$

where λ_I is the interaction length, f_{em} is the "electromagnetic fraction", and the parameters α , β , κ , and δ are logarithmically energy dependent. In the scintillator calorimeters, covering up to 2.9 in

pseudorapidity, the lateral shower profile is approximated by a Gaussian of width $2.00X_0$ in the case of electromagnetic showers, and $0.75\lambda_r$ in the case of hadronic showers. The Gaussian shape is not a good approximation to the actual lateral shower profile. However, in the region $\eta < 2.9$, the granularity is so coarse that the details of the shower profile does not affect dramatically the final results. The Gaussian parametrization gives the right order of magnitude to the smearing of the pseudorapidity distributions.

The situation is quite different in the hadronic section of the ULAC. A Gaussian lateral shower profile cannot be used, because the granularity is such that a given shower extends over many (≈ 20) towers or strips. Also, if the effect of the projectile spectators is included in the Monte Carlo, these particles, that have by definition no transverse energy, will contribute to the simulated $dE_T/d\eta$ distribution *unless* their lateral profile *precisely* corresponds to the actual shower profile. When we have correctly parametrized the lateral shower profile, the $dE_T/d\eta$ will be precisely zero for an incident beam particle, since the analysis program was designed to produce zero for a beam particle. For all these reasons, in the hadronic part of the ULAC, the measured profile produced by an incident hadron was input into the code in the form of the fit to a sum of two exponentials already presented in section 3.6

Although the lateral shower profile varies as a function of shower age, the average lateral shower profile can be defined rather consistently. We do not need the details [77] of the evolution with shower age, because the strip structure is almost parallel to the direction of incidence of the secondary particles.

The ratio of the input of the PROPHET program to its output, which is our correction to $dE_T/d\eta$, is shown in Figure 39 for a Gaussian shaped input distribution of width 1.35 and center 2.5, the particle composition being given by the FRITIOF [50] event generator.

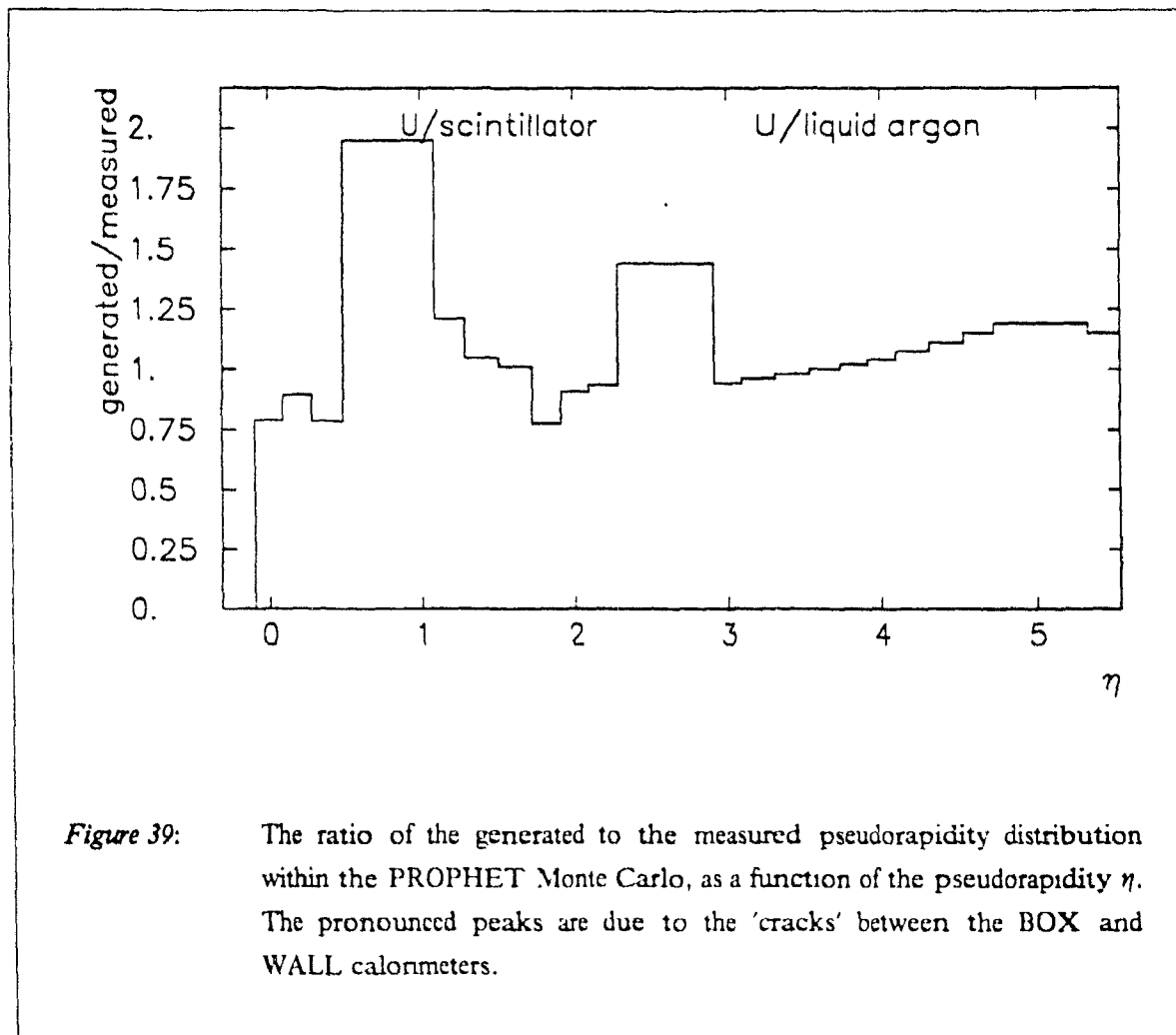


Figure 39: The ratio of the generated to the measured pseudorapidity distribution within the PROPHET Monte Carlo, as a function of the pseudorapidity η . The pronounced peaks are due to the 'cracks' between the BOX and WALL calorimeters.

3.8 Monte Carlo corrections for the transverse energy distributions

The transverse energy reconstructed offline with weights is only, for each event, an approximation to the actual transverse energy. Two kinds of errors are made: event-by-event fluctuations in the measurement of transverse energy, and systematic underestimation of the energy measured in the non-compensated part of the calorimeter for hadronic-showering particles. In this section, we will show the values obtained for these two numbers from the standard Monte Carlo simulation program. We will then show how the distributions can be corrected, using convenient geometric parametrizations. Finally, we will show that it is possible to measure, instead of calculate, the magnitude of the calorimetric fluctuations, using a method permitted by the full coverage of the energy flow measurement.

3.8.1 The corrections

The scatter plots of the generated and measured transverse energy with the PROPHET Monte Carlo, are consistently described by the following parameters:

- For the measurements with the scintillator calorimeters only, the measured transverse energy is 0.872 ($\equiv 1/1.147$) smaller than the generated transverse energy on average, and the magnitude of the fluctuations is $0.29\sqrt{E_{TB}}$
- For measurements with the ULAC, the measured transverse energy is 0.819 ($\equiv 1/1.22$) smaller than the generated transverse energy on average, and the magnitude of the fluctuations is $0.30\sqrt{E_{TF}}$
- For the measurements with all calorimeters, the measured transverse energy is 0.855 ($\equiv 1/1.17$) smaller than the generated transverse energy on average, and the magnitude of the fluctuations is $0.29\sqrt{E_T}$

3.8.2 Deconvolution of the distributions.

As we have seen, the measured transverse energy is related to the generated one, through the multiplication by a response factor, that takes into account the average loss of measured transverse energy (due to the e/π factor in a calorimeter with electron calibration, etc...), and through the addition of calorimetric fluctuations of a magnitude proportional to the square root of the transverse energy.

A first step in the correction is to multiply the transverse energy scale by the inverse of the response factor, known as the Monte Carlo correction factor f_{MC} , so that the average transverse energy is correct. Simultaneously, we divide the cross-section (and its statistical errors) by f_{MC} in order to conserve the total cross-section.

In a second step, the differential cross-sections have to be corrected for the finite resolution in the measurement of the transverse energy. These corrections are particularly important for the steeply falling tails of the $d\sigma/dE_T$ distributions, since the fluctuations have important effects when abundant events are close to bins with rare events.

As done in the case of $dE_T/d\eta$, we would like to invert the matrix that relates the population of the bins before and after the smearing, as in that case, a direct inversion is impossible. We will again use the method of the test distribution. In fact, because the magnitude of the calorimetric fluctuations is proportional to the square root of the transverse energy, just like the magnitude of the physical

fluctuations in NCM (Nuclear Collision Models), the smearing by the calorimeter resolution of a test distribution of the NCM type is another distribution of the NCM type with an increased fluctuations parameter. Let us recall here that in the Nuclear Collision Model [61] (see section 1.11) the nuclear collision is described as a superposition of N independent collisions. They produce a transverse energy $\forall \varepsilon_0$, with event-to-event fluctuations of magnitude $\sigma = \sqrt{N\omega\varepsilon_0^2}$. Quadratically adding calorimetric fluctuations of magnitude $\sigma = \kappa\sqrt{N\varepsilon_0}$ is equivalent to increasing ω by κ^2/ε_0 . The procedure of deconvolution is then simply to fit the smeared distribution with parameters ε_0 and ω , and then multiply the data by the ratio of the NCM distribution¹⁵ with parameters $\varepsilon_0, \omega - \kappa^2/\varepsilon_0$ to the NCM distribution with parameters ε_0, ω . It is not necessary to iterate, since we have found the test distribution that fits the corrected data, and produces a fit to the uncorrected data upon convolution with the calorimetric fluctuations

In this process, the errors on the cross-section are simply multiplied by the same factors as the cross-section. This is in order to conserve the number of equivalent events $\sum_{bins} \frac{\text{value}}{\text{error}^2}$. The total cross-section is conserved within errors in the deconvolution process since the two fitting NCM distributions have the same total cross-section.

3.8.3 A method of measurement of the transverse energy resolution

We will present here a method to determine the resolution of transverse energy measurements. This method gives as a by-product the magnitude of the vector sum of the transverse momenta vectors in two regions of pseudorapidity. This method is (to our knowledge) new, since it relies on full coverage of transverse energy in the center-of-mass and very high multiplicity which were realized in our experiment for the first time.

Consider N particles produced in a interaction, and two complementary domains of pseudorapidity $\eta_1 < \eta < \eta_2$ and $\eta_2 < \eta < \eta_3$. The transverse energy in the backward region can be defined as the sum of the lengths of the transverse momentum vectors \vec{p}_T :

$$E_{TB} \equiv \sum_{\eta_1 < \eta < \eta_2} |\vec{p}_T|$$

and the transverse energy in the forward region can be defined as:

¹⁵ The term κ^2/ε_0 amounts to 0.08 typical

$$E_{TF} \equiv \sum_{\eta_2 < \eta < \eta_3} |\vec{p}_T|$$

This agrees with the experimental definition of E_+ as $\sum E \sin\theta$, up to a factor E/p . $E/p \approx 1$ for the particles contributing the most to the transverse energy.

Similarly, we can measure the magnitude of the transverse momentum vector in the backward and forward regions. Because the sum of all transverse momentum vectors is exactly zero (by conservation of momentum) we call these: the forward and backward momentum imbalances I .

$$I_B = \left| \sum_{\eta_1 < \eta < \eta_2} \vec{p}_T \right|$$

$$I_F = \left| \sum_{\eta_2 < \eta < \eta_3} \vec{p}_T \right|$$

$$I_T = \left| \sum_{\eta_1 < \eta < \eta_3} \vec{p}_T \right|$$

In the absence of calorimetric fluctuations, the sum of all transverse momentum vectors is zero (giving $I_T = 0$), so that the backward and forward sum vectors are exactly opposite, and their magnitudes I_B and I_F are identical. However, in reality, all the quantities are affected by errors due to the finite resolution of the calorimeters. Since the errors are in general different, the two measurements I_B and I_F of the momentum imbalance are also different. The comparison of I_B with I_F , and the comparison with the transverse energy in each region, provides us with enough constraints to establish the resolution in each region.

The energy resolution is assumed to follow a law $\sigma = \kappa \sqrt{E}$. Considering only the calorimetric fluctuation, the average square of the momentum imbalance and the resolution of the transverse energy are related:

$$\begin{aligned} \langle I_B^2 \rangle &= (\langle I_{Bx} \rangle)^2 + 2 \langle I_{Bx} \times \text{fluctuations} \rangle + \sum_i \sin^2 \theta_i \cos^2 \phi_i \kappa_i^2 \frac{p_{Ti}}{\sin \theta_i} \\ &+ (\langle I_{By} \rangle)^2 + 2 \langle I_{By} \times \text{fluctuations} \rangle + \sum_i \sin^2 \theta_i \sin^2 \phi_i \kappa_i^2 \frac{p_{Ti}}{\sin \theta_i} \end{aligned}$$

$$= (\langle I_{Bx} \rangle)^2 + (\langle I_{By} \rangle)^2 + \sum_i \sin^2 \theta_i \kappa_i^2 \frac{P_{Ti}}{\sin \theta_i}$$

the average of the calorimetric fluctuations being zero, while :

$$\sigma(E_{TB})^2 = \sum_i \sin^2 \theta_i \kappa_i^2 \frac{P_{Ti}}{\sin \theta_i}$$

If the number of particles is sufficient, this can be written as:

$$\sigma(E_{TB})^2 = \int_{\eta_1}^{\eta_2} d\eta \sin^2 \theta \kappa^2(\eta) \frac{dE_T}{d\eta}$$

The average square imbalances in the forward region and in the full region of pseudorapidity are similarly related to the resolutions of the transverse energy in the forward and full regions.

Allowing now physical fluctuations, we obtain:

$$\langle I_B^2 \rangle = \langle I^2 \rangle_{phys} - \sigma^2(E_{TB})$$

$$\langle I_F^2 \rangle = \langle I^2 \rangle_{phys} - \sigma^2(E_{TF})$$

and:

$$\langle I_T^2 \rangle = \sigma^2(E_T) = \sigma^2(E_{TB}) + \sigma^2(E_{TF}) = \int_{\eta_1}^{\eta_3} d\eta \sin^2 \theta \kappa^2(\eta) \frac{dE_T}{d\eta}$$

We have thus shown the following results:

- If the shape $dE_T d\eta$ does not depend on E_T , or if the resolution factor κ does not depend on η , the resolution is simply proportional to the square root of the transverse energy. In practice, the shape of $dE_T d\eta$ varies little with E_T so that the resolution of the transverse energy obeys such a law.
- We can measure the *physical* average square imbalance, in other words the average square of the transverse momentum transfer between the backward and the forward region, by

$$1/2 \langle I_B^2 \rangle + \langle I_F^2 \rangle - \langle I_T^2 \rangle)$$

- The backward transverse energy resolution is $\langle I_B^2 \rangle - \langle I_T^2 \rangle_{phys.}$, that is, $1/2 \langle I_B^2 \rangle + \langle I_T^2 \rangle - \langle I_F^2 \rangle$, and similarly the resolution if the forward transverse energy is $\sigma^2(E_{TF}) = 1/2 \langle I_F^2 \rangle + \langle I_T^2 \rangle - \langle I_B^2 \rangle$. This was evaluated (in our calorimeter $\eta_1 = -0.1$, $\eta_2 = 2.9$, $\eta_3 = 5.5$), and it was found that the resolution on the backward transverse energy approximately scales as $0.41 \sqrt{E_{TB}}(\text{GeV})$ in all cases. In Figure 40, it is shown for a sample of $^{32}\text{S-Pt}$ collisions. The data are fitted to $0.41 \sqrt{E_{TB}}$, or even more precisely to $2 \oplus 0.39 \sqrt{E_{TB}}^{16}$, where the constant term of 2 GeV is a consequence of the uranium noise. Similarly, the resolution on the transverse energy in the forward region, $\sigma(E_{TF})$ was found to be about $0.43 \sqrt{E_{TF}}(\text{GeV})$.

Given the fact that the two coverages do not completely cover all pseudorapidities, and that the calorimetric fluctuations of the forward and backward regions, assumed implicitly to be uncorrelated, are in fact somewhat correlated (due to shower leakage, for example), these results cannot be expected to be perfectly exact. However, it is interesting to see that the number obtained for the resolution of the transverse energy in the backward region ($0.41 \sqrt{E_{TB}}$) is quite close to the result ($0.29 \sqrt{E_{TB}}$) of the Monte Carlo simulation, that does not have the various imperfections and inhomogeneities of the actual calorimeters.

¹⁶ $x \oplus y \equiv \sqrt{x^2 + y^2}$

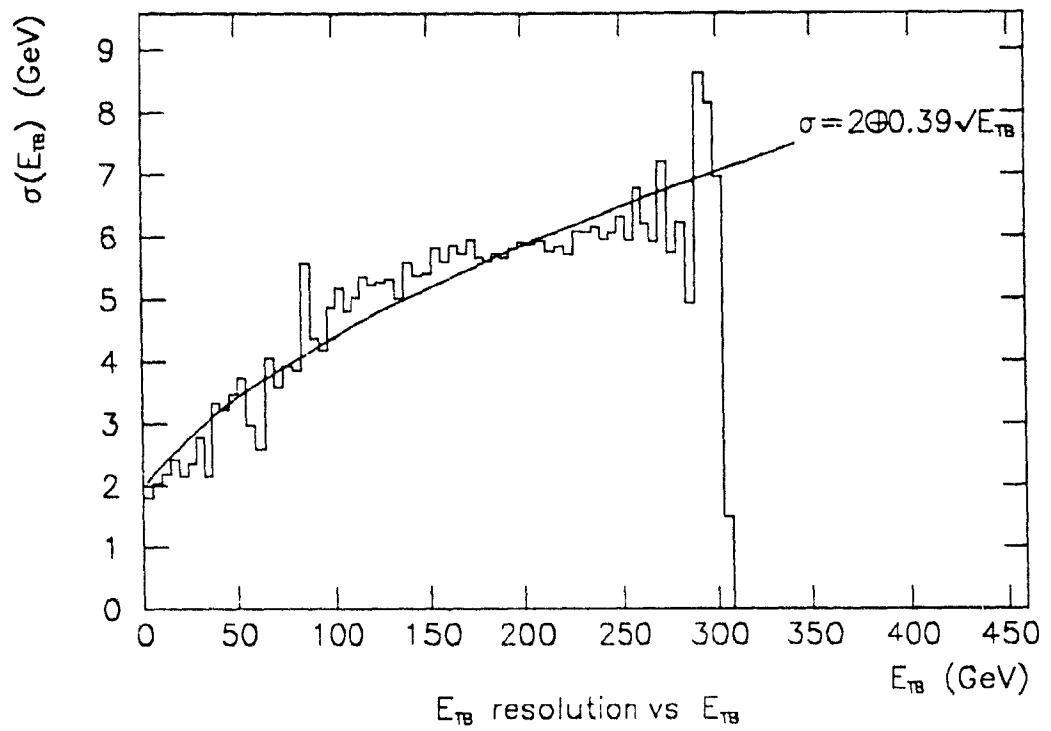


Figure 40: The transverse energy resolution measured by the method of imbalances: $\sigma(E_{TB})$ as a function of the backward transverse energy E_{TB}

Chapter 4

Experimental results and discussion

4.1 Introduction

We show in this chapter that the observables of transverse energy and multiplicity in heavy-collisions are measurements of the global properties of hot hadronic matter of large density.

Naively, the transverse energy distributions $d\sigma/dL_T$ represent the probability of creating states of large densities, and the pseudorapidity density of transverse energy $dL_T/d\eta$ then indicates the degree of thermalization achieved, with an isotropic distribution indicating total thermalization. However, we will see that the fluctuations in the geometry (fluctuations of the impact parameter and of the orientations of deformed nuclei) play a considerable role in determining the shape of the distribution. However, we attempt to extract as much *dynamical* information from the distributions of transverse energy as possible, in particular by comparing the distributions obtained in the backward half of the rapidity coverage ($-0.1 < \eta < 2.9$) with those obtained in the 'full' coverage ($-0.1 < \eta < 5.5$). These distributions are compared with extrapolations of the properties of hadron-hadron collisions given by the FRITIOF and IRIS Monte Carlos. In addition, we extract the average transverse energy of central collisions from the distributions of transverse energy; these transverse energy of central collisions can be conveniently fitted to a power law dependence on the atomic mass number of the target nucleus, and compared to some simple models, shedding light on the dynamics.

By examining the correlations of the transverse energy in the backward and forward regions, we get closer to isolating the dynamics of the collision. Similarly, the exact distribution of the transverse energy as a function of pseudorapidity is rich in informations on the dynamics. We compute the moments of these distributions, and their evolution as a function of transverse energy. The characteristics of these moments can be naturally explained in terms of a simple model of hydrodynamics expansion. In fact, most of the experimental features can be explained, although not uniquely, by this model. An early search for exclusive signatures of hydrodynamics in the small correlations of transverse energy has been attempted, but could not provide a definitive answer due to the magnitude of the errors remaining in this analysis.

We then compare the transverse energy and multiplicity flows. This comparison is a source of information concerning the nature of the collective hydrodynamic expansion, the cooling of the hypothetical thermalized macro-system, and entropy generation, which could itself be a source of information on phase transitions.

4.2 The differential cross-sections.

4.2.1 200 GeV/c proton

We define E_{TB} as the transverse energy in the backward pseudorapidity region $-0.1 < \eta < 2.9$. The differential cross-sections versus E_{TB} for 200 GeV proton projectiles against Al, Cu, W and U targets are displayed in Figure 41. These differential cross-sections were obtained with statistics of 32500, 49000, 54000, and 60000 events when the beam of 200 GeV protons impinged on targets of thicknesses of 7.87mm Al, 3.02mm Cu, 2.00mm W, and 2.12 mm U respectively.

These distributions asymptotically converge to a constant slope ($\approx 0.61 \text{ GeV}^{-1}$), reflecting a similar property of proton-proton collisions. The shape assumed in hadron-hadron collisions, including the exponential tail, is itself due (in the major trend of theories) to the random nature of the process of creation of quark-antiquark pairs in a strong chromo-electric field.

We have used the following form to fit the data:

$$\sigma_0 \frac{E_T}{E_0} \exp\left(-\frac{E_T}{E_0}\right) \left(\sum_{i=0}^{N-1} \frac{\left(\frac{E_T}{E_0}\right)^i}{i!} \right)$$

where the fit parameters N and E_0 are related to the parameters of the NCM by $N_{cent} E_0 = NE_0$, and $\omega = N_{cent}/N$, N_{cent} being the number of collisions given by geometry in the central case. This form incorporates the 'triangular' distribution of overlap integrals expected for 'hard sphere' geometry.

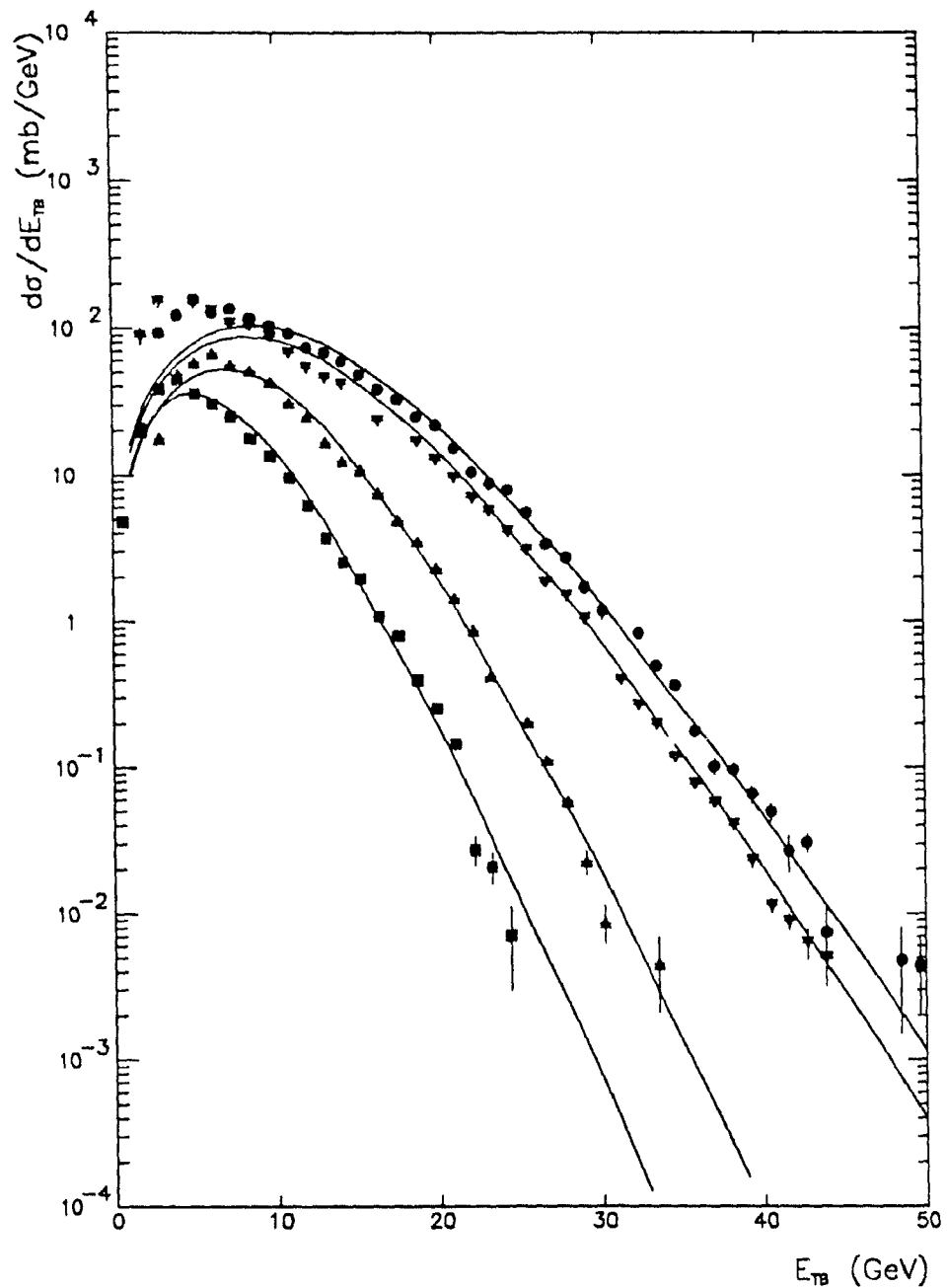


Figure 4: Transverse energy differential cross-section measured in $-0.1 < \eta < 2.9$ for a 200 GeV p beam. The distributions $d\sigma/dE_{T\perp}$ are shown for Al (■), Cu (▲), W (▼), and U (●) targets. $E_{T\perp}$ is defined as $\sum E_i^{*u} \sin\theta$ where $E_i^{*u} = \sqrt{p^2 + m^2}$ except for nucleons where $E_i^{*u} = \sqrt{p^2 + m^2} - m$. The curves are fits with a geometrical parametrization described in the text.

4.2.2 60 GeV/nucleon oxygen

The differential cross-sections for the production of E_{TB} in collisions of 60 GeV/nucleon ^{16}O projectiles against Al, Ag, W targets have appeared in [85], are listed in Table 3 to Table 5.

Table 3: ^{16}O -Al backward transverse energy differential cross-section at 60 GeV/nucleon.

E_{TB} [GeV]	Bin half-width [GeV]	$d\sigma/dE_{TB}$ [mb/GeV]	Error [mb/GeV]
14.9	3.4	$2.20 \times 10^{+1}$	$6.51 \times 10^{+0}$
21.8	3.4	$1.30 \times 10^{+1}$	$4.78 \times 10^{+0}$
28.7	3.4	$1.23 \times 10^{+1}$	$1.70 \times 10^{+0}$
35.6	3.4	$8.88 \times 10^{+0}$	$1.14 \times 10^{+0}$
42.4	3.4	$4.02 \times 10^{+0}$	5.90×10^{-1}
49.3	3.4	$1.28 \times 10^{+0}$	1.29×10^{-1}
56.2	3.4	1.57×10^{-1}	4.25×10^{-2}
64.2	2.3	2.89×10^{-2}	1.67×10^{-2}
68.8	2.3	3.37×10^{-3}	1.14×10^{-3}
73.4	2.3	3.90×10^{-3}	1.19×10^{-3}

Table 4: ^{16}O -Ag backward transverse energy differential cross-section at 60 GeV/nucleon.

E_{TB} [GeV]	Bin half-width [GeV]	$d\sigma/dE_{\text{TB}}$ [mb/GeV]	Error [mb/GeV]				
				81.4	1.1	$5.68 \times 10^{+0}$	2.88×10^{-1}
14.9	3.4	$2.32 \times 10^{+1}$	$1.73 \times 10^{+1}$	83.7	1.1	$4.83 \times 10^{+0}$	2.65×10^{-1}
21.8	3.4	$1.78 \times 10^{+1}$	$1.18 \times 10^{+1}$	86.0	1.1	$3.32 \times 10^{+0}$	2.19×10^{-1}
28.7	3.4	$1.80 \times 10^{+1}$	$4.50 \times 10^{+0}$	88.3	1.1	$2.14 \times 10^{+0}$	6.82×10^{-2}
35.6	3.4	$1.87 \times 10^{+1}$	$3.13 \times 10^{+0}$	90.6	1.1	$1.86 \times 10^{+0}$	6.39×10^{-2}
42.4	3.4	$1.67 \times 10^{+1}$	$1.73 \times 10^{+0}$	92.9	1.1	$1.14 \times 10^{+0}$	2.21×10^{-1}
49.3	3.4	$1.57 \times 10^{+1}$	7.10×10^{-1}	95.2	1.1	$1.02 \times 10^{+0}$	4.73×10^{-2}
56.2	3.4	$1.31 \times 10^{+1}$	6.21×10^{-1}	97.5	1.1	7.34×10^{-1}	4.01×10^{-2}
60.8	1.1	$1.29 \times 10^{+1}$	$1.04 \times 10^{+0}$	99.8	1.1	5.49×10^{-1}	3.46×10^{-2}
63.1	1.1	$1.20 \times 10^{+1}$	$1.00 \times 10^{+0}$	102.1	1.1	2.14×10^{-1}	1.44×10^{-2}
65.4	1.1	$1.08 \times 10^{+1}$	9.48×10^{-1}	104.4	1.1	1.46×10^{-1}	1.17×10^{-2}
67.7	1.1	$1.25 \times 10^{+1}$	$1.02 \times 10^{+0}$	106.7	1.1	1.25×10^{-1}	1.09×10^{-2}
70.0	1.1	$9.45 \times 10^{+0}$	3.73×10^{-1}	109.0	1.1	6.23×10^{-2}	7.45×10^{-3}
72.3	1.1	$8.43 \times 10^{+0}$	3.53×10^{-1}	111.3	1.1	3.90×10^{-2}	5.80×10^{-3}
74.6	1.1	$7.89 \times 10^{+0}$	3.41×10^{-1}	113.6	1.1	2.41×10^{-2}	4.50×10^{-3}
76.8	1.1	$7.12 \times 10^{+0}$	3.23×10^{-1}	117.0	2.3	9.04×10^{-3}	1.93×10^{-3}
79.1	1.1	$6.15 \times 10^{+0}$	3.00×10^{-1}	121.6	2.3	5.56×10^{-3}	1.99×10^{-3}

Table 5: ^{16}O -W backward transverse energy differential cross-section at 60 GeV/nucleon.

ΔE [GeV]	Bin half-width [GeV]	$d\sigma/d\Delta E$ [mb/GeV]	Error [mb/GeV]	ΔE [GeV]	$d\sigma/d\Delta E$ [mb/GeV]	Error [mb/GeV]
14.9	3.4	$4.65 \times 10^{+1}$	$2.70 \times 10^{+1}$	99.8	$7.49 \times 10^{+0}$	2.82×10^{-1}
21.8	3.4	$3.26 \times 10^{+1}$	$2.08 \times 10^{+1}$	102.1	$6.75 \times 10^{+0}$	2.67×10^{-1}
28.7	3.4	$2.80 \times 10^{+1}$	$1.90 \times 10^{+1}$	104.4	$5.38 \times 10^{+0}$	1.17×10^{-1}
35.6	3.4	$2.71 \times 10^{+1}$	$1.70 \times 10^{+1}$	106.7	$4.57 \times 10^{+0}$	1.08×10^{-1}
42.4	3.4	$2.36 \times 10^{+1}$	$1.84 \times 10^{+1}$	109.0	$3.90 \times 10^{+0}$	9.98×10^{-2}
49.3	3.4	$1.93 \times 10^{+1}$	$1.16 \times 10^{+1}$	111.3	$3.13 \times 10^{+0}$	8.96×10^{-2}
56.2	3.4	$1.75 \times 10^{+1}$	$1.27 \times 10^{+1}$	113.6	$2.47 \times 10^{+0}$	7.96×10^{-2}
60.8	1.1	$1.66 \times 10^{+1}$	7.81×10^{-1}	115.8	$1.85 \times 10^{+0}$	6.89×10^{-2}
63.1	1.1	$1.45 \times 10^{+1}$	7.29×10^{-1}	118.1	$1.57 \times 10^{+0}$	6.38×10^{-2}
65.4	1.1	$1.63 \times 10^{+1}$	7.75×10^{-1}	120.4	$1.05 \times 10^{+0}$	5.19×10^{-2}
67.7	1.1	$1.57 \times 10^{+1}$	7.60×10^{-1}	122.7	8.05×10^{-1}	4.53×10^{-2}
70.0	1.1	$1.48 \times 10^{+1}$	7.37×10^{-1}	125.0	6.75×10^{-1}	4.14×10^{-2}
72.3	1.1	$1.49 \times 10^{+1}$	7.42×10^{-1}	127.3	3.80×10^{-1}	1.37×10^{-2}
74.6	1.1	$1.55 \times 10^{+1}$	7.55×10^{-1}	129.6	2.65×10^{-1}	1.13×10^{-2}
76.8	1.1	$1.47 \times 10^{+1}$	7.36×10^{-1}	131.9	1.77×10^{-1}	9.03×10^{-3}
79.1	1.1	$1.38 \times 10^{+1}$	7.13×10^{-1}	134.2	1.21×10^{-1}	7.33×10^{-3}
81.4	1.1	$1.40 \times 10^{+1}$	3.87×10^{-1}	136.5	7.51×10^{-2}	5.62×10^{-3}
83.7	1.1	$1.35 \times 10^{+1}$	3.80×10^{-1}	138.8	5.68×10^{-2}	4.84×10^{-3}
86.0	1.1	$1.26 \times 10^{+1}$	3.67×10^{-1}	141.1	2.80×10^{-2}	3.27×10^{-3}
88.3	1.1	$1.21 \times 10^{+1}$	3.60×10^{-1}	143.4	1.66×10^{-2}	2.48×10^{-3}
90.6	1.1	$1.07 \times 10^{+1}$	3.38×10^{-1}	145.7	1.51×10^{-2}	2.39×10^{-3}
92.9	1.1	$9.55 \times 10^{+0}$	5.32×10^{-1}	149.1	4.17×10^{-3}	8.62×10^{-4}
95.2	1.1	$9.76 \times 10^{+0}$	3.22×10^{-1}	154.8	1.17×10^{-3}	3.63×10^{-4}
97.5	1.1	$8.54 \times 10^{+0}$	3.01×10^{-1}	161.7	7.24×10^{-4}	1.60×10^{-4}

The same data are displayed in Figure 42. These differential cross-sections were obtained with statistics of 11167, 19166, and 75889 events for a total flux of 8.5×10^8 , 4.8×10^8 , and 1.6×10^9 nuclei traversing targets of thicknesses of 0.5mm Al, 0.2mm Ag, and 0.1/0.2 mm W respectively. (In the case of W, about half of the data was taken with a thickness of 0.2 mm and half with a thickness of 0.1 mm in order to evaluate the possible effects of multiple interactions in the target on the differential cross-sections. This effect was found to be below the statistical errors for both the 0.1 and the 0.2 mm targets. There was a measurable target thickness effect for a sample taken at 200 GeV/c with a 1 mm W target thickness [71], but these data are not reported here)

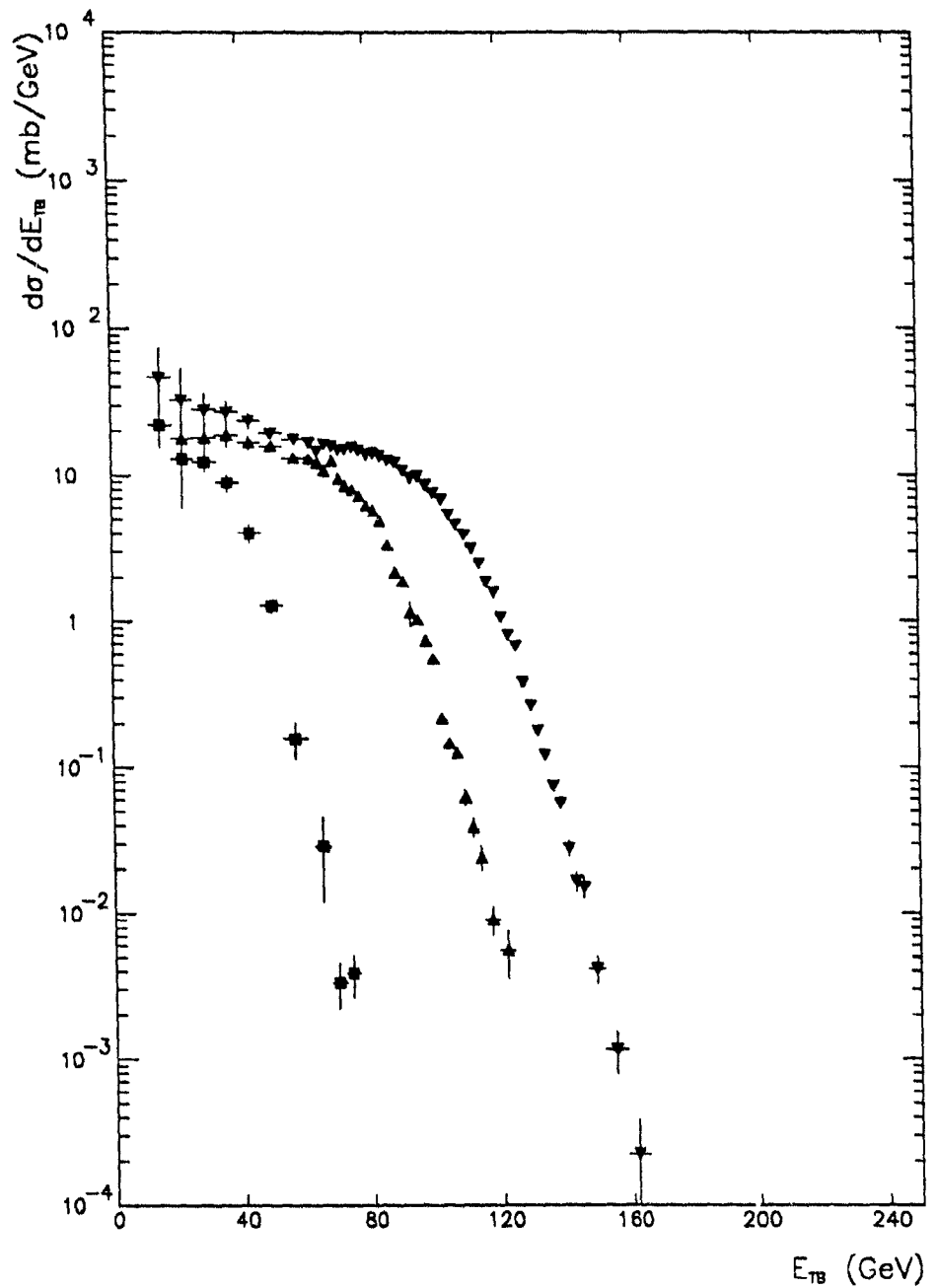


Figure 42: Transverse energy differential cross-section measured in $-0.1 < \eta < 2.9$ for a 60 GeV/nucleon ^{16}O beam. The distributions $d\sigma/dE_{\text{TB}}$ are shown for Al (■), Ag(▲), and W(▼) targets. E_{TB} is defined as $\sum E_i^{*u} \sin\theta$.
 $E_i^{*u} = \sqrt{p^2 + m^2}$ except for nucleons where $E_i^{*u} = \sqrt{p^2 + m^2} - m$.

These distributions do not seem to approach a constant slope, but instead the shape of the tail appears to be parabolic, such a behaviour is expected in as much as the central-limit theorem applies. At the level of statistics that we are considering presently, the central theorem applies, as the slope is everywhere small compared to the equivalent slope for an individual hadron-hadron collision. A fluctuation of transverse energy is then most probably resulting from a sum of small fluctuations in many collisions. If the central-limit theorem ceases to apply, as we go to sufficiently low differential cross-sections, then the fluctuations are dominated by the fluctuations of a single collision, and the slope should saturate at the hadron-hadron value. The slopes reached in the far tails approach this condition; if the distributions extended for about 3 more decades in cross-section, either measurable deviations from Gaussian fluctuations would occur, or the heavy-ion slopes would exceed the hadron-hadron ones.

The plateau observed for the Ag and W targets is a prediction of geometry, for geometrical reasons, it can also be expected that there will not be a plateau in the case of Al.

4.2.3 200 GeV/nucleon oxygen

The differential cross-sections versus $E_{\perp} B$ have been published in [85], are shown for 200 GeV.nucleon ^{16}O projectiles against Al, Ag, W targets in Table 6 to Table 8, and are plotted in Figure 43.

These differential cross-sections were obtained with statistics of 772, 2393, and 50094 events for a total flux of 7.9×10^8 , 3.8×10^8 and 2.3×10^8 nuclei hitting targets of thicknesses of 0.5mm Al, 0.2mm Ag, and 0.1mm W respectively.

The transverse energy observed at 200 GeV nucleon is approximately 25% larger than the same observed at 60 GeV/nucleon. The increase would be larger in the full rapidity interval, since the distributions at 60 GeV.nucleon are centered at smaller rapidities than at 200 GeV nucleon.

Table 6: ^{16}O -Al backward transverse energy differential cross-section at 200 GeV/nucleon.

Γ [B] [GeV]	Bin half-width [GeV]	$d\sigma/d\Gamma$ [B] [mb GeV]	Error [mb/GeV]
16.1	4.6	$1.80 \times 10^{+1}$	$8.85 \times 10^{+0}$
25.2	4.6	$1.39 \times 10^{+1}$	$3.44 \times 10^{+0}$
34.4	4.6	$1.50 \times 10^{+1}$	$2.78 \times 10^{+0}$
43.6	4.6	$7.33 \times 10^{+0}$	$1.32 \times 10^{+0}$
52.8	4.6	$2.59 \times 10^{+0}$	6.72×10^{-1}
61.9	4.6	1.76×10^{-1}	1.47×10^{-1}
71.1	4.6	3.92×10^{-2}	1.32×10^{-2}

Table 7: ^{16}O -Ag backward transverse energy differential cross-section at 200 GeV/nucleon.

Γ [B] [GeV]	Bin half-width [GeV]	$d\sigma/d\Gamma$ [B] [mb GeV]	Error [mb/GeV]				
				98.6	2.3	$4.24 \times 10^{+0}$	4.71×10^{-1}
				103.2	2.3	$3.36 \times 10^{+0}$	3.30×10^{-1}
				107.8	2.3	$2.00 \times 10^{+0}$	1.25×10^{-1}
18.4	6.9	$3.36 \times 10^{+1}$	$9.45 \times 10^{+0}$	112.4	2.3	$1.43 \times 10^{+0}$	1.05×10^{-1}
32.1	6.9	$2.40 \times 10^{+1}$	$5.20 \times 10^{+0}$	117.0	2.3	7.98×10^{-1}	7.85×10^{-2}
45.9	6.9	$1.58 \times 10^{+1}$	$3.10 \times 10^{+0}$	121.6	2.3	5.47×10^{-1}	6.46×10^{-2}
57.4	4.6	$1.35 \times 10^{+1}$	$3.02 \times 10^{+0}$	126.2	2.3	3.15×10^{-1}	4.87×10^{-2}
65.4	3.4	$1.42 \times 10^{+1}$	$3.61 \times 10^{+0}$	130.8	2.3	1.18×10^{-1}	3.05×10^{-2}
72.3	3.4	$9.03 \times 10^{+0}$	$1.37 \times 10^{+0}$	135.3	2.3	8.69×10^{-2}	2.19×10^{-2}
79.1	3.4	$1.05 \times 10^{+1}$	6.08×10^{-1}	139.9	2.3	2.54×10^{-2}	4.82×10^{-3}
84.9	2.3	$7.61 \times 10^{+0}$	6.33×10^{-1}	144.5	2.3	1.41×10^{-2}	3.79×10^{-3}
89.5	2.3	$6.68 \times 10^{+0}$	5.93×10^{-1}	152.6	5.7	4.76×10^{-3}	1.35×10^{-3}
94.1	2.3	$4.77 \times 10^{+0}$	5.06×10^{-1}				

Table 8: ^{16}O -W backward transverse energy differential cross-section at 200 GeV/nucleon.

Γ [GeV]	Bin half-width [GeV]	$d\sigma/d\Gamma$ [mb/GeV]	Error [mb/GeV]				
14.9	3.4	$4.02 \times 10^{+1}$	$4.09 \times 10^{+0}$	120.4	1.1	$6.79 \times 10^{+0}$	2.00×10^{-1}
21.8	3.4	$3.01 \times 10^{+1}$	$4.15 \times 10^{+0}$	122.7	1.1	$5.93 \times 10^{+0}$	1.86×10^{-1}
28.7	3.4	$2.93 \times 10^{+1}$	$3.58 \times 10^{+0}$	125.0	1.1	$5.45 \times 10^{+0}$	1.79×10^{-1}
35.6	3.4	$2.47 \times 10^{+1}$	$2.89 \times 10^{+0}$	127.3	1.1	$4.70 \times 10^{+0}$	1.66×10^{-1}
42.4	3.4	$1.82 \times 10^{+1}$	$3.34 \times 10^{+0}$	129.6	1.1	$4.30 \times 10^{+0}$	1.58×10^{-1}
49.3	3.4	$2.02 \times 10^{+1}$	$2.03 \times 10^{+0}$	131.9	1.1	$3.77 \times 10^{+0}$	1.48×10^{-1}
56.2	3.4	$1.72 \times 10^{+1}$	$1.40 \times 10^{+0}$	134.2	1.1	$3.25 \times 10^{+0}$	1.37×10^{-1}
60.8	1.1	$1.54 \times 10^{+1}$	7.22×10^{-1}	136.5	1.1	$2.81 \times 10^{+0}$	5.08×10^{-2}
63.1	1.1	$1.28 \times 10^{+1}$	7.77×10^{-1}	138.8	1.1	$2.38 \times 10^{+0}$	4.68×10^{-2}
65.4	1.1	$1.35 \times 10^{+1}$	6.80×10^{-1}	141.1	1.1	$2.07 \times 10^{+0}$	4.37×10^{-2}
67.7	1.1	$1.48 \times 10^{+1}$	6.80×10^{-1}	143.4	1.1	$1.67 \times 10^{+0}$	3.93×10^{-2}
70.0	1.1	$1.37 \times 10^{+1}$	6.55×10^{-1}	145.7	1.1	$1.38 \times 10^{+0}$	3.58×10^{-2}
72.3	1.1	$1.37 \times 10^{+1}$	6.53×10^{-1}	148.0	1.1	$1.21 \times 10^{+0}$	3.34×10^{-2}
74.6	1.1	$1.45 \times 10^{+1}$	6.74×10^{-1}	150.3	1.1	9.78×10^{-1}	3.01×10^{-2}
76.8	1.1	$1.45 \times 10^{+1}$	6.72×10^{-1}	152.6	1.1	7.79×10^{-1}	2.68×10^{-2}
79.1	1.1	$1.26 \times 10^{+1}$	6.27×10^{-1}	154.8	1.1	6.30×10^{-1}	2.41×10^{-2}
81.4	1.1	$1.33 \times 10^{+1}$	6.44×10^{-1}	157.1	1.1	5.20×10^{-1}	2.18×10^{-2}
83.7	1.1	$1.34 \times 10^{+1}$	6.47×10^{-1}	159.4	1.1	4.11×10^{-1}	1.94×10^{-2}
86.0	1.1	$1.26 \times 10^{+1}$	6.28×10^{-1}	161.7	1.1	3.08×10^{-1}	1.67×10^{-2}
88.3	1.1	$1.20 \times 10^{+1}$	6.13×10^{-1}	164.0	1.1	2.31×10^{-1}	1.44×10^{-2}
90.6	1.1	$1.15 \times 10^{+1}$	5.99×10^{-1}	166.3	1.1	1.81×10^{-1}	1.27×10^{-2}
92.9	1.1	$1.20 \times 10^{+1}$	6.12×10^{-1}	168.6	1.1	1.37×10^{-1}	1.10×10^{-2}
95.2	1.1	$1.16 \times 10^{+1}$	6.03×10^{-1}	170.9	1.1	1.03×10^{-1}	5.93×10^{-3}
97.5	1.1	$1.22 \times 10^{+1}$	6.19×10^{-1}	173.2	1.1	7.35×10^{-2}	4.96×10^{-3}
99.8	1.1	$1.10 \times 10^{+1}$	2.54×10^{-1}	175.5	1.1	5.82×10^{-2}	4.39×10^{-3}
102.1	1.1	$1.06 \times 10^{+1}$	2.50×10^{-1}	177.8	1.1	4.07×10^{-2}	3.64×10^{-3}
104.4	1.1	$1.04 \times 10^{+1}$	2.48×10^{-1}	180.1	1.1	3.20×10^{-2}	3.21×10^{-3}
106.7	1.1	$9.71 \times 10^{+0}$	2.39×10^{-1}	182.4	1.1	2.11×10^{-2}	2.60×10^{-3}
109.0	1.1	$8.98 \times 10^{+0}$	2.30×10^{-1}	184.7	1.1	1.46×10^{-2}	2.14×10^{-3}
111.3	1.1	$8.65 \times 10^{+0}$	2.26×10^{-1}	187.0	1.1	1.22×10^{-2}	1.96×10^{-3}
113.6	1.1	$7.96 \times 10^{+0}$	2.16×10^{-1}	190.4	2.3	5.87×10^{-3}	9.54×10^{-4}
115.8	1.1	$7.75 \times 10^{+0}$	2.13×10^{-1}	195.0	2.3	2.89×10^{-3}	6.79×10^{-4}
118.1	1.1	$6.91 \times 10^{+0}$	2.02×10^{-1}	200.7	3.4	1.33×10^{-3}	4.02×10^{-4}

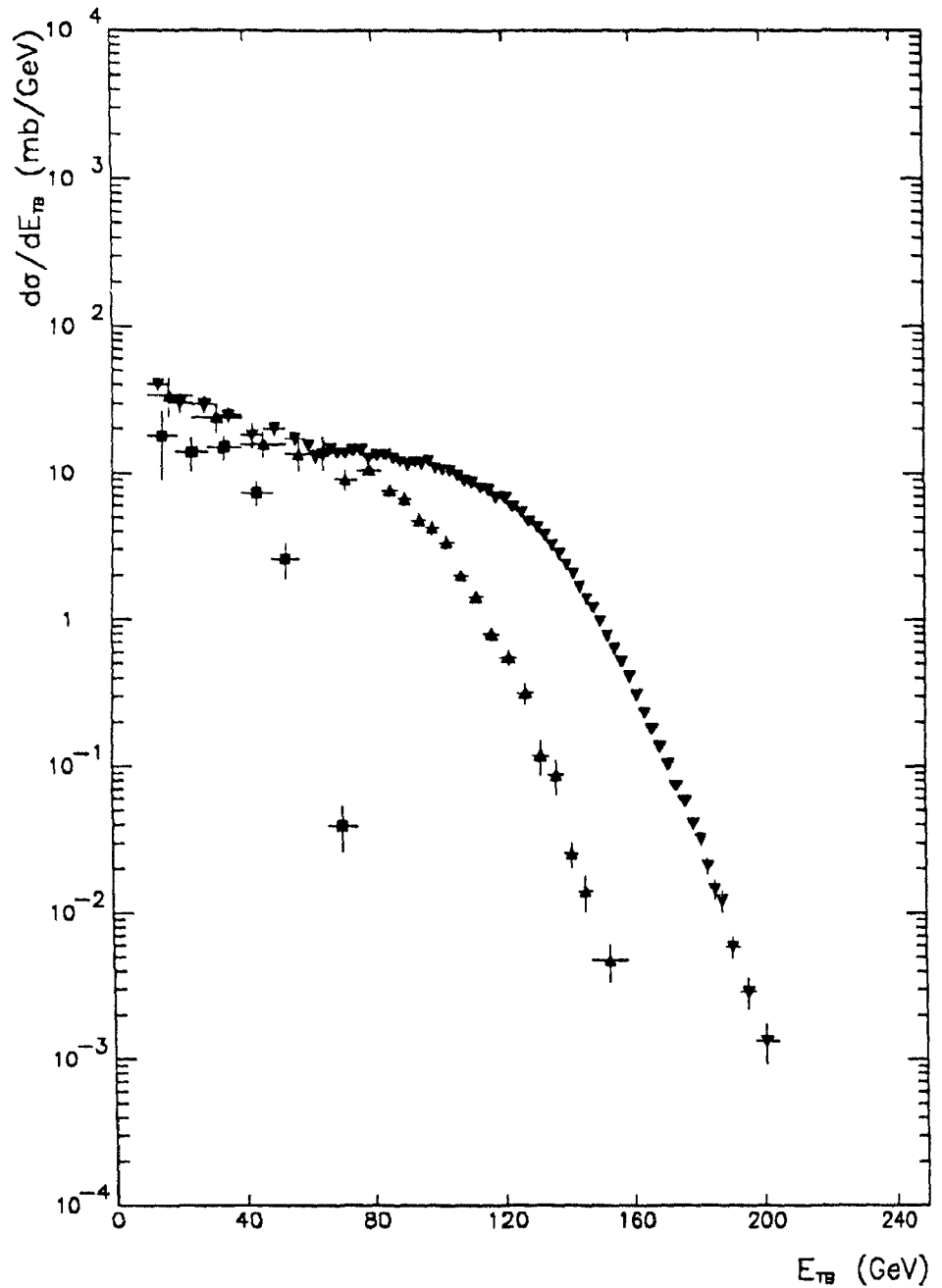


Figure 43: Transverse energy differential cross-section measured in $-0.1 < \eta < 2.9$ for a 200 GeV/nucleon ^{16}O beam. The distributions $d\sigma/dE_{TB}$ are shown for Al (■), Ag (▲), and W (▼) targets. E_{TB} is defined as $\sum E_i^{*u} \sin\theta$ where $E_i^{*u} = \sqrt{p^2 + m^2}$ except for nucleons where $E_i^{*u} = \sqrt{p^2 + m^2} - m$.

4.2.4 200 GeV/nucleon sulfur

The differential cross-sections versus E_{TB} are listed for 200 GeV/nucleon ^{32}S projectiles against Al, Ag, W, Pt, Pb, and U targets in Table 9 to Table 14, and shown in Figure 44. These data have been published in [86].

Table 9: ^{32}S -Al backward transverse energy differential cross-section at 200 GeV/nucleon.

E_{TB} [GeV]	Bin half-width [GeV]	$d\sigma/dE_{TB}$ [mb/GeV]	Error [mb/GeV]
11.5	2.3	$3.14 \times 10^{+1}$	$4.22 \times 10^{+0}$
16.1	2.3	$3.90 \times 10^{+1}$	$4.47 \times 10^{+0}$
20.6	2.3	$2.65 \times 10^{+1}$	$4.64 \times 10^{+0}$
25.2	2.3	$2.85 \times 10^{+1}$	$4.32 \times 10^{+0}$
29.8	2.3	$2.58 \times 10^{+1}$	$4.14 \times 10^{+0}$
34.4	2.3	$2.56 \times 10^{+1}$	$3.53 \times 10^{+0}$
39.0	2.3	$2.32 \times 10^{+1}$	$3.09 \times 10^{+0}$
43.6	2.3	$1.43 \times 10^{+1}$	$2.53 \times 10^{+0}$
48.2	2.3	$1.45 \times 10^{+1}$	$2.14 \times 10^{+0}$
52.8	2.3	$1.13 \times 10^{+1}$	$2.12 \times 10^{+0}$
57.4	2.3	$9.06 \times 10^{+0}$	$1.76 \times 10^{+0}$
61.9	2.3	$7.77 \times 10^{+0}$	$1.41 \times 10^{+0}$
66.5	2.3	$7.94 \times 10^{+0}$	$1.66 \times 10^{+0}$
71.1	2.3	$3.81 \times 10^{+0}$	$1.06 \times 10^{+0}$
75.7	2.3	$1.89 \times 10^{+0}$	6.78×10^{-1}
80.3	2.3	6.26×10^{-1}	2.27×10^{-1}
84.9	2.3	2.34×10^{-1}	2.00×10^{-1}
89.5	2.3	4.77×10^{-2}	2.77×10^{-2}
94.1	2.3	2.74×10^{-2}	2.19×10^{-2}

Table 10: $^{32}\text{S-Ag}$ backward transverse energy differential cross-section at 200 GeV/nucleon.

$E_{\text{T}B}$ [GeV]	Bin half-width [GeV]	$d\sigma/dE_{\text{T}B}$ [mb/GeV]	Error [mb/GeV]				
9.2	4.6	$1.14 \times 10^{+2}$	$4.29 \times 10^{+1}$				
18.4	4.6	$1.46 \times 10^{+1}$	$2.54 \times 10^{+0}$	137.6	4.6	$4.52 \times 10^{+0}$	2.07×10^{-1}
27.5	4.6	$1.16 \times 10^{+1}$	$2.40 \times 10^{+0}$	146.8	4.6	$3.66 \times 10^{+0}$	1.83×10^{-1}
36.7	4.6	$9.88 \times 10^{+0}$	$1.96 \times 10^{+0}$	156.0	4.6	$3.12 \times 10^{+0}$	1.59×10^{-1}
45.9	4.6	$8.25 \times 10^{+0}$	$1.82 \times 10^{+0}$	165.2	4.6	$2.01 \times 10^{+0}$	9.22×10^{-2}
55.1	4.6	$7.31 \times 10^{+0}$	$1.69 \times 10^{+0}$	174.3	4.6	$1.07 \times 10^{+0}$	3.69×10^{-2}
73.4	13.7	$7.21 \times 10^{+0}$	7.40×10^{-1}	183.5	4.6	5.48×10^{-1}	2.54×10^{-2}
91.8	4.6	$7.86 \times 10^{+0}$	5.39×10^{-1}	192.7	4.6	2.44×10^{-1}	1.19×10^{-2}
100.9	4.6	$7.29 \times 10^{+0}$	2.59×10^{-1}	201.9	4.6	7.41×10^{-2}	7.07×10^{-3}
110.1	4.6	$6.40 \times 10^{+0}$	3.72×10^{-1}	211.0	4.6	2.72×10^{-2}	4.28×10^{-3}
119.3	4.6	$5.56 \times 10^{+0}$	2.44×10^{-1}	220.2	4.6	3.34×10^{-3}	1.67×10^{-3}
128.5	4.6	$5.54 \times 10^{+0}$	2.28×10^{-1}	227.1	2.3	2.29×10^{-3}	2.29×10^{-3}

Table 11: $^{32}\text{S-W}$ backward transverse energy differential cross-section at 200 GeV/nucleon.

$E_{\text{T}B}$ [GeV]	Bin half-width [GeV]	$d\sigma/dE_{\text{T}B}$ [mb/GeV]	Error [mb/GeV]				
6.9	2.3	$4.06 \times 10^{+1}$	$8.05 \times 10^{+0}$	158.3	6.9	$6.72 \times 10^{+0}$	8.23×10^{-2}
11.5	2.3	$2.57 \times 10^{+1}$	$2.99 \times 10^{+0}$	172.1	6.9	$6.15 \times 10^{+0}$	7.86×10^{-2}
20.6	6.9	$2.34 \times 10^{+1}$	$1.75 \times 10^{+0}$	185.8	6.9	$5.07 \times 10^{+0}$	3.46×10^{-2}
34.4	6.9	$1.95 \times 10^{+1}$	$1.49 \times 10^{+0}$	199.6	6.9	$3.80 \times 10^{+0}$	2.88×10^{-2}
48.2	6.9	$1.23 \times 10^{+1}$	$1.16 \times 10^{+0}$	213.3	6.9	$2.47 \times 10^{+0}$	2.30×10^{-2}
61.9	6.9	$1.11 \times 10^{+1}$	9.07×10^{-1}	227.1	6.9	$1.33 \times 10^{+0}$	1.71×10^{-2}
75.7	6.9	$1.21 \times 10^{+1}$	7.44×10^{-1}	240.9	6.9	6.08×10^{-1}	1.15×10^{-2}
89.5	6.9	$1.10 \times 10^{+1}$	7.90×10^{-1}	254.6	6.9	2.22×10^{-1}	7.03×10^{-3}
103.2	6.9	$7.93 \times 10^{+0}$	2.74×10^{-1}	268.4	6.9	6.75×10^{-2}	3.91×10^{-3}
117.0	6.9	$7.64 \times 10^{+0}$	1.19×10^{-1}	282.2	6.9	1.76×10^{-2}	2.58×10^{-3}
130.8	6.9	$7.38 \times 10^{+0}$	8.58×10^{-2}	297.5	6.9	3.15×10^{-3}	1.36×10^{-3}
144.5	6.9	$6.94 \times 10^{+0}$	8.32×10^{-2}	309.7	2.3	6.41×10^{-4}	6.41×10^{-4}

Table 12: ^{32}S -Pt backward transverse energy differential cross-section at 200 GeV/nucleon.

E_{TB} [GeV]	Bin half-width [GeV]	$d\sigma/dE_{\text{TB}}$ [mb/GeV]	Error [mb/GeV]				
11.5	6.9	$4.20 \times 10^{+1}$	$5.53 \times 10^{+0}$	162.9	6.9	$7.11 \times 10^{+0}$	3.06×10^{-1}
25.2	6.9	$1.33 \times 10^{+1}$	$3.05 \times 10^{+0}$	176.6	6.9	$6.93 \times 10^{+0}$	3.03×10^{-1}
39.0	6.9	$1.70 \times 10^{+1}$	$2.95 \times 10^{+0}$	190.4	6.9	$6.25 \times 10^{+0}$	2.49×10^{-1}
52.8	6.9	$1.66 \times 10^{+1}$	$2.62 \times 10^{+0}$	204.2	6.9	$4.79 \times 10^{+0}$	1.52×10^{-1}
66.5	6.9	$1.47 \times 10^{+1}$	$2.35 \times 10^{+0}$	217.9	6.9	$3.41 \times 10^{+0}$	9.50×10^{-2}
80.3	6.9	$1.38 \times 10^{+1}$	$2.17 \times 10^{+0}$	231.7	6.9	$1.81 \times 10^{+0}$	6.90×10^{-2}
94.1	6.9	$1.09 \times 10^{+1}$	$1.97 \times 10^{+0}$	245.5	6.9	7.85×10^{-1}	4.22×10^{-2}
107.8	6.9	$8.88 \times 10^{+0}$	9.94×10^{-1}	259.2	6.9	2.42×10^{-1}	1.26×10^{-2}
121.6	6.9	$8.77 \times 10^{+0}$	3.46×10^{-1}	273.0	6.9	7.06×10^{-2}	6.92×10^{-3}
135.3	6.9	$7.96 \times 10^{+0}$	3.24×10^{-1}	286.7	6.9	1.38×10^{-2}	2.88×10^{-3}
149.1	6.9	$8.19 \times 10^{+0}$	3.29×10^{-1}	305.1	6.9	1.67×10^{-3}	9.62×10^{-4}

Table 13: ^{32}S -Pb backward transverse energy differential cross-section at 200 GeV/nucleon.

E_{TB} [GeV]	Bin half-width [GeV]	$d\sigma/dE_{\text{TB}}$ [mb/GeV]	Error [mb/GeV]				
26.1	11.0	$2.42 \times 10^{+1}$	$1.39 \times 10^{+0}$	167.6	6.9	$7.69 \times 10^{+0}$	2.30×10^{-1}
43.8	6.9	$1.65 \times 10^{+1}$	$1.17 \times 10^{+0}$	181.5	6.9	$7.29 \times 10^{+0}$	2.30×10^{-1}
57.5	6.9	$1.59 \times 10^{+1}$	$1.01 \times 10^{+0}$	195.3	6.9	$6.41 \times 10^{+0}$	2.09×10^{-1}
71.6	6.9	$1.35 \times 10^{+1}$	8.98×10^{-1}	209.0	6.9	$4.98 \times 10^{+0}$	1.77×10^{-1}
85.2	6.9	$1.11 \times 10^{+1}$	7.92×10^{-1}	222.7	6.9	$3.46 \times 10^{+0}$	6.35×10^{-2}
98.9	6.9	$1.09 \times 10^{+1}$	7.86×10^{-1}	236.5	6.9	$1.87 \times 10^{+0}$	4.61×10^{-2}
112.5	6.9	$9.70 \times 10^{+0}$	7.93×10^{-1}	250.4	6.9	8.21×10^{-1}	2.95×10^{-2}
126.6	6.9	$9.16 \times 10^{+0}$	2.59×10^{-1}	264.1	6.9	2.50×10^{-1}	1.63×10^{-2}
140.3	6.9	$8.58 \times 10^{+0}$	2.37×10^{-1}	277.7	6.9	5.19×10^{-2}	7.19×10^{-3}
153.9	6.9	$7.57 \times 10^{+0}$	2.19×10^{-1}	285.6	1.9	3.47×10^{-2}	1.13×10^{-2}

Table 14: ^{32}S -U backward transverse energy differential cross-section at 200 GeV/nucleon.

E_{TB} [GeV]	Bin half-width [GeV]	$d\sigma/dE_{\text{TB}}$ [mb/GeV]	Error [mb/GeV]
183.5	4.6	$8.59 \times 10^{+0}$	5.06×10^{-1}
192.7	4.6	$7.04 \times 10^{+0}$	3.59×10^{-1}
201.9	4.6	$6.69 \times 10^{+0}$	2.00×10^{-1}
211.0	4.6	$5.87 \times 10^{+0}$	2.51×10^{-1}
220.2	4.6	$4.89 \times 10^{+0}$	1.71×10^{-1}
229.4	4.6	$3.87 \times 10^{+0}$	1.52×10^{-1}
238.6	4.6	$2.93 \times 10^{+0}$	1.32×10^{-1}
247.8	4.6	$2.19 \times 10^{+0}$	5.71×10^{-2}
256.9	4.6	$1.52 \times 10^{+0}$	4.73×10^{-2}
266.1	4.6	9.91×10^{-1}	3.81×10^{-2}
275.3	4.6	6.12×10^{-1}	2.99×10^{-2}
284.5	4.6	3.68×10^{-1}	2.32×10^{-2}
293.6	4.6	1.95×10^{-1}	1.67×10^{-2}
302.8	4.6	9.58×10^{-2}	1.18×10^{-2}
312.0	4.6	4.37×10^{-2}	7.85×10^{-3}
321.2	4.6	1.88×10^{-2}	5.95×10^{-3}
330.3	4.6	6.76×10^{-3}	3.08×10^{-3}
339.5	4.6	5.46×10^{-3}	2.73×10^{-3}

These differential cross-sections were obtained with statistics of 19000, 22000, 264000, 24000, 15000, and 23000 events for a total flux of 5.11×10^8 , 1.17×10^8 , 3.11×10^8 , 7.3×10^7 , 1.11×10^8 , 5.2×10^7 incident nuclei traversing targets of thicknesses of 1.0mm Al, 0.3mm Ag, 0.2mm W, 0.25mm Pt, 0.2mm Pb and 0.32mm U respectively.

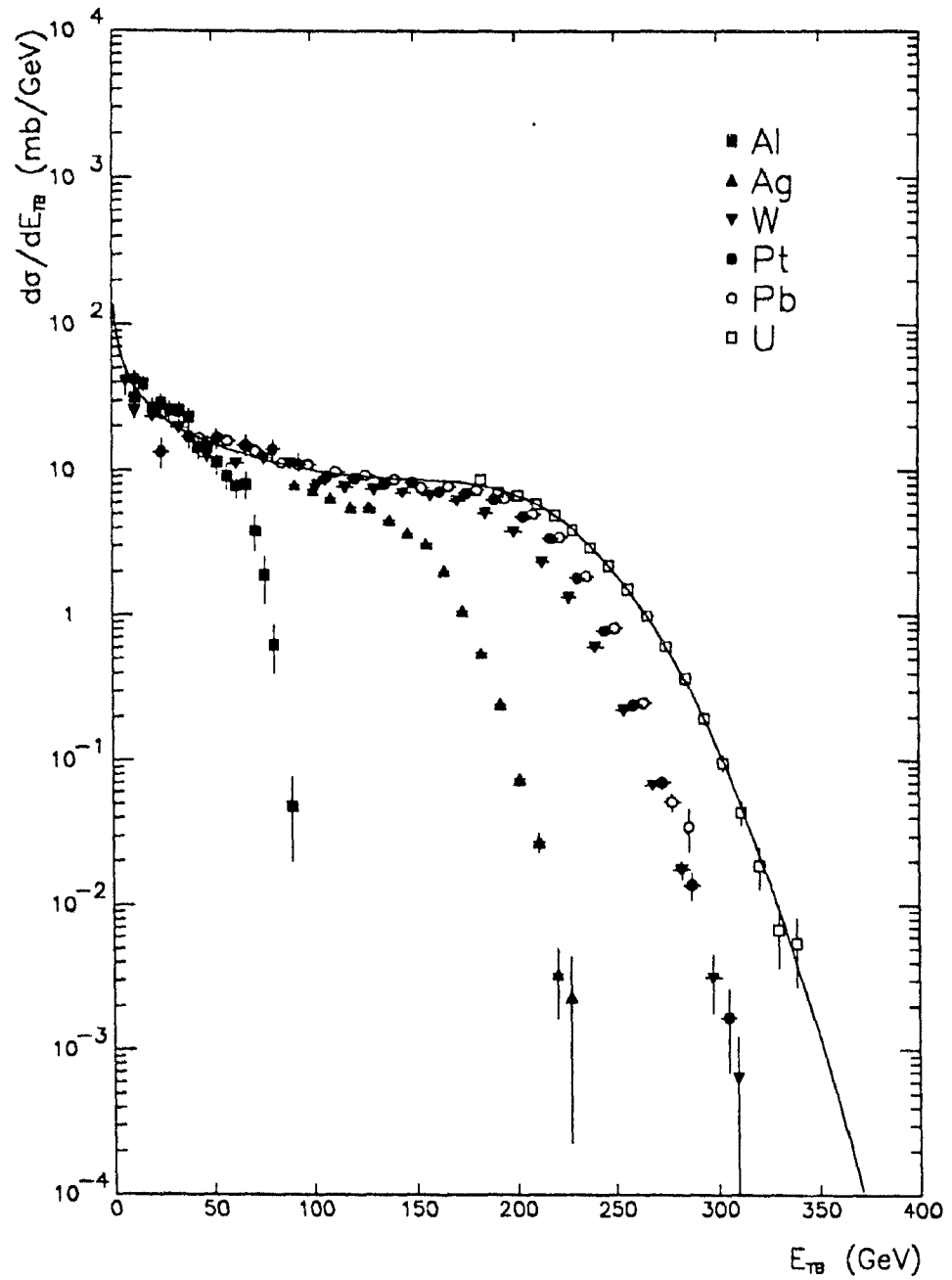


Figure 44: Transverse energy differential cross-section measured in $-0.1 < \eta < 2.9$ for a 200 GeV/nucleon ^{32}S beam. The distributions $d\sigma/dE_{\text{TB}}$ are shown for Al, Ag, W, Pt, Pb, and U targets. The line indicates the parametrization in terms of ε_0 and ω for the case of U.

In the backward pseudorapidity region, the transverse energy production with a ^{32}S projectile is about 1.70 the transverse energy production with a ^{16}O projectile at the same energy per nucleon. The expectation of the NCM is that the average central collision of a ^{32}S should have twice the transverse energy as the average central ^{16}O collision. The fluctuations appear slightly reduced for ^{32}S compared to ^{16}O .

4.2.5 Sulfur cross-sections for E_T in a large domain of η

Completing the measurement of the transverse energy in the backward region of pseudorapidity $-0.1 < \eta < 2.9$ by a measurement of the transverse energy in the forward region $2.9 < \eta < 5.5$, we obtain a measurement of the total transverse energy (The transverse energy at $\eta < -0.1$ or at $\eta > 5.5$ is very small and can safely be neglected) Thus, in the next discussion, E_T is the transverse energy in the pseudorapidity region $-0.1 < \eta < 5.5$ For 200 GeV nucleon ^{32}S projectiles against Al, Ag, W, Pt, Pb and U targets, we show the differential cross-sections versus E_T in Table 15 to Table 20, and in Figure 45. The data shown here are reported in [87].

Table 15: ^{32}S -Al transverse energy differential cross-section at 200 GeV/nucleon.

E_T [GeV]	Bin half-width [GeV]	$d\sigma/dE_T$ [mb/GeV]	Error [mb/GeV]				
36.5	2.4	$9.94 \times 10^{+0}$	4.68×10^{-1}	119.2	2.4	$3.74 \times 10^{+0}$	2.38×10^{-1}
41.4	2.4	$9.07 \times 10^{+0}$	4.52×10^{-1}	124.1	2.4	$2.98 \times 10^{+0}$	2.11×10^{-1}
46.2	2.4	$9.13 \times 10^{+0}$	4.44×10^{-1}	129.0	2.4	$2.94 \times 10^{+0}$	2.07×10^{-1}
51.1	2.4	$9.27 \times 10^{+0}$	4.35×10^{-1}	133.8	2.4	$2.41 \times 10^{+0}$	1.87×10^{-1}
56.0	2.4	$8.62 \times 10^{+0}$	4.16×10^{-1}	138.7	2.4	$1.76 \times 10^{+0}$	1.72×10^{-1}
60.8	2.4	$8.75 \times 10^{+0}$	4.12×10^{-1}	143.6	2.4	$1.92 \times 10^{+0}$	1.72×10^{-1}
65.7	2.4	$7.07 \times 10^{+0}$	3.77×10^{-1}	148.4	2.4	$1.44 \times 10^{+0}$	1.49×10^{-1}
70.6	2.4	$6.87 \times 10^{+0}$	3.71×10^{-1}	153.3	2.4	$1.02 \times 10^{+0}$	1.24×10^{-1}
75.4	2.4	$6.75 \times 10^{+0}$	3.57×10^{-1}	158.2	2.4	5.31×10^{-1}	8.87×10^{-2}
80.3	2.4	$5.41 \times 10^{+0}$	3.26×10^{-1}	163.0	2.4	4.90×10^{-1}	8.66×10^{-2}
85.2	2.4	$5.65 \times 10^{+0}$	3.20×10^{-1}	167.9	2.4	3.99×10^{-1}	8.99×10^{-2}
90.0	2.4	$5.69 \times 10^{+0}$	3.16×10^{-1}	172.8	2.4	2.40×10^{-1}	7.43×10^{-2}
94.9	2.4	$4.96 \times 10^{+0}$	2.87×10^{-1}	177.6	2.4	1.15×10^{-1}	4.19×10^{-2}
99.8	2.4	$4.81 \times 10^{+0}$	2.79×10^{-1}	182.5	2.4	6.07×10^{-2}	7.83×10^{-3}
104.6	2.4	$4.74 \times 10^{+0}$	2.70×10^{-1}	187.4	2.4	2.92×10^{-2}	6.21×10^{-3}
109.5	2.4	$4.50 \times 10^{+0}$	2.61×10^{-1}	192.2	2.4	1.23×10^{-2}	4.74×10^{-3}
114.4	2.4	$3.97 \times 10^{+0}$	2.45×10^{-1}	197.1	2.4	4.08×10^{-3}	3.71×10^{-3}

Table 16: ^{32}S -Ag transverse energy differential cross-section at 200 GeV/nucleon.

E_T [GeV]	Bin half-width [GeV]	$d\sigma/dE_T$ [mb/GeV]	Error [mb/GeV]
4.7	4.7	$3.30 \times 10^{+2}$	$2.58 \times 10^{+2}$
14.1	4.7	$8.22 \times 10^{+1}$	$6.59 \times 10^{+1}$
23.5	4.7	$2.36 \times 10^{+1}$	$3.07 \times 10^{+0}$
38.1	9.4	$1.54 \times 10^{+1}$	$1.95 \times 10^{+0}$
51.7	4.7	$8.91 \times 10^{+0}$	$2.69 \times 10^{+0}$
61.1	4.7	$9.53 \times 10^{+0}$	$2.50 \times 10^{+0}$
79.9	14.1	$4.83 \times 10^{+0}$	$1.17 \times 10^{+0}$
108.2	14.1	$2.76 \times 10^{+0}$	8.78×10^{-1}
127.0	4.7	$6.02 \times 10^{+0}$	$1.49 \times 10^{+0}$
145.8	14.1	$4.40 \times 10^{+0}$	7.80×10^{-1}
164.6	4.7	$3.64 \times 10^{+0}$	8.83×10^{-1}
174.0	4.7	$4.31 \times 10^{+0}$	9.89×10^{-1}
183.4	4.7	$4.65 \times 10^{+0}$	$1.10 \times 10^{+0}$
192.8	4.7	$4.15 \times 10^{+0}$	2.08×10^{-1}
202.2	4.7	$4.15 \times 10^{+0}$	2.08×10^{-1}
211.6	4.7	$4.14 \times 10^{+0}$	2.08×10^{-1}
221.0	4.7	$3.65 \times 10^{+0}$	1.96×10^{-1}
230.4	4.7	$3.51 \times 10^{+0}$	1.92×10^{-1}
239.8	4.7	$3.17 \times 10^{+0}$	1.83×10^{-1}
249.2	4.7	$2.97 \times 10^{+0}$	1.76×10^{-1}
258.6	4.7	$2.72 \times 10^{+0}$	1.72×10^{-1}
268.1	4.7	$2.66 \times 10^{+0}$	1.67×10^{-1}
277.5	4.7	$1.92 \times 10^{+0}$	1.42×10^{-1}
286.9	4.7	$1.65 \times 10^{+0}$	1.31×10^{-1}
296.3	4.7	9.89×10^{-1}	1.01×10^{-1}
305.7	4.7	5.40×10^{-1}	7.43×10^{-2}
315.1	4.7	3.48×10^{-1}	2.24×10^{-2}
324.5	4.7	1.78×10^{-1}	1.58×10^{-2}
333.9	4.7	7.33×10^{-2}	9.88×10^{-3}
343.3	4.7	2.33×10^{-2}	4.01×10^{-3}
352.7	4.7	8.69×10^{-3}	2.25×10^{-3}
362.1	4.7	1.33×10^{-3}	9.41×10^{-4}

Table 17: ^{32}S -W transverse energy differential cross-section at 200 GeV.nucleon.

E_T [GeV]	Bin half-width [GeV]	$d\sigma/dE_T$ [mb/GeV]	Error [mb/GeV]
32.9	4.7	1.25×10^{-1}	1.75×10^{-0}
42.3	4.7	1.58×10^{-1}	1.45×10^{-0}
51.7	4.7	1.13×10^{-1}	1.45×10^{-0}
61.1	4.7	1.00×10^{-1}	1.32×10^{-0}
70.5	4.7	1.06×10^{-1}	1.24×10^{-0}
79.9	4.7	8.97×10^{-2}	1.00×10^{-0}
89.4	4.7	5.63×10^{-2}	9.91×10^{-1}
98.8	4.7	7.10×10^{-2}	8.68×10^{-1}
108.2	4.7	6.02×10^{-2}	7.87×10^{-1}
117.6	4.7	7.11×10^{-2}	6.82×10^{-1}
127.0	4.7	7.66×10^{-2}	4.75×10^{-1}
136.4	4.7	6.78×10^{-2}	3.68×10^{-1}
145.8	4.7	7.38×10^{-2}	3.25×10^{-1}
155.2	4.7	7.00×10^{-2}	3.15×10^{-1}
164.6	4.7	6.76×10^{-2}	3.15×10^{-1}
174.0	4.7	6.19×10^{-2}	3.02×10^{-1}
183.4	4.7	5.98×10^{-2}	2.96×10^{-1}
192.8	4.7	6.18×10^{-2}	3.02×10^{-1}
202.2	4.7	6.06×10^{-2}	3.00×10^{-1}
211.6	4.7	5.14×10^{-2}	1.11×10^{-1}
221.0	4.7	4.61×10^{-2}	7.95×10^{-2}
230.4	4.7	4.67×10^{-2}	7.93×10^{-2}
239.8	4.7	5.10×10^{-2}	7.11×10^{-2}
249.2	4.7	4.98×10^{-2}	7.02×10^{-2}
258.6	4.7	4.93×10^{-2}	6.97×10^{-2}
268.1	4.7	4.99×10^{-2}	7.02×10^{-2}
277.5	4.7	4.96×10^{-2}	7.05×10^{-2}
286.9	4.7	4.81×10^{-2}	6.90×10^{-2}
296.3	4.7	4.66×10^{-2}	6.77×10^{-2}
305.7	4.7	4.32×10^{-2}	6.49×10^{-2}
315.1	4.7	4.06×10^{-2}	6.32×10^{-2}
324.5	4.7	3.70×10^{-2}	4.17×10^{-2}
333.9	4.7	3.14×10^{-2}	3.85×10^{-2}
343.3	4.7	2.46×10^{-2}	2.71×10^{-2}
352.7	4.7	1.79×10^{-2}	2.32×10^{-2}
362.1	4.7	1.18×10^{-2}	1.33×10^{-2}
371.5	4.7	7.95×10^{-3}	1.08×10^{-2}
380.9	4.7	4.73×10^{-3}	8.32×10^{-3}
390.3	4.7	2.79×10^{-3}	6.38×10^{-3}
399.7	4.7	1.34×10^{-3}	4.38×10^{-3}
409.1	4.7	6.12×10^{-4}	2.93×10^{-3}
418.5	4.7	2.84×10^{-4}	2.03×10^{-3}
427.9	4.7	1.28×10^{-4}	1.38×10^{-3}
437.4	4.7	3.48×10^{-5}	7.47×10^{-4}
446.8	4.7	1.49×10^{-5}	8.65×10^{-4}
456.2	4.7	5.80×10^{-6}	3.36×10^{-4}

Table 18 ^{32}S -Pt transverse energy differential cross-section at 200 GeV/nucleon

Γ_T [GeV]	Bin half-width [GeV]	$d\sigma/dl_T$ [mb GeV]	Error [mb GeV]
32.9	14.1	1.39×10^{-1}	7.63×10^{-2}
61.1	14.1	8.23×10^{-2}	1.77×10^{-2}
89.4	14.1	9.31×10^{-3}	1.54×10^{-3}
117.6	14.1	9.29×10^{-4}	1.35×10^{-4}
145.8	14.1	6.30×10^{-5}	1.10×10^{-5}
174.0	14.1	6.40×10^{-6}	1.03×10^{-6}
202.2	14.1	6.81×10^{-7}	1.05×10^{-7}
221.0	4.7	5.93×10^{-7}	3.38×10^{-8}
230.4	4.7	5.93×10^{-8}	3.38×10^{-9}
239.8	4.7	5.30×10^{-9}	3.19×10^{-10}
249.2	4.7	4.53×10^{-10}	2.95×10^{-11}
258.6	4.7	5.43×10^{-11}	3.23×10^{-12}
268.1	4.7	5.51×10^{-12}	3.26×10^{-13}
277.5	4.7	4.86×10^{-13}	3.06×10^{-14}
286.9	4.7	5.27×10^{-14}	3.19×10^{-15}
296.3	4.7	5.25×10^{-15}	3.18×10^{-16}
305.7	4.7	4.66×10^{-16}	3.00×10^{-17}
315.1	4.7	5.26×10^{-17}	3.19×10^{-18}
324.5	4.7	4.71×10^{-18}	3.02×10^{-19}
333.9	4.7	3.72×10^{-19}	2.68×10^{-20}
343.3	4.7	3.61×10^{-20}	2.64×10^{-21}
352.7	4.7	2.85×10^{-21}	1.05×10^{-22}
362.1	4.7	2.07×10^{-22}	8.89×10^{-24}
371.5	4.7	1.34×10^{-23}	7.12×10^{-25}
380.9	4.7	8.63×10^{-25}	5.68×10^{-26}
390.3	4.7	4.56×10^{-26}	4.10×10^{-27}
399.7	4.7	2.35×10^{-27}	2.91×10^{-28}
409.1	4.7	1.56×10^{-28}	2.34×10^{-29}
418.5	4.7	4.83×10^{-30}	1.29×10^{-30}
427.9	4.7	1.42×10^{-31}	3.46×10^{-32}
437.4	4.7	8.12×10^{-33}	2.57×10^{-33}
446.8	4.7	3.14×10^{-34}	1.57×10^{-34}

Table 19: ^{32}S -Pb transverse energy differential cross-section at 200 GeV/nucleon.

E_T [GeV]	Bin half-width [GeV]	$d\sigma/dE_T$ [mb/GeV]	Error [mb/GeV]
44.2	4.9	$1.73 \times 10^{+1}$	$1.83 \times 10^{+0}$
54.1	4.9	$1.22 \times 10^{+1}$	$1.43 \times 10^{+0}$
73.7	14.7	$9.41 \times 10^{+0}$	7.35×10^{-1}
103.2	14.7	$8.53 \times 10^{+0}$	5.98×10^{-1}
132.7	14.7	$6.94 \times 10^{+0}$	5.17×10^{-1}
162.2	14.7	$7.06 \times 10^{+0}$	4.77×10^{-1}
191.7	14.7	$5.79 \times 10^{+0}$	4.21×10^{-1}
211.4	4.9	$6.40 \times 10^{+0}$	7.64×10^{-1}
221.2	4.9	$6.29 \times 10^{+0}$	7.93×10^{-1}
231.0	4.9	$5.40 \times 10^{+0}$	7.11×10^{-1}
240.9	4.9	$5.79 \times 10^{+0}$	2.49×10^{-1}
250.7	4.9	$5.73 \times 10^{+0}$	2.48×10^{-1}
260.5	4.9	$5.38 \times 10^{+0}$	2.40×10^{-1}
270.4	4.9	$5.23 \times 10^{+0}$	2.37×10^{-1}
280.2	4.9	$5.57 \times 10^{+0}$	2.47×10^{-1}
290.0	4.9	$5.60 \times 10^{+0}$	2.46×10^{-1}
299.9	4.9	$4.95 \times 10^{+0}$	2.31×10^{-1}
309.7	4.9	$5.59 \times 10^{+0}$	2.45×10^{-1}
319.5	4.9	$5.37 \times 10^{+0}$	2.41×10^{-1}
329.4	4.9	$4.61 \times 10^{+0}$	2.23×10^{-1}
339.2	4.9	$4.35 \times 10^{+0}$	2.17×10^{-1}
349.0	4.9	$3.60 \times 10^{+0}$	1.97×10^{-1}
358.9	4.9	$2.79 \times 10^{+0}$	1.73×10^{-1}
368.7	4.9	$1.79 \times 10^{+0}$	1.38×10^{-1}
378.5	4.9	$1.29 \times 10^{+0}$	1.21×10^{-1}
388.4	4.9	8.01×10^{-1}	4.02×10^{-2}
398.2	4.9	3.34×10^{-1}	2.41×10^{-2}
408.0	4.9	1.34×10^{-1}	1.56×10^{-2}
417.9	4.9	5.20×10^{-2}	9.05×10^{-3}
427.7	4.9	2.30×10^{-2}	6.31×10^{-3}
442.4	9.8	9.30×10^{-3}	9.30×10^{-3}

Table 20 ^{238}U transverse energy differential cross-section at 200 GeV/nucleon

E_T [GeV]	Bin half-width [GeV]	$d\sigma/dE_T$ [mb GeV]	Error [mb GeV]				
37.6	9.4	9.72×10^{-10}	4.93×10^{-10}	286.9	4.7	5.55×10^{-10}	4.06×10^{-10}
51.7	4.7	1.20×10^{-9}	6.39×10^{-10}	296.3	4.7	5.52×10^{-10}	4.00×10^{-10}
61.1	4.7	6.80×10^{-10}	6.67×10^{-10}	305.7	4.7	5.79×10^{-10}	4.10×10^{-10}
70.5	4.7	9.36×10^{-10}	4.91×10^{-10}	315.1	4.7	5.88×10^{-10}	4.14×10^{-10}
79.9	4.7	4.62×10^{-9}	3.96×10^{-10}	324.5	4.7	5.47×10^{-10}	3.99×10^{-10}
98.8	14.1	5.64×10^{-9}	2.46×10^{-10}	333.9	4.7	4.43×10^{-10}	3.59×10^{-10}
117.6	4.7	6.20×10^{-9}	3.07×10^{-10}	343.3	4.7	4.92×10^{-10}	3.78×10^{-10}
136.4	14.1	4.12×10^{-9}	2.95×10^{-10}	352.7	4.7	4.04×10^{-10}	1.53×10^{-10}
155.2	4.7	3.82×10^{-9}	2.29×10^{-10}	362.1	4.7	3.57×10^{-10}	1.44×10^{-10}
164.6	4.7	9.24×10^{-10}	2.86×10^{-10}	371.5	4.7	2.62×10^{-10}	1.23×10^{-10}
174.0	4.7	5.65×10^{-9}	2.34×10^{-10}	380.9	4.7	2.11×10^{-10}	1.10×10^{-10}
183.4	4.7	5.95×10^{-9}	2.25×10^{-10}	390.3	4.7	1.60×10^{-10}	9.60×10^{-11}
192.8	4.7	6.83×10^{-9}	2.33×10^{-10}	399.7	4.7	1.18×10^{-10}	8.23×10^{-11}
202.2	4.7	3.36×10^{-9}	1.64×10^{-10}	409.1	4.7	6.82×10^{-11}	6.22×10^{-11}
211.6	4.7	5.68×10^{-9}	2.05×10^{-10}	418.5	4.7	4.43×10^{-11}	2.50×10^{-11}
221.0	4.7	6.84×10^{-9}	4.45×10^{-11}	427.9	4.7	2.61×10^{-11}	1.91×10^{-11}
230.4	4.7	5.49×10^{-9}	4.16×10^{-11}	437.4	4.7	1.73×10^{-11}	1.55×10^{-11}
239.8	4.7	5.77×10^{-9}	4.14×10^{-11}	446.8	4.7	8.90×10^{-12}	1.10×10^{-11}
249.2	4.7	5.65×10^{-9}	4.05×10^{-11}	456.2	4.7	4.33×10^{-12}	7.65×10^{-12}
258.6	4.7	4.99×10^{-9}	3.85×10^{-11}	465.6	4.7	2.13×10^{-12}	5.34×10^{-12}
268.1	4.7	5.92×10^{-9}	4.19×10^{-11}	475.0	4.7	6.58×10^{-13}	2.94×10^{-12}
277.5	4.7	5.17×10^{-9}	3.92×10^{-11}	484.4	4.7	2.59×10^{-13}	1.83×10^{-12}

These differential cross-sections were obtained with statistics of 19000, 22000, 264000, 24000, 15000, and 23000 events for a total flux of 5.11×10^8 , 1.17×10^8 , 6.26×10^8 , 7.3×10^7 , 1.11×10^8 , 5.2×10^7 incident nuclei traversing targets of thicknesses of 1.0mm Al, 0.3mm Ag, 0.2mm W, 0.25mm Pt, 0.2mm Pb and 0.32mm U respectively.

With respect to the shapes assumed in the backward region of pseudorapidity, the measurements in the full region of pseudorapidity appear to be shifted, without affecting very much change in the shape. This result is expected if the forward transverse energy becomes rather independent of the backward transverse energy, and does not have large fluctuations by itself. We are going to see in section 4.5.1 that this is the case.

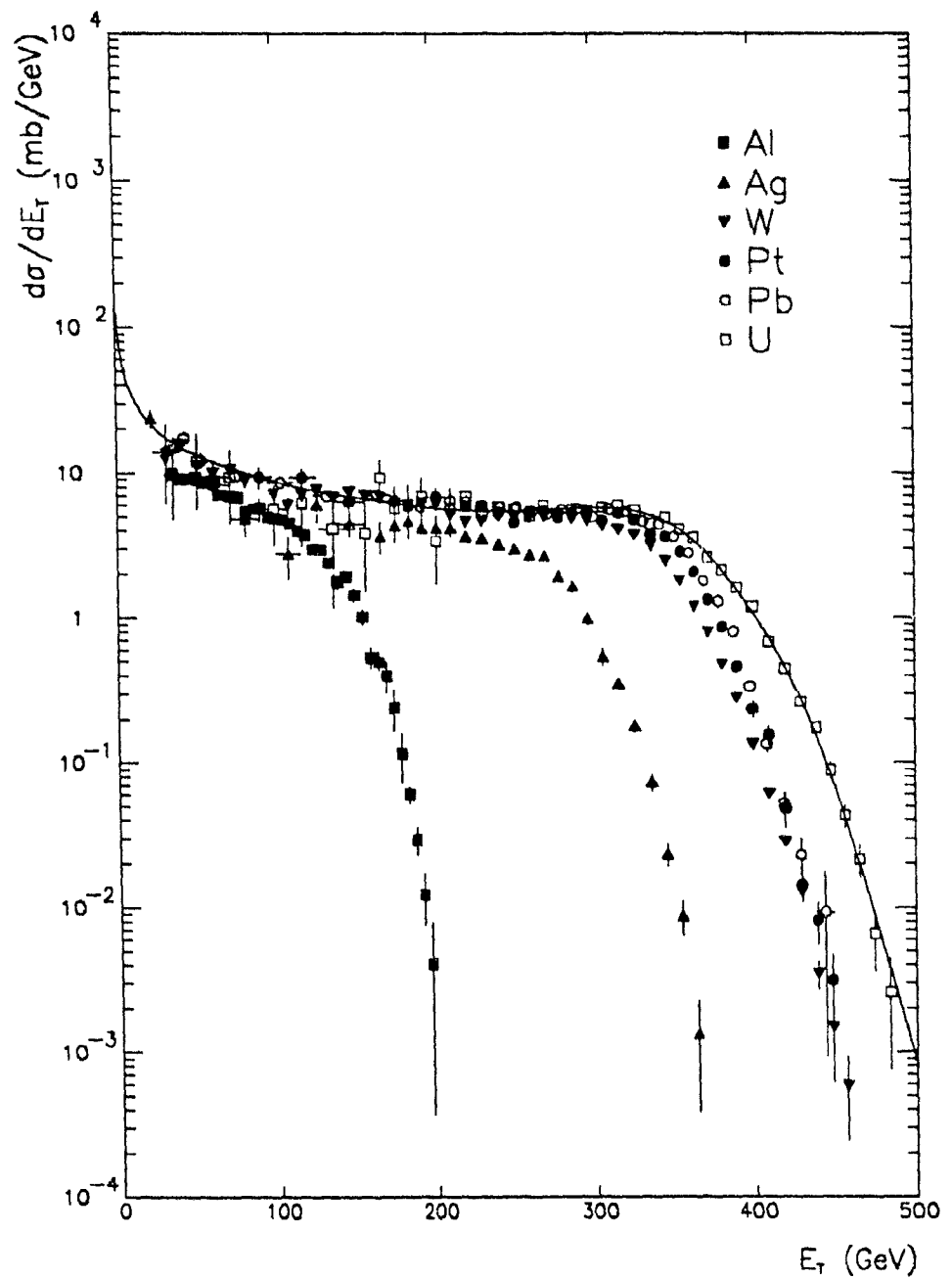


Figure 45: Transverse energy differential cross-section measured in $-0.1 < \eta < 5.5$ for a 200 GeV/nucleon ^{32}S beam. The distributions $d\sigma/dE_T$ are shown for Al, Ag, W, Pt, Pb, and U targets. The line indicates the NCM fit for U. E_T is defined as $\Sigma E_i^{*u} \sin\theta$ where $E_i^{*u} = \sqrt{p^2 + m^2}$ except for nucleons where $E_i^{*u} = \sqrt{p^2 + m^2} - m$.

4.2.6 ^{16}O -W E_T distributions at several energies

The differential cross-section versus E_T are reported for 60(200) GeV nucleon ^{16}O projectiles colliding in a W target in Table 21 (Table 22) and shown in Figure 46. For the data shown at 60 GeV nucleon, we have used a measure of the transverse energy in the forward region based on the reconstruction of the transverse energy in IRSALZ calorimeter. The detailed discussion of the choice of weights in this calorimeter will not be included here, the corrections were established, however, by requiring the same forward transverse energy is produced in ^{16}O -W collisions at 200 GeV nucleon with the 1986 set-up (IRSALZ) and with the 1987 set-up (ULAC). The corrections are then used to find the transverse energy produced in the forward pseudorapidity region¹⁷ by 60 GeV nucleon ^{16}O collisions, for which no data could be taken with the ULAC installed.

Table 21 ^{16}O -W transverse energy differential cross-section at 60 GeV nucleon

E_T [GeV]	Bin half-width [GeV]	$d\sigma/dE_T$ [mb/GeV]	Error [mb/GeV]	E_T	Bin	$d\sigma/dE_T$	Error
55.0	1.0	$1.92 \times 10^{+1}$	$2.30 \times 10^{+0}$	103.0	1.0	$9.97 \times 10^{+0}$	3.76×10^{-1}
57.0	1.0	$1.59 \times 10^{+1}$	$2.09 \times 10^{+0}$	105.0	1.0	$9.12 \times 10^{+0}$	3.60×10^{-1}
59.0	1.0	$1.40 \times 10^{+1}$	$1.96 \times 10^{+0}$	107.0	1.0	$8.91 \times 10^{+0}$	3.55×10^{-1}
61.0	1.0	$1.68 \times 10^{+1}$	$2.15 \times 10^{+0}$	109.0	1.0	$7.35 \times 10^{+0}$	3.23×10^{-1}
63.0	1.0	$1.21 \times 10^{+1}$	$1.82 \times 10^{+0}$	111.0	1.0	$6.42 \times 10^{+0}$	3.02×10^{-1}
65.0	1.0	$1.29 \times 10^{+1}$	$1.88 \times 10^{+0}$	113.0	1.0	$5.10 \times 10^{+0}$	2.69×10^{-1}
67.0	1.0	$1.24 \times 10^{+1}$	$1.84 \times 10^{+0}$	115.0	1.0	$4.02 \times 10^{+0}$	2.39×10^{-1}
69.0	1.0	$1.37 \times 10^{+1}$	2.55×10^{-1}	117.0	1.0	$3.57 \times 10^{+0}$	2.25×10^{-1}
71.0	1.0	$1.37 \times 10^{+1}$	2.56×10^{-1}	119.0	1.0	$2.71 \times 10^{+0}$	1.96×10^{-1}
73.0	1.0	$1.38 \times 10^{+1}$	2.58×10^{-1}	121.0	1.0	$2.03 \times 10^{+0}$	1.69×10^{-1}
75.0	1.0	$1.39 \times 10^{+1}$	2.60×10^{-1}	123.0	1.0	$1.53 \times 10^{+0}$	2.01×10^{-2}
77.0	1.0	$1.29 \times 10^{+1}$	2.31×10^{-1}	125.0	1.0	$1.17 \times 10^{+0}$	6.11×10^{-2}
79.0	1.0	$1.38 \times 10^{+1}$	2.59×10^{-1}	127.0	1.0	8.70×10^{-1}	5.28×10^{-2}
81.0	1.0	$1.41 \times 10^{+1}$	2.66×10^{-1}	129.0	1.0	6.40×10^{-1}	4.52×10^{-2}
83.0	1.0	$1.29 \times 10^{+1}$	2.33×10^{-1}	131.0	1.0	4.48×10^{-1}	3.79×10^{-2}
85.0	1.0	$1.38 \times 10^{+1}$	2.59×10^{-1}	133.0	1.0	2.50×10^{-1}	2.83×10^{-2}
87.0	1.0	$1.43 \times 10^{+1}$	2.70×10^{-1}	135.0	1.0	1.76×10^{-1}	2.37×10^{-2}
89.0	1.0	$1.35 \times 10^{+1}$	2.49×10^{-1}	137.0	1.0	1.44×10^{-1}	2.15×10^{-2}
91.0	1.0	$1.22 \times 10^{+1}$	2.12×10^{-1}	139.0	1.0	1.02×10^{-1}	1.81×10^{-2}
93.0	1.0	$1.33 \times 10^{+1}$	2.44×10^{-1}	141.0	1.0	4.16×10^{-2}	1.15×10^{-2}
95.0	1.0	$1.32 \times 10^{+1}$	2.40×10^{-1}	143.0	1.0	2.56×10^{-2}	2.05×10^{-3}
97.0	1.0	$1.10 \times 10^{+1}$	6.76×10^{-2}	145.0	1.0	2.56×10^{-2}	2.05×10^{-3}
99.0	1.0	$1.24 \times 10^{+1}$	4.19×10^{-2}	147.0	1.0	9.60×10^{-3}	5.54×10^{-3}
101.0	1.0	$1.06 \times 10^{+1}$	3.88×10^{-2}	149.0	1.0	6.40×10^{-3}	4.52×10^{-3}

¹⁷ This contribution is relatively small. [85]

Table 22: ^{16}O -W transverse energy differential cross-section, at 200 GeV nucleon

E_T [GeV]	Bin half-width [GeV]	$d\sigma/dE_T$ [mb GeV]	Error [mb GeV]				
124.6	2.4	6.92×10^{-2}	2.31×10^{-2}				
129.3	2.4	1.05×10^{-1}	1.00×10^{-1}	109.9	2.4	4.40×10^{-2}	6.48×10^{-2}
134.0	2.4	9.71×10^{-2}	3.67×10^{-2}	204.6	2.4	2.29×10^{-2}	4.67×10^{-2}
138.7	2.4	9.34×10^{-2}	9.48×10^{-2}	209.3	2.4	2.09×10^{-2}	4.45×10^{-2}
143.4	2.4	9.04×10^{-2}	1.00×10^{-1}	214.0	2.4	1.89×10^{-2}	4.22×10^{-2}
148.1	2.4	8.58×10^{-2}	9.10×10^{-2}	218.7	2.4	1.07×10^{-2}	1.42×10^{-2}
152.8	2.4	8.97×10^{-2}	9.31×10^{-2}	223.4	2.4	8.96×10^{-3}	1.29×10^{-2}
157.5	2.4	7.05×10^{-2}	8.25×10^{-2}	228.1	2.4	6.86×10^{-3}	1.13×10^{-2}
162.2	2.4	7.82×10^{-2}	8.69×10^{-2}	232.8	2.4	3.68×10^{-3}	8.23×10^{-3}
166.9	2.4	6.47×10^{-2}	7.91×10^{-2}	237.5	2.4	2.92×10^{-3}	7.30×10^{-3}
171.6	2.4	7.05×10^{-2}	8.25×10^{-2}	242.2	2.4	1.27×10^{-3}	4.78×10^{-3}
176.4	2.4	5.79×10^{-2}	7.48×10^{-2}	246.9	2.4	7.16×10^{-4}	3.58×10^{-3}
181.1	2.4	6.56×10^{-2}	7.95×10^{-2}	251.6	2.4	3.55×10^{-4}	2.51×10^{-3}
185.8	2.4	4.91×10^{-2}	6.88×10^{-2}	256.3	2.4	3.51×10^{-4}	2.48×10^{-3}
190.5	2.4	5.96×10^{-2}	7.57×10^{-2}	265.7	2.4	1.93×10^{-4}	5.93×10^{-3}
195.2	2.4	4.60×10^{-2}	6.64×10^{-2}	270.4	2.4	3.38×10^{-4}	3.38×10^{-3}

These differential cross-sections were obtained with statistics of 14500 and 40000 events for a total flux of 4.9×10^7 and 1.0×10^8 beam particles impinging on a 0.2 mm thick W target. Note that the data were taken in different years.

An energy scan with a fixed geometry of the total production of transverse energy in the full region of pseudorapidity is a sensitive test of models because that quantity is not affected by the rapidity shift that inevitably occurs in a fixed target experiment when the energy of the beam is changed. One of the most straightforward tests of the hydrodynamic model is to investigate if the production of transverse energy is proportional to $E(\text{beam})^4$ as in [5], the experimental factor of 1.75 between the $E_T(\text{central})$ of ^{16}O -W at 200 GeV nucleon and ^{16}O -W at 60 GeV nucleon is quite far from $(200/60)^4 = 1.35$. In fact, we do not expect an exact 1.4 power, since the hypothesis of a flat rapidity plateau [5] is not realized. The factor is closer to the ratio of the center-of-mass energies, $\approx (200/60)^2 = 1.52$.

This ends our presentation of transverse energy differential cross-sections. As mentioned in the preceding chapter, E_T is defined here as $\sum E^* \times \sin\theta$ where E^* is the kinetic energy for the baryons and the total energy for all other particles including antibaryons. The systematic uncertainty on the E_{TB} scale is estimated to be $\sim 1\%$ (5.9% from the Monte Carlo rescaling factor and 4% from the overall energy calibration). A systematic uncertainty of 5% arises in the Monte Carlo correction of the E_{TF} in the ULAC, due principally to uncertainties in the fractions of the transverse energy which

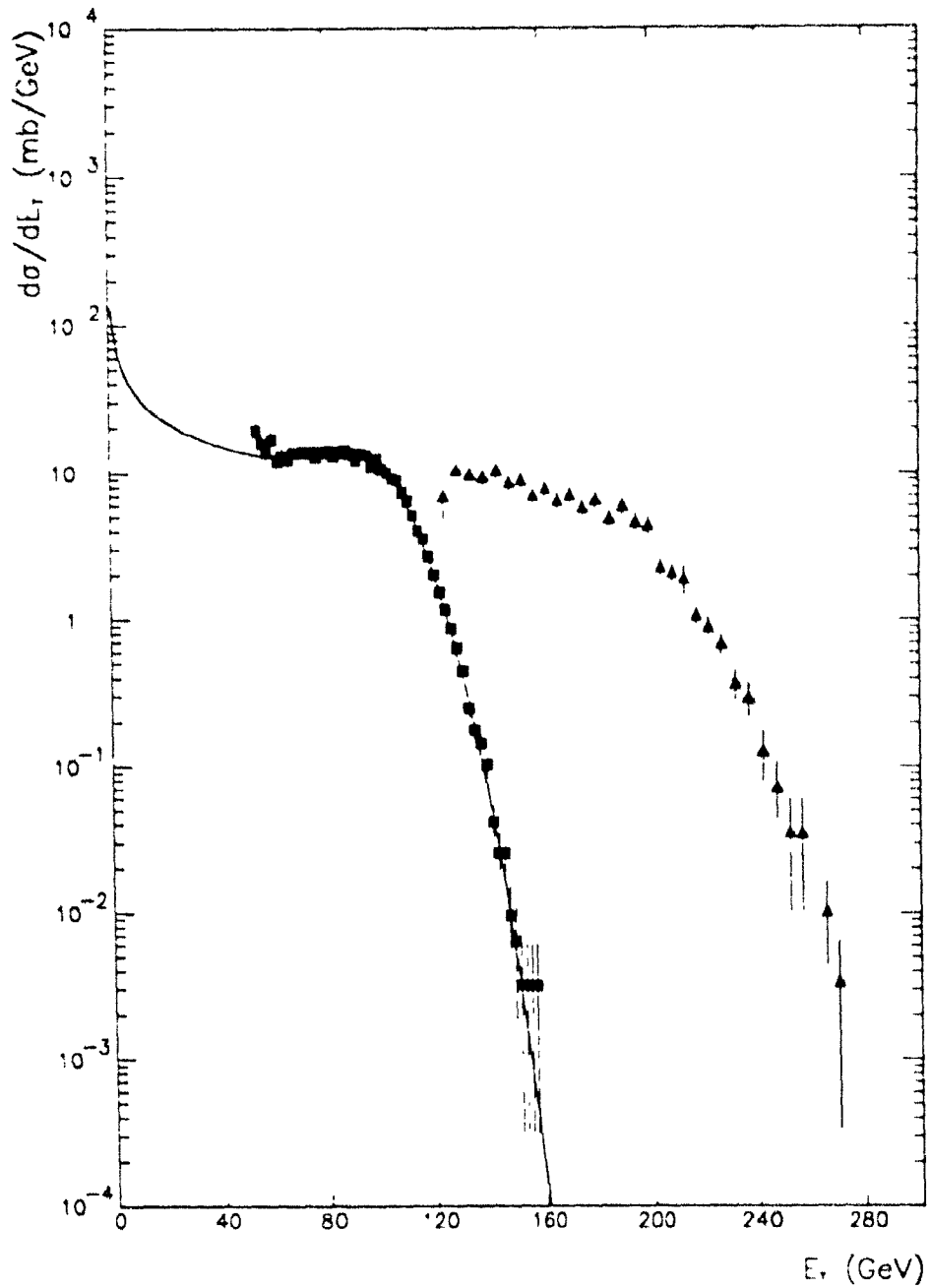


Figure 46: Transverse energy differential cross-section measured in $-0.1 < \eta < 5.5$ for 60 and 200 GeV nucleon ^{16}O beams. The target is 2 mm W disk. The fit in terms of ε_0 and ω is indicated for 60 GeV. E_{T1} is defined as $\Sigma E_i^{*u} \sin\theta$, $E_i^{*u} = \sqrt{p_i^2 + m^2}$ except for nucleons where $E_i^{*u} = \sqrt{p_i^2 + m^2} - m$

are carried by charged and neutral pions (4%), and uncertainty of the e/π factor affecting the hadronic part (3%). The combined uncertainty on the E_T scale varies with the proportions of E_{TB} and E_{TF} contributing to it, from 4 to 7 %. It can be taken as 7% maximum. The relative comparison of the various data sets is essentially free of these systematic uncertainties. The intercalibration of E_{TF} with E_{TB} is also known with a better precision than suggested by the above numbers, as we will see in 4.5.1

The overall systematic uncertainty on the normalization of the differential cross-sections is of order 2-3% and increases to 5-10% in the low E_T regions (< 50 GeV) due to the uncertainty on the no-target contamination.

4.2.7 Multiplicity

In Figure 47, we show the differential cross-section $d\sigma/dN_{ch}$ for the production of a charged multiplicity N_{ch} in the pseudorapidity interval $1.4 < \eta < 3.5$. This distribution was obtained from the distribution of the number of RING2 elements that measured an ionization between 0.7 and 4.0 times the peak of the Landau distribution for minimum ionizing particles, as was described in 2.4.1. The distribution was then corrected for double hits and dead RING elements using the procedures explained in detail in [71][88].

The shape of the multiplicity distribution is very similar to the shapes of the transverse energy distributions: it is dominated by geometry, and can be fitted by an NCM parametrization. This is a consequence of the fact that each particle contributes, on average, a constant amount of transverse energy, independently of the centrality of the collisions.

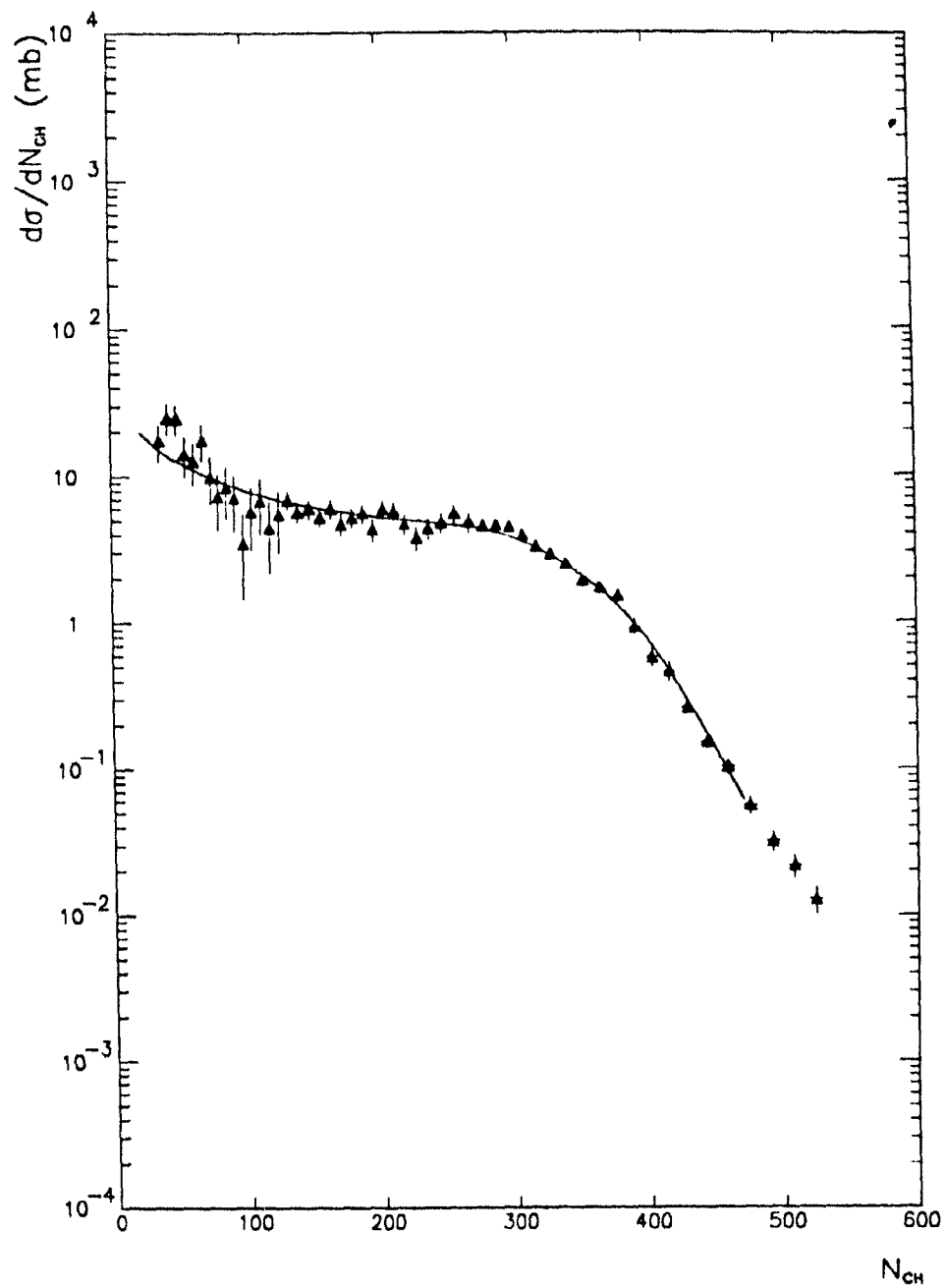
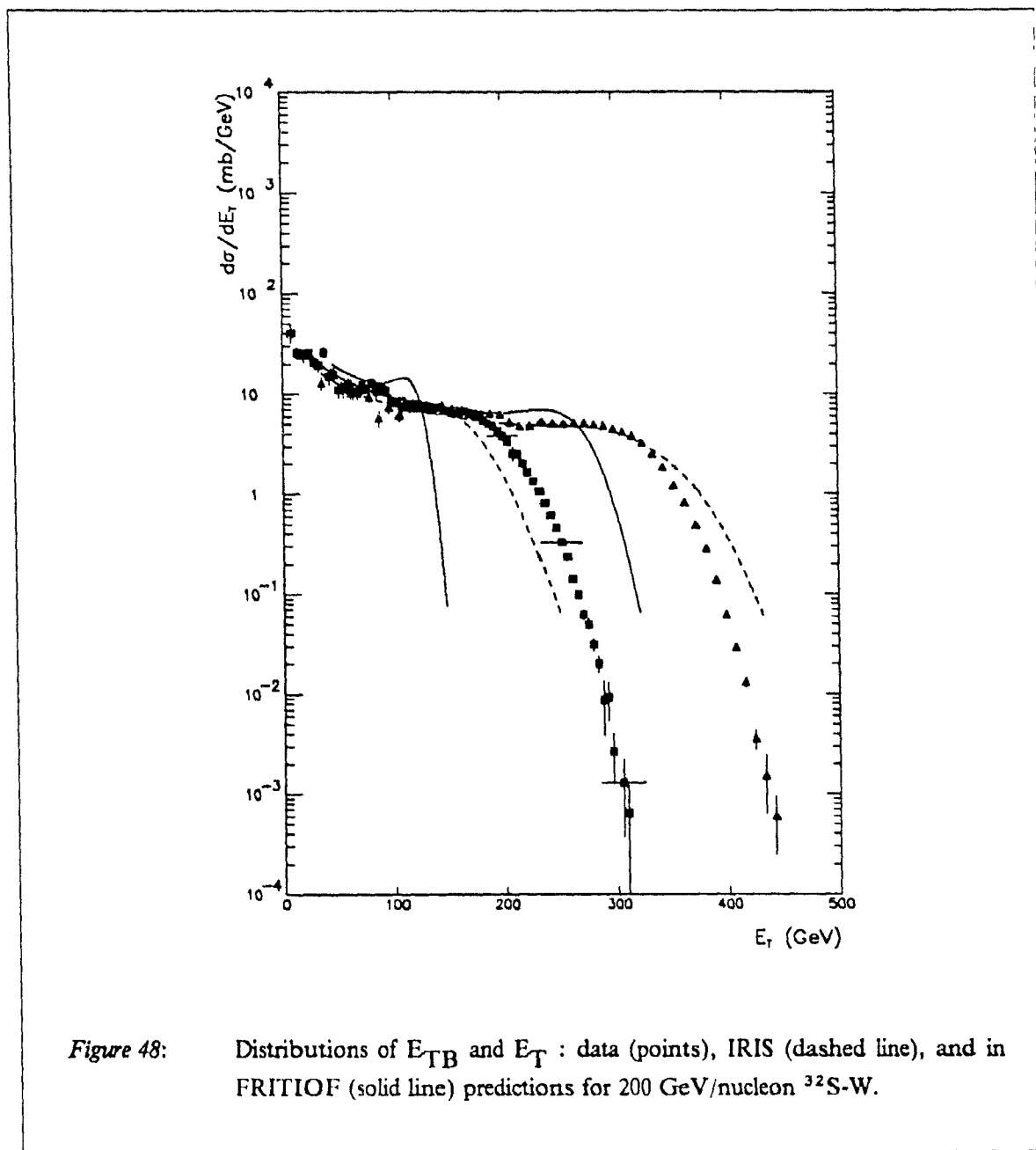


Figure 47: Differential cross-section for the production of a charged multiplicity N_{ch} in $^{32}\text{S} - \text{W}$ collisions. The pseudorapidity interval is 1.5 to 3.5.

4.2.8 Comparison with IRIS and FRITIOF Monte Carlo

In Figure 48, we compare the distributions of E_{TB} and E_T produced by IRIS and FRITIOF with the ^{32}S -W data at 200 GeV/nucleon.



The E_T distribution of IRIS bends very gradually, indicating large fluctuations in the forward region $2.9 < \eta < 5.5$. This very distinct behaviour is probably linked with the erroneous prediction by IRIS

of the average pseudorapidity. It appears that IRIS underestimate the tail of $d\sigma/dE_T^B$, and overestimates the tail of $d\sigma/dE_T^F$. The first effect has been attributed to cascading [86][87]; the second effect has been attributed to insufficient energy loss of the projectile in the IRIS Monte Carlo [87]. Cascading has also been invoked to explain the difference between the FRITIOF prediction and the data, in the absence of a more plausible explanation. However we have computed in section 1.6.1 that cascading on the spectators causes at most 6 GeV additional transverse energy, whereas 20 GeV would be needed in order to make IRIS fit, and about 100 GeV would be needed in order to make FRITIOF fit. It must be stressed [85] that the models fit rather well the data for relatively small target nuclei (Al); this is to be expected, since we approach the limit case of the most trivial kind of superposition of nucleon-nucleon collisions. In any case, the following fact remains: the ratio of forward transverse energy to backward transverse energy is too large in IRIS and FRITIOF compared to the data.

4.2.9 The main features of the ion distributions

The distributions of transverse energy for heavy-ions all share the same properties. At low transverse energies, where most of the cross-section is concentrated, $d\sigma/dE_T \approx C \times E_T^{-0.4}$. In models where the transverse energy production is proportional to the overlap integral, the asymptotic behaviour of the overlap integral at large impact parameters gives this dependence with an exponent of $-2/5$. In models where the transverse energy is proportional to the number of wounded nucleons, the exponent would be $-1/2$ [89]. In practice, the large statistical errors encountered at low transverse energies make the definition of the 'asymptotic exponent' very awkward. The experimental value of this exponent is found to be -0.43 for distributions of $^{16}\text{O-W}$ collisions at 200 GeV/nucleon, close to the NCM prediction.

At higher transverse energies, the differential cross-sections become approximately constant: this is called the plateau region. This plateau region is obtained when the impact parameter is varied. Each value of the transverse energy corresponds to a rather precise impact parameter. The correspondence between impact parameter and transverse energy is not linear, as will be shown in section 4.2.12. In the case of O-Al and S-Al, there is not properly speaking a plateau, in the sense of a temporary stop of the decrease of the differential cross-section with increasing transverse energy, but instead a region where the slope becomes its minimum.

The knee separates the region of almost constant cross-section from a region where the cross-section falls steeply. We will see shortly how the exact half of the plateau height has a special theoretical significance.

In the tail region, finally, the logarithmic derivative of the differential cross-section (so-called 'slope') increases apparently indefinitely. It appears as an almost parabolic arc in log/linear plots of the differential cross-section.

When exploiting our data, we have much better precision in the plateau and tail regions than on the initial power-law fall-off, a somewhat unusual situation. We have very reduced statistics and a large contamination by non-target interactions in the region of the power-law falloff, where an untriggered experiment would have very high statistics.

4.2.10 Reduction of the data from the curves: NCM parametrization

The NCM suggests a parametrization of the distributions of transverse energy. In this model, the nucleons travel in straight lines and there is a collision producing a transverse energy ϵ_0 each time two nucleons come within a certain short distance of each other, the cross-section being taken equal to the proton-proton inelastic cross-section $\sigma_{in} = 32$ mb. We are assuming a constant nuclear density ρ_B of 0.170 baryons/fm³ to obtain the number of collisions N_{cent} in the central case using the analytical formula (13) given in appendix. The distribution of transverse energy given off in the N collisions is the N -convolution of the distribution of transverse energy produced by a proton-proton collision. While with a proton projectile, the exponential tail is sometimes still recognizable, with a heavy-ion beam instead, the number of collisions (≈ 100) is such that the central limit theorem applies and the N -th convolution approaches a Gaussian very precisely. The square of the width of the Gaussian in the NCM is $N\omega\epsilon_0^2$, where ω represents the square of the ratio of the width to the average for the original distribution being convoluted ω will be considered as a free parameter in the present parametrization.

The distribution of overlap integrals was given by the hard-sphere geometry equation (12) to be found in appendix. Although a computer program is still needed to evaluate the distribution of this overlap integral, it has the advantage of a concise mathematical definition. The values of the fit parameters extracted from all the differential cross-sections we have presented in this thesis are shown in Table 23. The equivalent of ϵ_0 for multiplicity distributions, n_0 , represents the multiplicity per nucleon-nucleon collision.

An implicit fit parameter is the total cross-section. It was left as a free parameter, and the 'fitted total cross-sections' agreed within errors with those predicted by the standard parametrizations for total cross-sections ($\sigma_{tot} = (75 \pm 15) (A_p^{1/3} + A_t^{1/3} - 1.4 \pm 0.7)^2$ mb) or measured by other experiments [90]. The errors on ϵ_0 and ω are somewhat correlated. This occurs in our transverse-energy triggered data because a given cross-section in the tail can be reached either by increasing ϵ_0 or by increasing ω . Typically, the correlation is such that if one of the two variables is fixed, the error on the other gets reduced by half.

The free parameters ϵ_0 and ω provide a convenient compact parametrization of the data, of good precision (most χ^2/NDF are less than 1.5, and many are very close to 1.0). However, they cannot be fully interpreted as physics parameters since too many important effects are hidden or

Table 23: Summary of all geometrical parametrizations.

(T): E_T distributions, (B): E_{TB} distributions, (N_{ch}): charged multiplicity distribution.

System	N_{cent}	ε_0 [GeV]	$E_T(cent)$ [GeV]	ω	ω_{deff}	ω_{true}
p-Al 200 GeV(B)	3.38	1.97	6.70	0.68	—	0.68
p-Cu 200 GeV(B)	4.58	2.09	9.59	0.65	—	0.65
p-W 200 GeV(B)	6.53	1.75	11.44	1.08	0.03	1.05
p-U 200 GeV(B)	7.12	1.68	12.00	1.19	0.06	1.13
^{16}O -Al 60 GeV(B)	46.5	0.86	39.8 ± 1.5	2.14	—	2.14
^{16}O -Ag 60 GeV(B)	82.9	0.92	76.5 ± 0.6	2.13	0.13	2.00
^{16}O -W 60 GeV(B)	100.8	0.99	99.5 ± 0.4	2.04	0.41	1.63
^{16}O -Al 200 GeV(B)	46.5	0.96	44.3 ± 3.4	2.37	—	2.37
^{16}O -Ag 200 GeV(B)	82.9	1.07	87.5 ± 4.8	3.68	0.13	3.55
^{16}O -W 200 GeV(B)	100.8	1.20	119.9 ± 0.5	3.03	0.41	2.62
^{32}S -Al 200 GeV(B)	77.8	0.89 ± 0.10	69.9 ± 6.0	1.46 ± 0.7	—	1.46
^{32}S -Ag 200 GeV(B)	135.9	0.97 ± 0.02	155.0 ± 3.0	2.98 ± 0.6	0.22	2.76
^{32}S -W 200 GeV(B)	196.5	1.01 ± 0.01	198.0 ± 2.0	4.51 ± 0.4	0.81	3.70
^{32}S -Pt 200 GeV(B)	200.9	1.04 ± 0.01	208.0 ± 2.0	3.31 ± 0.4	0.28	3.03
^{32}S -Pb 200 GeV(B)	204.7	1.04 ± 0.03	213.0 ± 6.0	3.30 ± 0.6	—	3.30
^{32}S -U 200 GeV(B)	216.5	1.02 ± 0.02	220.0 ± 5.0	5.75 ± 1.2	1.75	4.00
^{32}S -Al 200 GeV(T)	77.8	1.91	148.4 ± 4.1	1.10	—	1.10
^{32}S -Ag 200 GeV(T)	159.2	1.74	278.0 ± 3.8	1.96	0.22	1.74
^{32}S -W 200 GeV(T)	196.5	1.70	335.2 ± 3.6	1.83	0.81	1.02
^{32}S -Pt 200 GeV(T)	200.9	1.73	347.5 ± 5.1	1.44	0.28	1.16
^{32}S -Pb 200 GeV(T)	204.7	1.72	351.5 ± 6.0	1.34	—	1.34
^{32}S -U 200 GeV(T)	216.5	1.67	361.5 ± 2.6	2.36	1.75	0.61
^{16}O -W 200 GeV(T)	100.8	1.84	185.5	1.99	0.41	1.58
^{16}O -W 60 GeV(T)	100.8	1.05	106.0	1.44	0.41	1.03
System	N_{cent}	n_0	$N_{ch}(cent)$	ω	ω_{deff}	ω_{true}
^{32}S -W 200 GeV(N_{ch})	196.5	1.70	335.0	6.25	0.81	5.44

ignored (e.g. energy conservation and nature of the objects participating to the multiple-scattering processes, cascading of secondary particles, etc) In particular, it is interesting to treat separately the effect of the nuclear deformation, as it will be shown in the next paragraph.

4.2.11 The effect of nuclear deformation on transverse energy fluctuations

The large nuclei are known to have an ellipsoidal, instead of spherical, outer shape. The count of the number of nucleon-nucleon collisions is therefore fluctuating because of variations, not only of the impact parameter, but also of the orientation of the target nucleus ellipsoid.

Considering central collisions of large nuclei, we can compute the fluctuations of the length of the central tunnel dwelled in the target nucleus by the projectile nucleus. The radius of that tunnel, determined by the one of the projectile nucleus, does not vary with the orientation of the large target nucleus.

Calling ψ the polar angle of the major axis of the target whose long axis is a factor $1 + \delta$ longer than the minor axis, the length of the central tunnel is $r_0 A^{1/3} (1 - \delta/3 + \delta \cos^2 \psi)$ where A is the atomic mass number of the target.

If we assume that the transverse energy is proportional to the number of nucleon-nucleon collisions, the transverse energy of a central collision fluctuates to $N_{\text{cent}} \varepsilon_0 (1 - \delta/3 + \delta \cos^2 \psi)$ instead of $N_{\text{cent}} \varepsilon_0$. Integrating over all solid angles defined by the orientation of the target nucleus major axis, the root mean square fluctuations are:

$$\begin{aligned}
 & N_{\text{cent}} \varepsilon_0 \sqrt{\frac{1}{4\pi} \int_{-1}^{+1} 2\pi d(\cos\psi) \left(-\frac{\delta}{3} + \delta \cos^2 \psi\right)^2} \\
 &= N_{\text{cent}} \varepsilon_0 \sqrt{\frac{\delta^2}{2} \int_{-1}^{+1} dz \left(\frac{1}{9} - \frac{2z^2}{3} + z^4\right)} = N_{\text{cent}} \varepsilon_0 \sqrt{\left(\frac{1}{9} - \frac{2}{3} \frac{1}{3} + \frac{1}{5}\right) \delta^2} = N_{\text{cent}} \varepsilon_0 \sqrt{\frac{4}{45} \delta^2}
 \end{aligned}$$

The 'dynamical' fluctuations amount to $\sqrt{N_{\text{cent}} \omega \varepsilon_0^2}$, therefore the effect of deformation on a sample of central collisions is effectively an increase of the fluctuations equivalent to an increase of ω by $N_{\text{cent}} \frac{4}{45} \delta^2$. The deformation δ is 0 for Al and Pb, 0.13 for Ag and Pt, 0.22 for W and 0.31 for U.

The measured fluctuations ω are thus the sum of true fluctuations ω_{true} due to the properties of the collision and fluctuations ω_{deff} due to variations of the angle assumed by the target nuclei. The

estimated values of ω_{def} , and the resulting values of ω_{true} are shown in Table 23. The ω_{true} values are less dispersed than the ω values and approach the ω value of the spherical nucleus Pb. From these considerations, one understands that the events from the extreme tail of the E_T distributions are events where the target nucleus is aligned with the beam. We estimate that the uranium nuclei are 75% aligned in the tail of the $^{32}\text{S-U}$ transverse energy distribution (see Figure 44). Since the achieved transverse energy is proportional to the product of the thicknesses of the two colliding nuclei, an uranium nucleus with its long axis longitudinally aligned produces a transverse energy as large as the one which would be produced by a spherical nucleus of atomic number 400.

Although these questions seem anecdotic, they may guide the builders of future ion accelerators [41] for the choice of the most appropriate nuclei to collide. In the present context, the main usefulness of the geometrical parametrization is to give us the mean transverse energy of central collisions, which is given by the product of the parameter ϵ_c by the number of collisions. The central collisions are themselves used only because they represent a better determined geometry than peripheral or semiperipheral collisions and because they reach large densities over large volumes.

4.2.12 Extraction of the mean transverse energy of central collisions

In heavy-ion collisions, the number of collisions is sufficiently large that the effects of geometry and of the dynamics can be efficiently separated. A quite general property of the distributions, which we will show here, is that the average transverse energy of an exactly central collision ($b = 0$) is given to a very good approximation by the point at which the cross-section reaches half the plateau value, this point marks the limit between abundant and rare collisions. This can be shown to be true in the framework of the geometrical model. However, it is a general property, obeyed quite generally by transverse energy distributions (or multiplicity distributions, for example) in a wide class of models, provided a single numerical condition is satisfied. Therefore we will make the proof quite generally, using only the hypotheses that the mean transverse energy is a function of the impact parameter expressible as a Taylor expansion in the impact parameter, and that the fluctuations are small compared to the mean transverse energy and do not change too fast.

First, we establish that the Taylor series contains only even powers of the impact parameter. This can be seen by considering that the average transverse energy must be a continuously differentiable function of the impact parameter vector in the two transverse dimensions. By symmetry, there is no azimuth dependence, so that only even powers are permitted. Let us suppress temporarily the fluctuations and compute the differential cross-section to produce an $\langle E_T \rangle$. The cross-section for the production of an average transverse energy depends only on geometry. Define $\langle E_T \rangle$ by its Taylor series

$$\langle E_T \rangle(b) = A + Bb^2 + Cb^4 + \mathcal{O}(b^6)$$

then the cross-section for the production of $\langle E_T \rangle$ is given by:

$$\sigma_D = \frac{d\sigma}{d\langle E_T \rangle} = \frac{2\pi b}{\frac{d\langle E_T \rangle}{db}}$$

Differentiating:

$$\sigma_D = \frac{2\pi b}{|2Bb + 4Cb^3 + O(b^5)|} = 2 \frac{\pi}{|2B + 4Cb^2 + O(b^4)|}$$

Now comes the condition: we require that the maximum average transverse energy is produced by central collisions, and therefore $A \equiv \langle E_T \rangle_{\max}$ and $B < 0$. Then b^2 can be expressed as a function of $\langle E_T \rangle$:

$$b^2 = \frac{-B - \sqrt{B^2 - 4C(\langle E_T \rangle_{\max} - \langle E_T \rangle)}}{2C} \quad (9)$$

The maximum average transverse energy is produced by central collisions if B is negative. If B is positive, and C is negative, central collisions would not produce the maximum average transverse energy. In that case, the maximum average transverse energy would be produced at a non-zero impact parameter, and the parabolic shape of $\langle E_T \rangle$ as a function of b near the maximum would cause a cusp-like 'bump', resulting from an accumulation of events near the maximum transverse energy. This distinct possibility is probably at the origin of large 'peaks' seen in some differential cross-sections for energy measured in different pseudorapidity intervals by the WA80 collaboration [91].

In the following, we only need equation (9) to a precision of b^2 , and so, neglecting terms in b^4 , we write:

$$b^2 \approx \frac{\langle E_T \rangle_{\max} - \langle E_T \rangle}{|B|}$$

so that, finally,

$$\begin{aligned} \sigma_D &= 2 \frac{\pi}{|2B + \frac{4C}{|B|}(\langle E_T \rangle_{\max} - \langle E_T \rangle) + O(b^4)|} \\ &= \frac{\pi}{|B|} \left(1 - \frac{2C}{B|B|}(\langle E_T \rangle_{\max} - \langle E_T \rangle) + O(b^4) \right) \end{aligned}$$

$$= \frac{\pi}{|B|} \exp\left(\frac{2C}{B^2} (\langle E_T \rangle_{\max} - \langle E_T \rangle)\right) + O(b^4)$$

We have chosen to express σ_D as an exponential because there exists an exact formula for the gaussian smearing of the product of an exponential with a step function. Now we re-introduce fluctuations of a r.m.s. strength of w

$$\frac{d\sigma}{dE_T} = \int dz e^{-\frac{1}{2}(E_T - z)^2/(2w^2)} \sigma_D(z)$$

where $\sigma_D(z)$ is the differential cross-section to produce a transverse energy z if it were not for the fluctuations. This gives:

$$\frac{d\sigma}{dE_T} = \frac{\pi}{|B|} e^{-\frac{2C}{B^2}(E_T - \langle E_T \rangle_{\max})^2} \mathbf{P}\left(\frac{\langle E_T \rangle_{\max} - E_T}{w} + \frac{2Cw}{B^2}\right)$$

Where \mathbf{P} is the error function already introduced in 3.2.1. For small values of $2Cw/B^2$, it is easy to see that the point where the function reaches half of its plateau (defined by minimum slope) is shifted by $\approx 2Cw/B^2$. In particular, if $C=0$, then $\mathbf{P}(0) = 1/2$ precisely. $E_T(1/2 \text{ plateau})$ would then differ from $\langle E_T \rangle_{\max}$ by $f(C) w^2 / \langle E_T \rangle_{\max}$ where $f(C) = 2C \langle E_T \rangle_{\max} / B^2$ is a dimensionless number expected to be smaller than 1 in reasonable models of transverse energy production. Numerically, in the NCM parametrization, $|f(C)| \approx 0.5$, and $w^2 / \langle E_T \rangle_{\max} = \omega^2 / N_{coll} \cdot L_T \cdot \langle E_T \rangle_{\max}$ is a few GeV at most, and the $E_T(1/2 \text{ plateau})$ is different from $\langle E_T \rangle_{\max}$ by less than 2 GeV.

The reader can check for himself or herself that the values of the transverse energy resulting from taking the 1/2 plateau are always within 2 GeV of the central transverse energy in the NCM parametrization given in Table 23. As an example, the average E_{TB} for $^{32}\text{S-W}$ central collisions is 198 GeV in the NCM parametrization, while a differential cross-section of $3.5 \cdot 10^{-6}$ mb/GeV, corresponding to half of the plateau value of $\approx 7.0 \cdot 10^{-6}$ mb/GeV, is reached at $E_{TB} = 200$ GeV. The advantage of the NCM parametrization method over the half plateau method lies in the case where the plateau is difficult to define, for example in low-statistics $^{32}\text{S-Al}$ samples.

Note that the $\langle E_T \rangle_{\max}$ is also characterized by a maximum value of the derivative of $d\sigma/dE_T$ with respect to E_T , which might provide yet another way to extract it from the data.

4.3 The A-dependence of the transverse energy production

The geometrical cross-sections of Figure 45 show a sharp edge followed by a steep fall beyond the point where the colliding nuclei fully overlap. This 'turning point' is determined by the maximum transverse energy the collision would produce in the absence of fluctuations, that is, it indicates the average transverse energy that central collisions would have. It is customary to study the mean transverse energy as a function of A . However, the measurement of the average transverse energy of *central* collisions is more accurate, since it is not affected by the problems of low statistics and potential contamination by non-target interactions, present at low transverse energy, which do affect the measurement of the mean transverse energy. The other advantage of the study of average *central* collisions over the study of the average collision is that the geometry is well-known and simple. For these reasons, we have not attempted the study of mean transverse energies, and focussed our attention on the average transverse energy of *central* collisions. We use the NCM parametrization to provide the transverse energy of a central collision and the statistical error on it. Obtaining the same quantity via other parametrizations, or via the method of the 1.2 plateau value, results in changes less than the statistical error.

The values of $\langle E_T^{central} \rangle$, as a function of the atomic number A of the target nuclei, can be used to parametrize the target dependence of the average central collisions. These values $\langle E_T^{central} \rangle$ are shown in Figure 49 as a function of A of the target for all cases where we have a sufficient number of different target nuclei. It is observed that the A -dependence can be fitted by a power law constant A^α where the exponent α is rather large. The values in the target region ($-0.1 < \eta < 2.9$) are $\alpha = 0.48 \pm 0.02$ and 0.53 ± 0.04 for 60 and 200 GeV nucleon incident ^{16}O respectively, and $\alpha = 0.50 \pm 0.03$ for 200 GeV nucleon incident ^{32}S . This exponent decreases (it has to decrease for kinematics reasons) when considering the full pseudorapidity range ($-0.1 < \eta < 5.5$) to $\alpha = 0.39 \pm 0.04$.

It is quite natural that the exponent α changes with rapidity. Similar measurements with multiplicity [92] by the WA80 collaboration, and comparison with the A -dependence observed for transverse energy in $2.2 < \eta < 3.8$ by the NA35 Collaboration [93] ($\alpha \sim 1.3$) indicate that the exponent depends rather strongly on rapidity. Yet, it must be remembered that the transverse energy production is dominated by the central domain of pseudorapidity. This justifies defining an A -dependence of the total transverse energy production.

If the transverse energy had become independent of the atomic mass number of the target, it would have been an indication of full stopping. The converse is not necessarily true, if the effect of the hydrodynamic expansion is included. In the advent of full stopping, in our model of hydrodynamic expansion, the exponent would asymptotically approach 1.6 for collisions with very large nuclei measured in the full pseudorapidity interval. Since the asymptotic limit of very large nuclei, and the full stopping, have not been reached, the fact that the exponent 0.39 ± 0.04 is larger than 1.6 is not inconsistent with the near full stopping that will be discussed in section 4.7.4.

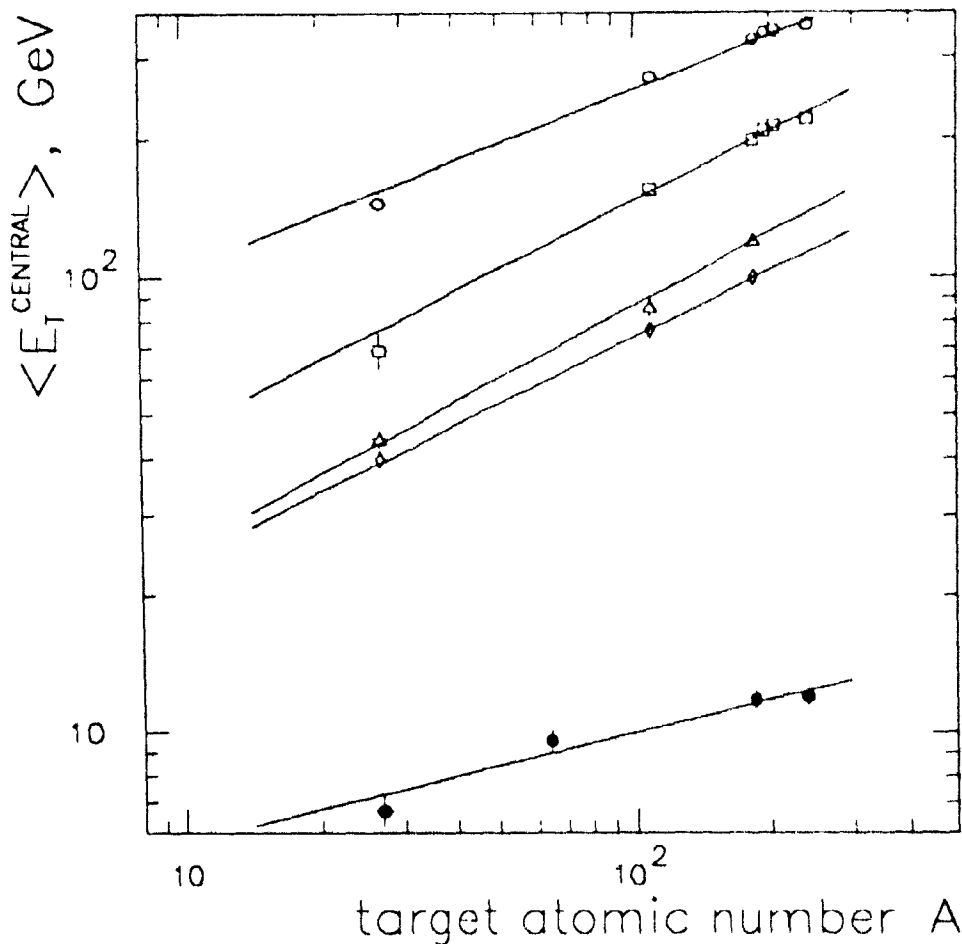


Figure 49: E_{TB} for average central collisions versus the atomic mass number of the target nuclei for 200 GeV protons (\bullet), 60 GeV/nucleon ^{16}O (\diamond), 200 GeV/nucleon ^{16}O (Δ), and 200 GeV/nucleon ^{32}S (\square) incident beam, and E_T for average central collisions of 200 GeV/nucleon ^{32}S (\circ). The solid lines are fits to the data of the form $constant \cdot A^\alpha$. The best estimates of the free parameter α are $\alpha = 0.24 \pm 0.03$ for 200 GeV protons, $0.48 \pm .02$ and $0.53 \pm .04$ for the 60 and 200 GeV/nucleon ^{16}O incident energies, $0.50 \pm .02$ for ^{32}S , and $0.39 \pm .04$ for ^{32}S with full coverage.

4.4 Interpretation of the transverse energy in central collisions

By making the differential cross-sections for the production of transverse energy in the nucleus-nucleus collisions, we obtain the average transverse energy of a central collision and the magnitude of the event-to-event fluctuations of the transverse energy of central collisions

Ignoring temporarily the question of fluctuations, we will compare numerically the transverse energy production against simple mechanisms.

However, we have to remember that what is actually obtained, by means of the 1,2 plateau method, is an extrapolation of the characteristics of central collisions from the characteristics of quasi-central collisions. In the case of the proton-nucleus collisions, it is much more difficult to obtain the characteristics of the central collisions, as many impact parameters contribute simultaneously to a given bin of E_T . The method that we have adopted is to extrapolate the transverse energy in a central collision from the average transverse energy produced

4.4.1 Comparison with the Wounded Nucleon Model (WNM)

A possible model for the production of transverse energy in the range $-0.1 < \eta < 2.9$ is that each of the participating nucleon in the target is responsible for some transverse energy. The number of projectile wounded nucleons would then be neglected because of the large rapidity gap with the projectile. The transverse energy per wounded nucleon is shown as a function of the number of wounded nucleons in Figure 50

The data indicate that the transverse energy in the pseudorapidity range $-0.1 < \eta < 2.9$ is approximately proportional to the number of wounded target nucleons. It is seen however that the transverse energy per wounded nucleon increases somewhat with increasing atomic number of the projectile and with increasing atomic number of the target. In the framework of the wounded nucleon model, this would be explained by the fact that the nucleons are more completely wounded when hit by many projectile nucleons, and/or that the transverse energy in the pseudorapidity range $-0.1 < \eta < 2.9$ depends partly on the number of projectile wounded nucleons.

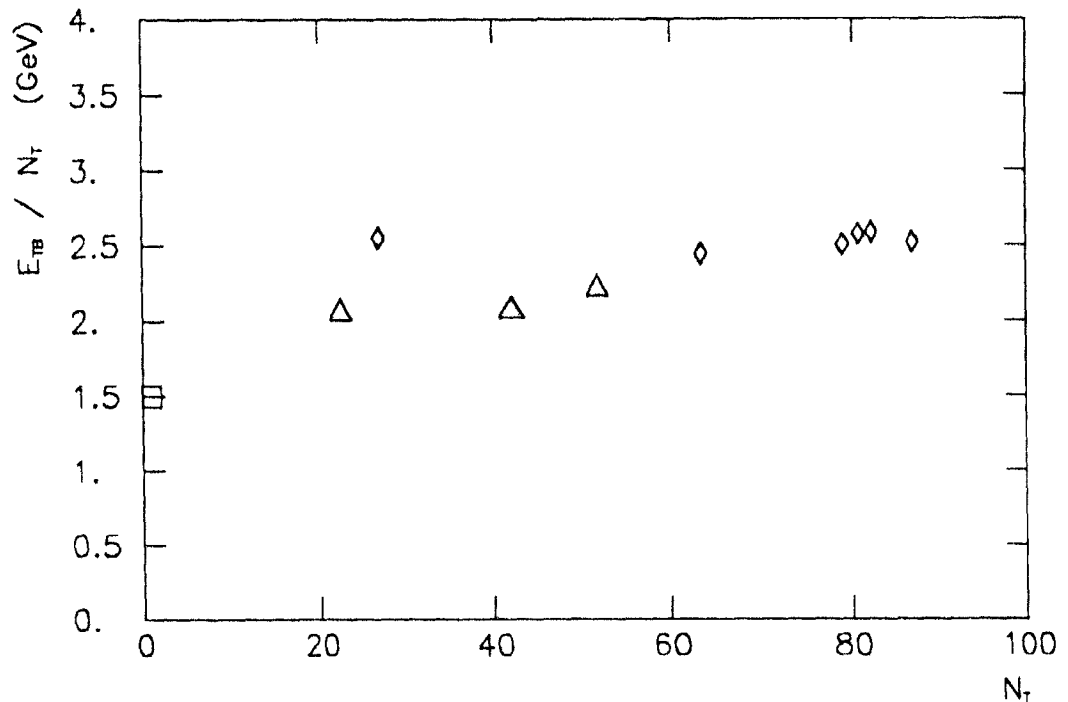


Figure 50: The backward transverse energy per wounded nucleon E_{TB}/N_T as a function of the number of target wounded nucleons N_T . The transverse energy is measured in the pseudorapidity range $-0.1 < \eta < 2.9$. The beam energy is 200 GeV/nucleon.

4.4.2 Comparison with the Nucleon collision model (NCM)

Similarly, we can try to compute the transverse energy in the pseudorapidity interval $-0.1 < \eta < 2.9$ and in the pseudorapidity interval $-0.1 < \eta < 5.5$ for central collisions assuming that an amount of transverse energy is produced in each collision under the assumption of straight line geometry. The amount of transverse energy per nucleon-nucleon collision as a function of the number of nucleon-nucleon collision is shown in Figure 51 and Figure 52 for the backward and complete pseudorapidity coverage respectively.

It does not seem possible to judge from these data if there is a constant transverse energy per participant or per collisions. In fact, the data seems to deviate from either hypothesis.

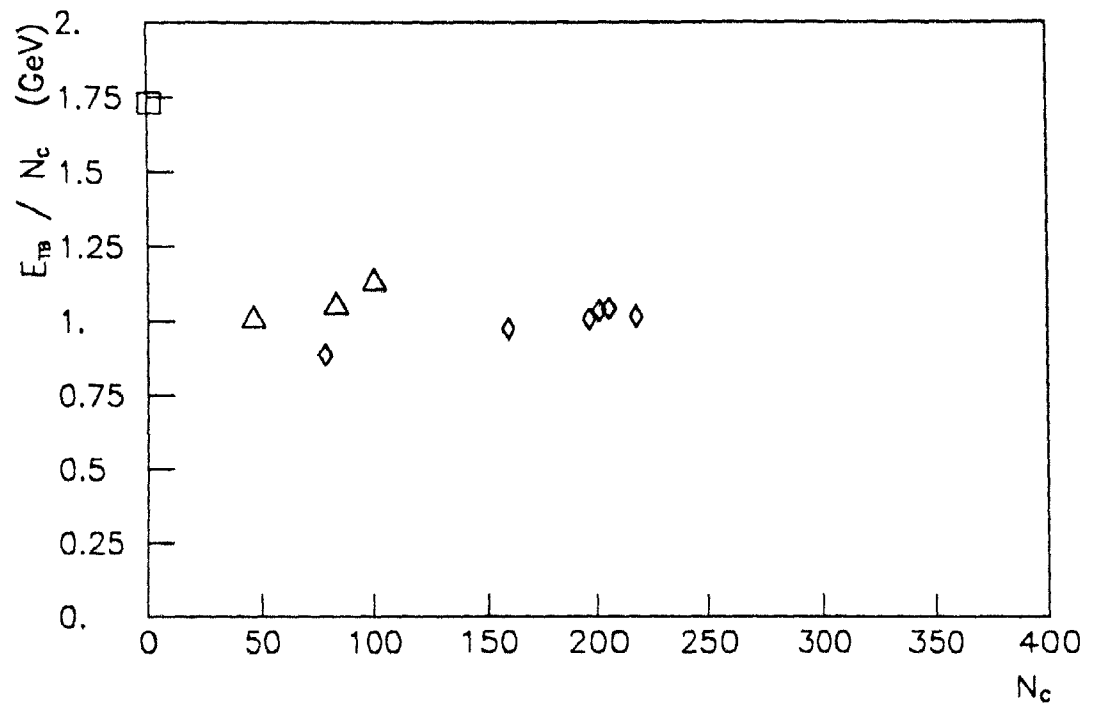


Figure 51: The backward transverse energy per collision E_{TB}/N_C as a function of the number of nucleon-nucleon collisions N_C . The transverse energy is in the pseudorapidity range $-0.1 < \eta < 2.9$.

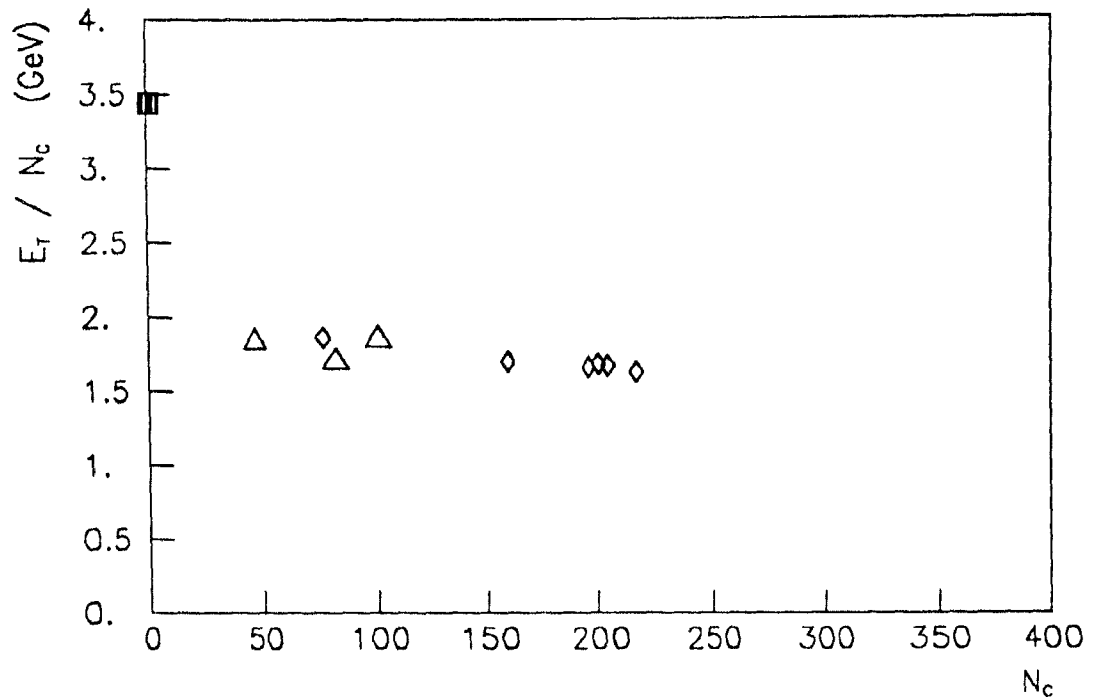


Figure 52: The transverse energy per collision E_T/N_C as a function of the number of nucleon-nucleon collisions N_C . The transverse energy is in the pseudorapidity range $-0.1 < \eta < 5.5$.

4.5 Correlations between the forward and the backward transverse energy

It is instructive to look directly at the correlation between the transverse energy in the pseudorapidity ranges $-0.1 < \eta < 2.9$ and $2.9 < \eta < 5.5$ in order to understand the comparisons of their respective distributions. From the comparison of Figure 44 and Figure 45, it appears that the distributions of transverse energy are shifted, and not scaled up, when increasing the pseudorapidity range. The explanation of this surprising fact is that the forward transverse energy becomes approximately constant for central collisions¹⁸.

¹⁸ The E_{TF} is also A-independent to some extent

When studying correlations of transverse energy in large domains of pseudorapidity, we must first of all observe that the amount of transverse energy produced in heavy-ion collisions, in all the pseudorapidity ranges, is largely determined by the impact parameter which is unique for each event. Without the fluctuations, a scatter plot of the transverse energy produced in a given interval versus the transverse energy produced in another interval, would concentrate on a line. Since we have used the geometrical model to fit the differential cross-sections for the production of E_T and multiplicity in various domains of pseudorapidity, the production of E_T and multiplicity from every region must be proportional to the overlap integral, as a consequence we expect them to be proportional to each other, and the scatter plot should be a straight line. However, the limited statistics of the differential cross-sections allow some freedom, and in fact a curvature is quite apparent in some of the graphs that are shown next. We will consider two cases that are representative of the others, $^{32}\text{S-Al}$, representing the limit of collisions of nuclei of equal mass, and $^{32}\text{S-W}$, representing the limit of the collision of a small nucleus on a large one. $^{32}\text{S-Ag}$ collisions present intermediate features.

4.5.1 Double differential cross-section $d^2\sigma/dE_{TB}dE_{TF}$

Let us first study $^{32}\text{S-W}$ collisions at 200 GeV nucleon. A remarkable feature of the distribution of transverse energy in the pseudorapidity range $-0.1 < \eta < 5.5$ is that its tail does not extend much farther than the corresponding tail for $-0.1 < \eta < 2.9$. The reason for this appears clearly when considering Figure 53 which shows the contour plot of the double differential cross-section

$$\frac{d^2\sigma}{dE_{TB}dE_{TF}}$$

for the production of a transverse energy E_{TB} in the pseudorapidity range $-0.1 < \eta < 2.9$, and of a transverse energy E_{TF} in the pseudorapidity range $-0.1 < \eta < 5.5$. It appears that the most probable forward transverse energy is proportional to the backward transverse energy up to a value of backward transverse energy close to $\langle E_{TB} \rangle (b=0)$, the average transverse energy produced by central collisions. E_{TF} appears to be independent of the backward transverse energy at higher values.

This independence can be interpreted in at least two ways: either the mechanism for the production of E_{TF} is independent of the mechanism of production of E_{TB} in the backward region, as for example in the two-fireball or in diffractive excitation models [94]¹⁹, or a single mechanism is responsible for the production of transverse energy, both forward and backward, but the conservation of the available energy, or the backward rapidity shift occurring when more target nucleons are participating, force the fraction of the transverse energy in the forward region to decrease, such that E_{TF} is approximately independent of E_{TB} at large enough transverse energy. In contrast, the transverse energy contained in two backward regions of pseudorapidity remain proportional to each other, with the result that the shape of the pseudorapidity distribution of E_T [86] in the backward region is almost constant. This is actually due to a particularity of the backward region in heavy-ion collision where the target is more massive than the projectile. The production of transverse energy,

¹⁹ This also happens in the DPM in the limit where the contribution of the sea-sea chains is negligible

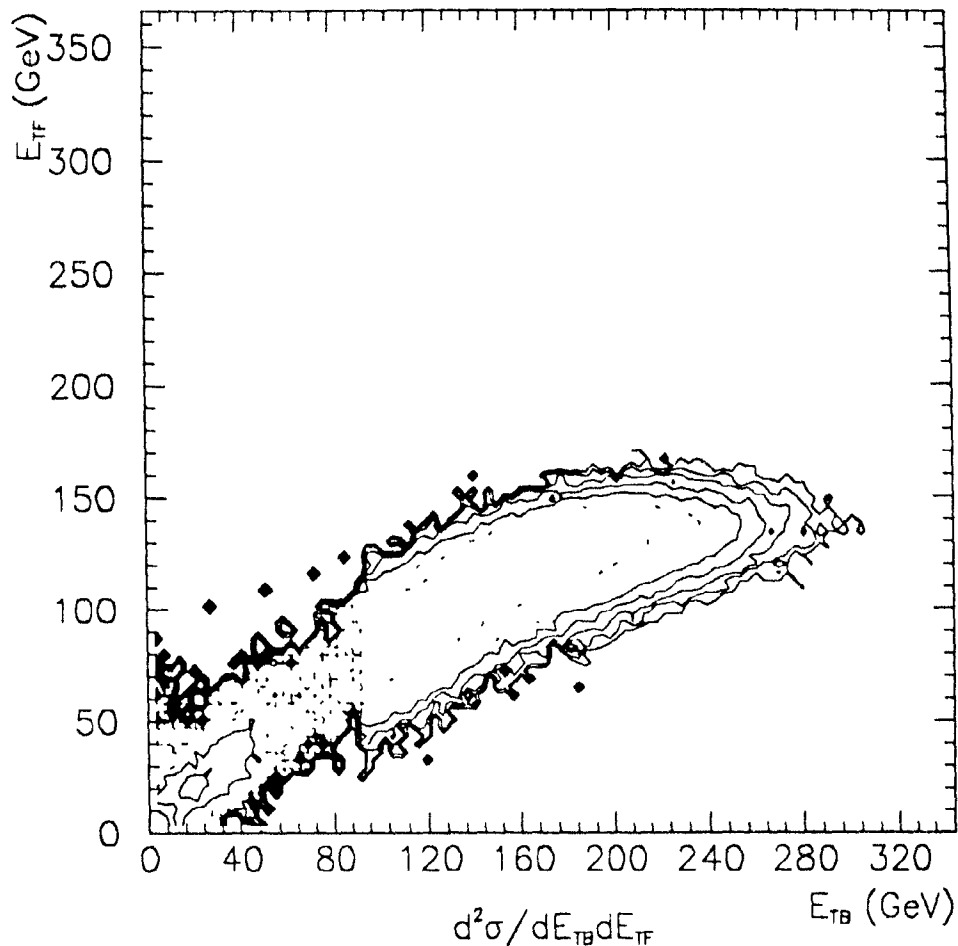


Figure 53: The contour plot of the double differential cross-section for E_{TB} and E_{TF} in ^{32}S -W collisions at 200 GeV/nucleon. Two contours are separated by a factor $1/e$.

being more narrow and more backwards, keeps approximately the same shape in a small interval.

The two regressions are shown in Figure 54 and Figure 55 for ^{32}S -W collisions at 200 GeV per nucleon. It is seen that for increasing backward transverse energy the forward transverse energy ceases to rise, perhaps even shows a decrease.

In contrast, the regression of the backward transverse energy as a function of the forward transverse energy shows an increase up to the largest values.

Noting that for proton-proton collisions, the two chosen domains are symmetric, the completely different behaviour of the two regressions is significant. In the hemisphere where the largest nucleus

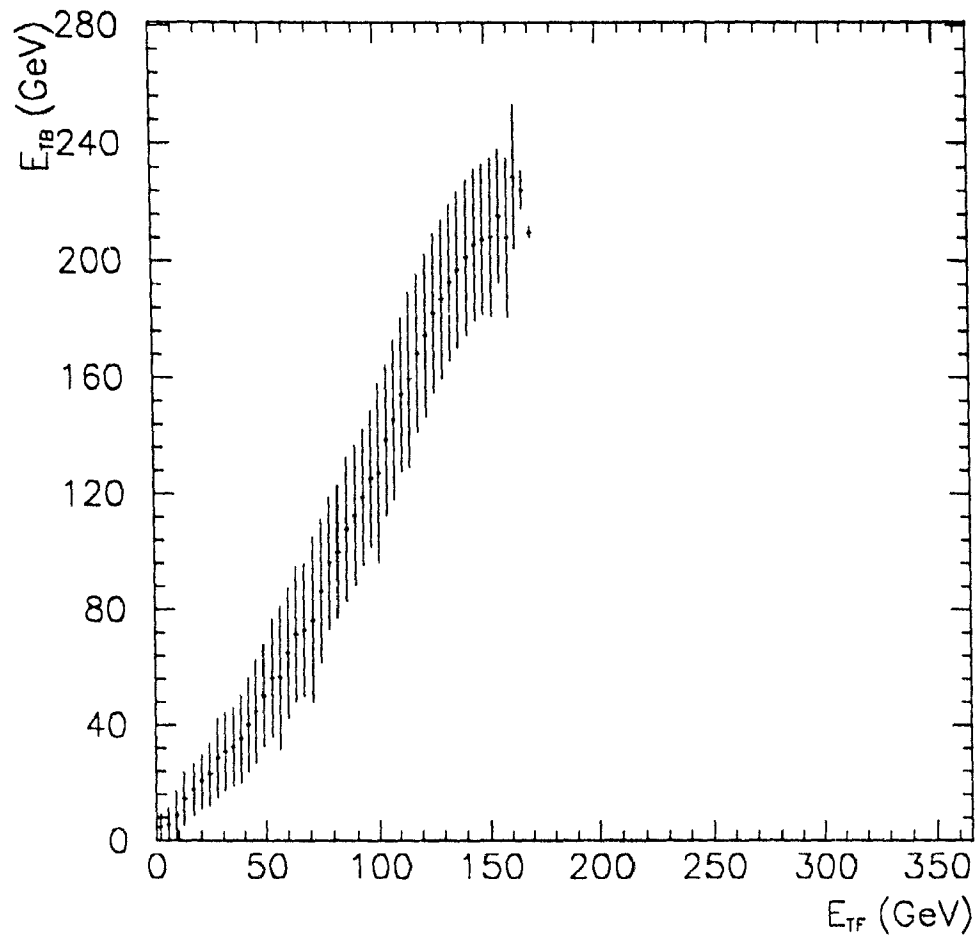


Figure 54: The regression of the forward transverse energy as a function of the backward transverse energy for ^{32}S -W collisions at 200 GeV/nucleon. The error bars indicate the magnitude of the event-to-event fluctuations.

is, there exist event-to-event fluctuations that are not present in the other hemisphere. This extra transverse energy with large fluctuations limited to the backward hemisphere, where the large nucleus sits, might be a manifestation of cascading.

The comparison of the backward and forward transverse energies for ^{32}S -Al collisions is motivated by experimental reasons. The contour plot of the double differential cross-section for the production of E_{TB} in the pseudorapidity region $-0.1 < \eta < 2.9$ and of E_{TF} in the forward region $2.9 < \eta < 5.5$ is shown in Figure 56. The contour is very well described by Gaussian fluctuations of

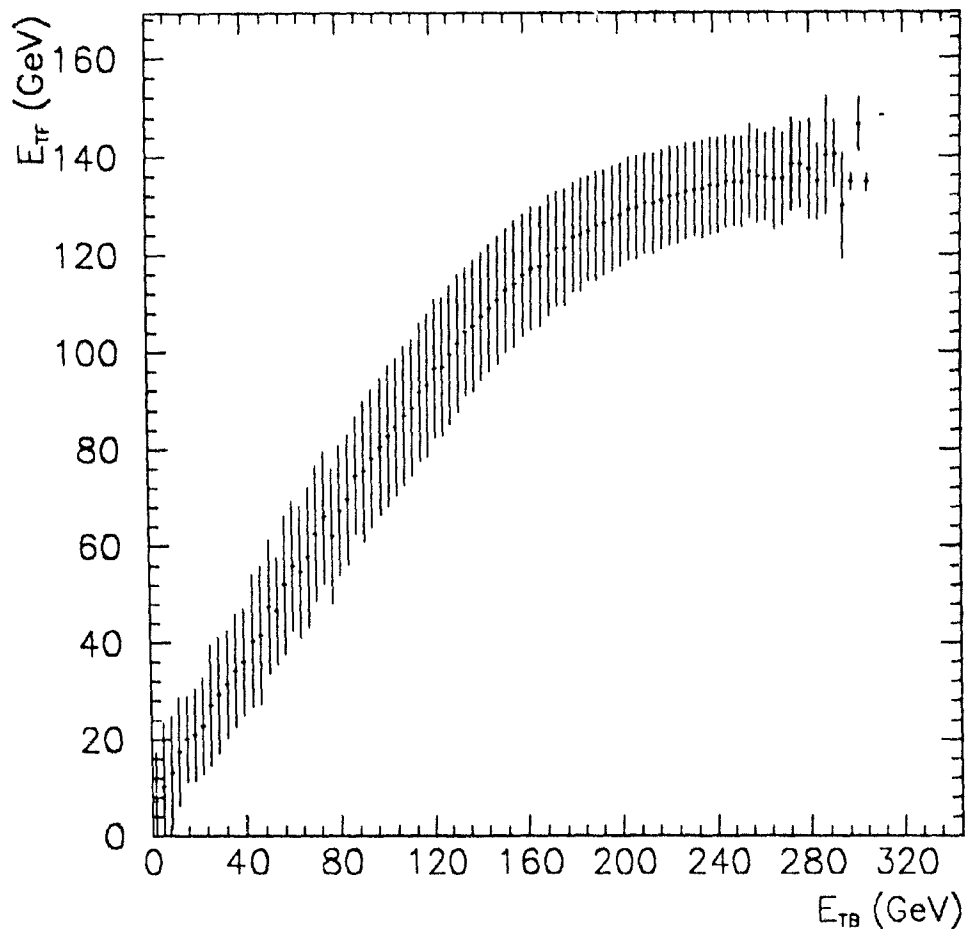


Figure 55: The regression of the backward transverse energy as a function of the forward transverse energy for ^{32}S -W collisions at 200 GeV/nucleon. The error bars indicate the magnitude of the event-to-event-fluctuations.

magnitude ≈ 5 GeV in both axes, around a straight line domain $E_{TF} = (1.25 \pm 0.02)E_{TB}$.

If:

1. The pseudorapidity was exactly equivalent to rapidity,
2. The separation between the forward and backward regions was located exactly at half the rapidity of the beam $\frac{1}{4} \ln \frac{E_{beam} + P_{beam}}{E_{beam} - P_{beam}}$,

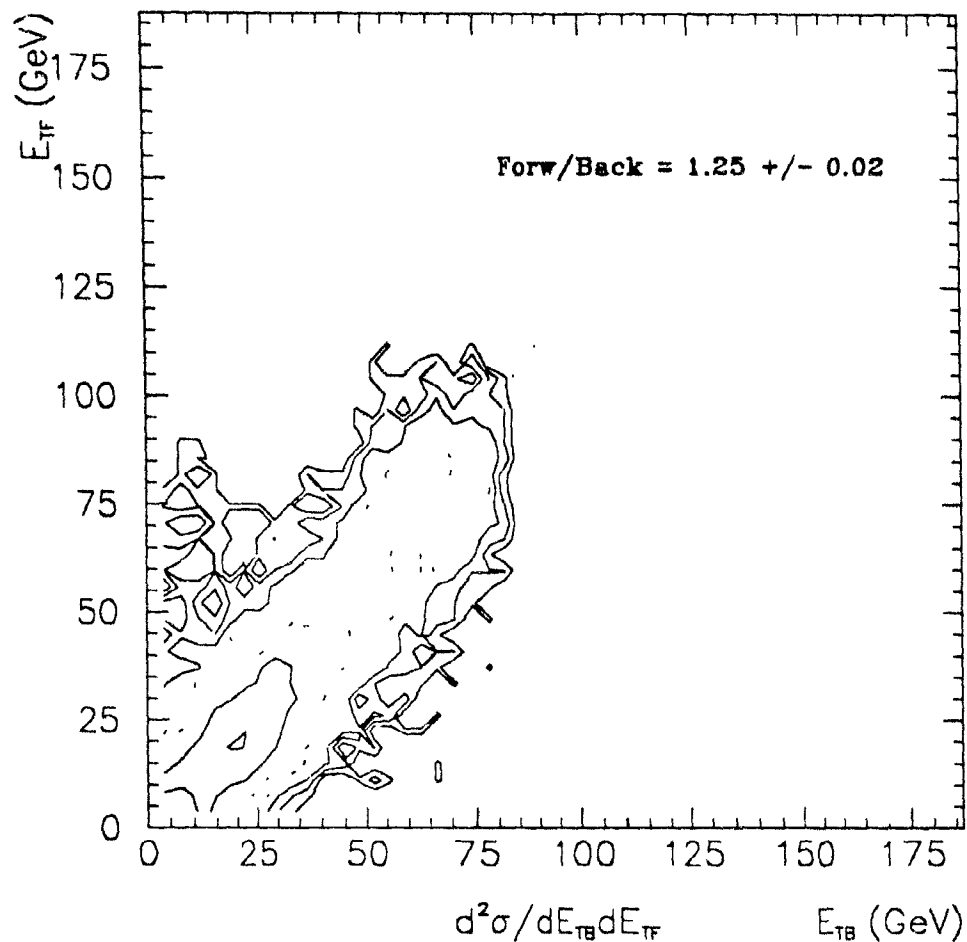


Figure 56: Contour plot of the double differential cross-section for the production of E_{TB} and E_{TF} in ^{32}S -Al collisions at 200 GeV/nucleon.

3. The atomic number of the projectile was exactly that of the target,

all ratios of forward to backward (Forw/Back) transverse energy would be exactly equal to one, by forward/backward symmetry of nature. Because these three conditions are not satisfied exactly, we expect a value somewhat different from (but close to) 1.00. However, it is possible to estimate the effects of these three 'asymmetries' quite reliably and to exploit this unique possibility to use a natural symmetry, to verify the intercalibration of the calorimeters.

In order to evaluate the effects of the three sources of forward backward asymmetries, let us remember that we are comparing the area of the 'right hand side' of a symmetric rapidity distribution of transverse energy with the 'left hand side', the borderline being at the center of symmetry in the ideal case. Then we can treat the three source of asymmetries as sources of small rapidity shifts of the borderline, and the ratio is given by.

$$\frac{E_{TF}}{E_{TB}} = \frac{\frac{1}{2}E_T + \left(\frac{dE_T}{dy}\right)_{\max} y_{sh}}{\frac{1}{2}E_T - \left(\frac{dE_T}{dy}\right)_{\max} y_{sh}} = 1 + 4 \frac{(dE_T/dy)_{\max}}{E_T} y_{sh} + 8 \left(\frac{(dE_T/dy)_{\max}}{E_T} \right)^2 y_{sh}^2 + \dots \quad (10)$$

where y_{sh} is the sum of all the rapidity shifting effects, and the maximum $dE_T/d\eta$, as well as the total E_T , can be obtained from the data.

Let us proceed to the numerical evaluation. The average shift of η with respect to y , y_{sh1} , can be evaluated if we assume that the transverse energy is mostly carried by relativistic pions, having a transverse momentum distribution $\exp(-p_T/p_0)$. Then

$$y_{sh1} \approx \frac{\int_0^m p_T p_T dp_T \frac{1}{2} \ln\left(\frac{p_T}{m}\right)}{\int_0^\infty p_T p_T dp_T \exp\left(-\frac{p_T}{p_0}\right)} = \frac{1}{18} \frac{m^3}{p_0^3} \quad (11)$$

With $m = 1350$ MeV and $p_0 = 180$ MeV, y_{sh1} amounts to 0.023. The very small value of the shift of $dE_T/d\eta$ compared to dE_T/dy obtained by this simplified analytical calculation is confirmed by elaborate Monte Carlo studies [95]. The second source of shift y_{sh2} is the difference between the nucleon-nucleon center-of-mass rapidity of 3.027 and the edge of our domain at 2.9. $y_{sh2} = 0.127$. Finally, we evaluate the added shift y_{sh3} due to the difference between ^{32}S and ^{27}Al by considering the spanned range of values of the rapidity of the center-of-mass of participants. y_{sh3} can be expected to lie between $1/12 \ln(32/27) = 0.014$ and $1/2 \ln\left(\frac{[32 - (32^{2/3} - 27^{2/3})^2]}{27}\right) = 0.067$, so we take $y_{sh3} = 0.04 \pm 0.03$.

The total $y_{sh} = y_{sh1} + y_{sh2} + y_{sh3}$ is 0.19 ± 0.03 , and using the experimental $(dE_T/dy)_{\max} E_T \approx 0.3$, equation (10) gives us an expected forward/backward ratio of 1.25 ± 0.04 .

The fact that the measured ratio of forward to backward transverse energy agrees with a theoretical prediction based on a fundamental symmetry of nature is important as it gives us confidence that the calibrations in each region, and the corrections to the transverse energy were good. The intercalibration of the forward with the backward transverse energy would have been even

more precise if we had used a sulfur target instead of aluminium: a large part of the remaining uncertainty is due to the a-priori uncertainty on the effect of the projectile/target asymmetry.

4.6 Fractional E_T density in pseudorapidity

The transverse energy spectra give an oversimplified picture of the interaction. In the most naive picture of the collision, a fraction of the energy incoming in the center-of-mass is stopped and isotropically re-emitted, while the remaining fraction continues undisturbed in the longitudinal direction. The average distributions of transverse energy, coming from the analysis of the energy flow in the calorimeters, carry instead a rich structure that has possible implications both at the level of the mechanism of production in hadron-hadron collisions, and on the collective evolution (hydrodynamics) indeed, the energy flow (except for variations in azimuth) from a collision is uniquely and completely specified by the $dE_T/d\eta$ distribution. Since the pseudorapidity distributions of transverse energy depend on the impact parameter, on the energy, and on the size of the colliding nuclei, it is impossible to present in a reasonable space all these distributions. Their moments contain most of the relevant information for comparisons with theory, so we will show them instead.

First, it is observed [85] that the shape of the pseudorapidity distribution of transverse energy depends on the transverse energy E_T . This dependence reflects both the effect of varying the impact parameter (high $E_T \equiv$ small impact parameters), and the 'trigger bias' due to the simple fact that we are selecting events with large transverse energy in a certain pseudorapidity domain. The trigger bias effect, since it depends on the pseudorapidity domain over which the measurement of E_T is carried out, does not bring much insight on the dynamics. By varying the impact parameter, we compare in minute details the shape of the pseudorapidity distributions of transverse energy of peripheral collisions that are equivalent to a few hadron-hadron collisions with that of central collisions where a large volume may undergo a phase transition. In this respect, the ideal would be to be able to measure the impact parameter in a way completely independent of transverse energy. A selection using the measured transverse energy in the almost complete coverage of the pseudorapidity $-0.1 < \eta < 5.5$ approaches this goal, since all bins are represented equally at the moment of the selection.

By varying the atomic number of the projectile and target, and the impact parameter via the transverse energy selection, we are probing the detailed dynamics of fireballs of different longitudinal and transverse sizes. Since the amount of this data is very large, it is desirable to find empirical laws to describe these distributions. These empirical laws may not have direct theoretical significance, but can easily be compared to the predictions of the models.

We observe that the $dE_T/d\eta$ distributions are generally well fitted by a simple Gaussian form (see Figure 57). Since a Gaussian shape is completely specified by two parameters, the position of its center and its width, we are justified to study primarily the first and second moments of the pseudorapidity distributions of transverse energy. The third and fourth moments could also be studied, or equivalently the skewness and the kurtosis. The study of higher moments is however hindered by the statistical fluctuations of $dE_T/d\eta$ of individual events, and by the systematic errors due to intercalibration uncertainties. The analysis of higher moments will not be done.

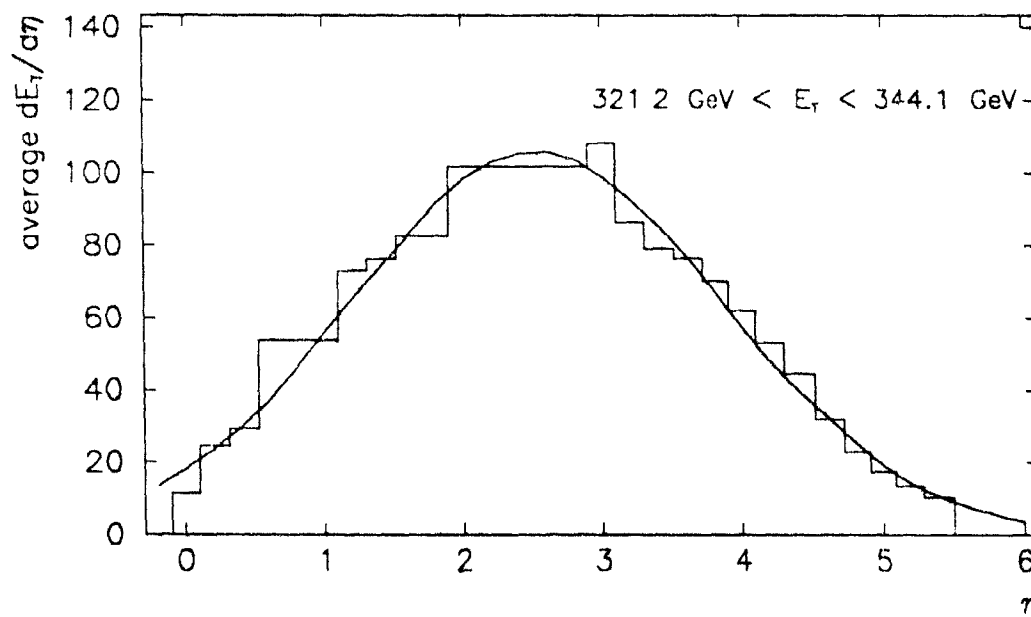


Figure 57: The average $dE_T/d\eta$ in $^{32}\text{S-W}$ quasi-central collisions, selected by $321.2\text{GeV} < E_T (-0.1 < \eta < 5.5) < 344.1\text{GeV}$. The function is the Gaussian of center $\langle \eta \rangle$ and parameter w .

Some general properties of the moments of pseudorapidity distribution of transverse energy will now be examined. The first moment of the pseudorapidity distribution of transverse energy is defined as:

$$\langle \eta \rangle = \frac{\int \eta \frac{dE_T}{d\eta}}{\int \frac{dE_T}{d\eta}}$$

In proton-proton collisions, the longitudinal boost invariance of special relativity and the projectile/target symmetry impose that $\langle y \rangle = \left(\int y \frac{dE_T}{dy} \right) \left(\int \frac{dE_T}{dy} \right)^{-1}$ is $\frac{y(\text{proj}) + y(\text{target})}{2}$. In other words, the transverse energy production is forward backward symmetric in the frame of reference of the center-of-mass of the two protons. $\langle y \rangle$ amounts to 3.0 for an energy of 200 GeV and 2.4 for an energy of 60 GeV.

The experimentally measured $\langle \eta \rangle$ in heavy-ion collisions is significantly different from these values; the distributions are 'shifted'.

Let us note here that a first effect contributes to the shift: The change from the variable η to the variable y when the transverse energy is carried by massive particles. We have seen, with equation (11) in section 4.5.1 that this shift is quite small: $1.18 m^3 p_0^3$, that amounts to 0.023 if we assume the dominance by pions of mass 135 MeV and inverse slope 180 MeV. The effect is small²⁰ because the particles that contribute most to the transverse energy are the most relativistic - this effect will effectively be neglected in the sequel.

The fact that the target and projectile are of unequal sizes results in a much larger contribution to the shift. If there was a complete thermalization of the participants, with isotropic re-emission of the energy, $\langle \eta \rangle$ would simply be the rapidity of the center-of-mass of the participants. This is a rapidly changing function of the ratio q of the number of participants

$$y(\text{cms}) = y(\text{cms}, q=1) + \frac{1}{2} \ln \left(\frac{1 + (1 + \beta)\gamma q}{1 + (1 - \beta)\gamma q} \right) - \frac{1}{2} \left(\frac{1 + (1 + \beta)\gamma}{1 + (1 - \beta)\gamma} \right) \approx y(\text{cms}, q=1) + \frac{1}{2} \ln q$$

In an opposite extreme, let us consider a collision between two quasi-transparent nuclei, where only a few nucleon-nucleon collisions occur. In that case, $\langle \eta \rangle$ is simply the rapidity of the proton-proton center-of-mass, no matter how large is the difference between the projectile and target atomic numbers. The reality is probably in between the two extreme situations. That is, we know that a large fraction of the transverse energy does not come from isolated nucleon-nucleon collisions, but on the other hand, there is no absolute evidence for thermalization.

Another possible cause of change in $\langle \eta \rangle$ is the trigger bias. The selection of central, intermediate, or peripheral collisions is made using windows of measured transverse energy. If the

²⁰ In dN_{ch}/dy , the effect can be more important

transverse energy is measured in the range $-0.1 < \eta < 2.9$, the mere selection of the events will favor transverse energy in the range $-0.1 < \eta < 2.9$ with respect to the other region, decreasing $\langle \eta \rangle$. The strength of this trigger bias effect depends on the strength of the correlation of the transverse energy between the backward and the forward pseudorapidity regions, and since the correlations were already studied in 4.5, this subject will not be further discussed here. To avoid the trigger bias, the transverse energy in our full η acceptance is used for the selection of the events. The selection with this E_T is the closest we have to an actual selection of impact parameter, with a minimum effect on $dE_T/d\eta$.

The second moment w of the pseudorapidity distribution of transverse energy is defined by:

$$w^2 = \frac{\int (\eta - \langle \eta \rangle)^2 \frac{dE_T}{d\eta}}{\int \frac{dE_T}{d\eta}}$$

If we assume that there are only a few isolated nucleon-nucleon collisions, the second moment will be the same as that of proton-proton collisions. At fixed energies, the characteristics of proton-proton collisions are known, and also therefore the value of w . At very high energy, there appears a 'plateau', and we get.

$$w = \frac{v(\text{proj}) - v(\text{target})}{\sqrt{12}}$$

The opposite extreme would be a perfect thermalization with isotropic re-emission of the energy. In that case, w is a mathematical constant

$$w^2 = \frac{\int_{-\infty}^{\infty} dy^2 \cosh^3 y}{\int_{-\infty}^{\infty} dy \cosh^3 y} = 2 \left(\frac{\pi^2}{8} - 1 \right) \approx 0.46 \quad w \approx 0.68$$

The actual w can be expected to lie between these two extremes $0.68 < w < 1.7$ at 200 GeV and $0.68 < w < 1.36$ at 60 GeV. Note that the fact that $w > 0.68$ implies that the 'event shape' viewed in the center-of-mass is prolate along the beam directions.

The third moment of the pseudorapidity distribution of transverse energy can also be used as a sensitive test of models [96]. However the third moment is zero both for the plateau/transparency limit and the thermalization/isotropy limit. More complex models of the collision could produce non-zero third moments, but we have decided not to present third moments in this work. The

observed skewnesses are sufficiently small (-0.05 to 0.10 were measured) that the distributions can be fitted with Gaussians.

Besides the mean values, the event-to-event fluctuations of the first and second moments can be considered. It was observed that the event-to-event fluctuation of the average pseudorapidity decreases approximately as the inverse of the transverse energy, as shown in Figure 58, for the case of ^{32}S -W collisions. The naive expectation is that the magnitude of fluctuations of the average in a sampling of the pseudorapidity distribution with N particles, should be $w \sim 1/\sqrt{N}$. Since multiplicity and transverse energy are proportional, the data are in contradiction with this naive expectation. The cause might be the addition of impact parameter fluctuations, for a study of fluctuations see [97]. The event-to-event fluctuations of the width are about half of the fluctuations of the first moment (a factor $1/\sqrt{2}$ is expected for the sampling of a distribution with N particles). The only importance of this for our discussion is that it shows that the fluctuations of moments are small. Therefore, in heavy-ions, the average event represents rather well most individual events.

We summarize the values of $\langle \eta \rangle$ for ^{32}S on various target nuclei in Figure 59. Similarly, Figure 60 shows the value of w for ^{32}S colliding with Al, Ag, W, Pt, and U nuclei as a function of E_T , defined in the region $-0.1 < \eta < 5.5$. The IRIIIOF and IRIS Monte Carlo underestimate the backward rapidity shift.

In the collisions of oxygen or sulfur nuclei with large target nuclei, we observe a decrease of the first moment of the pseudorapidity density of transverse energy $\langle \eta \rangle$ with increasing transverse energy. The presence of this effect in the case of collisions of oxygen nuclei with tungsten nuclei was already noted in reference [85], but it was shown for transverse energy in the pseudorapidity range -0.1 to 2.9 which is 'backwards', so that the observed effect can be due to 'trigger bias'. With E_T measured over a practically complete domain of pseudorapidity, transverse energy, we still observe a shift towards the target side for large transverse energy. This must then be due to an increase of the projectile-target asymmetry at small impact parameters compared to large impact parameters. A confirmation of the reality of this effect is given by the Sulfur-Aluminium collisions, where no shift is observed. In that case, since the target nucleus is not larger than the projectile nucleus, there should not be any backwards shift with increasing transverse energy (if anything, there should be a forward shift, obviously).

We can tentatively provide an understanding of these results by assuming that $\langle \eta \rangle$ is the rapidity of the center-of-mass system of the participants. The number of participants in each nuclei can be determined from the volume of intersection of a sphere with a cylinder, for which a rather complicated analytical expression exists [89]. We will consider two limit cases that were also derived in the reference [89].

In the peripheral limit, the volume of intersection of a sphere of radius r with a cylinder of radius R at impact parameter b is:

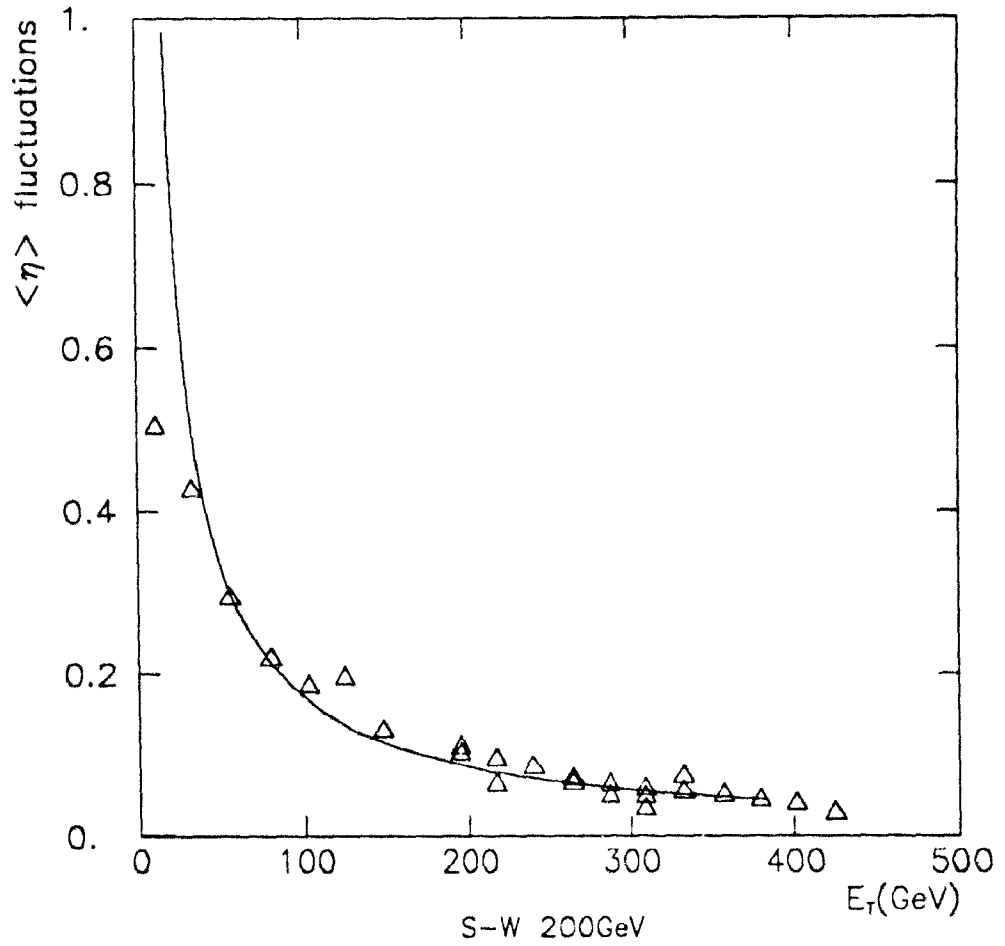


Figure 58: The measured fluctuations of $\langle \eta \rangle$ as a function of the E_T . It is fitted to a $1/E_T$ law.

$$\pi r R^{1/2} b^{-1/2} (b-r-R)^2$$

therefore the ratio of the number of participants is $q = \left(\frac{A_p}{A_T}\right)^{1/6}$ and the center of mass rapidity is the proton-proton center of mass rapidity plus $\frac{1}{2} \ln\left(\left(\frac{A_T}{A_p}\right)^{1/6}\right) = \frac{1}{12} \ln\left(\frac{A_T}{A_p}\right)$. In the central case, for a large target, the ratio of the number of participants is $q = \frac{3}{2} \frac{A_T^{1/3}}{A_p^{1/3}}$, and therefore the center of mass rapidity differs from the proton-proton one by $\frac{1}{2} \ln\left(\frac{3}{2} \frac{A_T^{1/3}}{A_p^{1/3}}\right) = \frac{1}{2} \ln \frac{3}{2} + \frac{1}{6} \ln\left(\frac{A_T}{A_p}\right)$

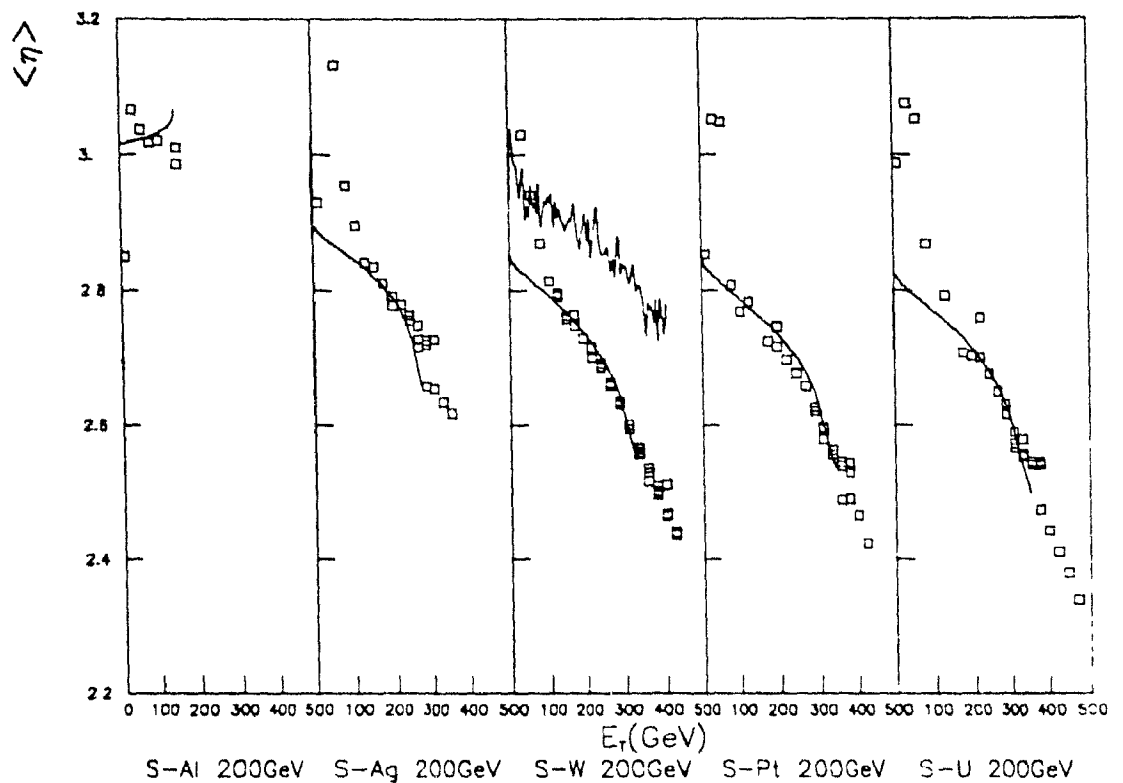


Figure 59: The first moment of the pseudorapidity density of transverse energy $\langle \eta \rangle$ as a function of transverse energy for various targets. They are fitted with the prediction of the rapidity of the center-of-mass of the participants given by [89], the impact parameter being obtained from the value of E_T using WNM geometrical fits. The upper curve represents the prediction of IRIS.

Thus, we see that when the target nucleus is larger than the projectile nucleus, the central collisions are more backwards than the peripheral ones, simply by kinematics and geometry.

The case of partial stopping with a plateau is particularly interesting since it entails a relationship between $\langle \eta \rangle$ and w . We will use it as a 0th order approximation for the behaviour of 'string' models. The assumption is the following: The leading baryons carry no transverse energy, it is all carried by the produced mesons. The transverse energy is produced in a flat plateau between the rapidities of the two sets of leading baryons, in agreement with the inside/outside cascade picture. As a consequence, depending on the degree of stopping, $\langle \eta \rangle$ will vary from the proton-proton center-of-mass to the center-of-mass of the participants.

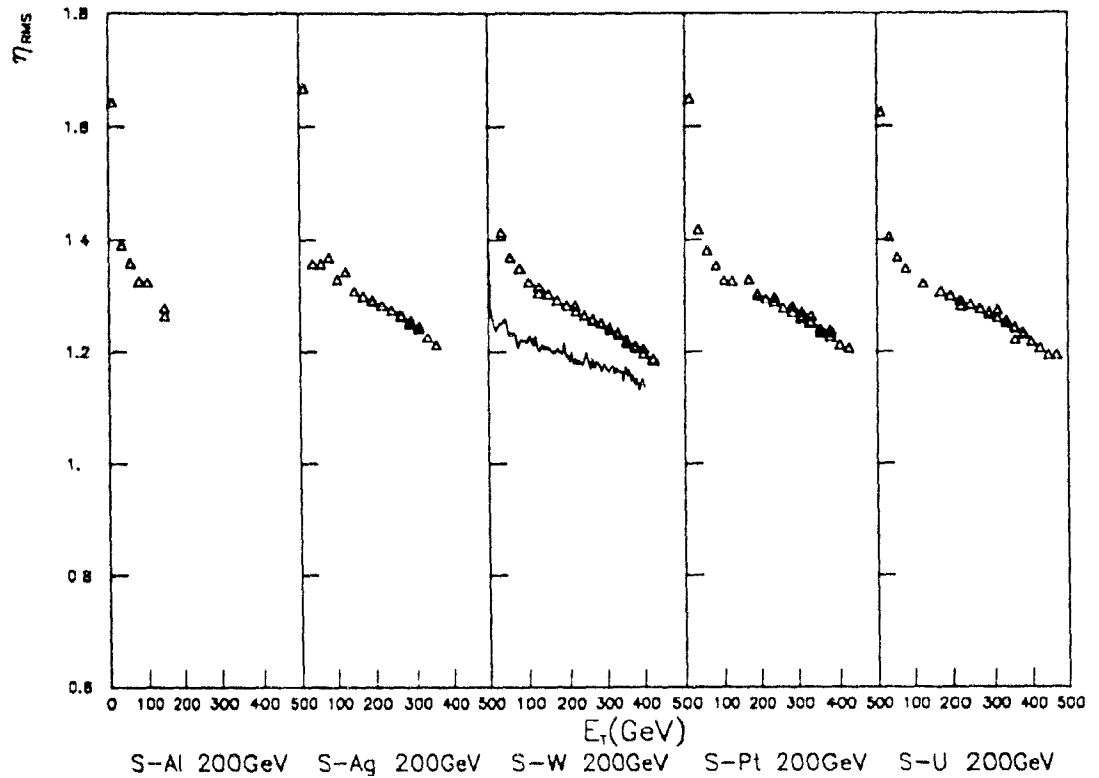


Figure 60: The width w of the pseudorapidity distributions of transverse energy, as a function of E_T . The curve is the IRIS prediction.

In order to proceed, let us call H the height of the plateau, y_1 the rapidity of the target participants (of total mass M_1), and y_2 the rapidity of the projectile participants (of total mass M_2). The conservation of energy and longitudinal momentum, together with the assumption of a flat plateau, make it possible to deduce y_1 and y_2 as a function of H . The symmetry argument which is at the base of the flatness of the plateau is likely to break down when the two baryons are too close in rapidity ($y_2 - y_1 < 1$). Not considering these problems, we are left to solve:

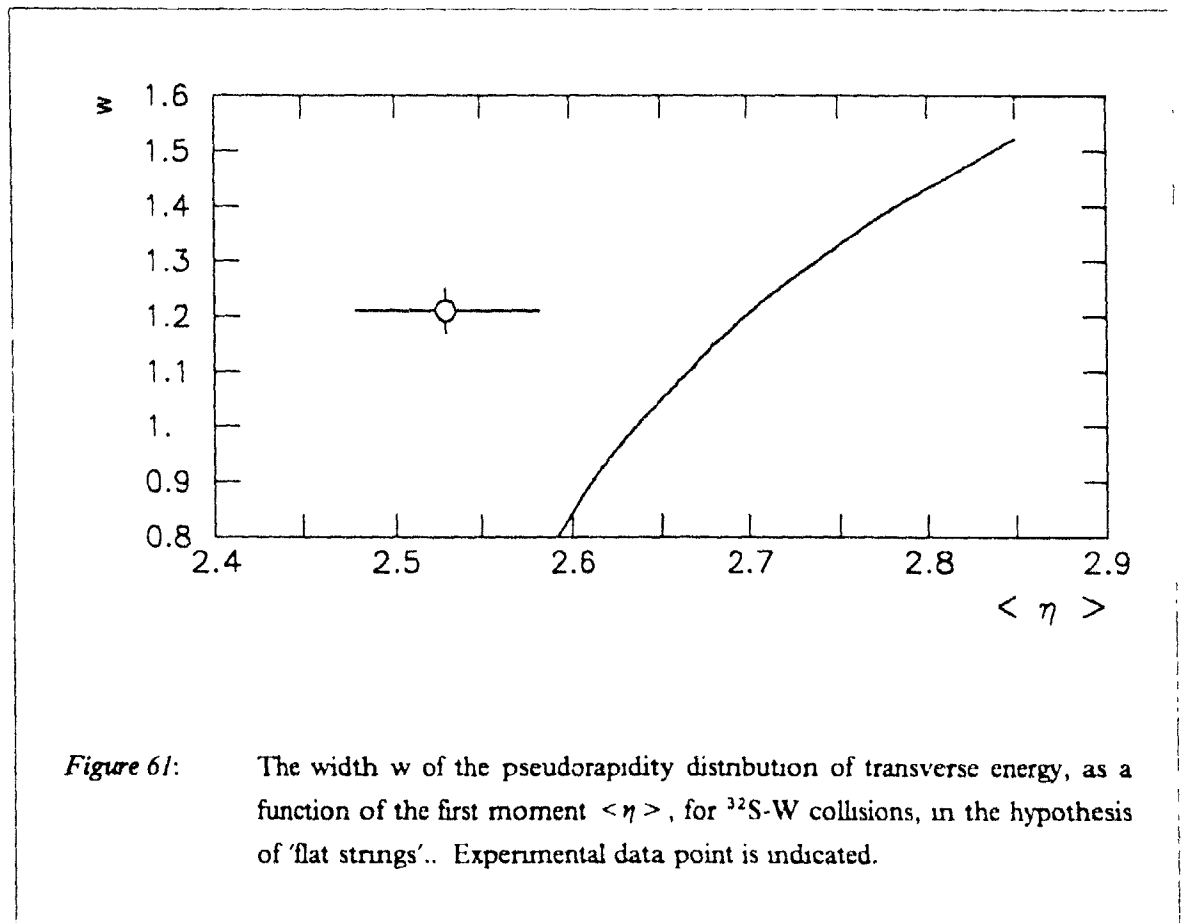
$$\begin{cases} E = M_1 \cosh y_1 + M_2 \cosh y_2 + H(\sinh y_2 - \sinh y_1) \\ p = M_1 \sinh y_1 + M_2 \sinh y_2 + H(\cosh y_2 - \cosh y_1) \end{cases}$$

where the terms in H represent the integrated energy and momentum carried in the plateau of constant height H . This is a second degree equation in y_1, y_2 with solution:

$$y_1 = \ln \left(\frac{M_{CM}^2 + M_1^2 - M_2^2 - \sqrt{(M_{CM}^2 + M_1^2 - M_2^2)^2 - 4M_{CM}^2(M_1^2 - H^2)}}{2M_1 - H(E - P_L)} \right)$$

$$y_2 = \ln \left(\frac{M_{CM}^2 + M_2^2 - M_1^2 + \sqrt{(M_{CM}^2 + M_2^2 - M_1^2)^2 - 4M_{CM}^2(M_2^2 - H^2)}}{2M_2 + H(E - P_L)} \right)$$

In these equations, M_{CM}^2 is the square of the energy available in the center of mass (also called s). $E - P_L$, the difference between the energy and the momentum in the laboratory frame of reference is very well approximated by the mass of the target M_1 . The relationship between $w = (y_2 - y_1) \sqrt{12}$ and $\langle \eta \rangle = y_2 + y_1$ that is obtained for sulfur tungsten collisions is plotted in Figure 61. The data points appear to disagree; the false assumption of the existence of a flat plateau in nucleon-nucleon collisions is the most obvious reason (but maybe not the only) of the failure of this model



In conclusion, we have seen that the pseudorapidity distributions of transverse energy in heavy-ion collisions are well described using simple Gaussians. We have checked the accuracy of the experimental reconstruction of these curves by verifying the effect of the projectile/target symmetry. It appears that the production of transverse energy is centered about the center-of-mass system of the participating nucleons, as if there was a complete stopping followed by an isotropic reemission, whereas the width in rapidity of this production of transverse energy significantly disagrees.

4.7 Hydrodynamic phenomenology and estimates of the energy density

The fact that the average pseudorapidity of the transverse energy production is the pseudorapidity of the center-of-mass, while the transverse energy emission is not isotropic, is best explained by the hydrodynamic model of longitudinal expansion. In section 1.13, we have been using some drastic simplifications: we are making a strictly one-dimensional computation while it is known that an expansion also takes place transversely; we have supposed that due to the initial high viscosity, the shock waves are 'damped off' while they could carry a large amount of transverse momentum; and we have considered that the fireball has an initial Gaussian density, while quite different shapes of density are perhaps created.

Even hindered by these oversimplifications, the hydrodynamic model of longitudinal expansion enables us to reproduce the shape (see Figure 62), first moment of pseudorapidity (the average pseudorapidity), the width of the pseudorapidity distribution, and the constancy of the average transverse momentum per particle (due to a more-or-less constant freeze-out temperature). On this last point, it must be said that an extremely constant average transverse momentum has been suggested as a signature of the first-order phase transition [98].

A direct prediction of our model of longitudinal expansion is that the pions are emitted from a volume that is quite large compared to that of the initial 'compressed nuclear pancakes', particularly in the longitudinal direction. The interferometric measurements of the NA35 collaboration seem to confirm this [99] [100].

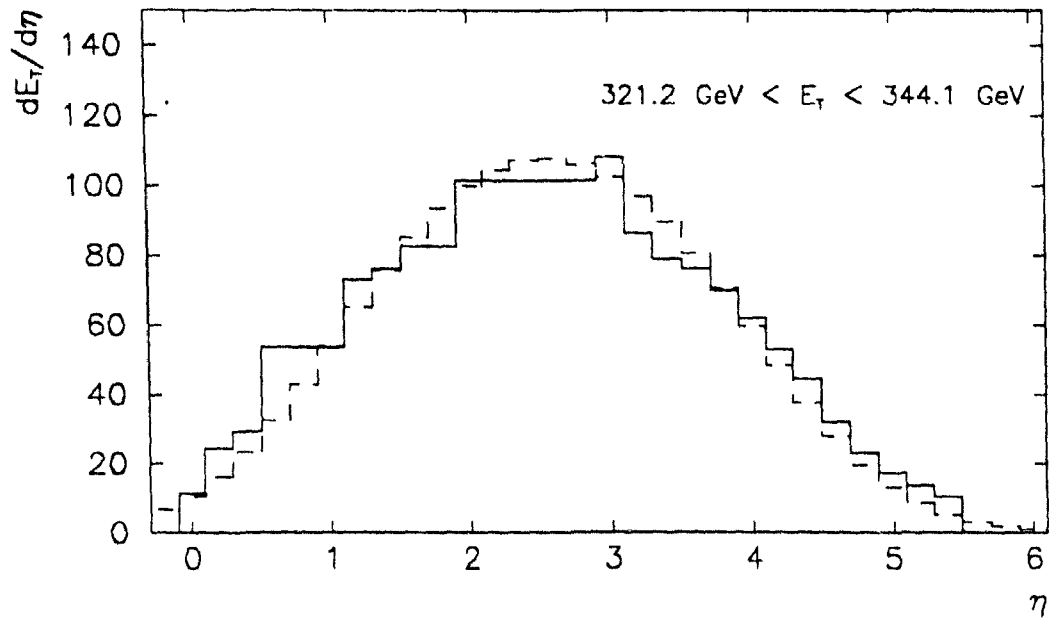


Figure 62: The experimental $dE_T/d\eta$ (solid line). This is compared to our hydrodynamics prediction (dashed line) of section 1.13 with $\tau = 9$

4.7.1 Comparison with first moment

In this hydrodynamic model, the first moment of the pseudorapidity is by definition the rapidity of the center-of-mass of the participants. We have seen in the Figure 59 that the data agrees to a very good precision with this prediction. For values of the transverse energy up to the value which corresponds to the central collisions, the impact parameter corresponding to a given transverse energy can be calculated in a straightforward way. The $\langle \eta \rangle$ at larger values of the transverse energy, in the framework of the hydrodynamic model, would be explained by a rare fluctuations of the number of target participants, while the number of projectile participants is fixed to 32. When the derivative of the forward transverse energy with respect to the number of target participants is taken, the increase due to the increase of \sqrt{s} is compensated by a decrease due to the rapidity shift. This can be calculated in the framework of our simple hydrodynamic model, and numerically, the cancellation is almost perfect in S-W collisions, providing a quantitative explanation for the independence of E_{TF} from E_{TB} at least in the case of W.

4.7.2 Comparison with width

As seen in the introduction, longitudinal expansion during a time of 8 ± 2 units times the initial size of the gaussian results in widths of the pseudorapidity distribution of the order of 1.2. This is a slight underestimate of the data. In addition, the narrowing of the distributions with increasing transverse energy is not explained by our simple hydrodynamic model. A broadening of the distribution comes from the variation of the rapidity of the center-of-mass along the impact parameter direction when the impact parameter is non-zero, but the magnitude does not appear to be sufficient. Presumably the width, at very small transverse energies, is ultimately determined by the characteristics of individual nucleon-nucleon collisions. It is speculated that more complex and realistic hydrodynamic models might account for an increased width with respect to the width that we obtain starting from a Gaussian profile at rest

Nonetheless, it must be remembered that the agreement with the model of longitudinal expansion is much better than with the prediction of isotropy ($w = 0.68$).

4.7.3 Attempt to identify an exclusive signature of hydrodynamics

We have attempted to confirm unambiguously the hydrodynamic model by the observation of the small expected correlation between rapidity and azimuth, when the impact parameter is non-zero, as discussed in section 1.3.1 of the introduction. It would appear as a positive correlation, appearing at medium transverse energy (in order to select rather large impact parameters), between the transverse energy of two regions separated by 180 degrees in azimuth, and located on different sides of the center-of-mass rapidity.

In order to investigate this possibility, we have summed the transverse energy of the scintillator calorimeters photomultipliers and of the electromagnetic part of the ULAC in 64 regions making an 8×8 grid in pseudorapidity and azimuth. The regions are about 0.7 in rapidity and exactly 45 degrees in azimuth. The measure of the correlation is subject to systematic errors that include the effect of trigger bias, and intercalibration errors. Our sample of $\approx 1\,000\,000$ events was divided in 20 bins of raw multiplicity in RING2. The correlation between two regions i and j is calculated by:

$$C_w = \frac{\langle E_i E_j \rangle - \langle E_i \rangle \langle E_j \rangle}{\langle E_i \rangle \langle E_j \rangle}$$

The magnitude of the statistical error has been estimated by taking the same correlation with several pairs of regions rotated in azimuth; In order to get rid of spurious (non-hydrodynamic) correlations, we have subtracted the correlation at 90 degrees from the correlation at 180 degrees. The most obvious correlation at large distances is the effect of the conservation of momentum, which results in a correlation inversely proportional to the total multiplicity. In Figure 63 we plot the product of the

raw RING2 multiplicity by the correlation between the regions of pseudorapidity $0.9 < \eta < 2.0$ and $2.9 < \eta < 3.6$. These two regions are located on the two sides of the maximum of $dE_T/d\eta$, and therefore we should observe the hydrodynamic correlation defined in section 1.13.1 peaking at intermediate impact parameters.

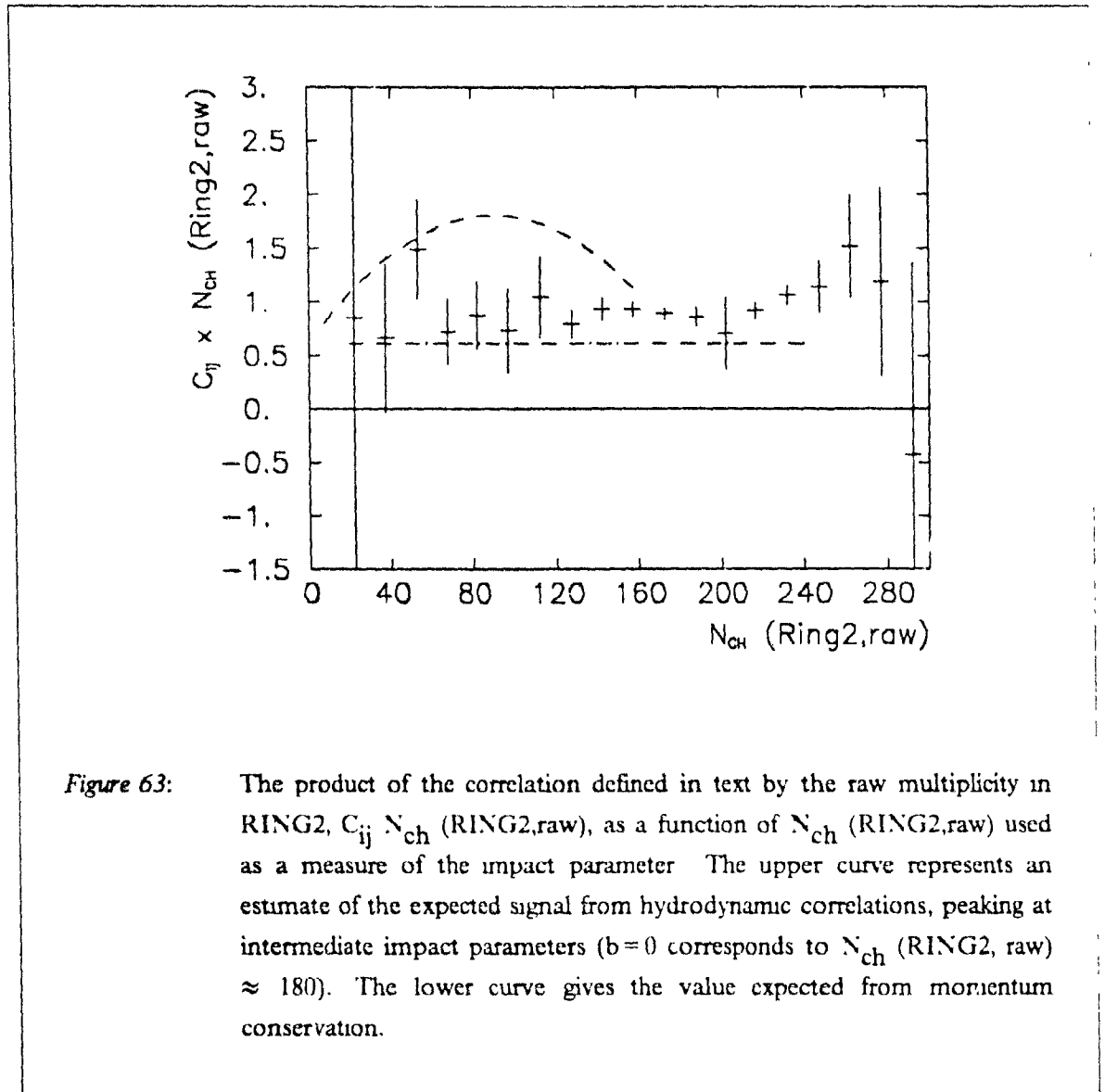


Figure 63: The product of the correlation defined in text by the raw multiplicity in RING2, $C_{ij} N_{ch} \text{ (RING2,raw)}$, as a function of $N_{ch} \text{ (RING2,raw)}$ used as a measure of the impact parameter. The upper curve represents an estimate of the expected signal from hydrodynamic correlations, peaking at intermediate impact parameters ($b=0$ corresponds to $N_{ch} \text{ (RING2,raw)} \approx 180$). The lower curve gives the value expected from momentum conservation.

The excess correlation at medium transverse energy amounts to: $C_{ij} \text{ (additional)} = 0.004 \pm 0.002$. It is compatible with the order of magnitude expected for the hydrodynamically induced correlation from our model (0.014), but does not agree with it, and a null effect is not totally excluded. This data might suggest that an hydrodynamic behaviour only establishes at nearly central collisions. A similar conclusion of very small collective net transverse momenta was reached in a study [101] of

the target fragmentation region by the WA80 collaboration.

The correlation between other regions of pseudorapidity gave consistent results. In a systematic study for net collective transverse momenta, all the correlations would be combined together to reduce the statistical errors. This is outside the scope of this work.

Another exclusive signature of our hydrodynamic model would be that the rapidity density of participant baryons should be the same as the rapidity density of energy density, that is, strongly peaked at the center-of-mass rapidity.

4.7.4 Stopping, energy density and Equation Of State (EOS).

The estimate of the energy density discussed in the introduction can be used as an experimental measure of the energy density provided we take into account the fact that a fraction of the energy of the two nuclei may leave the interaction region without having contributed to the energy density. This leads to the following formula for the energy density.

$$\varepsilon = \varepsilon_M \frac{E_T}{E_{T,max}}$$

where ε_M is the energy density of equation (4) discussed in the introduction.

The energy density has often been computed [85] [86] by assuming that the fireball of high energy density decays isotropically, resulting in $E_{T,max} = \pi/4(\sqrt{s} - m(N_T + N_p))$.

In the framework of our simple model of longitudinal expansion, this gets reduced to $E_{T,max} = \pi/4(\sqrt{s} - m(N_T + N_p) - \alpha_L)$, where $\alpha_L = 0.35 \pm 0.10 \sqrt{s}$. Therefore, higher energy densities are produced.

The values of stopping, naïve expression of the energy density²¹, and energy density taking into account the work of the longitudinal expansion, are listed in Table 24

²¹ The factor $\pi/4$ discussed in the introduction is present here

Table 24: Summary of the stopping fractions for average central collisions

nuclei	E_T [GeV]	stopping(naive)	stopping	ϵ (naive) [GeV/fm ³]	ϵ [GeV/fm ³]
O - W 200 GeV	180.	0.46	0.76	3.4	5.6
S - W 200 GeV	335	0.49	0.80	4.7	7.8

The large values of stopping obtained in the framework of our model are consistent with the observation [102] that the leading baryon is shifted backwards by ≈ 2.5 units of rapidity in central collisions of protons with large nuclei like W, and with the fact that the distributions of energy at zero degree measured by the WA80 collaboration extend down to about 1/10 of the beam energy [103], both of which imply stoppings of the order of 0.90.

Another interesting consequence is that the final multiplicity, the final width of the pseudorapidity distribution, and p_T per particle are more influenced by the properties of the matter itself than by the characteristics of the initial production mechanisms (baryon collisions). This provides with powerful new tools to investigate the question of the phase transition

For example, it is relatively easy to show that the final distribution of rapidity in the given volume cannot possibly result from an adiabatic expansion of an ideal pion gas. The Stephan-Boltzmann expressions for the energy density and particle density of an ideal pion gas are

$$\epsilon = 3 \left(\frac{\pi^2}{30} \right) \frac{(kT)^4}{\hbar^3}$$

$$\rho = 3 \left(\frac{\zeta(3)}{\pi^2} \right) \frac{(kT)^3}{\hbar^3}$$

where ζ is the Riemann zeta function, the average energy per particle is $3\zeta(4)/\zeta(3)kT \approx 2.7kT$. Charged and neutral pions are assumed. The experimental width of the pseudorapidity distribution in ³²S-W collisions gives (using the assumption of an ideal pion gas) the initial energy density²², temperature, and multiplicity density (total multiplicity is ≈ 1000) of 9.2 GeV/fm^3 , $180 \times (16)^{1/4} = 360$

²² calculated as discussed in the section 1.6 of the introduction

MeV, and 18 fm^3 respectively. Here, the number 16 corresponds to the ratio of the final to the initial energy density given by Figure 8 for the measured expansion $\tau \approx 9$, and for an ideal gas, the temperature ratio is the quartic root of the density ratio. These numbers do *not* agree with the Stephan-Boltzmann expression. For $T \approx 360 \text{ MeV}$, ϵ would have been $\approx 2 \text{ GeV fm}^3$. There are too many particles with too small temperature in the final state, for the initial, and intermediate stages to have been perfect pion gases. Stachel and Braun-Munzinger [39] have suggested that this might be an indication of a phase with quark and gluon degrees of freedom.

4.8 Results from the external spectrometer

In the framework of the hydrodynamic phenomenology and of the possibilities of very large stoppings, there are two experimental points where the external spectrometer can possibly increase the evidence in favour of the hydrodynamic model. Firstly, there is the question of the transverse momentum per particle. It is predicted that the distribution of secondaries should reflect the production from the freeze-out of a thermalized system. Therefore, the spectra of transverse momenta should stay more-or-less identical if we vary rapidity, impact parameter, or size of nuclei. The experimental results from the external spectrometer reveal that the spectra of transverse momentum are identical to a very large precision (Figure 64). Having studied the variation of the p_T per particle as a function of transverse energy, it remains to be studied as a function of rapidity. The preliminary results [104][88], using the pseudorapidity distribution of multiplicity measured by the silicon detectors compared to the pseudorapidity distributions of transverse energy, seem to indicate that the average P_T per particle does not vary much with pseudorapidity, which would suggest that the p_T spectra are independent of rapidity. A similar result is found for the average p_T per particle of the neutrals [105].

Secondly, using the particle identification capability of the external spectrometer [69], we should investigate the baryon-meson ratio as a function of rapidity. If this ratio is almost constant, it will be evidence for the applicability of hydrodynamics and of a large stopping. However, at the present stage, the analysis of the data from the external spectrometer is at an early stage. Preliminary results from the NA35 collaboration [106] indicating a large net baryon density at the center-of-mass rapidity in central ^{32}S - ^{32}S collisions, are favouring this possibility.

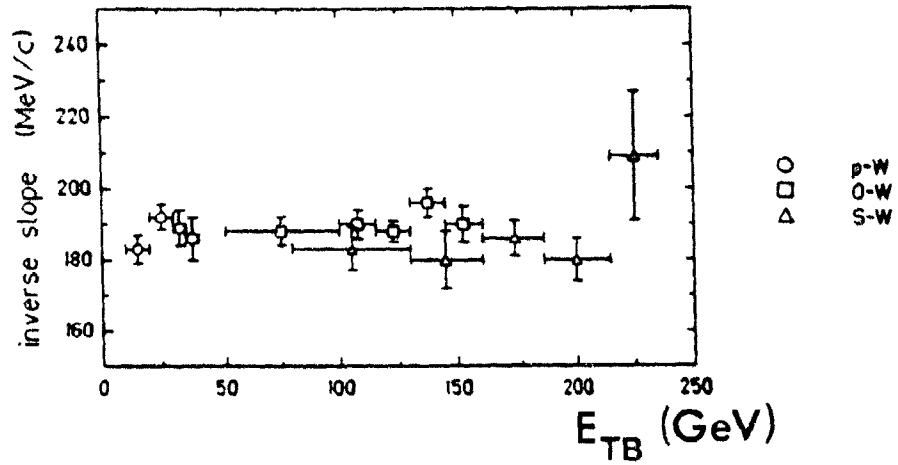


Figure 64: The inverse slope of the p_T distribution of negative particles, as a function of E_{TB} , in the external spectrometer acceptance ($0.9 < y < 1.9$). This completes a scan of nuclear sizes and impact parameters.

Chapter 5

Conclusions

The HELIOS experiment has been successfully operated during the two 2 weeks periods of heavy-ion running of the CERN SPS in 1986 and 1987, these represented the first time that temperatures of the order of 200 MeV over large volumes have been achieved in a laboratory environment. Careful calibrations of the calorimeters maintained over long periods of time through measurements of the signal produced by the radioactivity of the depleted Uranium, and by pulsing with high-precision test charges, permit a precision of 7% on the absolute transverse energy scale and of the order of 1 to 2% on the relative energy scale. An electronic trigger system allows the fast recognition of the energy flow characteristics of an event for the high-statistics collection of central collisions and of rare events in the tail of transverse energy density. Small silicon hodoscopes and a spectrometer covering a fraction of solid angle characterize the transverse energy flow.

After the events from several targets are separated from the background of non-target interactions, recognizable by peculiar correlations of the hits in the silicon hodoscope, we maintain precisions of the order of a few percents through the correction of the pseudorapidity distributions and the distributions of transverse energy. These corrections are made using Monte Carlo simulation of the detectors guided by our calibration measurements and confirmed by measurements as far as the calorimeter fluctuations are concerned.

The shape of the differential cross-sections of transverse energy reflects the geometry of impact parameters and alignment of deformed nuclei. We have established how to extract the physical parameters of central collisions from these distributions. The transverse energy of a central collision is a power function of the atomic mass number where the exponent is varying with the pseudorapidity coverage of the transverse energy measurement. The fact that our pseudorapidity acceptance is separated in a backward and a forward region provides additional insight on the dynamics, suggesting that the mechanism of transverse energy production in the forward region may be independent of the mechanism of transverse energy production in the backward region in collisions with large target nuclei. It also provides a way to intercalibrate the transverse energy using a symmetry of nature.

The examination of the pseudorapidity distributions of transverse energy shows that while a large fraction of the energy available initially in the center-of-mass is going into the formation of a fireball, the energy flow from this fireball is not isotropic. This suggests that the final energy flow is largely determined by a very large fraction of the energy being stopped in the center of mass and undergoing a hydrodynamic expansion where the longitudinal expansion dominates. A simple model, where a gaussian profile of an ideal gas expands until freeze-out conditions are met, essentially reproduces all the characteristics of the final energy flow. If this scenario is true, the final characteristics of the energy flow are much more determined by the multiple reinteractions of the secondaries - possibly by the Equation of State (EOS) - than by their initial distributions in proton-proton collisions. No feature of the final distributions is found which disagrees with this interpretation. In particular, we have seen that the first moment of the pseudorapidity distribution of transverse energy is rather well determined by the centre-of-mass rapidity of the participants, an empirical fact that any proposed model will have to reproduce. However, an exclusive signature of hydrodynamics is still needed. This signature would have to be comparable to the evidence gathered in favour of hydrodynamics in lower-energy experiments with heavy-ions. We have started, in the present work, to develop the techniques (Measurement of cross-sections at half plateau, correlations of transverse energy in rapidity and azimuth, among others) allowing the extraction of the dynamical informations on the energy flow from distributions where the collision geometry plays an important role. A very detailed understanding of the geometry is needed in order to reach that goal, and a description of the nuclear geometry defined in terms of spheres and ellipsoids with sharp edges, although already very detailed, is probably not sufficient. However the analytic formulae derived with this geometry provide useful guidelines for a situation where the nuclear geometry description will become even more justified if large nuclei such as Pb, or U, are accelerated in the future.

Very large values of the stopping, measured by the transverse energy divided by the maximum transverse energy, have been observed with the largest target nuclei; this suggests that the hydrodynamic description of hadronic matter, which has to be valid for very large nuclei, is more and more relevant as we increase the size of both the target and the projectile.

If we now make an outlook of these results, we see that the measurement of hydrodynamic quantities are compulsory in order to measure the equation of state (EOS). As a first step, we would need an exclusive signature of hydrodynamics, together with the observation, with increasing nuclear sizes, of the onset of a hydrodynamic behaviour above the behaviour dictated by the superposition of nucleon-nucleon collisions.

The width of the observed pseudorapidity distribution would then give us the amount of expansion that has taken place. From that, and the observed final temperature, *assuming the EOS of an ideal relativistic gas*, we can obtain the initial temperature. Since we also know the initial energy density (this knowledge was improved in our study by recognizing that the energy flow does not have to be isotropic), we have a first measure of the terms of the EOS ($\epsilon(T)$).

If the measured EOS corresponds to that assuming an ideal relativistic gas, then the logic loop is closed. In the case this condition is not satisfied, we cannot directly measure the EOS because we do not know the initial temperature. We still have, however, a measure of the EOS, but since the initial temperature is then itself dependent on the EOS (in a way that must be established by computer simulations), a solution will be found only by solving a polynomial equation in the EOS (or equivalently a polynomial equation in the initial temperature), instead by a straightforward measurement.

We have seen in 4.7.4 that the EOS experimentally differs from that of an ideal pion gas, the deviation indicates that the initial high-temperature state had more degrees of freedom than the final state. Thus we will have to follow the program outlined above in order to realize progress on the measurement of the EOS. This implies that very high statistics data would be needed and considerable efforts from the theory side requested for its better understanding. There exists a strong motivation for these studies in view of the large energy densities that are created in any case in these collisions (for an estimate à la Bjorken see [85][86] [10⁷]), and of the very large ones that are created if our understanding of the longitudinal expansion is correct.

Indeed, the energy density, when the effect of the hydrodynamic work done by the longitudinal expansion is included, is found to be of the order of 10 GeV fm^3 , and therefore clearly much above the critical value of about 2.5 GeV fm^3 obtained from lattice QCD calculations for the deconfinement transition [15], and clearly larger than the energy density of $\approx 0.15 \text{ GeV fm}^3$ inside the nucleon.

Appendix A

Exact formulae for hard-sphere nuclei.

The approximation that the nuclei are spherical, with a uniform density inside the nuclear radius, is often used. This limit becomes increasingly valid for large nuclei. In this limit, there exist exact analytic expressions for certain quantities

A.1 The number of nucleons in the central tunnel

The volume of the central tunnel is often approximated by taking the diameter of the larger nucleus times the circular area of the smallest nucleus. It corresponds to 'making the edges of the tunnel flat'. It is instead possible to compute this volume exactly:

$$V = \int_0^r 2\pi x dx (2\sqrt{R^2 - x^2})$$

changing variable to $z = x^2$, we obtain a binomial form:

$$V = \int_0^{r^2} 2\pi dz (R^2 - z)^{1/2} = \left[-4/3\pi (R^2 - z)^{3/2} \right]_0^{r^2} = \frac{4\pi}{3} [r^3 - (r^2 - R^2)^{3/2}]$$

multiplying through by the density, developing the factor $4\pi/3$, this formula gives a particularly simple formula for the number of participants in the largest nucleus:

$$N = A - (A^{2/3} - B^{2/3})^{3/2}$$

(A being the number of nucleons of the nucleus with radius R, and B the number of nucleons of the smaller nucleus with radius r)

A.2 The number of collisions and the overlap integral in the central case

Assuming the nucleus is spherical with uniform density, the expectation value of the number of collisions is given by the overlap integral.

$$I = \int_0^r x dx \int d\phi (2\sqrt{r^2 - x^2})(2\sqrt{R^2 - b^2 - 2bx \cos\phi - x^2}) \rho^2 \sigma_{in} \quad (12)$$

This overlap integral is easy to compute with a small computer program, but it is very hard, and perhaps impossible, to make the integral analytically in the general case. It is possible in the central case. When the impact parameter b is zero, equation (12) is just

$$I = \int_0^r 2\pi x dx (2\sqrt{r^2 - x^2})(2\sqrt{R^2 - x^2}) \rho^2 \sigma_{in}$$

where we recognize the product of the thicknesses. Simplifying:

$$I = \int_0^r 8\pi x dx \sqrt{(r^2 - x^2)(R^2 - x^2)} \rho^2 \sigma_{in}$$

changing variable to $z = x^2$:

$$I = \int_0^{r^2} 4\pi dz \sqrt{(r^2 - z)(R^2 - z)} \rho^2 \sigma_{in}$$

changing variable to $y = \frac{r^2 + R^2}{2} - z$:

$$I = \int_{\frac{R^2 - r^2}{2}}^{\frac{R^2 + r^2}{2}} 4\pi dy \sqrt{y^2 - \frac{1}{4}(r^2 - R^2)^2} \rho^2 \sigma_{in}$$

The primitive of the hyperbola $\sqrt{y^2 - K^2}$ is found by integrals by parts, it is $\frac{1}{2}y\sqrt{y^2 - K^2} - \frac{K^2}{2}\cosh^{-1}y/K$

Therefore:

$$I = 4\pi\rho^2\sigma_{in} \left[\frac{1}{2} \frac{r^2 + R^2}{2} \sqrt{\left(\frac{R^2 + r^2}{2}\right)^2 - \left(\frac{R^2 - r^2}{2}\right)^2} - \frac{1}{2} \left(\frac{R^2 - r^2}{2}\right)^2 \cosh^{-1}\left(\frac{R^2 + r^2}{R^2 - r^2}\right) \right]$$

The final simplification, using $\cosh^{-1}\left(\frac{R^2 + r^2}{R^2 - r^2}\right) = \ln\left(\frac{R+r}{R-r}\right)$, gives:

$$I = \pi\rho^2\sigma_{in} \left[rR(r^2 + R^2) - \frac{1}{2}(R^2 - r^2)^2 \ln\left(\frac{R+r}{R-r}\right) \right] \quad (13)$$

A.3 Participant volume at non-zero impact parameter

The expression for the volume of intersection of a sphere (radius r) with a cylinder (radius R) at impact parameter b is:

$$V = \frac{4\pi}{3}r^3\theta(R-b) + \frac{4}{3\sqrt{A-C}} \left[\Pi \frac{A^2s}{C} - K(As - \frac{(A-B)(A-C)}{3}) - E(A-C)(s + \frac{4A-2B-2C}{3}) \right]$$

when $r > b + R$,

$$\frac{4\pi}{3}r^3\theta(R-b) + \frac{4/3}{\sqrt{A-C}} \left[\Pi \frac{B^2s}{C} + K[s(A-2B) + (A-B)\frac{3B-C-2A}{3}] + E(A-C)(-s + \frac{2A+2C-4B}{3}) \right]$$

when $r < b + R$, and

$$\frac{4\pi}{3}r^3\theta(R-b) + \frac{4}{3}r^3 \tan^{-1}\left(\frac{2\sqrt{bR}}{b-R}\right) - \frac{4}{3}\sqrt{A-C}(s + \frac{2}{3}(A-C))$$

when $r = b + R$.

Here θ is the unit step function, $K \equiv K(k)$ is the complete elliptic integral of the first kind, $E \equiv E(k)$ is the complete elliptic integral of the second kind, and $\Pi \equiv \Pi(k, -\alpha^2)$ is the elliptic function of the third kind, and:

$$\left\{ \begin{array}{l} A = \max(r^2, (b+R)^2) \\ B = \min(r^2, (b+R)^2) \\ C = (b-R)^2 \\ k^2 = \frac{B-C}{A-C} \\ -\alpha^2 = \frac{B-C}{C} \\ s = (b+R)(b-R) \end{array} \right.$$

The derivation of this formula, the numerical methods needed to use it, and examples of applications are given in ref.[89].

References

1. G. 'tHooft and M.Veltman, "regularization and renormalization of gauge Fields" Nucl. Phys B44 (1972) p 189.
2. G.Gerbier et al., "Charges and Angular distributions of fast fragments produced in 3.2TeV ^{16}O collisions with Pb ", Phys. Rev. Lett. 59 (1987) p 2535.
3. Quark Matter Formation and Heavy Ion Collisions, Proceedings of the Bielefeld Workshop May 1982, M. Jacob and H. Satz (Editors), [World Scientific, Singapore, 1982],
Quark Matter '83, Brookhaven, F.W. Ludlam and H.E. Wegner (Editors), Nucl. Phys. A418(1984),
Quark Matter 1984, Helsinki. K. Kajantie (Editor), Lecture notes in Physics 221(1984), Springer, Heidelberg,
Quark Matter '86, Asilomar, L.S. Schroeder and M. Gyulassy (Editors), Nucl. Phys. A461(1987)
4. A.C. Benvenuti et al., Phys. Lett. B195 (1987) p.97.
5. L.D. Landau "Collected papers" No. 88 Izv. Akad. Nauk, Ser. Fiz. 17 (1953) p 51.
6. L.D. Landau and E.M. Lifshitz, "Fluid Mechanics", Pergamon Press (1959) p.499.
7. F. Abe et al., CDF collaboration, "Measurement of the inclusive jet cross-section in $p\bar{p}$ collisions at $\sqrt{s} = 1.8 \text{ TeV}$ ", Phys. Rev. Lett. 62 (1989) p 613.
8. see among others S. Weinberg, "A model of leptons", Phys. Rev. Lett. 19 (1967) p.1264.
9. J.B. Kogut, "The lattice gauge theory approach to quantum chromodynamics", Rev. Mod. Phys. 55 (1983) p.775
10. L.P. Csernai and J.I. Kapusta, "Entropy and cluster production in nuclear collisions", Phys. Rep. 131 (1986) p.223.

11. E.V. Shuryak, "Quantum chromodynamics and the theory of superdense matter", Phys. Rep. 61, (1980) p.69.
12. P. Baclien et al., "Order of the deconfinement phase transition in pure-gauge QCD", Phys. Rev. Lett. 61 (1988) p 1545.
13. R. Hagedorn, "Remarks on the thermodynamical model of strong interactions", Nucl. Phys. B24 (1970) p 93.
14. R. Hagedorn, "How we got to QCD matter from the hadron side by trial and error", in Quark Matter 1984, Helsinki, K. Kajantie (Editor), Lecture notes in Physics 221(1984), Springer, Heidelberg p 53.
15. J. Engels, J. Fingberg, K. Redlich, H. Satz and M. Weber, "The onset of deconfinement in SU(2) lattice gauge theory", Z. Phys. C42 (1989) p.341.
16. JACEE Collaboration, F H. Burnett et al., "High energy cosmic ray events of ultra-relativistic nucleus-nucleus collisions", Nucl. Phys. A447 (1985) p.189.;
17. E.V. Shuryak, "Can recent CERN experiments with 200 GeV/N ^{16}O ions be explained by the independent NN collisions?", Phys. Lett. B207 (1988) p 345.
18. E.V. Shuryak, O.V. Zhironov, "Is the explosion of a quark-gluon plasma found?", Phys. Lett. B171 (1986) p.99.
19. M. Gyulassy, K. Kajantie, H. Kurki-Suonio and L. McLerran, "Deflagrations and detonations as a mechanism of hadron bubble growth in supercooled quark-gluon plasmas", Nucl.Phys. B237 (1984) p 477.
20. A. Bialas and R. Peschanski, "Moments of rapidity distributions as a measure of short-range fluctuations in high-energy collisions", Nucl. Phys. B273 (1986) p 703.
21. R. Albrecht et al., WA80 collaboration, "Fluctuations and intermittency in 200 A GeV $^{16}\text{O} + (\text{C}, \text{Au})$ reactions", Phys. Lett. B221 (1989) p.427.
22. S. Nagamiya, J. Randrup and T.J.M. Symons, "Nuclear Collisions at High Energies", Ann. Rev. Nucl. Part. Sci. 34(1987) p 155.
23. P.J. Siemens and J.O. Rasmussen, "Evidence for a Blast Wave from Compressed Nuclear Matter" Phys. Rev. Lett. 42(1979) p.880.

24. I.R. Halemanc and A.Z. Mekjan, "Particle production, chemical equilibrium, and the quasiergodic hypothesis in high-energy collisions", *Phys. Rev. C* 25 (1982) p 2398.
25. C.M.Ko and I.Xia, "K⁺ π⁺ enhancement in heavy-ion collisions", *Phys. Rev. C* 38 (1988) p. 179.
26. J. Rafelski and B. Müller, *Phys. Rev. Lett.* 48(1982) p 1066; P. Koch, B. Müller and J. Rafelski, *Phys. Rep.* 142 (1986) p 167, C. Greiner, P. Koch and H. Stocker, *Phys. Rev. Lett.* 58 (1987) p 1825;
27. F. Karsch and H.W. Wyld, "Screening of the QCD heavy-quark potential at finite temperature", *Phys. Lett. B* 213 (1988) p 505.
28. R.D. Pisarski, "Phenomenology of the chiral phase transition", *Phys. Lett. B* 110 (1982) p 155
29. T. Matsui and H. Satz, "J/ψ suppression by quark-gluon plasma formation", *Phys. Lett. B* 178 (1986) p 416.
30. M.C. Abreu et al., NA38 collaboration, "The production of J/ψ in 200 GeV/A oxygen-uranium interactions", *Z. Phys. C* 38 (1988) p.117.
31. A. Chodos, R.L. Jaffe, K. Johnson, C.B. Thorn and V.F. Weisskopf, "New extended model of hadrons", *Phys. Rev. D* 9 (1974) p 3471
32. A. Casher, H. Neuberger and S. Nussinov, "Chromoelectric-flux-tube model of particle production", *Phys. Rev. D* 20 (1979) p. 179.
33. J. Schwinger, "On gauge invariance and vacuum polarization" *Phys. Rev.* 82 (1951) p. 664.
34. K. Gottfried, F.E. Low, "Classical space-time concepts in high energy collisions", *Phys. Rev. D* 17 (1978) p. 2487.
35. L. McLerran, "Summary of the hydrodynamics parallel sessions: a layman's review" (part of Quark Matter '83), *Nucl. Phys. A* 418 (1984) p.401.
36. J.D. Bjorken, "Highly relativistic nucleus-nucleus collisions. The central rapidity region", *Phys. Rev. D* 27 (1983) p 140.
37. R. Anishetty, P. Koehler and L. McLerran, "Central collisions between heavy nuclei at extremely high energies: The fragmentation region", *Phys. Rev. D* 22 (1980) p.2793.

38. B. Bassalleck et al , E814, "Transverse energy distributions in Si-nucleus collisions at 10 GeV/nucleon", Z. Phys. C38 (1988) p.45.
39. J. Stachel and P. Braun-Munzinger, "Stopping in high energy nucleus-nucleus collisions. analysis in the Landau hydrodynamic model", Phys Lett. B216(1989) p 1.
40. F. Lamarche and C. Leroy, "Longitudinal expansion of hadronic matter in high energy nuclear collisions", Helios note no 383; F. Lamarche and C. Leroy, "Longitudinal expansion of hadronic matter in high energy nuclear collisions", in Proceedings of the Hadronic Session of the XXIVth Rencontre de Monond, J. Trân Thanh Vân (Editor), Editions Frontières, March 12-18 (1989)
41. T.W. Ludlam and N P Samios "The relativistic heavy ion collider project. a status report", Z. Phys. C38 (1988) p 353
42. C. De Marzo et al., "Multiparticle production on hydrogen, argon and xenon targets in a streamer chamber by 200 GeV/c proton and antiproton beams", Phys. Rev. D26 (1982) p.1019.
43. D. Kisielewska, "Intranuclear cascade in high energy collisions", Acta Phys Pol. B15 (1984) p.1111.
44. A. Shor and R. Longacre, "Effects of secondary interactions in proton-nucleus and nucleus-nucleus collisions using the HIJET event generator", Phys. Lett. B218 (1989) p.100.
45. M.A. Faessler, "Experiments with alpha particles at the CERN intersecting storage rings", Phys. Rep. 115 (1984) p.1.
46. A. Giovannini and L. Van Hove, "Negative binomial multiplicity distributions in high energy hadron collisions" Z. Phys. C30 (1986) p.391.
47. T. Sjöstrand, "The LUND Monte Carlo for jet fragmentation and e^+e^- physics - JETSET version 6.2", Comput. Phys. Commun. 39 (1986) p.347.
48. A. Capella, U. Sukhatme and J. Trân Thanh Vân, "Soft multihadron production from partonic structure and fragmentation functions", Z. Phys C3 (1980) p.329.
49. W.D. Myers, "A model for high-energy heavy-ion collisions", Nucl. Phys. A 296 (1978) p.177.

50. B. Nilsson-Almqvist, "Interactions between hadrons and nuclei. The Lund Monte Carlo - FRITIOF version 1.6 - ", *Comput. Phys. Commun.* 43 (1987) p.387.
51. T. Akesson et al., "Three-jet production in p p collisions at $\sqrt{s} = 63$ GeV and a determination of α_s ", *Z. Phys.* C32 (1986) p.317.
52. C.G. Wohl et al., Particle Data Group, "Review of particle properties", *Rev. Mod. Phys.* 56 (1984) p.61, and references therein.
53. A. Capella and J. Trân Thanh Vân, "A new parton model description of soft hadron-nucleus collisions", *Phys. Lett.* B93 (1980) p.146
54. R. Feynman and R. Field, "Quark Elastic scattering as a source of high-transverse-momentum mesons", *Phys. Rev.* D15 (1977) p.2590.
55. M. Basile et al., "The leading baryon effect in strong, weak and electromagnetic interactions", *Lett. Nuovo Cimento* 32 (1981) p.321
56. J.P. Pansart, "A Monte Carlo for nucleon-nucleus and nucleus-nucleus collisions at very high energies", DPhPE 86-06, Saclay (1986); *Nucl. Phys.* A461 (1987) p.521c.
57. J. Ranft, "Transverse energy distributions in nucleus-nucleus collisions in the dual Monte Carlo multichain fragmentation model", *Phys. Lett.* B188 (1987) p.379
58. A. Bialas, M. Bleszynski and W. Czyz, "Multiplicity distributions in nucleus - nucleus collisions at high energies", *Nucl. Phys.* B111 (1976) p.461.
59. G. Baym, P. Braun-Munzinger and V. Ruuskanen, "Transverse energy production in proton - nucleus and nucleus - nucleus collisions", *Phys. Lett.* B190 (1987) p.29.
60. M.G. Albrow et al., "Negative particle production in the fragmentation region at the CERN ISR", *Nucl. Phys.* B56 (1973) p.333;
M.G. Albrow et al., "Positive particle production in the fragmentation region at the CERN ISR", *Nucl. Phys.* B73 (1974) p.40;
P. Capiluppi et al., "Charged particle production in proton - proton inclusive reactions at very high energies", *Nucl. Phys.* B79 (1974) p.189,
B. Alper et al., "Inclusive spectra of π^{+-} K^{+-} p^{+-} at large angles in proton-proton collisions at the CERN intersecting storage rings", *Nucl. Phys.* B100 (1975) p.237;
K. Guettler et al., "Inclusive production of low momentum charged pions, kaons, protons at $x=0$ at the CERN intersecting storage rings", *Nucl. Phys.* B116 (1976) p.77.

61. A.D. Jackson and H. Boggild, "A model of transverse energy production in high energy nucleus - nucleus collisions", Nucl. Phys. A470 (1987) p.669.
62. E.L. Feinberg, "Initial state formation in the hydrodynamical theory of nucleon-nucleon collisions", Z. Phys C38 (1988) p.229.
63. P. Carruthers and M. Duong-Van, "New scaling law based on the hydrodynamical model of particle production", Phys. Lett. B41 (1972) p.597.
64. M. Gyulassy and T. Matsui, "Quark-gluon-plasma evolution in scaling hydrodynamics", Phys. Rev. D29 (1984) p 419.
65. L. Van Hove, "Quark matter formation and heavy ion collisions, the theoretical situation", in Proceedings of the Quark Matter 1982
66. A.A. Amsden, G.F. Bertsch, F.H. Harlow and J.R. Nix, "Relativistic hydrodynamic theory of heavy-ion collisions", Phys. Rev. Lett. 35 (1979) p.905.
67. F.H. Harlow, A.A. Amsden and J.R. Nix, "Relativistic fluid dynamics calculations with the particle-in-cell technique", J. Comp. Phys. 20 (1976) p.119.
68. P. Danielewicz and G. Odyniec, "Transverse momentum analysis of collective motion in relativistic nuclear collisions", Phys. Lett. B157 (1985) p.146.
69. N. Di Giacomo, "Particle identification in ultrarelativistic nuclear collisions", Nucl. Phys. A461 (1987) p.403c.
70. G. Vasseur, "Low mass muon pairs production in sulfur-nucleus collisions", in Proceedings of the Hadronic Session of the XXIVth Rencontre de Moriond, J. Trân Thanh Vân (editor), Editions Frontières, March 12-18 (1989).
71. Y. Sirois, "Probes of quark matter formation in high energy ^{16}O - nucleus collisions", Ph.D. thesis, McGill University (1988)
72. P. Giubellino et al, "Performance of the silicon ring counters for the HELIOS experiment at CERN", Nucl. Instr. Meth. A275 (1989) p.89.
73. R.H. Beuttenmuller et al., "Performance of a novel silicon detector", Nucl. Inst. Meth. A252 (1986) p.471.
R.H. Beuttenmuller et al., "Silicon position sensitive detectors for the HELIOS (NA34) experiment", Nucl. Inst. Meth. A253 (1987) p.500.

74. T. Akesson et al., "Performance of the uranium/plastic scintillator calorimeter for the HELIOS experiment at CERN", Nucl. Inst. Meth. A262 (1987) p.243
75. F. Lamarche and Y. Sirois, "1986 Calibration of HELIOS calorimeters", Helios note 204 (1987)
76. M. Murray, "Uranium liquid argon calorimeter", Helios note 174 (1985)
77. C. Leroy, Y. Sirois and R. Wigmans, "An experimental study of the contribution of nuclear fission to the signal of uranium hadron calorimeters", Nucl. Inst. Meth. A252 (1986) p.4.
78. R. Wigmans, "On the energy resolution of uranium and other hadron calorimeters", Nucl. Inst. Meth. A259 (1987) p.389.
79. F. Corneveau, "Trigger weight calculations", Helios note 91 (1985)
80. S. Dagan, "PROPHET calorimeter simulation program", Helios note 184 (1986).
81. R.K. Bock, T. Hansl-Kozanecka and T.P. Shah, "Parametrization of the longitudinal development of hadronic showers in sampling calorimeters", Nucl. Inst. Meth. 186 (1981) p.533.
82. A. Bamberger et al., NA35 Collaboration, "Multiplicity and transverse energy in $^{16}\text{O} + \text{Pb}$ at 200 GeV per nucleon", Phys. Lett. B184 (1987) p.271.
83. S. Dagan, " T_{\perp} evaluation in the ULAC hadronic (a maximum entropy method)", Helios note 306 (1988).
84. C.W. Fabjan, "Calorimetry in high-energy physics", in "Techniques and concepts of high energy physics III", ed by T. Ferbel, (Plenum, 1985) p.295
85. T. Akesson et al., HELIOS collaboration, "The transverse energy distributions in ^{16}O -nucleus collisions at 60 and 200 GeV per nucleon", Z. Phys. C38 (1988) p.383.
86. T. Akesson et al., HELIOS collaboration, "The transverse energy distributions of ^{32}S -nucleus collisions at 200 GeV per nucleon", Phys. Lett. B214 (1988) p.295.
87. T. Akesson et al., HELIOS collaboration, "The measurement of the transverse energy flow in nucleus-nucleus collisions at 200 GeV per nucleon", to be submitted to Phys. Lett. B

88. T. Akesson et al., HELIOS collaboration, "Charged particle multiplicity distributions in oxygen-nucleus collisions at 60 and 200 GeV per nucleon", (to be) submitted to Phys. Lett. B
89. F. Lamarche and C. Leroy, "Fast evaluation of the number of wounded nucleons by elliptic integrals", submitted to J. Comp. and Appl. Math.
90. E. Andersen et al., NA36 collaboration, "A measurement of cross-section for ^{32}S interactions with Al, Fe, Cu, Ag, and Pb at 200 GeV/c per nucleon", Phys. Lett. B220 (1989) p 328.
91. P. Sorensen et al., WA80 collaboration, "Oxygen induced reactions at 60A and 200A GeV studied by calorimetry", Z. Phys. C38 (1988) p 3.
92. R. Albrecht et al., WA80 Collaboration, "Charged-particle distributions in ^{16}O induced nuclear reactions at 60 and 200 A GeV", Phys. Lett. B202 (1988) p 596.
93. A. Bamberger et al., NA35 Collaboration, "Study of the energy flow in ^{16}O - nucleus collisions at 60 and 200 GeV/nucleon", Z. Phys. C38 (1988) p.19.
94. A. Dar and J. Vary, "Method to distinguish between multiparticle production mechanisms", Phys. Rev. D6, 2412 (1972)
95. M. Neubert, "Kinematical relations between transverse energy and multiplicity distributions", Helios note 275 (1988).
96. F. Lamarche and J. Hébert, "Central collisions of an unequal-mass pair of nuclei at 1.5 GeV/nucleon", Phys. Lett. B182 (1986) p.395.
97. M. McCubbin, "A search for quark-gluon plasma in high-energy ^{16}O -W collisions", Ph.D. thesis, University of London (1989).
98. E.V. Shuryak, "The QCD vacuum and the quark-gluon plasma", Z. Phys. C38 (1988) p.141.
99. T.J. Humanic et al., "Pion interferometry with ultrarelativistic heavy-ion collisions from the NA35 experiment", Z. Phys. C38 (1988) p.79.
100. J.W. Harris et al., "Recent Results from the NA35 collaboration at CERN", Proceedings of the 7th Int. Conf. on Ultrarelativistic Nucleus-Nucleus Collisions (Quark Matter '88) Lennox (Mass.), USA 26 - 30 September 1988 (to appear in Nucl. Phys. A)

101. H.R. Schmidt et al, WA80 collaboration, "Target fragmentation in proton-nucleus and ^{16}O -nucleus reactions at 60 and 200 GeV nucleon", *Z. Phys. C* 38 (1987) p 109.
102. W. Busza and A.S. Goldhaber, "Nuclear stopping power", *Phys. Lett.* B139 (1984) p 235
103. H. Å. Gustafsson et al, "Nucleus-nucleus collisions at relativistic energies", in Proceedings of the Hadronic Session of the XVIIIth Rencontre de Moriond, J. Trân Thanh Vân (editor), Editions Frontières, March 13-19 (1988)
104. J. Schukraft et al, HELIOS collaboration, "Measurement of multiplicity distributions in oxygen-tungsten collisions at 200 GeV per nucleon", *Z. Phys. C* 38 (1987) p 63
105. R. Albrecht et al, WA80 collaboration, "Photon and neutral pion distributions in 60 and 200 A GeV ^{16}O + nucleus and proton + nucleus reactions", *Phys. Lett.* B201 (1988) p 390
106. D. Rohrlich, NA35 collaboration, in Proceedings of the Hadronic Session of the XXIVth Rencontre de Moriond, J. Trân Thanh Vân (editor), Editions Frontières, March 12-18 (1989)
107. F. Lamarche et al, HELIOS collaboration, in Proceedings of the Hadronic Session of the XXIII^d Rencontre de Moriond, J. Trân Thanh Vân (editor), Editions Frontières, March 13-19 (1988).